

EFFECT OF TRANSITION METAL SUBSTITUTION AND THERMAL  
TREATMENT ON MAGNETIC PROPERTIES AND CATION  
DISTRIBUTION IN THE M DOPED COBALT  
FERRITES (M = Mn, Cu, Zn)



A THESIS SUBMITTED IN PARTIAL FULFILLMENT  
OF THE REQUIREMENT FOR THE DEGREE OF  
DOCTOR OF PHILOSOPHY IN NANOSCIENCE AND NANOTECHNOLOGY  
COLLEGE OF NANOTECHNOLOGY  
KING MONGKUT'S INSTITUTE OF TECHNOLOGY LADKRABANG

2017

KMITL-2017-NT-D-001-003

This material is reserved for educational use only, not allowed for commercial use.

Forbidden to modify the content, and cite the document when use.

ผลของการแทนที่ด้วยโลหะทรานสิชันและอิทธิพลทางความร้อนที่มีต่อสมบัติ  
แม่เหล็กและการกระจายตัวของไอออนบวกในโคบอลเฟอร์ไรต์  
เจือด้วยแมงกานีส ทองแดง และสังกะสี

Effect of Transition Metal Substitution and Thermal Treatment  
on Magnetic Properties and Cation Distribution in the  
M Doped Cobalt Ferrites (M = Mn, Cu, Zn)



วิทยานิพนธ์นี้เป็นส่วนหนึ่งของการศึกษาตามหลักสูตรปริญญาปรัชญาดุษฎีบัณฑิต  
สาขาวิชานาโนวิทยาและนาโนเทคโนโลยี  
วิทยาลัยเทคโนโลยีพระจอมเกล้าเจ้าคุณทหารลาดกระบัง

พ.ศ. 2560

KMITL-2017-NT-D-001-003

This material is reserved for educational use only, not allowed for commercial use.

Forbidden to modify the content, and cite the document when use.



**COPYRIGHT 2017**

**COLLEGE OF NANOTECHNOLOGY**

**KING MONGKUT'S INSTITUTE OF TECHNOLOGY LADKRABANG**

This material is reserved for educational use only, not allowed for commercial use.

Forbidden to modify the content, and cite the document when use.

Thesis Title	Effect of Transition Metal Substitution and Thermal Annealing on Magnetic Properties and Cation Distribution in the M Doped Cobalt Ferrites (M = Mn, Cu, Zn)
Student	Rachanusorn Roongtao
Student ID	54670106
Degree	Doctor of Philosophy
Program	Nanoscience and Nanotechnology
Year	2017
Thesis Advisor	Assoc. Prof. Dr. Naratip Vittayakorn
Thesis Coadvisor	Dr. Wantana Klysubun

## ABSTRACT

This research investigated the relationships between the substituted transition metal and thermal annealing on the cation distribution in the spinel ferrites of  $\text{CoM}_x\text{Fe}_{2-x}\text{O}_4$  (where M = Mn, Cu, or Zn) system. Dense ceramics were prepared by the solid state reaction method. To investigate the cation distribution in octahedral/tetrahedral hole in the spinel structure, the solubility limit of the binary spinel compound was considered. Afterwards, the effect of thermal annealing at different temperatures, time, and atmosphere on the cation distribution were also investigated. The structure and lattice parameter of the samples were determined by the X-ray diffraction (XRD) and Rietveld refinement method. The local structure information was investigated by X-ray absorption spectroscopy techniques. This research found that, the distribution of cation on the octahedral or tetrahedral site in a spinel structure was significantly influenced by the composition, difference type of transitions metal and thermal annealing temperature. Furthermore, the results of extended X-ray absorption fine structure (EXAFS) analysis exhibited that thermal annealing at suitable temperatures and time in air influenced to increase cation migration on their site preference.

**Keywords :** Cobalt Ferrite Doping, Cation Distribution, XAS technique

This material is reserved for educational use only, not allowed for commercial use.

Forbidden to modify the content, and cite the document when use.

หัวข้อวิทยานิพนธ์	ผลของการแทนที่ด้วยโลหะทรานสิชั่นและอิทธิพลทางความร้อนที่มีต่อสมบัติแม่เหล็กและการกระจายตัวของไอออนบวกในโคบอลเฟอร์ไรต์เจือด้วยแมงกานีส ทองแดง และสังกะสี
นักศึกษา	ราชานุสรณ์ รุ่งเต่า
รหัสประจำตัว	54670106
ปริญญา	ปรัชญาดุษฎีบัณฑิต
สาขาวิชา	นาโนวิทยาและนาโนเทคโนโลยี
พ.ศ.	2560
อาจารย์ที่ปรึกษาวิทยานิพนธ์	รศ. ดร. นราธิป วิทยากร
อาจารย์ที่ปรึกษาวิทยานิพนธ์ร่วม	ดร. วันทนา คล้ายสุบรรณ

### บทคัดย่อ

งานวิจัยนี้ได้ทำการศึกษาความสัมพันธ์ระหว่างการแทนที่ด้วยโลหะทรานสิชั่น และกระบวนการทางความร้อนที่มีต่อการกระจายตัวของไอออนบวกของสารประกอบสปีเนลเฟอร์ไรต์ในระบบ  $\text{CoM}_x\text{Fe}_{2-x}\text{O}_4$  เมื่อ M คือแมงกานีส ทองแดง หรือสังกะสี โดยทำการเตรียมด้วยวิธีปฏิกิริยาสถานะของแข็ง งานวิจัยศึกษาการกระจายตัวของไอออนบวกในช่องว่างออกตรอะตอมและเตตระอะตอมในโครงสร้างสปีเนล รวมทั้งจุดอิมิตัวการละลายของสารประกอบทวิสปีเนล หลังจากนั้นได้ทำการพิจารณาผลของกระบวนการทางความร้อนที่มีต่อการกระจายตัวของไอออนบวกที่อุณหภูมิและระยะเวลาในการเผาของอากาศต่างๆ โดยทำการวิเคราะห์โครงสร้างผลึกและค่าแลตทิซของสารตัวอย่างด้วยเทคนิคการเลี้ยวเบนของรังสีเอ็กซ์และวิธีรีทเวคเตอร์ไฟลเมนต์ รวมทั้งหาตำแหน่งของไอออนบวกในโครงสร้างด้วยเทคนิคการดูดกลืนของรังสีเอ็กซ์ งานวิจัยนี้พบว่าอิทธิพลของสัดส่วนองค์ประกอบ ชนิดของโลหะทรานสิชั่น และอุณหภูมิที่ใช้ในกระบวนการทางความร้อนที่แตกต่างกัน มีผลต่อการกระจายตัวของไอออนบวกในตำแหน่งออกตรอะตอม และเตตระอะตอมในโครงสร้างสปีเนล นอกจากนี้ผลการวิเคราะห์โครงสร้างโดยละเอียดของการดูดกลืนรังสีเอ็กซ์แสดงให้เห็นว่าอุณหภูมิและเวลาที่เหมาะสมในบรรยากาศปกติในกระบวนการทางความร้อนมีผลทำให้ไอออนบวกย้ายไปอยู่ในตำแหน่งที่ต้องการมากขึ้น

**คำสำคัญ :** การเจือโคบอลเฟอร์ไรต์ การกระจายตัวของไอออนบวก เทคนิคการดูดกลืนรังสีเอ็กซ์

## ACKNOWLEDGEMENT

This thesis had been accomplished in the Electroceramics Research Laboratory (ECRL), College of Nanotechnology, King Mongkut's Institute of Technology Ladkrabang, Bangkok, Thailand and supported with the scholarship by the Synchrotron Light Research Institute (Public Organization), SLRI.

First of all, I would like to thank Assoc. Prof. Dr. Naratip Vittayakorn, my research supervisor for the valuable suggestions, good supervisions, and all support he has given me throughout my education. Also, I would like to thank Asst. Prof. Dr. Wanwilai Vittayakorn for all kindly advices, helpful suggestions, and great opportunities.

I would like to thank Dr. Wantana Klysubun, my research co-supervisor and the beamline manager of beamline 8 at SLRI for useful advice, constructive recommendations, and continual support in the X-ray absorption spectroscopy analysis.

I would like to acknowledge Asst. Prof. Dr. Pongsakorn Jantaratana, Department of Physics, Faculty of Science, Kasetsart University for his permission to use their Vibrating Sample Magnetometer (VSM).

Finally, I am very grateful to my parents and my family for their support, understanding, and encouragement throughout my educational life.

**Rachanusorn Roongtao**

## TABLE OF CONTENTS

	Page
ABSTRACT (ENGLISH)	I
ABSTRACT (THAI)	II
ACKNOWLEDGEMENTS	III
TABLE OF CONTENTS	IV
LIST OF TABLES	VII
LIST OF FIGURES	X
ABBREVIATIONS AND SYMBLOS	XVIII
CHAPTER 1 INTRODUCTION	1
1.1 Overview	1
1.2 Scope of this work	2
1.3 Objectives of this work	3
References	4
CHAPTER 2 LITERATURE REVIEWS	6
2.1 Spinel Ferrite	6
2.1.1 Spinel Ferrite Structure	6
2.1.2 Site Preferences of the Ions	7
2.1.3 Number of Unpaired Electron	10
2.1.4 Superexchange Interaction	11
2.1.5 Structural Anisotropy	13
2.1.6 Catalyst	15
2.2 Ferrite Literature Reviews	22
2.2.1 Metals Ferrite	22
2.2.2 Cobalt Ferrite Substitution	25
2.3 Thermal Annealing	37
2.3.1 General Heat Treating Processes	38
2.3.2 Annealing Processes	39

This material is reserved for educational use only, not allowed for commercial use.

Forbidden to modify the content, and cite the document when use.

	Page
2.4 X-Ray Absorption Spectroscopy (XAS) Technique	45
2.4.1 X-Ray Absorption and Fluorescence	45
2.4.2 XANES Interpretation	52
2.4.3 EXAFS Interpretation	57
References	75
<b>CHAPTER 3 EXPERIMENTAL PROCEDURES</b>	<b>79</b>
3.1 Sample Preparation	79
3.1.1 Powder Preparation	79
3.1.2 Ceramic Fabrication	83
3.2 Sample Annealing	85
3.2.1 Effects of Annealing Temperature	85
3.2.2 Annealing Atmosphere	85
3.2.3 Annealing Time	86
3.3 Sample Characterization	86
3.3.1 Phase Analysis	86
3.3.2 Densification Analysis	87
3.3.3 Scanning Electron Microscopy (SEM)	88
3.3.4 X-ray Absorption Spectroscopy (XAS)	88
3.3.5 Vibrating Sample Magnetometer (VSM)	89
3.3.6 Ultraviolet–Visible Spectrophotometer (UV-Vis)	90
References	92
<b>CHAPTER 4 RESULTS AND DISCUSSION</b>	<b>93</b>
4.1 Effect of Transition Metal Substitution	93
4.1.1 $\text{CoFe}_{2-x}\text{Mn}_x\text{O}_4$ System	93
4.1.2 $\text{CoFe}_{2-x}\text{Cu}_x\text{O}_4$ System	108
4.1.3 $\text{CoFe}_{2-x}\text{Zn}_x\text{O}_4$ System	124
4.2 Effect of Thermal Treatment	138
4.2.1 $\text{CoFe}_{2-x}\text{Mn}_x\text{O}_4$ System	138

	Page
4.2.2 CoFe <sub>2-x</sub> Cu <sub>x</sub> O <sub>4</sub> System	156
4.2.3 CoFe <sub>2-x</sub> Zn <sub>x</sub> O <sub>4</sub> System	164
References	168
CHAPTER 5 CONCLUSIONS	171
APPENDIX	
BIOGRAPHY	



## LIST OF TABLES

Table	Page
2.1 Crystal field stabilization energies for metal cation transition on tetrahedral and octahedral spinel sites	9
2.2 Outer-shell electron configuration and number of unpaired electrons for several spinel-forming ions	11
2.3 The anisotropic constants of all significant ferrites	14
2.4 The oxidation potential scale	20
2.5 Color reduction of synthetic dyes after 24 hours treatment with catalysts	22
2.6 The average particle sizes, saturated magnetization, remanence magnetic, $M_r/M_s$ ratio, and coercive field in $\text{CoFe}_2\text{O}_4$ samples synthesized in various conditions	24
2.7 Rietveld refinement parameters of $\text{MnFe}_2\text{O}_4$ nanocrystalline from neutron powder diffraction data	40
2.8 Apparent multiplicities in EXAFS, based on the general expression; $(\text{A}_{1-x}\text{B}_x)_{\text{tet}}(\text{A}_x\text{B}_{2-x})_{\text{oct}}\text{O}_4$ , where A is the divalent, B the trivalent cation, and x the inversion parameter	69
2.9 Results of EXAFS Co K-edge curve-fitting	70
2.10 The interatomic lengths, $R$ , coordination numbers, $N$ , and Debye-Waller Factors ( $\sigma$ ) for $\text{CoFe}_2\text{O}_4$ at the Co and Fe K-edge	72
2.11 The interatomic distances, $R$ , coordination numbers, $N$ , and Debye-Waller Factors ( $\sigma$ ) for A10_900 and A5_900 at the Co and Fe K-edge	73
3.1 Specifications of the starting materials used in this study	79
4.1 Lattice constant ( $a$ ) and Rietveld refinement result of $\text{CoFe}_{2-x}\text{Mn}_x\text{O}_4$ powders calcined at 900 °C for 48 h	96

Table	Page
4.2 Magnetic properties and Bohr magneton of $\text{CoFe}_{2-x}\text{Mn}_x\text{O}_4$ powders calcined at 900 °C for 48 h	102
4.3 Cation distribution and Bohr magneton result of $\text{CoFe}_{2-x}\text{Mn}_x\text{O}_4$ powders calcined at 900 °C for 48 h	104
4.4 Lattice constant ( $a$ ) and Rietveld refinement result of $\text{CoFe}_{2-x}\text{Cu}_x\text{O}_4$ powders calcined at 900 °C for 48 h	112
4.5 Magnetic properties and Bohr magneton of $\text{CoFe}_{2-x}\text{Cu}_x\text{O}_4$ powders calcined at 900 °C for 48 h	114
4.6 Cation distribution and Bohr magneton result of $\text{CoFe}_{2-x}\text{Cu}_x\text{O}_4$ powders calcined at 900 °C for 48 h	115
4.7 The $E_0$ value of $\text{CoFe}_{1.75}\text{Cu}_{0.25}\text{O}_4$ sample calcined at 900 °C for 48 h in air and the various standard	121
4.8 Degradation result of $\text{CoFe}_{2-x}\text{Cu}_x\text{O}_4$ powders calcined at 900 °C for 48 h	123
4.9 Lattice constant ( $a$ ) and Rietveld refinement result of $\text{CoFe}_{2-x}\text{Zn}_x\text{O}_4$ powders calcined at 900 °C for 48 h	127
4.10 Magnetic properties and Bohr magneton of $\text{CoFe}_{2-x}\text{Zn}_x\text{O}_4$ calcined at 900 °C for 48 h	130
4.11 Cation distribution and Bohr magneton result of $\text{CoFe}_{2-x}\text{Zn}_x\text{O}_4$ powders calcined at 900 °C for 48 h	131
4.12 The $E_0$ value of $\text{CoFe}_{1.9}\text{Zn}_{0.1}\text{O}_4$ sample calcined at 900 °C for 48 h in air and the various standard	136
4.13 Average particle size of $\text{CoFe}_{0.9}\text{Mn}_{1.1}\text{O}_4$ powders as a function of annealing temperatures for 100 h in air	141
4.14 Average particle size of $\text{CoFe}_{0.9}\text{Mn}_{1.1}\text{O}_4$ as a function of annealing time	144
4.15 Magnetic properties and Bohr magneton of $\text{CoFe}_{0.9}\text{Mn}_{1.1}\text{O}_4$ powders as a function of annealing temperatures for 100 h in air	145
4.16 Magnetic properties and Bohr magneton of $\text{CoFe}_{0.9}\text{Mn}_{1.1}\text{O}_4$ powders as a function of annealing time	149

Table	Page
4.17 The $E_0$ value of $\text{CoFe}_{0.90}\text{Mn}_{1.10}\text{O}_4$ sample annealed at 500 °C for 100 h in difference atmosphere and the various standard	154
4.18 Average particle size of $\text{CoFe}_{1.75}\text{Cu}_{0.25}\text{O}_4$ as a function of annealing time	158
4.19 Degradation of $\text{CoFe}_{1.75}\text{Cu}_{0.25}\text{O}_4$ powders as a function of annealing time	162
4.20 Average particle size of $\text{CoFe}_{1.45}\text{Zn}_{0.55}\text{O}_4$ as a function of annealing time	166



## LIST OF FIGURES

Figure	Page
2.1 The two subcell types in a unit cell of the spinel structure	7
2.2 Diagram presenting site occupation in (a) normal spinels, and (b) inverse spinels	8
2.3 Angles and interionic distances in different types of spinel structure for lattice site interactions	12
2.4 The low index planes of a normal spinel structure: oxygen anions, octahedral cations, and tetrahedral cations	17
2.5 Double pH drops	20
2.6 Time course to decolorization of Chicago Sky Blue in the catalysts and H <sub>2</sub> O <sub>2</sub> . Catalyst; MnO•Fe <sub>2</sub> O <sub>3</sub> , FeO•Fe <sub>2</sub> O <sub>3</sub> , CuO•Fe <sub>2</sub> O <sub>3</sub> , and CoO•Fe <sub>2</sub> O <sub>3</sub>	21
2.7 <i>M</i> and <i>H</i> curves of cobalt ferrite synthesized at 300 K by: (a) solid state reaction (b) citrate gel, and (c) polymer complex	23
2.8 (a) X-ray diffraction and (b) magnetic curves of the synthesized inverse spinel ferrite nanoparticles	25
2.9 The coercivities and saturated magnetization of Co <sub>0.9</sub> Mn <sub>0.1</sub> Fe <sub>2</sub> O <sub>4</sub> powders at different annealing temperatures	26
2.10 Microstructures of the CoMn <sub>x</sub> Fe <sub>2-x</sub> O <sub>4</sub> samples, where <i>x</i> = (a) 0.00, (b) 0.30, (c) 0.40, and (d) 0.60	27
2.11 VSM results for CoMn <sub>x</sub> Fe <sub>2-x</sub> O <sub>4</sub> samples	27
2.12 Magnetic curves of the samples, (a) MnFe <sub>2</sub> O <sub>4</sub> , (b) Mn <sub>0.5</sub> Co <sub>0.5</sub> Fe <sub>2</sub> O <sub>4</sub> , and (c) CoFe <sub>2</sub> O <sub>4</sub> , at room temperature	28
2.13 The Hysteresis loop of Co <sub>0.5</sub> Mn <sub>0.5</sub> Fe <sub>2</sub> O <sub>4</sub> nanoparticles calcinated at various temperatures; (a) 500°C, (b) 700°C, and (c) 900°C	29
2.14 The coercive force at different particle sizes	29
2.15 Saturated and remnant magnetization and coercivity for Mn <sub>0.1</sub> Co <sub>0.9</sub> Fe <sub>2</sub> O <sub>4</sub> as a function of temperature	30

Figure	Page
2.16 M–H Curves of $Mn_xCo_{1-x}Fe_2O_4$ nanoparticles at 10 K (a) and 300 K (b)	31
2.17 Difference of composition in the coercive field (a) and remanent magnetization (b) of $Mn_xCo_{1-x}Fe_2O_4$ nanoparticles	32
2.18 SEM morphology of $Co_xZn_{1-x}Fe_2O_4$ : (a) $x = 0.2$ , (b) $x = 0.4$ , and (c) $x = 0.8$	33
2.19 Magnetic hysteresis loops of $Co_xZn_{1-x}Fe_2O_4$ nanoparticles at 10 K	33
2.20 Saturated magnetization of varied Cu content at room temperature	34
2.21 Coercive field of varied Cu content at room temperature	35
2.22 SEM of $CoFe_{2-x}Cu_xO_4$ , where $x = 0.0-0.4$ nanoparticles	36
2.23 M–H curves of $CoFe_{2-x}Cu_xO_4$ ( $x = 0.0-0.3$ ) nanoparticles at room temperature	37
2.24 Calculated relative percentages of $Mn^{3+}$ and $Mn^{2+}$	41
2.25 SEM of 0.9PZT-0.1PZN samples (a) before annealing, (b) after annealing	42
2.26 The relative permittivity of temperature dependence before and after annealing samples at various frequencies	42
2.27 Electrical field and polarization of 0.9PZT-0.1PZN ceramics for non and annealed samples	43
2.28 TEM results of $Co_{1-x}Mn_xFe_2O_4$ powders annealed at 500°C	43
2.29 The M-H curve of $Co_{1-x}Mn_xFe_2O_4$ measured at various temperatures	44
2.30 The photo-electric effect on the absorbed X-ray photon, and the core level electron advancing from an atom	45
2.31 XAS measurements; an incident ray of monochromatic X-rays with $I_0$ intensity crossing through the sample of $t$ thickness and transmission ray with $I$ intensity	46
2.32 XAS measured spectrum presenting EXAFS and XANES regions	47

Figure	Page
2.33 The EXAFS phenomenon; outgoing photoelectron of the X-ray absorbed atom and backscattering photoelectron from the adjacent atom	48
2.34 Display of $\mu(E)$ of the $\Delta\mu_0$ edge-step and smooth background of $\mu_0(E)$	49
2.35 The $\chi(k)$ EXAFS of FeO, and the $k$ -weight EXAFS, $k^2\chi(k)$	50
2.36 Background subtraction, normalizing at the $k^3$ -weight of the Mo K-edge	51
2.37 Fourier transformation (solid curve) of Mo K-edge EXAFS	52
2.38 The Fe K-edge of Fe metal and some Fe compounds in XANES spectra	52
2.39 The Cr K-edge of XANES spectra in $\text{Cr}^{6+}$ and $\text{Cr}^{3+}$ oxides	53
2.40 The Fe K-edge of XANES spectra in Fe metal and many Fe oxides	54
2.41 (a) XANES spectra of Co075 and $\text{Co}_3\text{O}_4$ samples; (b) amplified picture of the Co K-edge profile in the same design as (a)	55
2.42 The XANES spectrum at the Co K-edge of CoO and Co075 samples	55
2.43 XANES curves close to the Fe K-edge of Mn–Zn samples. XANES spectra of H and L samples correlate with the iron foil, FeO and $\text{Fe}_2\text{O}_3$	56
2.44 XANES curves close to the Zn K-edge of Mn–Zn samples. XANES spectra of H and L samples correlate with the zinc foil and ZnO	56
2.45 XANES curves close to the Mn K-edge of Mn–Zn ferrites. XANES spectra of H and L samples correlate with MnO and $\text{Mn}_2\text{O}_3$	57
2.46 Fourier transformed from Fe EXAFS of the $\text{Ni}_{0.15}\text{Zn}_y\text{Fe}_{2.85-y}\text{O}_4$ films. All spectra were gained by a $k$ range of $2.5\text{--}12.4 \text{ \AA}^{-1}$ and $k^3$ weighting	58

Figure	Page
2.47 Picture (a), (c), and (e) including EXAFS data of the $\text{Ni}_{0.15}\text{Zn}_{0.16}\text{Fe}_{2.69}\text{O}_4$ sample. Picture (b), (d), and (f) showing trends of cation site occupancy	59
2.48 Saturated magnetization at difference Zn content	60
2.49 Fourier transformation of radial coordination versus Zn and Fe EXAFS data	61
2.50 The Fourier transformation of measurement data (dots) and the best fit (line) of Zn and Fe EXAFS results	62
2.51 The Fourier transformation of Fe EXAFS data for copper ferrite nanoparticles and standard samples	64
2.52 The Fourier transformation of Cu EXAFS data for copper ferrite nanoparticles and standard samples	64
2.53 Temperature versus $\Delta H_c$ of ferrite nanoparticles with various average sizes	65
2.54 (a) The Fourier transformation of Co EXAFS spectra at varied radius coordination, (b) the Fourier transformation of Fe EXAFS spectra at varied radius coordination	66
2.55 Experimental (—) and calculated (--) $k^3$ -weighted Fe EXAFS and its Fourier transformation for (a) CoFe(39) and (b) CoFe(16) ( $k$ -range, 2-12 $\text{\AA}^{-1}$ )	67
2.56 Experimental (—) and calculated (--) $k^3$ -weighted Co EXAFS and its Fourier transformation for (a) CoFe(39) and (b) CoFe(16) ( $k$ -range, 2-13 $\text{\AA}^{-1}$ )	68
2.57 The Fourier transformation of Fe K-edge, A, and Co K-edge, B, for A10 sample fitting results (•••) and experiment (—). (A) (s3) A10_900, (c) $\text{CoFe}_2\text{O}_4$ and (B) (s3) A10_900, and(c) $\text{CoFe}_2\text{O}_4$	71
3.1 Mixing and calcination processes for powder preparation	80
3.2 The processing route for $\text{CoFe}_{(2-x)}\text{Mn}_x\text{O}_4$ powders	81
3.3 The processing route for $\text{CoFe}_{(2-x)}\text{Cu}_x\text{O}_4$ powders	82
3.4 The processing route for $\text{CoFe}_{(2-x)}\text{Zn}_x\text{O}_4$ powders	83
3.5 Sample arrangement of the sintering process	84

This material is reserved for educational use only, not allowed for commercial use.

Forbidden to modify the content, and cite the document when use.

Figure	Page
3.6 The processing route for ceramic fabrication	84
3.7 The processing route for different annealing temperatures	85
3.8 The processing route for a different annealing atmosphere	85
3.9 The processing route for different annealing times	86
3.10 X-ray diffractometer	87
3.11 Scanning electron microscope	88
3.12 X-ray absorption spectroscopy	89
3.13 Vibrating sample magnetometer	90
3.14 UV-Visible spectrophotometer	91
4.1 X-ray diffraction patterns of $\text{CoFe}_{2-x}\text{Mn}_x\text{O}_4$ powders calcined at 900 °C for 48 h	94
4.2 X-ray diffraction patterns and the structure refinement of $\text{CoFe}_{2-x}\text{Mn}_x\text{O}_4$ powders calcined at 900 °C for 48 h	95
4.3 Lattice constant of $\text{CoFe}_{2-x}\text{Mn}_x\text{O}_4$ powders calcined at 900 °C for 48 h	97
4.4 The magnetic hysteresis loop of $\text{CoFe}_{2-x}\text{Mn}_x\text{O}_4$ powders as a function of compositions calcined at 900 °C for 48 h	99
4.5 Variations of saturated magnetization and coercivities for $\text{CoFe}_{2-x}\text{Mn}_x\text{O}_4$ powders as a function of compositions calcined at 900 °C for 48 h	100
4.6 Magnetic hysteresis loop of a magnet measured with field applied along the easy and hard axis	101
4.7 Variations of saturated magnetization and Bohr magneton for $\text{CoFe}_{2-x}\text{Mn}_x\text{O}_4$ powders as a function of compositions calcined at 900 °C for 48 h	103
4.8 The FT of (a) Co, (b) Fe, and (c) Mn EXAFS data for the $\text{CoFe}_{2-x}\text{Mn}_x\text{O}_4$ powders calcined at 900 °C for 48 h	107
4.9 X-ray diffraction of $\text{CoFe}_{2-x}\text{Cu}_x\text{O}_4$ powders calcined at 900 °C for 48 h	109
4.10 X-ray diffraction patterns and the structure refinement of $\text{CoFe}_{2-x}\text{Cu}_x\text{O}_4$ powders calcined at 900 °C for 48 h	110

This material is reserved for educational use only, not allowed for commercial use.

Forbidden to modify the content, and cite the document when use.

Figure	Page
4.11 Lattice constant of $\text{CoFe}_{2-x}\text{Cu}_x\text{O}_4$ powders calcined at 900 °C for 48 h	111
4.12 The magnetic hysteresis loop of $\text{CoFe}_{2-x}\text{Cu}_x\text{O}_4$ powders as a function of compositions calcined at 900 °C for 48 h	113
4.13 Variations of saturated magnetization and coercivities for $\text{CoFe}_{2-x}\text{Cu}_x\text{O}_4$ powders as a function of compositions calcined at 900 °C for 48 h	114
4.14 Trend of saturated magnetization and Bohr magneton for $\text{CoFe}_{2-x}\text{Cu}_x\text{O}_4$ powders calcined at 900 °C for 48 h	116
4.15 The FT of (a) Co, (b) Fe, and (c) Cu EXAFS data for the $\text{CoFe}_{2-x}\text{Cu}_x\text{O}_4$ powders calcined at 900 °C for 48 h	118
4.16 XANES spectra of $\text{CoFe}_{1.75}\text{Cu}_{0.25}\text{O}_4$ samples and the standards obtained at (a) Co K-edge, (b) Fe K-edge and (c) Cu K-edge	120
4.17 Decrease of color after 24 h treatment of reactive orange 16 With $\text{CoFe}_{2-x}\text{Cu}_x\text{O}_4$ catalysts	122
4.18 X-ray diffraction patterns of $\text{CoFe}_{2-x}\text{Zn}_x\text{O}_4$ powders calcined at 900 °C for 48 h	125
4.19 X-ray diffraction patterns and the structure refinement of $\text{CoFe}_{2-x}\text{Zn}_x\text{O}_4$ powders calcined at 900 °C for 48 h	126
4.20 Lattice constant of $\text{CoFe}_{2-x}\text{Zn}_x\text{O}_4$ powders calcined at 900 °C for 48 h	128
4.21 Magnetic hysteresis loops of $\text{CoFe}_{2-x}\text{Zn}_x\text{O}_4$ powders at room temperature	129
4.22 Variations of saturated magnetization and coercivities for $\text{CoFe}_{2-x}\text{Zn}_x\text{O}_4$ powders as a function of compositions calcined at 900 °C for 48 h	130
4.23 Trend of saturated magnetization and Bohr magneton for $\text{CoFe}_{2-x}\text{Zn}_x\text{O}_4$ powders calcined at 900 °C for 48 h	132
4.24 The FT of (a) Co, (b) Fe, and (c) Zn EXAFS data for the $\text{CoFe}_{2-x}\text{Zn}_x\text{O}_4$ powders calcined at 900 °C for 48 h	134

Figure	Page
4.25 XANES spectra of $\text{CoFe}_{1.9}\text{Mn}_{0.1}\text{O}_4$ samples and the standards obtained at (a) Co K-edge, (b) Fe K-edge and (c) Zn K-edge	137
4.26 The SEM micrographs of $\text{CoFe}_{0.90}\text{Mn}_{1.10}\text{O}_4$ powders annealed at (a) non annealing (b) 400 , (c) 500, (d) 600, and (e) 700 °C for 100 h in air	140
4.27 SEM micrographs of $\text{CoFe}_{0.90}\text{Mn}_{1.10}\text{O}_4$ powders with (a) no annealing, (b) annealing at 500 °C for 4 h and (c) annealing at 500 °C for 100 h	143
4.28 The magnetic hysteresis loop of $\text{CoFe}_{0.90}\text{Mn}_{1.10}\text{O}_4$ powders as a function of annealing temperature for 100 h in air	145
4.29 Variations of saturated magnetization and coercivity of $\text{CoFe}_{0.90}\text{Mn}_{1.10}\text{O}_4$ powders as a function of annealing temperature for 100 h in air	146
4.30 Saturated magnetization and Bohr magneton of $\text{CoFe}_{0.90}\text{Mn}_{1.10}\text{O}_4$ powders as a function of annealing temperature for 100 h in air	147
4.31 Magnetic hysteresis loops of $\text{CoFe}_{0.90}\text{Mn}_{1.10}\text{O}_4$ powders without annealing, and with annealing at 500 °C for 4 and 100 h	148
4.32 Variations of saturated magnetization and coercivities for $\text{CoFe}_{0.90}\text{Mn}_{1.10}\text{O}_4$ powders as a function of annealing time	149
4.33 Variations of saturated magnetization and Bohr magneton for $\text{CoFe}_{0.90}\text{Mn}_{1.10}\text{O}_4$ powders as a function of annealing time	150
4.34 Fourier transformation of (a) Co, (b) Fe and (c) Mn EXAFS data for $\text{CoFe}_{0.90}\text{Mn}_{1.10}\text{O}_4$ powders	152
4.35 XANES spectra of $\text{CoFe}_{0.90}\text{Mn}_{1.10}\text{O}_4$ samples and the standards obtained at (a) Co K-edge, (b) Fe K-edge and (c) Mn K-edge	155
4.36 SEM micrographs of $\text{CoFe}_{1.75}\text{Cu}_{0.25}\text{O}_4$ powders with (a) no annealing, (b) annealing at 500 °C for 4 h and (c) annealing at 500 °C for 100 h	157
4.37 Fourier transformation of (a) Co, (b) Fe and (c) Cu EXAFS data for $\text{CoFe}_{1.75}\text{Cu}_{0.25}\text{O}_4$ powders	160

Figure	Page
4.38 The degradation of reactive orange 16 in the $\text{CoFe}_{1.75}\text{Cu}_{0.25}\text{O}_4$ catalysts without annealing and with annealing powder at 500 °C for 4 and 100 h	162
4.39 The low index planes of spinel structure of (a) A (111), (b) B (111), (c) C (110), (d) D (110), (e) E (100), and (f) F (100). The white spheres represent the oxygen anions, the green spheres the octahedral cations and red spheres the tetrahedral cations	163
4.40 SEM micrographs of $\text{CoFe}_{1.45}\text{Zn}_{0.55}\text{O}_4$ powders with (a) no annealing, (b) annealing at 500 °C for 4 h and (c) annealing at 500 °C for 100 h	165
4.41 Fourier transformation of Co, Fe and Zn EXAFS data for $\text{CoFe}_{1.45}\text{Zn}_{0.55}\text{O}_4$ powders	167



## ABBREVIATIONS AND SYMBOLS

ASTM	American Society for Testing Materials
$a$	lattice parameter
BL8	beamline 8
$E_0$	absorption edge energy
EXAFS	extended X-ray absorption fine structure
FT	Fourier transform
$H$	magnetic field
$H_c$	coercivity
$hkl$	Miller plane
$I_0$	intensity of incident X-ray
$I_1$	intensity of transmitted X-ray
$i$	degree of inversion
JCPDS	joint committee on powder diffraction standards
KMITL	King Mongkut's Institute of Technology Ladkrabang
KU	Kasetsart University
$K_a$	anisotropy constant
$k$	wave vector of the photoelectron
$M$	magnetization
$M_r$	remnant magnetization
$M_s$	saturation magnetization
$N$	coordination number
$n_B$	amount of Bohr magneton
SEM	Scanning Electron Microscope
SLRI	Synchrotron Light Research Institute (Public Organization)
UV	ultra violet
Vis	visible
VSM	Vibrating Samples Magnetometer
XANES	X-ray absorption near-edge structure
XAS	X-ray absorption spectroscopy
XRD	X-ray diffraction

This material is reserved for educational use only, not allowed for commercial use.

Forbidden to modify the content, and cite the document when use.

$\mu$	X-ray absorption coefficient, permeability
$\mu_0$	permeability of vacuum
$\mu_B$	Bohr magneton
$\sigma^2$	Debye-Waller factor
$\chi(k)$	oscillations as a function of photoelectron wave



# CHAPTER 1

## INTRODUCTION

### 1.1 Overview

Over the past 60 years ceramic magnets have become firmly established as electrical and electronic engineering materials; most contain iron as a major constituent and are known collectively as ferrites. The history of ferrites began many centuries ago with the discovery of lodestone consisting of black ore magnetite ( $\text{Fe}_3\text{O}_4$ ), which attracts iron. Magnets were first applied in compasses [1, 2], and the roots of ferrite science and technology lie in the efforts made in the early part of last century. Electrical properties are viewed as semiconductors or insulators, in contrast to metallic magnetic materials that are electrical conductors. Consequently, the eddy currents produced by alternating magnetic fields, from which many devices generate, are limited in ferrites by their high intrinsic resistance. Keeping eddy currents to a minimum becomes of paramount importance, as the operating frequency increases, and this has led to the widespread introduction of ferrites for high-frequency inductor and transformer cores, for example [1].

Ferrites are the predominant class among magnetic ceramics. They have a cubic spinel structure with the chemical formula,  $\text{MOFe}_2\text{O}_3$ , where  $\text{Fe}_2\text{O}_3$  is iron oxide and MO refers to a combination of two or more divalent metal oxides, e.g., ZnO, NiO, MnO, and CuO. The addition of such metal oxides in various amounts allows the creation of many different materials, with properties that can be tailored for a variety of uses [2]. The attractive magnetic properties of this material are essentially due to its local structure. In the structure of ferrites, cations (bivalent and trivalent) reside on the tetrahedral and octahedral sites available in the close packing of oxygen anions. The cation distribution between octahedral and tetrahedral sites can vary and crucially influence magnetic, catalytic, and electronic properties [3, 4]. Thus, deciding on cation distribution between octahedral and tetrahedral sites in spinel ferrites plays an important role in determining the use of these materials, and this has been the subject of many studies [5 -8]. It is acknowledged that causes of cation

distribution over the spinel structure are composed of cation type [9-11], composition [12, 13], processing temperature [14, 15], and particle size [15, 16]. Furthermore, thermal annealing was reported, which influences efficiency noticeably in dielectric properties, ferroelectric properties, and the crystal structure of PZT-PZN ceramic [17] as well as magnetization properties [18]. However, the literature reviews did not contain information about the influence of thermal annealing on cation distribution in the structure. Therefore, this research focused on studying the effect of thermal annealing on the cation distribution of metal spinel ferrites, and also investigating the effect of annealing temperatures, annealing time, and annealing atmosphere on the metal doped cobalt ferrite system. The X-ray absorption spectroscopy technique was selected to examine detailed information of cation distribution in the ferrite structure, since it offers element specificity and sensitivity to the local structure. It is ideal for studying multicomponent dilution and disordered materials, besides being a powerful tool for determining cation distribution in ferrosinels [5, 8].

## 1.2 Scope of this work

The scope of this research is presented as follows:

- 1) To synthesize the  $\text{CoFe}_{2-x}\text{M}_x\text{O}_4$  system, where  $M = \text{Mn, Cu, Zn}$  and,  $x = 0.00 - 1.10$ , using the conventional solid state reaction method.
- 2) To characterize the phase formation, magnetization or degradation of the  $\text{CoFe}_{2-x}\text{M}_x\text{O}_4$  system, where  $M = \text{Mn, Cu, Zn}$  and,  $x = 0.00 - 1.10$ .
- 3) To investigate the effect of annealing temperatures, annealing time, and annealing atmosphere in the  $\text{CoFe}_{0.9}\text{Mn}_{1.1}\text{O}_4$  system.
- 4) To confirm the state of oxidation and micro structure after annealing in the  $\text{CoFe}_{2-x}\text{M}_x\text{O}_4$  system, where  $M = \text{Mn, Cu, Zn}$  and,  $x = 0.00 - 1.10$ .
- 5) To determine the influence of thermal annealing on the cation distribution in the structure before and after annealing of the  $\text{CoFe}_{2-x}\text{M}_x\text{O}_4$  system, where  $M = \text{Mn, Cu, Zn}$  and,  $x = 0.00 - 1.10$ .

### 1.3 Objectives of this work

This research pays attention to the preparation and characterization of spinel ferrites in the cobalt ferrites substitute transition metals in the  $\text{CoFe}_{2-x}\text{M}_x\text{O}_4$  system, where  $M = \text{Mn, Cu, Zn}$  and,  $x = 0.00 - 1.10$ , using the conventional solid state reaction method. The objective of this work was as follows:

- 1) To prepare the single phase of the  $\text{CoFe}_{2-x}\text{M}_x\text{O}_4$  system, where  $M = \text{Mn, Cu, Zn}$  and,  $x = 0.00 - 1.10$  using the solid state reaction method.
- 2) To examine the effect of annealing temperatures, annealing time, and annealing atmosphere in the  $\text{CoFe}_{0.9}\text{Mn}_{1.1}\text{O}_4$  system.
- 3) To investigate the cation distribution of the  $\text{CoFe}_{2-x}\text{M}_x\text{O}_4$  system, where  $M = \text{Mn, Cu, Zn}$  and,  $x = 0.00 - 1.10$  using the EXAFS spectra of X-ray absorption spectroscopy (XAS) technique.
- 4) To confirm the state of oxidation in each cation in the  $\text{CoFe}_{2-x}\text{M}_x\text{O}_4$  system, where  $M = \text{Mn, Cu, Zn}$  and,  $x = 0.00 - 1.10$  using XANES spectra of the XAS technique.
- 5) To understand the effect of thermal annealing on cation distribution, and magnetic and catalyst properties.

## References

- [1] A. J. Moulson and J. M. Herbert, *Electroceramics Materials and Application*, England, John Wiley & Sons, 2003.
- [2] R. C. Buchanan, *Ceramic Materials for Electronics*, USA, Marcel Dekker, 2004.
- [3] Y. Köseoğlu, A. Baykal, F. Gözüak and H. Kavas, "Structural and magnetic properties of  $\text{Co}_x\text{Zn}_{1-x}\text{Fe}_2\text{O}_4$  nanocrystals synthesized by microwave method", *Polyhedron*, **28**, 2887-2892 (2009).
- [4] Y. Köseoğlu, F. Alan, M. Tan, R. Yilgin and M. Öztürk, "Low temperature hydrothermal synthesis and characterization of Mn doped cobalt ferrite nanoparticles", *Ceram. Int.*, **38**, 3625-3634 (2012).
- [5] V. G. Harris, N. C. Koon, C. M. Williams, Q. Zhang, M. Abe and J. P. Kirkland, "Cation distribution in NiZn-ferrite films via extended x-ray absorption fine structure", *Appl. Phys. Lett.*, **68**, 2082 (1996).
- [6] S. A. Oliver, V. G. Harris, H. H. Hamdeh and J. C. Ho, "Large zinc cation occupancy of octahedral sites in mechanically activated zinc ferrite powders", *Appl. Phys. Lett.*, **76**, 2761 (2000).
- [7] J. A. Gomes, M. H. Sousa, G. J. da Silva, F. A. Tourinho, J. Mestnik-Filho, R. Itri, G. d. M. Azevedo and J. Depeyrot, "Cation distribution in copper ferrite nanoparticles of ferrofluids: A synchrotron XRD and EXAFS investigation", *J. Magn. Magn. Mater.*, **300**, e213-e216 (2006).
- [8] D. Carta, G. Mountjoy, G. Navarra, M. F. Casula, D. Loche, S. Marras and A. Corrias, "X-ray Absorption Investigation of the Formation of Cobalt Ferrite Nanoparticles in an Aerogel Silica Matrix", *J. Phys. Chem. C.*, **111**, 6308-6317 (2007).
- [9] W. C. Kim, S. W. Lee, S. J. Kim, S. H. Yoon and C. S. Kim, "Magnetic properties of Y-, La-, Nd-, Gd-, and Bi-doped ultrafine  $\text{CoFe}_2\text{O}_4$  spinel grown by using a sol-gel method", *J. Magn. Magn. Mater.*, **215-216**, 217-220 (2000).
- [10] K. P. Chae, J.-G. Lee, H. Su Kweon and Y. Bae Lee, "The crystallographic, magnetic properties of Al, Ti doped  $\text{CoFe}_2\text{O}_4$  powders grown by sol-gel method", *J. Magn. Magn. Mater.*, **283**, 103-108 (2004).

- [11] L. B. Tahar, M. Artus, S. Ammar, L. S. Smiri, F. Herbst, M. J. Vaulay, V. Richard, J. M. Grenèche, F. Villain and F. Fiévet, "Magnetic properties of  $\text{CoFe}_{1.9}\text{RE}_{0.1}\text{O}_4$  nanoparticles (RE = La, Ce, Nd, Sm, Eu, Gd, Tb, Ho) prepared in polyol", *J. Magn. Magn. Mater.*, **320**, 3242-3250 (2008).
- [12] O. Caltun, G. S. N. Rao, K. H. Rao, B. Parvatheeswara Rao, I. Dumitru, C.-O. Kim and C. Kim, "The influence of Mn doping level on magnetostriction coefficient of cobalt ferrite", *J. Magn. Magn. Mater.*, **316**, e618-e620 (2007).
- [13] M. Hashim, Alimuddin, S. Kumar, B. H. Koo, S. E. Shirsath, E. M. Mohammed, J. Shah, R. K. Kotnala, H. K. Choi, H. Chung and R. Kumar, "Structural, electrical and magnetic properties of Co-Cu ferrite nanoparticles", *J. Alloy. Compd.*, **518**, 11-18 (2012).
- [14] C. S. Kim, Y. S. Yi, K.-T. Park, H. Namgung and J.-G. Lee, "Growth of ultrafine Co-Mn ferrite and magnetic properties by a sol-gel method", *J. Appl. Phys.*, **85**, 5223 (1999).
- [15] M. K. Shobana, S. Sankar and V. Rajendran, "Characterization of  $\text{Co}_{0.5}\text{Mn}_{0.5}\text{Fe}_2\text{O}_4$  nanoparticles", *Mater. Chem. Phys.*, **113**, 10-13 (2009).
- [16] A. K. Giri, E. M. Kirkpatrick, P. Moongkhamklang, S. A. Majetich and V. G. Harris, "Photomagnetism and structure in cobalt ferrite nanoparticles", *Appl. Phys. Lett.*, **80**, 2341 (2002).
- [17] N. Vittayakorn, G. Rujijanagul and D. P. Cann, "Investigation of the influence of the thermal treatment on the morphologies, dielectric and ferroelectric properties of PZT-based ceramics", *J. Alloy. Compd.*, **440**, 259-264 (2007).
- [18] H. M. I. Abdallah, T. Moyo and J. Z. Msomi, "The Effect of Annealing Temperature on the Magnetic Properties of  $\text{Mn}_x\text{Co}_{1-x}\text{Fe}_2\text{O}_4$  Ferrites Nanoparticles", *J. Supercond. Nov. Magn.*, **25**, 2625-2630 (2011).

## CHAPTER 2

### LITERATURE REVIEW

The emphasis of this chapter is placed on the spinel structure, thermal annealing, and X-Ray Absorption Spectroscopy (XAS) technique. Firstly, it is necessary to describe the general background of the spinel ferrite, the catalyst and magnetic properties. The concept of thermal annealing is then described in more detail. Finally, the X-ray absorption spectroscopy technique investigates the oxidation state; the cation distribution in the structure is described; and the relevant literature on characterization of the spinel ferrite and cobalt ferrite substitution is reviewed.

#### 2.1 Spinel Ferrite

##### 2.1.1 Spinel Ferrite Structure

Many spinel ferrites are used extensively. The structure of the spinel is obtained from spinel mineral ( $\text{MgAl}_2\text{O}_4$ ) and was clarified by Bragg and Nishikawa in 1915. The common formula of magnetic spinels is similar to that of spinel mineral, as  $\text{XFe}_2\text{O}_4$ , where X is divalent metal. The trivalent (Al) is substituted usually by  $\text{Fe}^{3+}$  in association with other trivalents. The divalent  $\text{Mg}^{2+}$  in the spinels can be substituted by  $\text{Mn}^{2+}$ ,  $\text{Ni}^{2+}$ ,  $\text{Cu}^{2+}$ ,  $\text{Co}^{2+}$ ,  $\text{Fe}^{2+}$  or  $\text{Zn}^{2+}$ , or more often, combinations of those. The presence of  $\text{Fe}^{3+}$ ,  $\text{Fe}^{2+}$ ,  $\text{Ni}^{2+}$ ,  $\text{Co}^{2+}$  and  $\text{Mn}^{2+}$  can be used to give unpaired electrons, and as a result, the magnetic moment of materials. Other divalents such as  $\text{Mg}^{2+}$  and  $\text{Zn}^{2+}$  are not paramagnetic. However, they are used to disproportionate the  $\text{Fe}^{3+}$  on the crystal lattice in order to increase or provide the magnetic moment [1].

The lattice of the spinel is composed of cubic close-packed oxygen ordering in 32 oxygen ions that form a unit cell, which is the smallest repetition unit in a crystal network. If the middle layers of oxygen are imaged as simple spheres, there are spaces that may fit the metal ions, and these spaces, known as A-sites, are not the same. They are enclosed by or correlate with the four nearest adjacent ions of oxygen, which connect to the centre of the tetrahedral form. Therefore, the A-sites are called the tetrahedral site. The other site (B-sites) correlates with the six nearest adjacent ions of oxygen, which connect to the centre of the octahedral form.

This material is reserved for educational use only, not allowed for commercial use.

Forbidden to modify the content, and cite the document when use.

Therefore, the B-sites are called the octahedral site. There are 32 octahedral sites and 64 tetrahedral ones in a unit cell of 32 oxygen ions. If all of these sites were packed with metal ions of +2 or +3 valency, the positive charges would be very much greater than negative ones and then the structure could not be electrically neutral. Consequently, out of 64 tetrahedral sites and 32 octahedral ones, only 8 and 16, respectively, are filled. If the tetrahedral sites in the spinel mineral were filled by divalent ions and the octahedral sites with trivalent ones, the total positive charges would be  $8 \times (+2) = +16$  and  $16 \times (+3) = +48$ , respectively, or a total of +64, which is needed to balance the  $32 \times (-2) = -64$  for oxygen ions. There would be eight formula units of  $MFe_2O_4$  in the unit cell, and the spinel unit cell would include two subcell types (Figure 2.1). The alternative of two subcells would have a three dimensional arrangement. Therefore, each repeated unit cell would need eight subcells [1].

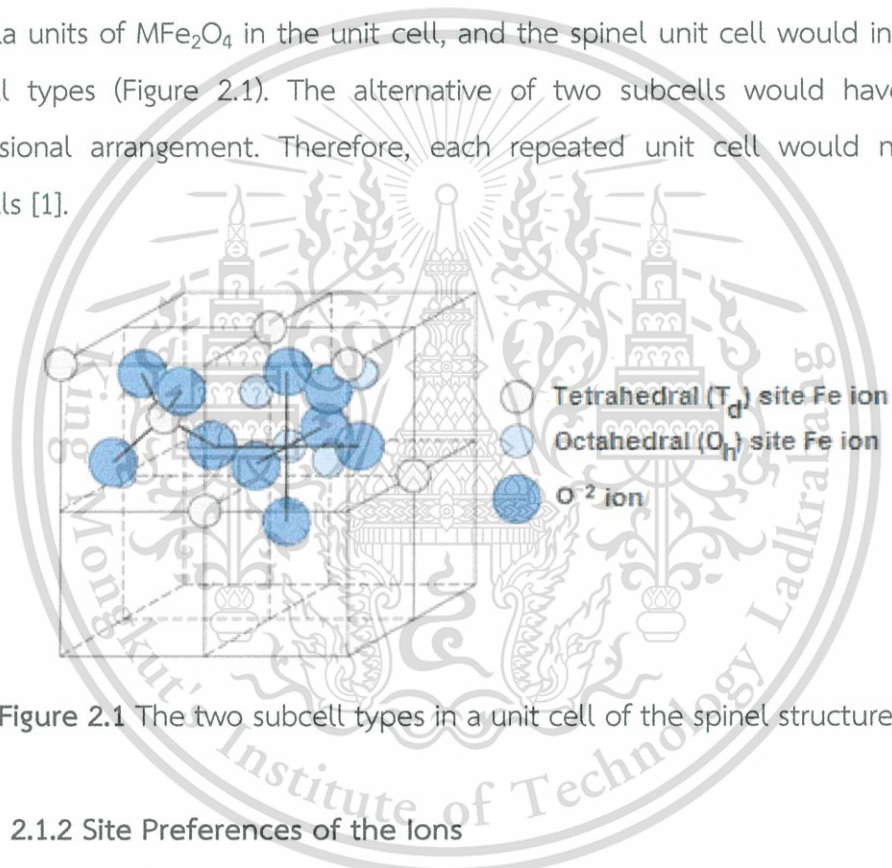


Figure 2.1 The two subcell types in a unit cell of the spinel structure [2].

### 2.1.2 Site Preferences of the Ions

The sites occupied in the spinel minerals are represented by the diagrams in Figure 2.2. The spinel mineral divalent ions ( $Mg^{2+}$ ) and trivalent ions ( $Al^{3+}$ ) occupy A- and B-sites, respectively [Figure 2.2(a)], and this is known as the normal spinel structure. In the case of spinel ferrites ( $XFe_2O_4$ ), different ions present different site preferences. In the nickel ferrite, the  $Ni^{2+}$  ions occupy B-sites together with an equal number of randomly distributed  $Fe^{3+}$  ions, while the remaining  $Fe^{3+}$  ions occupy A-sites, and are of an inverse spinel structure [Figure 2.2(b)]. In practice, the structures of spinel magnetic ceramics are a mixture of inverse and normal types, with the

distribution of oxidation states and cations amongst the lattice sites depending upon thermal history [3].

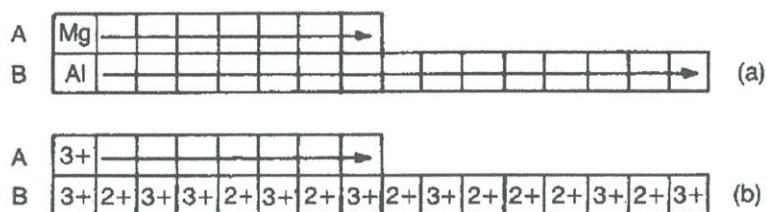


Figure 2.2 Diagram presenting site occupation in (a) normal spinels, and (b) inverse spinels [3].

Various properties of spinel compounds are obtained from possible multicomponent spinel synthesis by partially replacing cations in position A and B in the spinel structure. Among the spinels, inverse ones get special attention, due to the redox nature of metal ions and lack of site preference of the cations, which enable them to redistribute between octahedral and tetrahedral sites during the course of catalytic transformation, thus keeping the spinel structure intact. This accounts for the variety of reactions in which they have been used as catalysts. These compounds of the physical and chemical properties are restricted by the nature of ions, their distribution site and charge among octahedral and tetrahedral sites. It is therefore of major importance to understand the factors that influence the site of occupancy.

Romeijn, Adaunitz and Orgel were the first to suggest application of the crystal field theory in order to understand the site preference of the cations. McClare calculated octahedral site preference and energies of metal ion transition in oxide using the crystal field theory as shown in Table 2.1.

**Table 2.1** Crystal field stabilization energies for metal cation transition on tetrahedral and octahedral spinel sites [4]

Number of d electrons	Theoretical CFSE in terms of $Dq$		Cations	Estimated octahedral site preference energies (eV)
	Octahedral	Tetrahedral		
1	4	6	Ti <sup>3+</sup>	0.33
2	8	12	V <sup>3+</sup>	0.53
3	12	8	V <sup>2+</sup>	1.37
			Cr <sup>3+</sup>	2.02
4	6	4	Mn <sup>3+</sup>	1.10
			Cr <sup>2+</sup>	0.74
5	0	0	Fe <sup>3+</sup>	0
			Mn <sup>2+</sup>	0
6	4	6	Fe <sup>2+</sup>	0.17
			Co <sup>3+</sup>	0.82
7	8	12	Co <sup>2+</sup>	0.09
8	12	8	Ni <sup>2+</sup>	0.99
9	6	4	Cu <sup>2+</sup>	0.68
10	0	0	Zn <sup>2+</sup>	0

The data show that the systems with  $d^5$  and  $d^{10}$  configurations have no crystal field stabilization energy and hence no site preference. The  $d^3$  system has the highest octahedral site preference energy. The  $d^4$  and  $d^9$  ions can be stabilized further by Jahn-Teller distortion. In regular octahedral symmetry, octahedra of the surrounding anion is elongated or compressed in the  $z$  direction to give  $D_{4h}$  symmetry, the doublet ( $e_g$ ) and triplet ( $t_{2g}$ ) split levels. Splitting of the doublet is larger. In the case of elongation, the  $d_z^2$  orbital is stabilized when compared to the  $d_x^2 - y^2$  orbital. Fe[CuFe]O<sub>4</sub>, Mn[ZnMn]O<sub>4</sub>, and Zn[Mn<sub>2</sub>]O<sub>4</sub> are examples of tetragonally distorted spinels [4].

The most important investigation would seem to be on the related size of ion compared to the size of the lattice. Divalent ions are mainly larger than trivalent. This material is reserved for educational use only, not allowed for commercial use.

ones because their bigger charge generates electrostatic attraction and then pulls the external orbits internally. Tetrahedral sites also are smaller than octahedral ones. Consequently, it is sensible for divalent ions to go to the octahedral site and trivalent ones to tetrahedral sites. However, two exceptions were found.  $\text{Cd}^{2+}$  and  $\text{Zn}^{2+}$  ions prefer tetrahedral sites because the electronic configurations are desirable for tetrahedral bonding to oxygen ions. Therefore,  $\text{Zn}^{2+}$  prefers tetrahedral sites more than the  $\text{Fe}^{3+}$  ions do.  $\text{Co}^{2+}$  and  $\text{Zn}^{2+}$  have the same ionic radius, but  $\text{Co}^{2+}$  and  $\text{Zn}^{2+}$  prefer octahedral and tetrahedral sites, respectively, which is an exception in configuration.  $\text{Cr}^{3+}$  and  $\text{Ni}^{2+}$  have powerful preferences for octahedral sites, as other ions have weaker preferences [1].

### 2.1.3 Number of Unpaired Electrons

The contribution from orbital angular momentum is negligible from the transition of metal ions used in most ferrites, and the magnetic moment of an ion is determined by the number of unpaired electron spins. Each unpaired electron contributes a moment of one Bohr magneton ( $\mu_B = 9.27 \times 10^{-24} \text{ A m}^2/\text{electron}$ ). Hund's rule requires that electrons fill the orbital energy levels with aligned spins whenever possible. However, the Pauli exclusion principal allows only two electrons in any energy level and requires that their spins be opposite. Thus, in the transition metal series, where  $3d$ -shells are partially filled, the magnetic moment of an ion can be determined by filling the  $3d$ -shell with aligned spins at a maximum of up to five electrons, beyond which, the first five spins must be in antiparallel alignment. The moment is determined via the net number of unpaired spins. The resulting magnetic moments for the transition metal series are shown in Table 2.2 [5].

**Table 2.2** Outer-shell electron configuration and number of unpaired electrons for several spinel-forming ions [5]

Ion	Electron Configuration	Number of Unpaired Electrons
Mg <sup>2+</sup>	2p <sup>6</sup>	0
Al <sup>3+</sup>	2p <sup>6</sup>	0
O <sup>2-</sup>	2p <sup>6</sup>	0
Sc <sup>3+</sup>	3p <sup>6</sup>	0
Ti <sup>4+</sup> (Ti <sup>3+</sup> )	3p <sup>6</sup> (3d <sup>1</sup> )	0
V <sup>3+</sup> (V <sup>5+</sup> )	3d <sup>2</sup> (3p <sup>6</sup> )	2(0)
Cr <sup>3+</sup> (Cr <sup>2+</sup> )	3d <sup>3</sup> (3d <sup>4</sup> )	3(4)
Mn <sup>2+</sup> (Mn <sup>3+</sup> )(Mn <sup>4+</sup> )	3d <sup>5</sup> (3d <sup>4</sup> ) (3d <sup>3</sup> )	5(4)(3)
Fe <sup>2+</sup>	3d <sup>6</sup>	4
Fe <sup>3+</sup>	3d <sup>5</sup>	5
Co <sup>2+</sup> (Co <sup>3+</sup> )	3d <sup>7</sup> (3d <sup>6</sup> )	3(4)
Ni <sup>2+</sup>	3d <sup>8</sup>	2
Cu <sup>2+</sup> (Cu <sup>+</sup> )	3d <sup>9</sup> (3d <sup>10</sup> )	1(0)
Zn <sup>2+</sup>	3d <sup>10</sup>	0
Cd <sup>2+</sup>	4d <sup>10</sup>	0

#### 2.1.4 Superexchange Interaction

Whether a metal oxide containing magnetic ions is ferromagnetic, antiferromagnetic or ferromagnetic depends on the magnitude of the individual moments, type and number of sites that are occupied, and nature of the interaction between sites. The interaction of exchange between any two cations is mediated by intervening oxygen ions, and is known as a super exchange interaction, which is contrary to direct exchange in metals where atoms are on immediately adjacent sites. The super exchange interaction involves the temporary transfer of an electron from one of the dumbbell-shaped  $2p$  orbitals of the oxygen ion to one of the adjacent cations, leaving behind an unpaired  $2p$  electron to interact with the opposing cation. For cations with more than half-filled  $d$  levels, such as the transition

metals that appear in ferrites, this interaction generally results in antiparallel spin between cations [5].

When there is an exchange of force or negative interaction of ions at various sites along the lengths between the moments of oxygen and metal, and between oxygen and metals ions linked together at an angle in the middle of three ions, the strength of interactions in the moments on different sites is considered. This interaction is mostly at an angle of  $180^\circ$ , where the interatomic lengths are the shortest. Figure 2.3 presents the interatomic lengths and angles in the middle of the ions, with distinct types of interactions. In the case of B-B and A-A, the oxygen ions and lengths between metal ions are too long, or the angles are too acute. The best associations of lengths and angles exist in A-B interactions. The B-O-A angles in undistorted spinel are approximately  $154^\circ$  and  $125^\circ$  and the B-O-B angles are  $125^\circ$  and  $90^\circ$ , but one of the O-B lengths in the latter is long. In the case of A-A, the angle is nearly  $80^\circ$ . Consequently, interaction in the middle of moments on the B- and A-sites is strongest. The most undesirable situation appears in A-A interaction, while B-B interaction is much weaker. By investigating A-B interaction or the biggest contributors to orienting unpaired electrons of these antiparallel ions, Neel (1948) was able to describe the ferrimagnetism of ferrites. An individual B-site interacts with an A-site, but each B-site is connected to six units while each A-site is connected to four. Therefore, all B- and A-sites act as united blocks and are linked to antiparallel blocks in order to compose throughout the crystal [1].

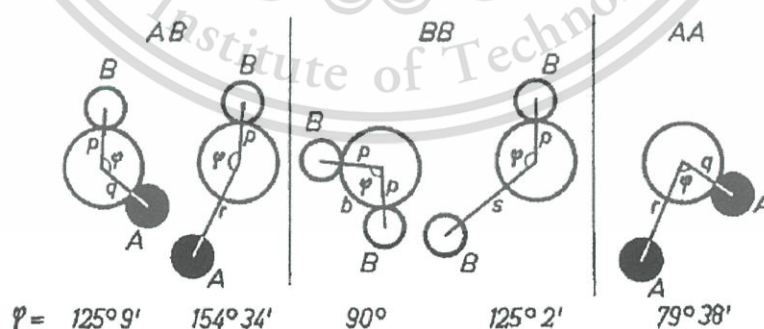


**Figure 2.3** Angles and interionic distances in different types of spinel structure for lattice site interactions [1].

An equal number of  $\text{Fe}^{3+}$  in inverse spinel containing iron ions, occupies both octahedral B-sites and tetrahedral A-sites to give a powerful interaction (A-O-B). This results in antiparallel spin alignment with no net resultant magnetic moment. However, inverse spinels can be doped with divalent oxides ( $\text{MeO}$ ), where Me prefers octahedral sites and so some of the octahedral (B) are filled with  $\text{Me}^{2+}$ . The strong (A-O-B) interaction between  $\text{Me}^{2+}$  in the octahedral site and  $\text{Fe}^{3+}$  in tetrahedral sites results in a net uncompensated moment of magnetization, which is proportional to the number of unpaired electrons in the  $\text{Me}^{2+}$ . That is to say, all of the  $\text{Fe}^{3+}$  alignment remains antiparallel [6].

### 2.1.5 Structural Anisotropy

The two basic forms of magnets are isotropic and anisotropic. While magnets prefer orientation with a substantially higher density of energy, isotropic magnets can be magnetized and set along all axes. To achieve optimal magnetic properties in spinel ferrites, it is necessary to consider anisotropic energies, which are related to the crystal structure and microstructure of the materials. These anisotropic energies control most useful macroscopic properties of magnetic materials, and are consecutively, (1) magnetocrystalline anisotropic energy, which favors spin alignment in an easy crystallographic direction, (2) magnetostrictive energy, which is related to strain anisotropy, and (3) magnetostatic energy that relates to shape anisotropy.

#### 1) Magnetocrystalline anisotropy

Magnetocrystalline anisotropy is a part of crystal energy that depends on the direction of magnetization in the lattice, and it can represent cubic material by the following type of equation:

$$E_A = K_1(\alpha_1^2\alpha_2^2 + \alpha_1^2\alpha_3^2 + \alpha_2^2\alpha_3^2) + K_2(\alpha_1^2\alpha_2^2\alpha_3^2) + \dots \quad (2.1)$$

where  $\alpha_1$ ,  $\alpha_2$ , and  $\alpha_3$  are the trend cosines of magnetic direction with respect to the cubic axis of the crystal, and the  $K_n$  is the anisotropic constants, which decrease rapidly with the order, n.  $K_1$  indicates value of the minimal energy position, which is an arbitrary constant, and  $K_2$  and  $K_3$  are the anisotropic constants of [110] and [111] directions, respectively. Easy directions in cubic systems are along the edges of the

cube, if  $K_1$  is positive and  $K_2$  less negative than  $-9K_1/4$ . When  $K_1$  is negative, as in nickel, simple directions are along the cube obliquely. When the simple direction of magnetization is parallel to a cube edge, the anisotropic energy is  $E_A = K_0 = 0$ , since  $\alpha_1 = \alpha_2 = \alpha_3 = 0$ , and thus  $K_2 = K_3 = 0$ . The easy direction for anisotropic energy with a diagonal face is  $E_A = K_0/4$ , since  $\alpha_1 = 0$  and  $\alpha_2 = \alpha_3 = 1/\sqrt{2}$ . The easy direction for anisotropic energy along a diagonal cube is equal to  $E_A = K_1/3 + K_2/27$ , since  $\alpha_3 = \alpha_2 = \alpha_1 = 1/\sqrt{3}$ . The  $\langle 100 \rangle$  directions of the cube are easy for magnetization or directions of minimal anisotropic energy in ferrites [3, 6].

Table 2.3 lists the anisotropic constants that predict the ferrites from the discussion point of simple cubic directions being [111], but in the case of filling cobalt, they are [100].

Table 2.3 The anisotropic constants of all significant ferrites [3]

Ferrite	$K_1/\text{kJ m}^{-3}$
$\text{Fe}_3\text{O}_4$	-11
$\text{NiFe}_2\text{O}_4$	-6.2
$\text{CuFe}_2\text{O}_4$	-6.0
$\text{Ni}_{0.5}\text{Zn}_{0.5}\text{Fe}_2\text{O}_4$	-3
$\text{Mn}_{0.98}\text{Fe}_{1.86}\text{O}_4$	-2.8
$\text{Mn}_{0.45}\text{Zn}_{0.55}\text{Fe}_2\text{O}_4$	-0.38
$\text{Co}_{0.8}\text{Fe}_{2.2}\text{O}_4$	+290
$\text{BaFe}_{12}\text{O}_{19}$	+330

## 2) Magnetostriction

Magnetostriction is another anisotropic effect that determines the properties of ferrites. The application of stress to magnetostrictive materials causes a change in energy of the crystal lattice and hence in the magnetic properties of that lattice. The inverse effect also is possible, whereby the application of a magnetic field causes measurable strain induced in the material. Ferrites usually display a small volume change, in the order of  $10^{-9}$ , under the influence of a magnetic field. This is caused by dependence of the exchange energy on atomic spacing. The length of crystal changes is parallel to the trend of the applied field, and increases with the applied

This material is reserved for educational use only, not allowed for commercial use.

Forbidden to modify the content, and cite the document when use.

field until saturation. This phenomenon is called magnetostriction and is due to the gradual orientation of domains under the influence of the applied field.

This magnetostrictive property can be applied directly to transducers by transferring the electrical energy into mechanical energy, or vice versa, for many common applications such as ultrasonic machining (drilling, welding, and cleaning), strain gauges, speedometers, mechanical filters, etc. The magnetostrictive, “piezomagnetic” ferrites are nickel ferrite-based, such as the NiZn, NiCu, NiMg, and NiCo systems [6].

### 3) Magnetostatic energy

Magnetostatic energy is related to shape anisotropy. Toroidal shapes, for example, are often selected for magnetic components because of their ability to minimize demagnetizing or fringing fields, which would otherwise represent an energy loss to the system. A steady magnetic force is retained in the core ( $H_{dc}$ ) while current passes through an inductor. Eighty five percent of the core flow for a medium to small gap is confined to a cross section of the core face adjacent to the gap, and the remaining 15% of the core flow is edging flow, which is made by turning the gap. The edging flow declines and the total disinclination of the magnetic path produces noticeable capacitance that is greater than the estimated value. Therefore, the large gaps sometimes crack into mostly smaller gaps that decrease edging [6].

#### 2.1.6 Catalyst

In biology and chemistry, a catalyst speeds up the rate of chemical reaction by the factor of a material, which is called catalysis that in itself is not engulfed by the total reaction. Catalysts take part in reactions, but are neither reactants nor products of the entire catalyzed reaction. The expression, catalysis, was invented in 1835 by Jöns Jakob Berzelius, who was the first to report that certain chemicals accelerated a reaction. A suitable catalyst has to possess both long cycle steadiness and high activity. However, its most important potential is selectivity that indicates the ability to direct alternation of reactants specifically.

Specific catalysis enables a chemical method to progress more efficiently with less waste. Recent industries have studied more and more about the benefits and applications of catalysis and various ways in how it brings down production costs.

Catalyst technologies usually involve lower operation costs, less capital investment, decreased environmental dangers and higher product purity. Therefore, the catalyst is very important in the chemical industry. The more restricted areas of commercial catalysts are in the pharmaceutical, environmental and petroleum industries.

A catalyst is a very important method from an industrial point of view, as it is involved in the production of many industrial chemicals. In recent years, significant advances have been made in research of the mechanism and surface structure of catalyst reaction. A common model for a heterogeneous catalyst concerns catalysis that provides a surface on which substrates (or reactants) are temporarily adsorbed. Substrate bonds become debilitated enough for new bonds to be made, with those in the middle of the catalysis and weaker products, before they are released. The nature of interaction may be a physical or chemical process. The total catalytic reaction velocity depends on these chemicals, physical processes or steps. Each step leads, to a lesser or greater extent, to the total reaction rate.

### 1) Spinel Catalyst

Mixed oxides that have the formula,  $AB_2O_4$ , are known as spinels, where A and B are metal cations with a charge of +2 and +3, respectively. There are simple and mixed spinels. The mixed metal oxides possess a spinel structure that has been examined by a number of workers, and they present attractive structural, magnetic and electrical properties. They also are suitable alternatives to both aluminium phenolate and zeolites for most alkylation reactions. Individual metal oxides lose catalyst activity quickly, owing to the construction period of coke above the catalysis surface. The spinel lattice reveals extra steadiness in the catalysis under different reaction conditions before these systems have maintained longer aging activities. Spinel with B ions as  $Fe^{+3}$  and  $Co^{+3}$  are known as ferrites and cobaltites, respectively, and they were chosen for this study. The attractive structural, magnetic catalyst and electrical properties of these compounds are governed by their chemical composition. Therefore, special care must be taken in the preparation stages of these compounds in order to obtain spinels with specific properties.

### 2) Surface of Catalytically Active Spinel

The surface structure and properties of spinels are of wide interest. The principal and interesting question remains of which states of plane, coordination

and valency are responsible for the catalytic activity and selectivity in spinels. Many reports have stated that the tetrahedral sites in spinels are not active, which could create stronger oxygen-metal bonds because of the lower coordination number and valency. Furthermore, tetrahedral sites are not accessible to the reactants. According to the literature, only low index spinels are taken into consideration usually when discussing the surface of spinels. Following the suggestion of Knozinger and Ratnasami, the use of their notation can distinguish between six different low-index surface planes, as shown in Figure 2.4, which follows that A (111), C (110), E (100) and F (100) planes have both tetrahedral and octahedral sites on the surface, while B (111) and D (110) planes expose only octahedrally coordinated cations.

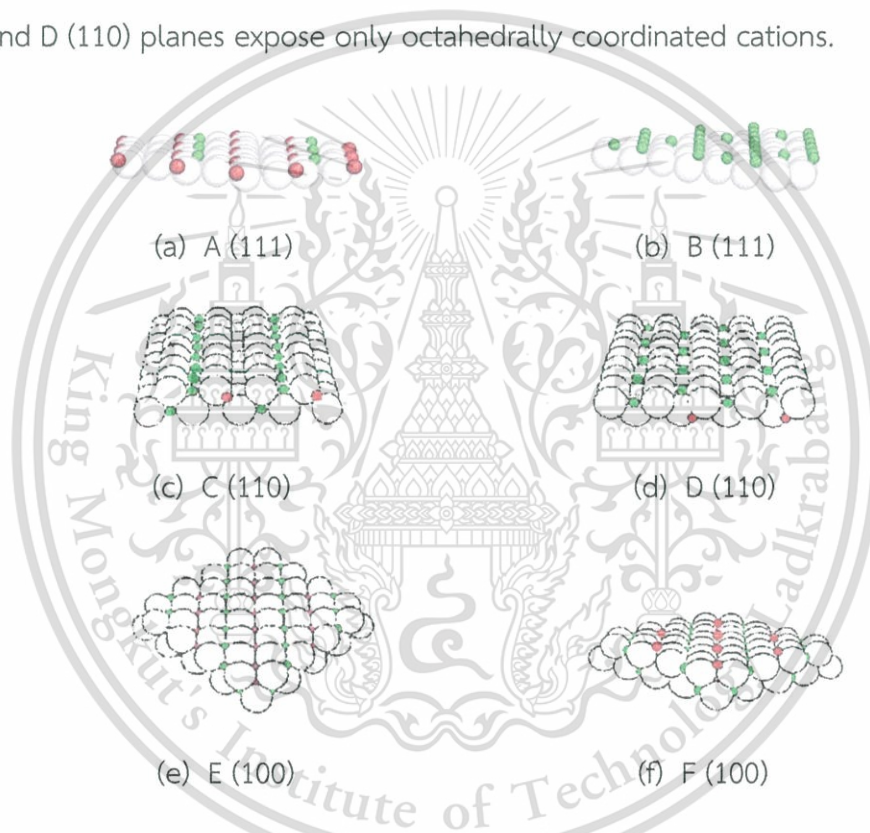


**Figure 2.4** The low index planes of a normal spinel structure: oxygen anions (open spheres), octahedral cations (solid spheres), and tetrahedral cations (hatched spheres) [4].

According to Ziolkowski and Barbaux, theoretical calculations show that A (111) and D (110) planes are preferred on the surface, but these hypotheses do not form a final conclusion. Shelef and co-workers made an experimental attempt to elucidate on the surface structure of spinels by using low energy ion scattering (LEIS), and they support the data stating that tetrahedrally coordinated cations are not

This material is reserved for educational use only, not allowed for commercial use.

accessible for reactant molecules. Barbaux and Beaufile examined the surface combination of a normal spinel using differential neutron diffraction (DND) techniques, and determined that the surface of spinels comprised a mix of (111) and (110) planes.

In comparing the models involving oxygen-argon length with the results of DND, they noticed that these planes include only oxygen anions and octahedral cations, respectively. Jacobs *et al.* confirmed this by using the LEIS technique. By substituting the Mn and Co cations in different sites in the spinel structure of  $Mn_3O_4$  and  $Co_3O_4$ , with other cations that were not active in the selective reduction of nitrobenzene to nitrosobenzene, they were able to study the role of these sites in catalytic reaction. Their results confirmed the idea that octahedral ions are almost exposed exclusively at the surface of the spinel oxide powders, and these sites only participate in the reaction. Only two index planes of the spinel structure can detect this condition, which is recognized as D (110) and B (111). The nonexistence of tetrahedral sites residing at the face is a more common property of spinels [4].

### 3) Fenton-Type Systems

In 1894, Henry John Horstman Fenton found that several metals had specific oxygen transfer, which attributed to the enhancement of hydrogen peroxide utilization. Actually, some metals have powerful catalytic potential to create highly reactive hydroxyl radicals ( $\cdot OH$ ). In this exposure, the iron catalyzing hydrogen peroxide is called Fenton's reaction, which is used currently to treat many kinds of water contamination such as that from rubber, chemicals, pesticides, phenols BTEX, formaldehyde, etc.

This method may be use for contaminated soil, sludge and wastewater using the following operations:

- Removal of color and odor
- Destruction of organic impurity
- Reduction of toxicity
- Destruction of resin in radioactive polluted sludge
- Extraction of BOD/COD
- Development of biodegradability

After the hydrogen peroxide and iron have been increased, they respond together in creating hydroxyl radicals, as displayed in the following equations:



Then, the hydroxyl radicals respond with impurities for oxidization. In fact, the hydroxyl radicals can respond accordingly to four types of reactions with impurities:



With Fenton's reaction total, the parameters adapt to promote the first two types of reaction between hydroxyl radicals and the pollutant.

The following is essential for the reaction:

- Modification of pH to 3-5; if the pH is too high, the iron accelerates in  $\text{Fe}(\text{OH})_3$  and breaks down the  $\text{H}_2\text{O}_2$  to oxygen. Generally, the best pH is between 3 and 6. Actually, it is important to concentrate on a lower double pH, due to the addition of  $\text{H}_2\text{O}_2$  and iron, as shown in Figure 2.5. Certainly, this addition is accountable for organic fragmentation to organic acids in the  $\text{FeSO}_4$  catalyst, which includes residual  $\text{H}_2\text{O}_2$  and  $\text{H}_2\text{SO}_4$ .

- Addition of the iron catalyst as  $\text{FeSO}_4$  solution.

- Slow addition of  $\text{H}_2\text{O}_2$ ; in order to operate increasing pH and temperature, pending the reaction, it is better to accomplish the reaction step by step with a continuous modification [7].

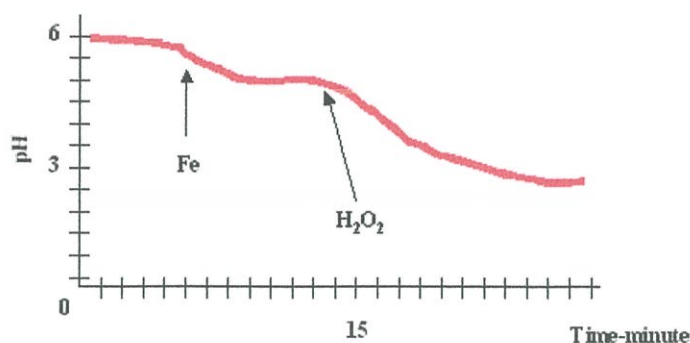


Figure 2.5 Double pH drops [7].

Hydrogen peroxide is used extensively due to its excellent properties. In fact  $\text{H}_2\text{O}_2$  is a powerful, harmless, versatile, and an efficient oxidant. Table 2.4 shows oxidation potential, for instance, hydrogen peroxide is more powerful than chlorine dioxide or chlorine. In the addition of catalysis, hydrogen peroxide can be changed to hydroxyl radicals that are the second most powerful oxidant after fluorine.

Table 2.4 The oxidation potential scale [8]

Oxidant	Oxidation Potential (V)
Chlorine	1.4
Chlorine dioxide	1.5
Potassium permanganate	1.7
Hydrogen peroxide	1.8
Ozone	2.1
Hydroxyl radical	2.8
Fluorine	3.0

The major applications of  $\text{H}_2\text{O}_2$  are varied, such as metal, organic, and toxic oxidation; disinfection; corrosion control; odor control; and BOD/COD removal. Furthermore, hydrogen peroxide can be combined with various processes to enhance the results of biotreatment, filtration, flocculation/precipitation, carbon adsorption, air flotation, incineration, and air scrubbers. The most difficult pollutant to oxidize may need  $\text{H}_2\text{O}_2$  stimulated with catalysis such as manganese, copper, iron

This material is reserved for educational use only, not allowed for commercial use.

Forbidden to modify the content, and cite the document when use.

or other transition compounds. Iron is the catalyst used most commonly with  $\text{H}_2\text{O}_2$  in Fenton's reaction [8].

Previous works found decolorization of synthetic dyes, with various catalysts using mixed iron oxides. In 2006, P. Baldrian *et al.* [9] used a heterogeneous based catalysis on mixed iron oxides ( $\text{MFe}_2\text{O}_4$  where  $\text{M} = \text{Cu}, \text{Co}, \text{Mn}, \text{Fe}$ ) for decolorization of many synthetic dyes. The magnetic oxides were synthesized using precipitation. The synthetic dyes ( $50 \text{ mg L}^{-1}$ ) were mixed with dry catalysts ( $25 \text{ mg mL}^{-1}$ ) in water and then the reaction was started by adding hydrogen peroxide ( $100 \text{ mmol L}^{-1}$ ). The decolorization result of Chicago Sky Blue 6B was very quick, with 30–70% decolorization recorded after only 5 minutes incubation (Figure 2.6). Then, after 24 hours, the decolorization of  $\text{FeO}\cdot\text{Fe}_2\text{O}_3$ ,  $\text{CoO}\cdot\text{Fe}_2\text{O}_3$ , and  $\text{CuO}\cdot\text{Fe}_2\text{O}_3$  was almost accomplished (over 93%), with  $\text{MnO}\cdot\text{Fe}_2\text{O}_3$  being slightly insufficient (81%).

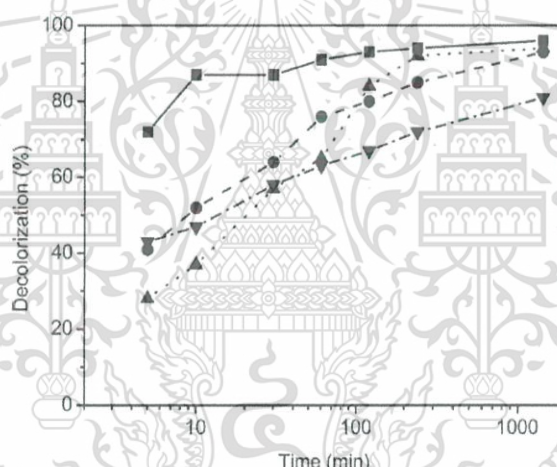


Figure 2.6 Time course to decolorization of Chicago Sky Blue in the catalysts and  $\text{H}_2\text{O}_2$ . Catalyst;  $\text{MnO}\cdot\text{Fe}_2\text{O}_3$  (inverted triangles),  $\text{FeO}\cdot\text{Fe}_2\text{O}_3$  (triangles),  $\text{CuO}\cdot\text{Fe}_2\text{O}_3$  (circles), and  $\text{CoO}\cdot\text{Fe}_2\text{O}_3$  (squares) [9].

After 24 hours decolorization, the synthetic dyes were tested with all catalysts. The decolorization capability varied significantly among the catalysts and dyes (Table 2.5).

**Table 2.5** Color reduction of synthetic dyes after 24 hours treatment with catalysts [9]

Dye	Decolorization/adsorption (%)			
	CoO·Fe <sub>2</sub> O <sub>3</sub>	CuO·Fe <sub>2</sub> O <sub>3</sub>	FeO·Fe <sub>2</sub> O <sub>3</sub>	MnO·Fe <sub>2</sub> O <sub>3</sub>
Bromophenol Blue	2 (0)	48 (15)	99 (9)	0 (0)
Chicago Sky Blue	93 (9)	95 (8)	98 (10)	91 (6)
Cu Phthalocyanine	70 (3)	75 (18)	92 (18)	19 (7)
Eosin Yellowish	25 (2)	53 (17)	85 (15)	12 (0)
Evans Blue	73 (16)	92 (9)	99 (18)	8 (2)
Naphthol Blue	68 (8)	95 (13)	93 (16)	75 (0)
Black				
Phenol Red	85 (4)	86 (12)	81 (0)	63 (0)
Poly B-411	0 (0)	7 (1)	38 (0)	0 (0)
Reactive Orange	21 (2)	86 (21)	77 (6)	6 (0)
16				

The values illustrate the total color decrease of supernatant after catalyst extraction, and dye adsorption to the catalysis is showed in parentheses.

Their research proved that mixed iron oxides and iron oxide were efficient catalysts with hydrogen peroxide for oxidizing decolorization in synthetic dyes. The catalysts presented the advantages of steady activity in succeeding catalyst cycles, and easy recovery from treated solution.

## 2.2 Ferrite Literature Reviews

### 2.2.1 Cobalt Ferrite

The Cobalt ferrite, CoFe<sub>2</sub>O<sub>4</sub>, is well recognized as having very high cubic magnetocrystalline anisotropy, moderate saturated magnetization, noticeable mechanical hardness and chemical steadiness, as well as high coercivity. So far, CoFe<sub>2</sub>O<sub>4</sub> is an important technological material that has been used many years for magnetic recording, permanent magnets, magnetic fluids, and catalysis [10-12]. Cobalt ferrite researches have been found in previous works. In 2008, P. C. R. Varma *et al.* [13] studied the magnetization properties of cobalt ferrite prepared by This material is reserved for educational use only, not allowed for commercial use.

polymerized complex, solid state reaction, and citrate precursor methods. The magnetization properties of all samples were found to act powerfully on particle size. Similar  $M$  versus  $H$  loops were obtained from all samples (Figure 2.7). The results found that when samples with bigger particle sizes exhibited saturated magnetization clearly, and other samples had smaller particle sizes, magnetizations at 60 kOe were not saturated completely or equally.

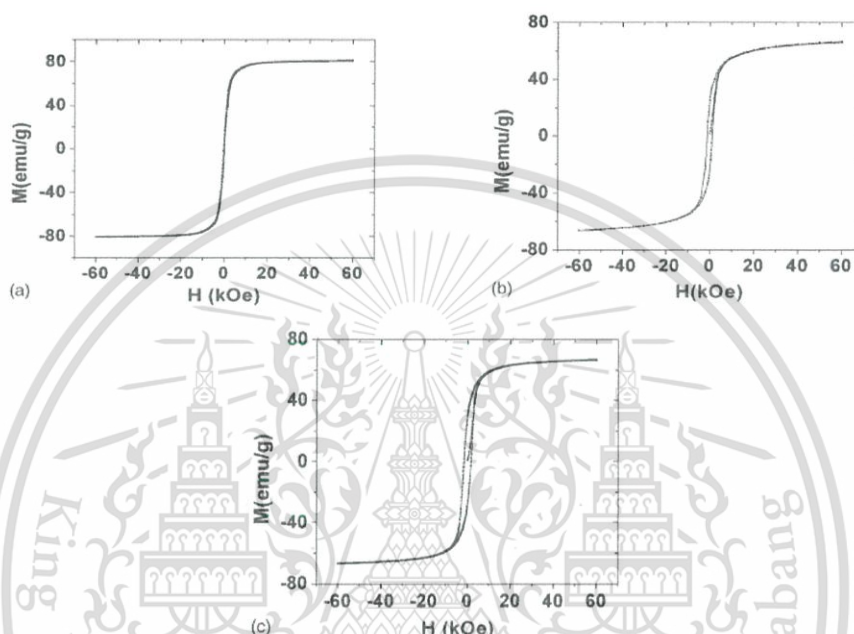


Figure 2.7  $M$  and  $H$  curves of cobalt ferrite synthesized at 300 K by; (a) solid state reaction (b) citrate gel, and (c) polymer complex [13].

Table 2.6 summarizes magnetic properties with an average particle size. It showed basically that microparticle sized samples synthesized by the solid state method have high saturated magnetization and smaller coercivity, which indicates a multidomain character in the samples. The polymer complex and citrate gel methods indicated that magnetization increases with increasing particle sizes. The exponential increase in coercivity with decreasing particle sizes and squareness ratios in a range of 0.3–0.4 implies that the particles are not predominately in a single domain, in the case of those that are nano-sized. Consequently, it is probable that the nanoparticle samples are composed of pseudo single domain particles.

**Table 2.6** The average particle sizes, saturated magnetization, remanence magnetic,  $M_r/M_s$  ratio, and coercive field in  $\text{CoFe}_2\text{O}_4$  samples synthesized in various conditions [13].

Preparation method and heat treatment conditions	Average particle sizes (XRD/TEM)	$M_s$ (emu/g)	$M_r$ (emu/g)	$M_r/M_s$	$H_c$ (Oe)
Solid state (1200 °C, 4 h)	290	82	14	0.17	304
Solid state (1200 °C, 8 h)	380	78	13	0.16	322
Solid state (1200 °C, 12 h)	530	81	7	0.09	219
Citrate gel (300 °C, 2 h)	24	66	26	0.39	1376
Citrate gel (600 °C, 2 h)	28	69	30	0.43	1525
Citrate gel (900 °C, 2 h)	48	80	37	0.46	979
Polymer complex ( $\mu\text{m}$ )	160	75	27	0.36	498
Polymer complex (nm)	32	67	30	0.45	1625

In 2009, D. H. Kim *et al.* [14] synthesized  $\text{MFe}_2\text{O}_4$ , where M;  $\text{Co}^{2+}\text{Mn}^{2+}$  and  $\text{Fe}^{2+}$  nanoparticles used diol reduction of organic metals. X-ray diffraction (XRD) showed a phase formation of inverse spinel structure [Figure 2.8(a)]. The synthesized ferrites were super paramagnetic at room temperature. The saturated magnetization of  $\text{CoFe}_2\text{O}_4$  was higher than that for  $\text{MnFe}_2\text{O}_4$  or  $\text{Fe}_3\text{O}_4$  [Figure 2.8(b)]. Each sample presented a ferromagnetic uncompensated magnetization moment between tetrahedral and octahedral sites. The divalent cations ( $\text{Co}^{2+}$ ,  $\text{Mn}^{2+}$ , and  $\text{Fe}^{2+}$ ) resided in incomplete tetrahedral or octahedral sites, leading to varied magnetization behavior.

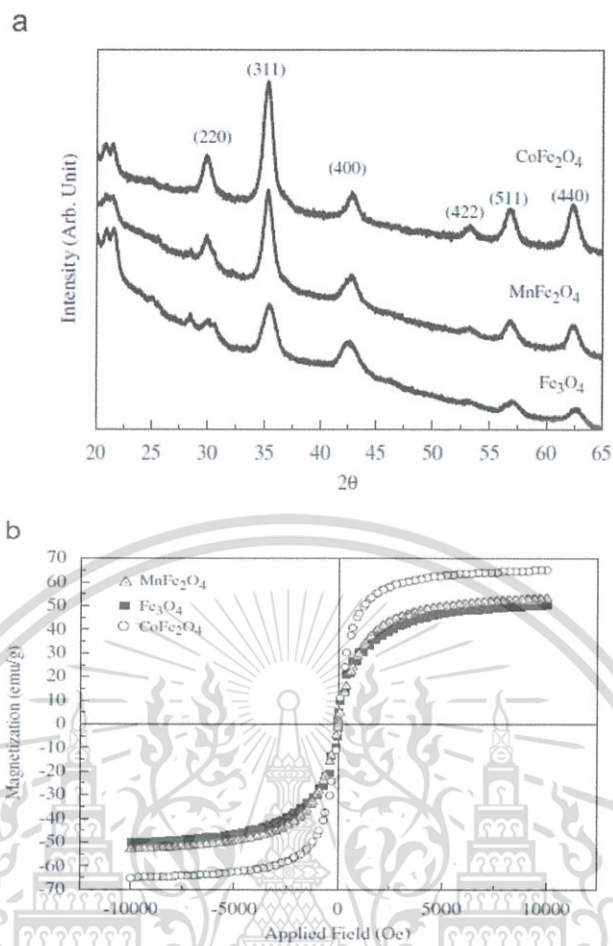


Figure 2.8 (a) X-ray diffraction and (b) magnetic curves of the synthesized inverse spinel ferrite nanoparticles [13].

The  $\text{CoFe}_2\text{O}_4$  showed the highest  $M_s$  when compared with  $\text{MnFe}_2\text{O}_4$  and  $\text{Fe}_3\text{O}_4$ . The size-dependent  $M_s$  in identical materials was caused by an inactive spin pinning surface layer, due to asymmetric surroundings of atoms adjacent to the surface. The magnetized nanoparticles displaying reduced  $M_s$ , with decreasing particle size, were attributed to an enlarged proportion of pinning shell magnetic moments. Additionally, the amplitude of the decrease in  $M_s$  was influenced by anisotropic energy; the  $M_s$  of nanoparticles with high anisotropy did not reduce as quickly when the particle sizes decreased with low anisotropic energy, as  $\text{MnFe}_2\text{O}_4$  and  $\text{Fe}_3\text{O}_4$  nanoparticles have lower anisotropies than  $\text{CoFe}_2\text{O}_4$ .

### 2.2.2 Cobalt Ferrite Substitution

The partial replacement of the transition metal in cobalt ferrite presents an excellent chance to engineer specifically magnetic interactions in the lattice.

Substituted cobalt ferrite transition metals were found in many previous works [15-23].

### 1) Manganese Substituted by Cobalt Ferrite

Mn is a transition metal that has five unpaired electrons in orbital  $3d$ , in which the magnetization moment results from the number of unpaired electrons [1]. Therefore, many researches have studied the magnetic properties of manganese substituted cobalt ferrite.

In 1999, C. S. Kim *et al.* [15] studied the growth of ultrafine  $\text{Co}_{0.9}\text{Mn}_{0.1}\text{Fe}_2\text{O}_4$  particles by using the sol-gel method. XRD determination exhibited peaks of  $\text{Co}_{0.9}\text{Mn}_{0.1}\text{Fe}_2\text{O}_4$  powders that were fired at and over  $400^\circ\text{C}$ , and obtained a single phase of spinel structure. Saturated magnetization increases radically with the expansion annealing temperature. Nevertheless, the coercive field reduces as soon as the annealing temperature reaches higher than  $600^\circ\text{C}$  (Figure 2.9).

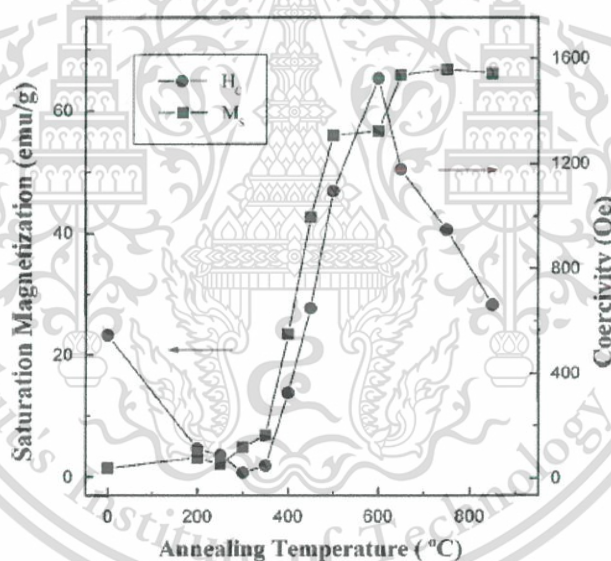


Figure 2.9 The coercivities and saturated magnetization of  $\text{Co}_{0.9}\text{Mn}_{0.1}\text{Fe}_2\text{O}_4$  powders at different annealing temperatures [15].

In 2007, O. Caltun *et al.* [16] prepared the  $\text{CoMn}_x\text{Fe}_{2-x}\text{O}_4$  system by using the conventional ceramic method, where  $x = 0.0, 0.3, 0.4,$  and  $0.6$ . Samples were calcined in air at  $800^\circ\text{C}$  and sintered at  $1,180^\circ\text{C}$  in air for 5 h. From the results, XRD testified the existence of a spinel structure. The microstructural materials exposing additional cobalt had effect on the average grain sizes. A small amount of Mn

(doping levels of up to  $x = 0.3$ ) in the densification process was enhanced, and decreasing grain sizes with increasing intergranular pores were observed above this concentration. Manganese ions like to generate flaw microstructures, and this could be due partially to their delineation from a dissolved cobalt ferrite matrix and condensate to grain boundaries (Figure 2.10).

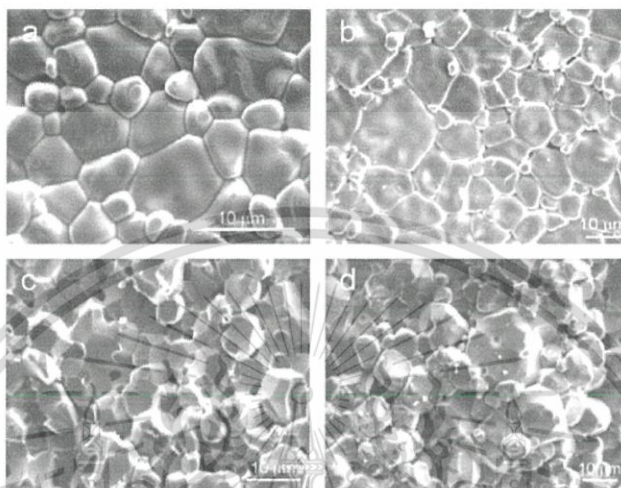


Figure 2.10 Microstructures of the  $\text{CoMn}_x\text{Fe}_{2-x}\text{O}_4$  samples, where  $x =$  (a) 0.00, (b) 0.30, (c) 0.40, and (d) 0.60 [16].

Measurements from the vibrating sample magnetometer (VSM) showed the saturated magnetization of samples, where  $x = 0.00$  and  $0.3$  were high values. This might be due to the small number of  $\text{Mn}^{2+}$  ions in the middle of  $\text{Mn}^{3+}$  ions in B-sites appearing to be bigger B sublattice magnetic donations to magnetization. Additionally, increased doping reduces the power in exchange interactions because it affects the smaller value of saturated magnetization, as expected (Figure 2.11).

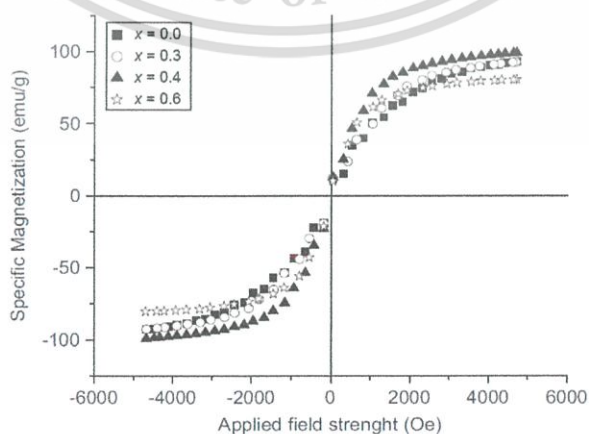


Figure 2.11 VSM results for  $\text{CoMn}_x\text{Fe}_{2-x}\text{O}_4$  samples [16].

This material is reserved for educational use only, not allowed for commercial use.

Forbidden to modify the content, and cite the document when use.

Furthermore, in 2009, H. N. Choi *et al.* [17] studied the  $\text{Mn}_{1-x}\text{Co}_x\text{Fe}_2\text{O}_4$  ( $x = 0.00, 0.50, 1.00$ ) system, which was synthesized using the high temperature thermal decomposition technique. From XRD pattern analysis, the structure was a single phase spinel one. Then, the magnetic properties were investigated, and from the results, saturated magnetization of Mn ferrite was higher than that in Co ferrite (Figure 2.12). However, the coercivities of cobalt ferrite were larger than those in manganese ferrite because the coercive field was associated with crystal anisotropy.

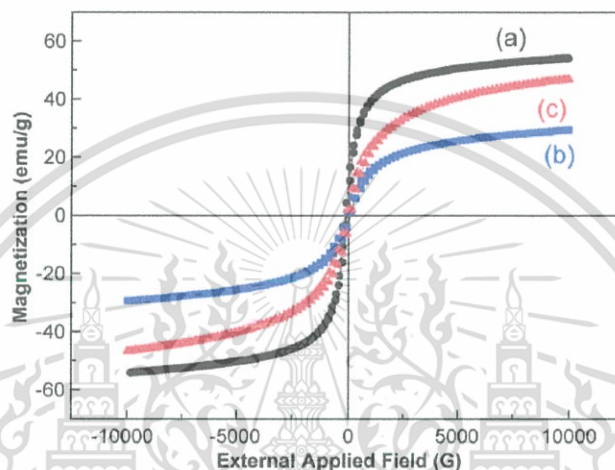


Figure 2.12 Magnetic curves of the samples, (a)  $\text{MnFe}_2\text{O}_4$ , (b)  $\text{Mn}_{0.5}\text{Co}_{0.5}\text{Fe}_2\text{O}_4$ , and (c)  $\text{CoFe}_2\text{O}_4$ , at room temperature [17].

Also in 2009, M. K. Shobana *et al.* [18] prepared the  $\text{Co}_{0.5}\text{Mn}_{0.5}\text{Fe}_2\text{O}_4$  by using the sol-gel combustion technique. The powders were calcined at  $500^\circ\text{C}$ ,  $700^\circ\text{C}$  and  $900^\circ\text{C}$ . The cubic spinel structure began to appear in the sample calcined at  $500^\circ\text{C}$  and the intensity and sharpness of the peaks were improved in the samples calcined at high temperatures. The XRD patterns agreed with the cubic spinel structure, and with no other peaks being noticed, nonexistence of a secondary phase was indicated. Magnetic characterization of  $\text{Co}_{0.5}\text{Mn}_{0.5}\text{Fe}_2\text{O}_4$  particles was performed using a VSM. The saturated magnetization reduced first and after that increased with calcination temperature. Then, the sample increased in size at high temperatures and induced the crystalline phase (Figure 2.13).

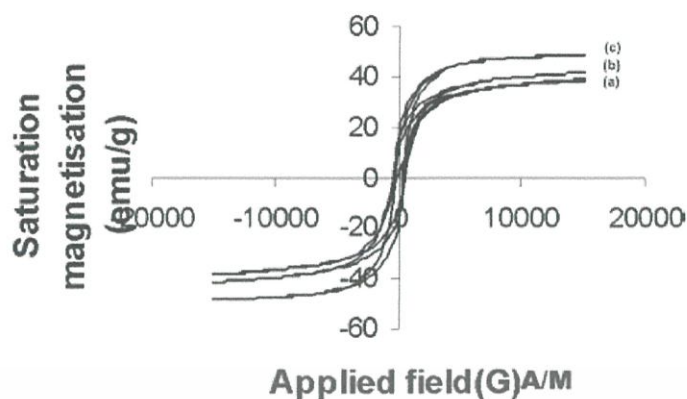


Figure 2.13 The Hysteresis loop of  $\text{Co}_{0.5}\text{Mn}_{0.5}\text{Fe}_2\text{O}_4$  nanoparticles calcinated at various temperatures; (a) 500°C, (b) 700°C, and (c) 900°C [18].

In addition, the coercive force increases with increasing crystalline size before it decreases gradually with increasing particle size (Figure 2.14). This is the result of coercivity affected by most factors, for example, packing density, crystal defects, shape, and grain size.

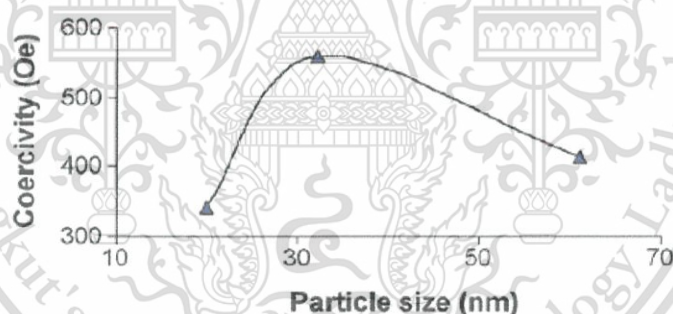


Figure 2.14 The coercive force at different particle sizes [18].

In 2011, J. Z. Msomi *et al.* [19] produced nanoparticles of  $\text{Mn}_x\text{Co}_{1-x}\text{Fe}_2\text{O}_4$  ( $x = 0.10, 0.50$ ) ferrites using the glycothermal reaction. XRD patterns of the as-prepared  $\text{Mn}_x\text{Co}_{1-x}\text{Fe}_2\text{O}_4$  show that the peaks were referred successfully to a cubic spinel structure. No secondary phases were noticed. The lattice constant of  $\text{Mn}_{0.5}\text{Co}_{0.5}\text{Fe}_2\text{O}_4$  was larger than that for  $\text{Mn}_{0.1}\text{Co}_{0.9}\text{Fe}_2\text{O}_4$ , which may attribute to the bigger size of Mn, ionic radius of 0.089 nm, substitution of Co, and ionic radius of 0.084 nm. The difference between coercive fields and saturated and remnant magnetization also were exhibited at various temperatures (Figure 2.15). From the results, the coercive

field increased at a lower temperature, while the remnant and saturated magnetizations reduced with increasing temperature.

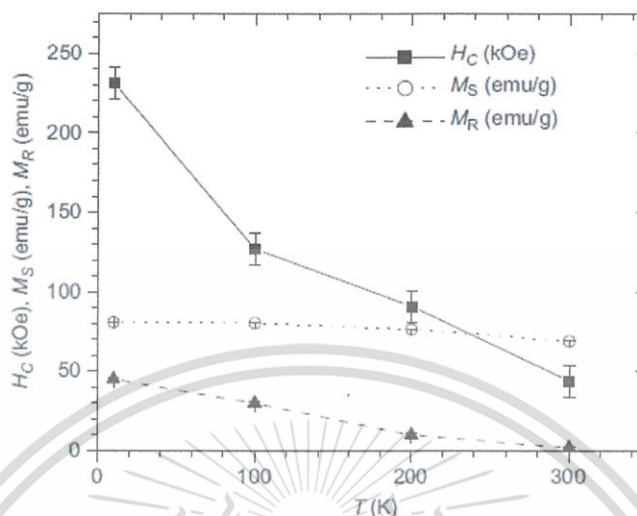


Figure 2.15 Saturated and remnant magnetization and coercivity for  $Mn_{0.1}Co_{0.9}Fe_2O_4$  as a function of temperature [19].

In 2012, Y. Köseoğlu *et al.* [20] prepared a series of manganese doped cobalt ferrites of  $Co_{1-x}Mn_xFe_2O_4$ , where  $x = 0.0 - 1.0$  via polyethylene glycol assisted by the hydrothermal technique. The autoclaves were placed in a stove at  $180^\circ C$  for 24 h. An XRD examination showed a single phase formation of cubic spinel structure in all of the samples. Lattice parameters were calculated by respective  $(h k l)$  parameters and  $d$ -spacing values from the classic method. The lattice parameters presented an almost linear decrease with increased manganese content, thus obeying Vegard's law, as the ionic radius of  $Co^{2+}$  ( $0.74 \text{ \AA}$ ) was larger than that of  $Mn^{2+}$  ( $0.66 \text{ \AA}$ ). The magnetic property measurements were achieved by a Quantum Design Vibrating Sample Magnetometer (QD-VSM). The  $M-H$  curve revealed that coercivity decreases when Mn doping increased because manganese is a soft magnetic property. Mn content also influences the remanent and saturated magnetization. It is known that magnetization is associated with magnitude of the magnetic dipole moment of an electron. In this context, it is recognized that  $Co^{2+}$  has  $3 \mu_B$  and  $Mn^{2+}$  has  $5 \mu_B$  as their dipole moments, and when Mn doping increased, saturated magnetization also increased, as shown clearly in Figure 2.16.

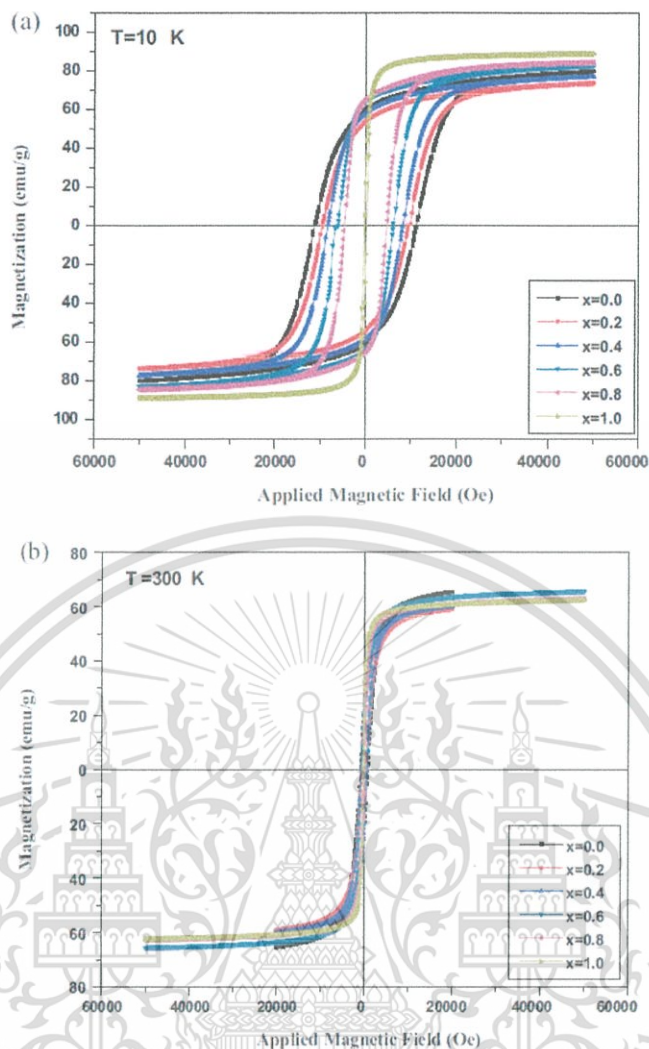


Figure 2.16 M–H Curves of  $\text{Mn}_x\text{Co}_{1-x}\text{Fe}_2\text{O}_4$  nanoparticles at 10 K (a) and 300 K (b) [20].

Besides, a decrease was noticed in the coercive field of all samples with increasing temperature and Mn content. Due to  $\text{CoFe}_2\text{O}_4$  being a hard magnetic material with large coercive field, and  $\text{MnFe}_2\text{O}_4$  a soft magnetic material, there is almost no coercive field. As a coercive field is the measure of magnetocrystalline anisotropy, increasing coercive field with Co doping can be attributed to Co ion anisotropic property. As shown in Figure 2.17, similar coercive variation as in Mn doping increased, and remanence was inclined to decrease, due to Mn ferrite having no remanent magnetization, since it is a soft magnetic material. Therefore, magnetic remanence appears from Co ions and is revealed in the samples.

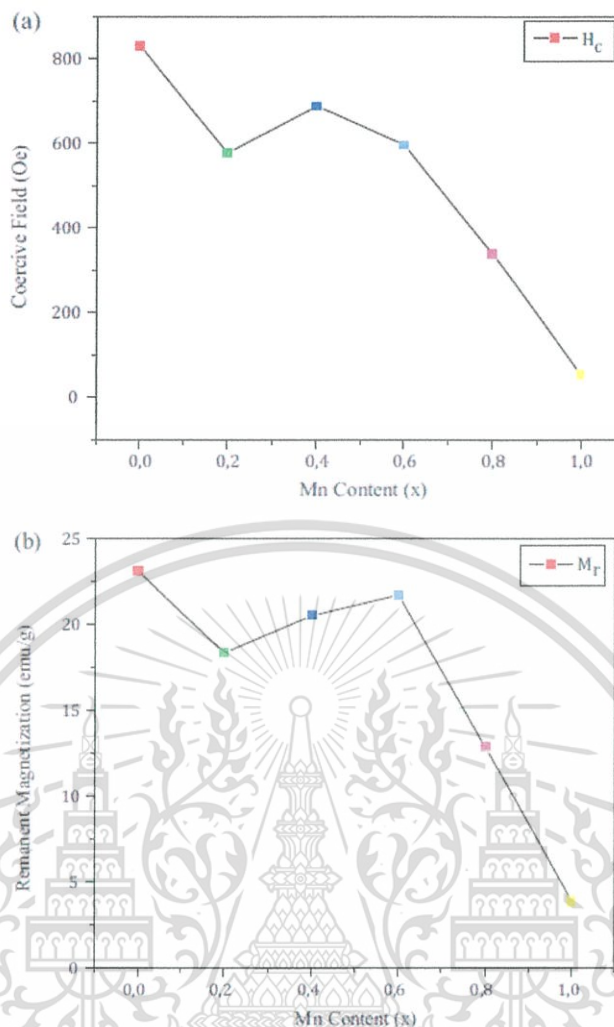


Figure 2.17 Difference of composition in the coercive field (a) and remanent magnetization (b) of  $Mn_xCo_{1-x}Fe_2O_4$  nanoparticles [20].

## 2) Zinc Substituted by Cobalt Ferrite

The increase of none magnetic zinc in cobalt ferrite increases saturated magnetization, because when none magnetic zinc is replaced by cobalt ferrite, due to zinc ferrite being a normal spinel, there is strong preference for the tetrahedral site and a decreased amount of  $Fe^{3+}$  in the A-site. The result is due to antiferromagnetic coupling, which raises the magnetic moment in the B-site and saturated magnetization [2]. In 2009, Y. Köseoğlu *et al.* [21] reported that replacement of the  $Zn^{2+}$  ion with a none magnetic moment gave preference to A-site occupation, resulting in decreasing super exchange interaction between B- and A-sites. Thus, it is possible to change magnetization by changing zinc substituted content, since cobalt doped zinc ferrite ( $Co_xZn_{1-x}Fe_2O_4$  where  $x = 0.2, 0.4, 0.8$ ) has

This material is reserved for educational use only, not allowed for commercial use.

been synthesized successfully by the microwave-induced combustion method. XRD patterns of the synthesized samples exhibited 11 reflection planes that imply the residence of a single phase cubic spinel. Furthermore, the lattice parameter of each composition was found to decrease with increasing Co content when following Vegard's law. This is due possibly to the difference in ionic radius of the  $\text{Co}^{2+}$  and  $\text{Zn}^{2+}$  cations, as the ionic radius of  $\text{Zn}^{2+}$  (0.82 Å) is larger than that of  $\text{Co}^{2+}$  (0.72 Å). A scanning electron micrograph (SEM) of  $\text{Co}_x\text{Zn}_{1-x}\text{Fe}_2\text{O}_4$  nanocrystals (Figure 2.18) showed all sample having large grain sizes, and much porosity occurred from gases leaving while combustion reacted.

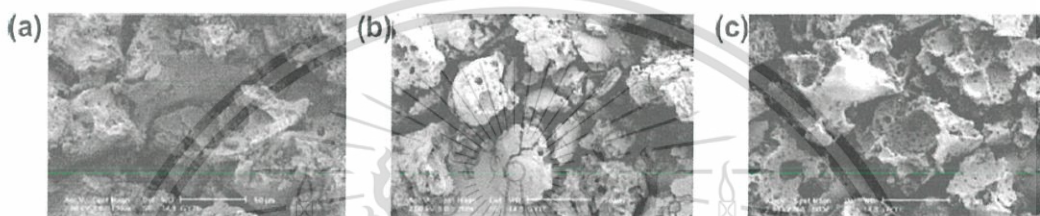


Figure 2.18 SEM morphology of  $\text{Co}_x\text{Zn}_{1-x}\text{Fe}_2\text{O}_4$ : (a)  $x = 0.2$ , (b)  $x = 0.4$ , and (c)  $x = 0.8$  [21].

Magnetization measurements indicated that as soon as the Co content increased so too did saturated magnetization because the magnetic characteristic of Co ions was replaced by none magnetic Zn cations, and the coercive field also increased due to the nature of cobalt anisotropy. It became known that  $\text{CoFe}_2\text{O}_4$  has the most anisotropic constant  $K_1$  among the spinel ferrites, due to the residence of  $\text{Co}^{2+}$  cations in the B-sites (Figure 2.19).

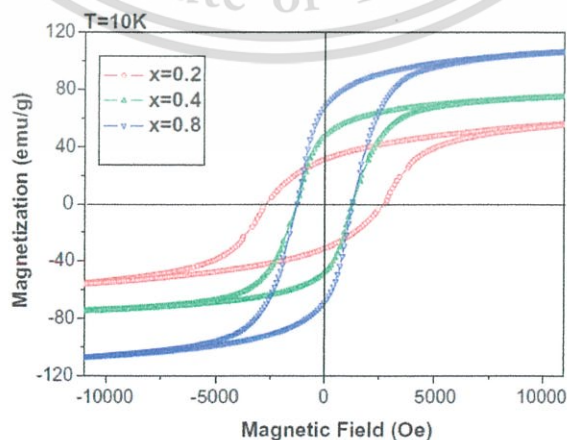


Figure 2.19 Magnetic hysteresis loops of  $\text{Co}_x\text{Zn}_{1-x}\text{Fe}_2\text{O}_4$  nanoparticles at 10 K [21]. This material is reserved for educational use only, not allowed for commercial use.

### 3) Copper Substituted by Cobalt Ferrite

In 2011, S. Y. An *et al.* [22] studied Cu replaced by Co ferrites;  $\text{Cu}_x\text{Co}_{1-x}\text{Fe}_2\text{O}_4$ , where  $0 \leq x \leq 0.5$ . The toroidal cores of Co substituting Cu samples were prepared by conventional ceramic processing. The mixed powders were calcined at  $800^\circ\text{C}$  in air for 2 h before sintering at  $860 - 940^\circ\text{C}$  in air for 2 h. The analyzed phase existed in an inverse spinel structure. There was no secondary phase for instant CuO and  $\alpha\text{-Fe}_2\text{O}_3$ . The lattice constants were determined by Rietveld analysis via the Fullprof program, and decreased with increasing Cu substitution. It can be anticipated that the ionic size for  $\text{Cu}^{2+}$  ions of  $0.70 \text{ \AA}$  is smaller than that for  $\text{Co}^{2+}$  ions of  $0.82 \text{ \AA}$ . The magnetization of sintering Co-Cu samples was decided by a VSM at room temperature. The saturated magnetization ( $M_s$ ) of the Co - Cu ferrite decreased drastically (Figure 2.20) and the coercive field ( $H_C$ ) decreased dramatically as the Cu content of  $x$  increased (Figure 2.21). This shows that  $H_C$  and  $M_s$  can be controlled by Cu concentration.

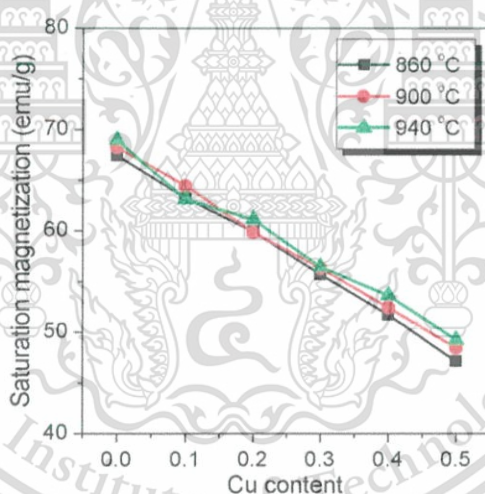


Figure 2.20 Saturated magnetization of varied Cu content at room temperature [22].

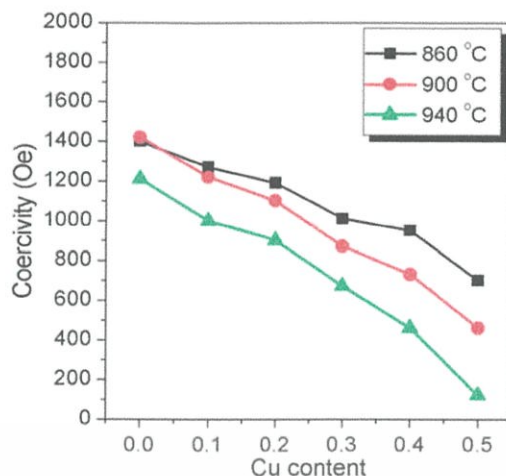


Figure 2.21 Coercive field of varied Cu content at room temperature [22].

In 2012, M. Hashim *et al.* [23] prepared different compositions of  $\text{CoFe}_{2-x}\text{Cu}_x\text{O}_4$  ferrite nanoparticles, where  $x = 0.0-0.5$ , by using the sol-gel technique. The gel was annealed for 24 h at  $200^\circ\text{C}$ . The resulting powder was heated at  $800^\circ\text{C}$  for 8 h in order to displace organic materials. The structural properties were analyzed by XRD and the samples exposed with  $2\theta$  values, corresponding to Bragg's reflection, which was attributed to a single phase for the cubic spinel structure. The lattice parameters were investigated from XRD patterns by Powder-X-software, which showed that they enlarged with increasing content of  $\text{Cu}^{2+}$  ions. The difference in lattice parameters may be due to the variation of ionic radius in replaced and doped ions. In the case of  $\text{Fe}^{3+}$  ions, substitution of  $\text{Cu}^{2+}$  ions with the ionic radius of  $\text{Fe}^{3+}$  ions ( $0.67 \text{ \AA}$ ) is smaller than that of  $\text{Cu}^{2+}$  ions ( $0.70 \text{ \AA}$ ) because smaller ions are expected to substitute larger ones rising in lattice parameters. The morphology of the examined samples was investigated via SEM micrographs. The particle sizes increased with increasing doping concentration, which was due probably to porosity and oxygen vacancies that block grain growth (Figure 2.22).

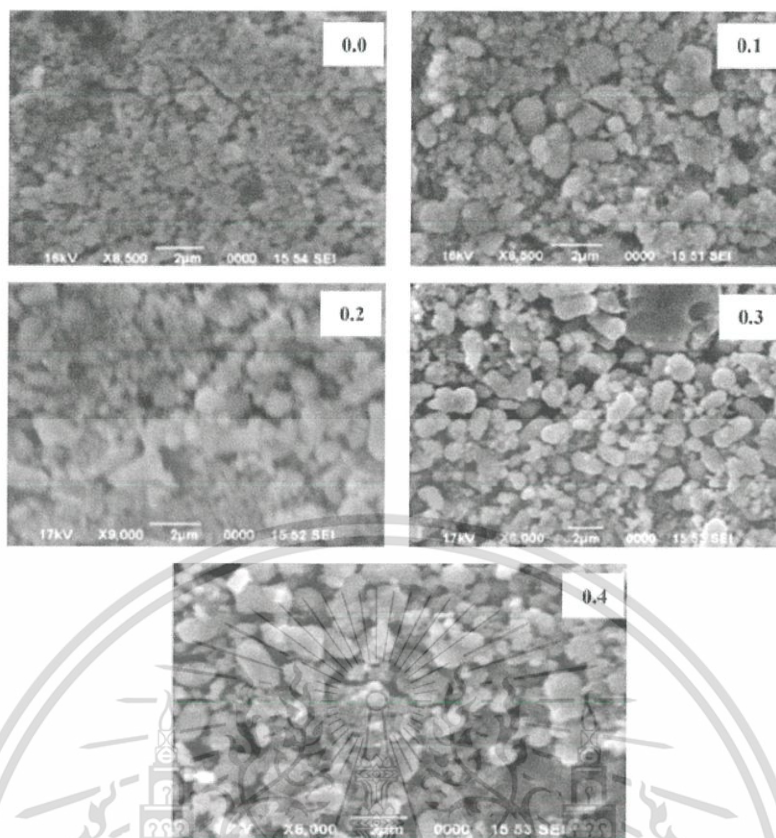


Figure 2.22 SEM of  $\text{CoFe}_{2-x}\text{Cu}_x\text{O}_4$ , where  $x = 0.0-0.4$  nanoparticles [23].

Magnetic hysteresis measurements at room temperature infer that saturated magnetization declines with increasing Cu substitution (Figure 2.23). This behavior is described in Neel's sublattice models. In this condition, saturated magnetization per unit is explained by the remaining magnetic moment in A- and B-sites. Interactions in the middle of octahedral (B) and tetrahedral (A) sublattices in the spinel structure, composed of intra sublattice (B–B) and (A–A), interchange with inter sublattice (A–B) super exchange interactions. The intra sublattice super exchange interactions on (B–B) and (A–A) are much weaker than those on (A–B). Magnetization can be estimated by the relationship of  $M = M_B - M_A$ , where  $M_B$  and  $M_A$  represent the overall magnetic moment of B and A sublattices. The magnetic moment of octahedral coordinated  $\text{Co}^{2+}$  ions and  $\text{Fe}^{3+}$  cations is  $3 \mu_B$  and  $5 \mu_B$ , respectively (spin only). The magnetic moment of  $\text{Cu}^{2+}$  ions has  $1 \mu_B$ , with  $\text{Cu}^{2+}$  cations obtaining a small magnetic moment when compared to  $\text{Fe}^{3+}$  ions. Then, saturated magnetization is shown to decrease with  $\text{Cu}^{2+}$  concentration.

This material is reserved for educational use only, not allowed for commercial use.

Forbidden to modify the content, and cite the document when use.

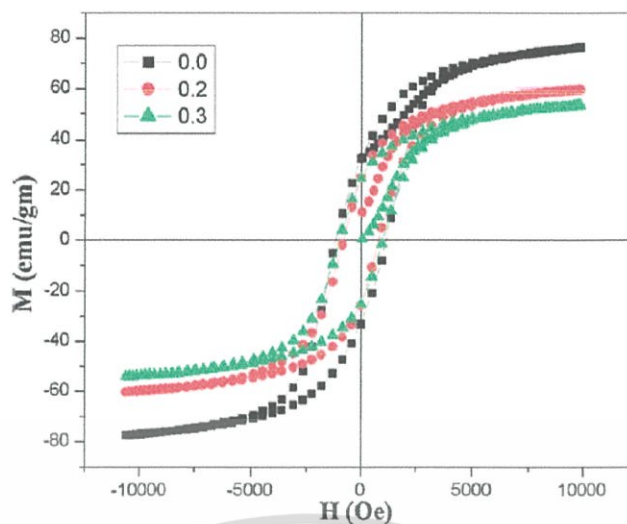


Figure 2.23 M–H curves of  $\text{CoFe}_{2-x}\text{Cu}_x\text{O}_4$  ( $x = 0.0\text{--}0.3$ ) nanoparticles at room temperature [23].

Discussion from the literature has concentrated on the phase formation of cobalt ferrite doping via XRD. The morphology was investigated using a SEM. Also, the magnetization of ferrites was examined using the VSM. However, the cation valence state and local structure of the  $\text{CoFe}_2\text{O}_4$  substitution could not be clarified completely by using the above mentioned techniques. The valency of the cation decides the occupation of these sites, which in turn, powerfully affects the electronic and magnetic properties of materials. Hence, this research described use of the conversion electron, X-ray absorption near the edge of spectroscopy, XANES, extended X-ray absorption of fine structure, and EXAFS, as instruments for investigating the cation site distribution of metal in ferrite structure. Since these techniques are element specific, chemically sensitive and a local structure, they are most appropriate for this research [23].

### 2.3 Thermal annealing

Thermal treatment is the phrase used to report all restricted cooling and heating performances achieved on materials in solid state, in order to modify their properties and/or microstructure. It should be reported that heat treatment is used in composites and ceramics also for adjusting their properties.

The main purposes of varied heat treatment are:

This material is reserved for educational use only, not allowed for commercial use.

Forbidden to modify the content, and cite the document when use.

1. Stabilize the physical or mechanical properties against transformation that might occur while exposed to assisting environments.
2. Soften the material to enhance ability.
3. Relax undesirably remaining stresses induced by pending parts of fabrication.
4. Increase the hardness or strength of materials.
5. Increase the resistance or toughness against the breakage of materials.
6. Certify part dimensional steadiness.

Various materials react to dissimilar temperatures in thermal treatment. Each material has a specifically chemical combination, which transforms in structure and physical properties at distinct critical temperatures. Even lower percentages of elements in the composition of materials mostly decide the time, method, rate, and temperature of heating and cooling, which needs to be used in the thermal treatment process. Depending on the heat treatment used the microstructure and/or atomic structure of materials change because of decreased or increased atom solubility, conversion of the crystal structure, movement of dislocations, new grain formation in different or same phases, enlarged grain sizes, and other mechanical aspects. Due to there being so many methods for metals that are heat treated, it is not practical to discuss them all.

### 2.3.1 General thermal treatment processes

Some of the more general terms used in heat treatment are presented below. It must be noted that not all of the expressions are suitable for all materials.

- Age Hardening is associated with a low temperature thermal treatment process that hardens materials and makes precipitation phases or componential materials from a supersaturated solid solution.

- Annealing is a process of softening metals that are heated after allowing them to cool gradually. The annealing objective is to soften the materials for enhancing formability, machinability, and controllability of magnetic properties.

- Normalizing is just the same as annealing, but the cooling process is much quicker. The result enhances strength, but little ductility in materials. Its objective is

to generate greater uniformed properties mechanically, eradicate surface and internal stresses, and improve grain structure.

- Precipitation Heat Treatment is a triple step method of quenching, age hardening and solution treatment to improve the hardness or strength of materials.

- Solution Heat Treatment involves heating the materials to a temperature that changes all elements into solid solution after cooling very quickly, and freezes the atoms in space.

- Stress Relieving is a low temperature thermal treatment that is used to decrease the level of remaining stresses in materials.

- Tempering relates to heating the hardened metal gently and permitting it to cool slowly in order to generate metal that is still hard and also a little brittle.

- Quenching is cooling hot materials rapidly. The way to quench materials can differ from using oil, water and forced air to other elements. Most steel is hardened via heating and quenching, which results in metals that are extremely hard, but also brittle [24].

Annealing in material science is thermal treatment, which modifies the chemical and physical properties of the materials in order to reduce their hardness and improve their ductility, while making them more workable. This involves heating materials to over their recrystallization temperature, and then retaining the appropriate temperature before cooling. During annealing, atoms transfer in the crystal lattice and the dislocations amount to reduction, which in turn induces hardness and ductility.

### 2.3.2 Annealing Process

Annealing refers to the thermal treatment of expanding time before cooling slowly for materials revealed at high temperature. Normally, annealing is performed to (1) enlarge ductility, toughness and softness, (2) generate specific microstructure, and (3) eradicate stresses. Differences of thermal annealing treatment are possible, as the process is indentified by transformations that are influenced many times by the microstructure and responsibility of modifying mechanical properties.

The annealing method comprises three steps; (1) heating to the required temperature, (2) soaking at that temperature, and (3) cooling normally to room

temperature. The time is an important parameter in these stages. While heating and cooling, temperature reduction exists between the internal and external parts as well as the magnitude of geometry and size of the materials. If variation of the temperature rate is too large, internal stresses and temperature may cause cracking or warping. Besides, the current annealing time should be long enough to permit some reactions of essential transformation. Also, examination of the annealing temperature is important, as annealing may accelerate with increasing temperature, due to the usual implication of diffusion processes. [25]

Thermal treatment on the properties of ceramics has been reported in previous works. In 1998, Z. J. Zhang *et al.* [26] studied temperature dependence of the oxidation state and cation distribution of normal spinel in Mn ferrite. The inversion degree (61%) of  $\text{Fe}^{3+}$  ions residing in tetrahedral sites was high in Mn ferrite nanoparticles synthesized using co-precipitation. After heat treatment at 25 to 485°C in a furnace with a vacuum, the distribution of cations became stable at 29% inversion (Table 2.7).

Rietveld refinement parameters of  $\text{MnFe}_2\text{O}_4$  nanocrystalline from neutron powder diffraction data [26]

measurement order	T (°C)	cell edge $a$ (Å)	site occupancies <sup>a</sup>		x (O)	agreement factors	
			A-site	B-site		$\chi^2$	$R_{wp}$ (%)
1	25	8.4811(3)	$\text{Mn}_{0.39}\text{Fe}_{0.61}$	$\text{Mn}_{0.82}\text{Fe}_{1.18}$	0.2589(2)	1.26	6.71
2	363	8.5131(3)	$\text{Mn}_{0.61}\text{Fe}_{0.39}$	$\text{Mn}_{0.52}\text{Fe}_{1.47}$	0.2597(2)	1.28	9.00
3	485	8.5272(2)	$\text{Mn}_{0.62}\text{Fe}_{0.38}$	$\text{Mn}_{0.56}\text{Fe}_{1.43}$	0.2597(2)	1.28	7.10
4	24	8.4884(2)	$\text{Mn}_{0.71}\text{Fe}_{0.29}$	$\text{Mn}_{0.50}\text{Fe}_{1.50}$	0.2606(2)	1.33	6.73

<sup>a</sup> Estimated standard uncertainties for site occupancies are  $\pm 0.01$ . <sup>b</sup> Fixed value.

The initial inversion of 61 % for cation distribution is due to random occupation of B- and A-sites. While nanoparticles formed at room temperature, the thermal energy was too low to overpower impediment energy and therefore arrange cation distribution. Once the particles had been heated, there was enough energy to enable ions to diffuse and generate a stable situation of approximately 29 % inversion.

This material is reserved for educational use only, not allowed for commercial use.

Forbidden to modify the content, and cite the document when use.

The oxidation state of manganese in Mn ferrite nanoparticles was investigated using electron energy loss spectroscopy (EELS). The constitution of  $\text{Mn}^{3+}$  ions may appear during the precipitation method, as  $\text{Mn}^{2+}$  is oxidized readily in largely basic solution. Regarding as-prepared Mn ferrite nanoparticles, each Mn ion has both +2 and +3 oxidation states of approximately 50% (Figure 2.24).  $\text{Mn}^{3+}$  ions are reduced gently to  $\text{Mn}^{2+}$  ions while the temperature is enhanced, and when the temperature reaches 600°C, practically all  $\text{Mn}^{3+}$  ions in the particles change to  $\text{Mn}^{2+}$  ions. Oxygen ions lost in particles and  $\text{Mn}^{3+}$  ions absorbing more electrons preserve the charge of equilibrium, and affect transformation of the Mn state, pending heating in a vacuum.

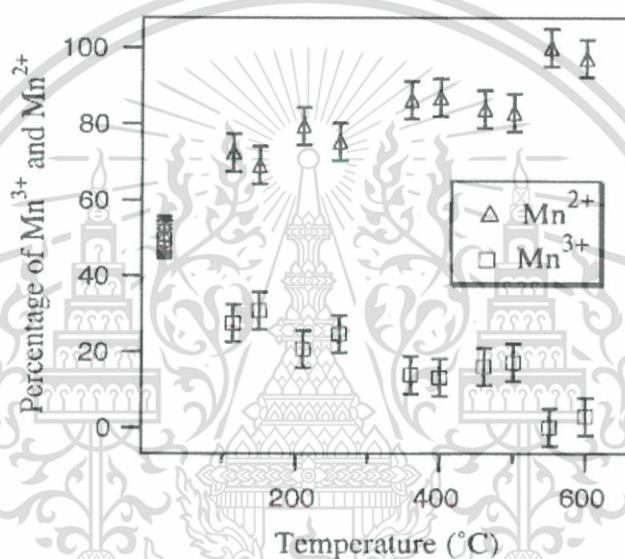


Figure 2.24 Calculated relative percentages of  $\text{Mn}^{3+}$  and  $\text{Mn}^{2+}$  [26].

In 2007, N. Vittayakorn *et al.* [27] investigated the effect of heat treatment on dielectric properties, ferroelectric properties, and morphologies of PZT-based materials. The results found that the microstructure of ceramics did not change the grain size before or after annealing, and there was no sign of unnatural grain growth in the annealed samples (Figure 2.25).

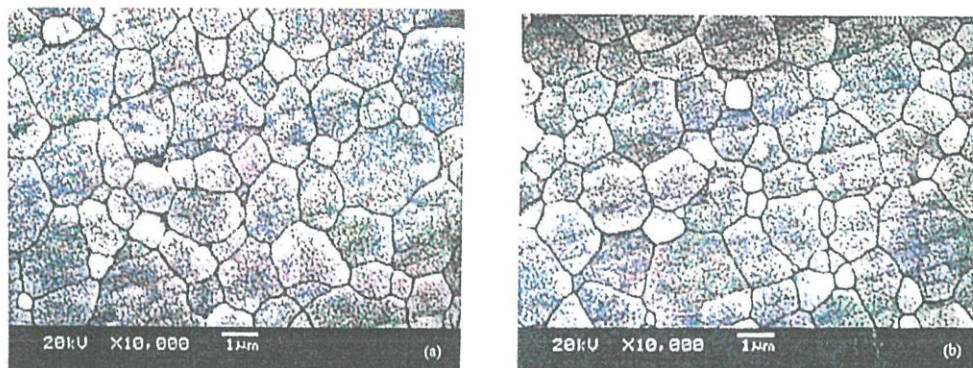


Figure 2.25 SEM of 0.9PZT-0.1PZN samples (a) before annealing, (b) after annealing [27].

The as-sintered ceramic presented a weak normal ferroelectric characteristic, which associated with low relative permittivity and the highest measurement at 1 kHz of 13,000. The annealing affected a change to a likely relaxor ferroelectric characteristic, with a shift at the highest dielectric temperature from 360 to 350°C, and dramatic enhancement of relative permittivity at 1 kHz to the highest value of 35,000 for long annealing (Figure 2.26).

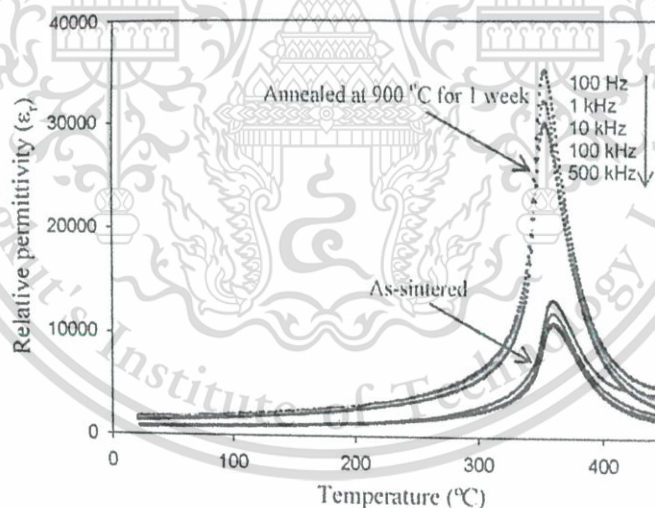


Figure 2.26 The relative permittivity of temperature dependence before and after annealing samples at various frequencies [27].

Remanence of polarization extended non annealed samples from 20.4  $\mu\text{C}/\text{cm}^2$  to 34.1  $\mu\text{C}/\text{cm}^2$ . It showed that annealed samples had higher remanence polarizations correlating with non annealed samples, meaning that the annealed samples were poled more easily and had better piezoelectric properties (Figure 2.27).

This material is reserved for educational use only, not allowed for commercial use.

Forbidden to modify the content, and cite the document when use.

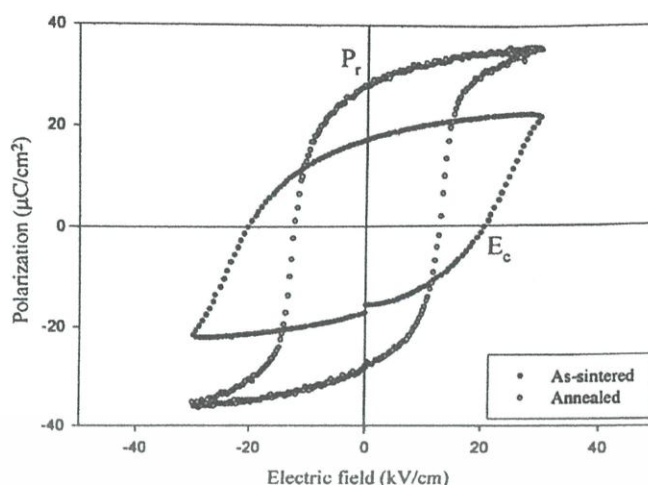


Figure 2.27 Electrical field and polarization of 0.9PZT-0.1PZN ceramics for non and annealed samples [27].

Furthermore, in 2011, H. M. I. Abdallah *et al.* [28] investigated the effect of annealing temperature on magnetic properties of  $Mn_xCo_{1-x}Fe_2O_4$  ferrite nanoparticles. The powders were prepared using the glycol thermal technique from high purity chlorides. The results of transmission electron microscopy (TEM) images are shown in Figure 2.28. The grain sizes were enlarged by the annealed temperature, as expected.

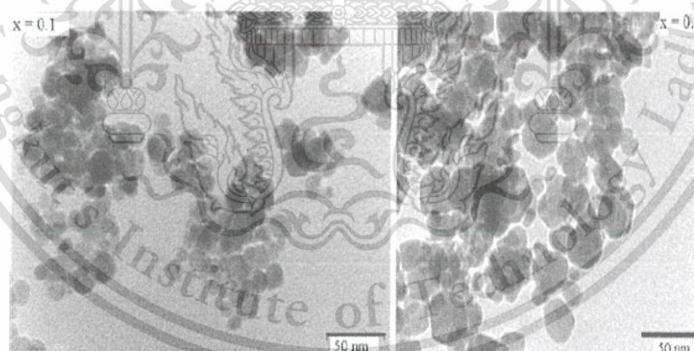


Figure 2.28 TEM results of  $Co_{1-x}Mn_xFe_2O_4$  powders annealed at 500°C [28].

Figure 2.29 shows that properties of magnetization such as saturated magnetizations and coercive field are influenced by varied Mn concentration. The coercivities are decreased essentially with Mn content, and affected by  $CoFe_2O_4$  and a large coercive field, due to the powerful anisotropy associated with Co ions. Therefore, replacement by Mn cations with smaller anisotropy induces decreasing  $H_C$ , remanent magnetization. This was noticed to an extent by increased annealing. This material is reserved for educational use only, not allowed for commercial use.

Forbidden to modify the content, and cite the document when use.

temperature that attributed to enhancing average particle sizes. Transformation of  $M_S$  and  $M_R$  can be described by the cation distribution of B- and A-sites and Neel's principle. The heat from annealing transforms cation distribution in the middle of B- and A-sites.

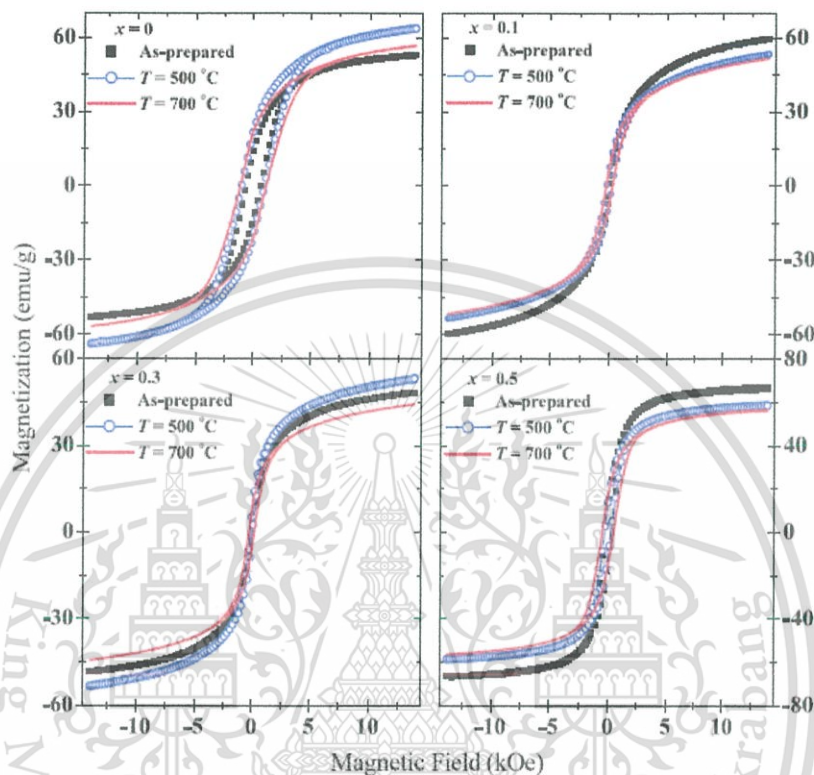


Figure 2.29 The M-H curve of  $\text{Co}_{1-x}\text{Mn}_x\text{Fe}_2\text{O}_4$  measured at various temperatures [28].

It is seen from the literature that thermal annealing was summarized as a significant improvement in electrical and magnetic properties. However, no concentration was attributed directly to the influence of thermal annealing temperature, annealing time, or annealing atmosphere on the cation distribution of cobalt substituted by metal ferrites. Furthermore, the main purpose of this research applied to the cation distribution of spinel ferrites. A variety of probes can be considered as informational on cation site distribution, for instance, mössbauer spectroscopy, neutron diffraction, and XRD, but the use of these techniques was limited. However, XAS has been shown as a potent tool, which is perfect for investigating disordered and multicomponent diluted materials. Therefore, the influence of thermal annealing on cation distribution was studied using XAS, which is

necessary for investigating and studying magnetic and catalyst properties of this material.

## 2.4 X-Ray Absorption Spectroscopy (XAS) Technique

XAS is a modulation of an atom with X-ray absorption, possibly because of the physical and chemical state of an atom. The XAS spectrum is especially responsive to the local coordination number, distances of the surrounding atoms, and oxidation state of the absorbing atom. With this nature, XAS presents a relatively easy and practical method for examining the local atomic structure and chemical state of a chosen atomic type. XAS can be used in bulk physical surroundings and different systems. Furthermore, it is used usually in an extensive range of scientific fields, including material science, environmental science, biology and catalyst research [29].

### 2.4.1 X-Ray Absorption and X-Ray Fluorescence

X-rays are electromagnetic waves having wavelengths from  $\sim 25 \text{ \AA}$  to  $0.25 \text{ \AA}$  or photon energies ranging from  $\sim 500 \text{ eV}$  to  $500 \text{ keV}$ . In this regime, the light is absorbed by all substances via photoelectric effect. In this process, the X-ray photon is absorbed by an electron in a strictly bound quantum core level, such as the 1s level of the atom (Figure 2.30).

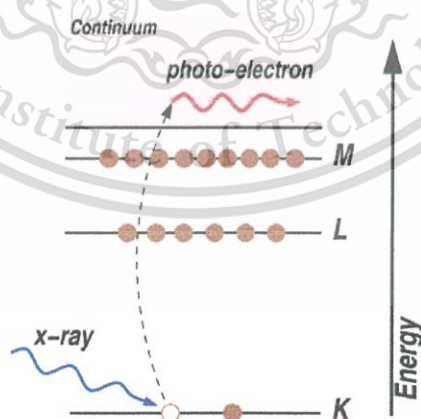


**Figure 2.30** The photo-electric effect on the absorbed X-ray photon, and the core level electron advancing from an atom [29].

In the orderly electronic core level that participates in absorption, the binding energy at this level has to be lower than the occasional X-ray energy. If the binding energy is smaller than the X-ray energy, the electron will be emitted from the well defined quantum state. The X-ray is absorbed and the photoelectron is created having energy being in excess of binding energy, if binding energy of the electron is higher than that of the X-ray, the bound electron would not be disturbed at the quantum level and the X-ray energy not absorbed. The full assumption of this method, while applied to solids, liquids and molecules, occurs in XAS.

X-ray absorption analysis is concerned mostly with the absorption coefficient ( $\mu$ ), which presents the possibility of X-rays being absorbed according to the Beer's Law:

$$I = I_0 e^{-\mu t} \quad (2.8)$$

where  $I_0$  is the X-ray intensity of the sample,  $I$  is the X-ray intensity transmitted through the sample, and  $t$  is the sample thickness, as displayed in Figure 2.31 [29].



**Figure 2.31** XAS measurements; an incident ray of monochromatic X-rays with  $I_0$  intensity crossing through the sample of  $t$  thickness and transmission ray with  $I$  intensity [29].

The X-ray absorption analysis comprises measurement of the X-ray absorption function and photon power in the neighborhood of the threshold atom. Synchrotron light source is required, since high intensity and tunable force are needed. X-rays can be monochromatized by using a diffracting crystal, with data collection achieved in the energy scanning mode, which is received from a step-by-step mechanical rotation of the crystal [30]. While the incidence of X-ray energy is equal to the binding energy of a core level electron, sharp absorption arises; with a continuous absorption edge according to promotion of the core level. As each atom has core level electrons with well-defined, specific binding energies, one can choose

This material is reserved for educational use only, not allowed for commercial use.

a probed element by tuning the X-ray energy to one of its suitable absorption edges. The energy of the absorption edge is well-known and tabulated, and the energy edge changes approximately with the second power of the atomic number with an atomic number of approximately  $Z^2$ .

For a sample concentration, of high an X-ray absorbing element, a XAS spectrum should be measured in the transmission mode. This mode suitably work for pure compounds, samples with concentrations of more than 10%. For thick samples or lower concentrations (of around the ppm level and lower), investigation by X-ray fluorescence is the promoted technique.

A typical XAS spectrum, collected in the transmission mode of FeO powders, is presented in Figure 2.32. The X-ray absorption spectrum is separated into two parts; X-ray absorption near edge structure (XANES) (lower than 50 eV), and extended X-ray absorption fine structure (EXAFS) (of around 50 eV higher than the edge). Although both parts have the same physical beginning, the difference is convenient for clarification. EXAFS depend on the coordination number, species and distances of the adjacent absorbed atom, while XANES is chemically sensitive to bonding geometry (such as tetrahedral and octahedral coordination) and the oxidation state of the absorbing atom [29].

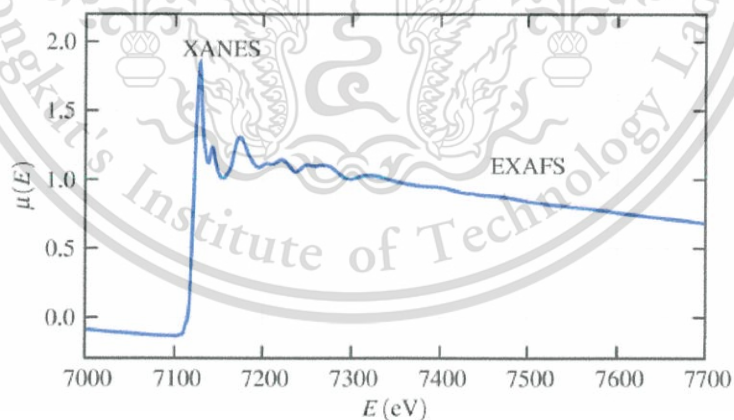


**Figure 2.32** Experimental XAS spectrum presenting EXAFS and XANES regions [29].

The photoelectron propagates from the X-ray absorption atom, and is scattered by the adjacent atoms, as shown in Figure 2.33. The result of the EXAFS spectrum is from the destructive and constructive interference between incoming and outgoing photoelectron waves at the absorber. This interference causes a

This material is reserved for educational use only, not allowed for commercial use.

Forbidden to modify the content, and cite the document when use.

modulated structure, with valleys and peaks, as a function of the incident X-ray energy, as in Figure 2.32. This process, known as the EXAFS phenomena, produces unique EXAFS of the absorbed atom that performs as both a detector and source of the interference [28]. However, the EXAFS is sensitive to short range order, and grants the radial interatomic length at nearly the upper absorption level of 4 or 5 Å [27].

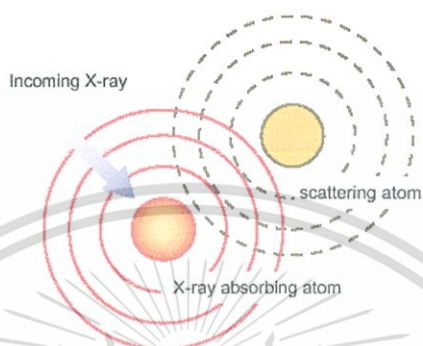


**Figure 2.33** The EXAFS phenomenon; outgoing photoelectron of the X-ray absorbed atom and backscattering photoelectron from the adjacent atom [29].

Since the EXAFS is superimposed on background absorption ( $\mu_0$ ) it is essential to extract the modulatory structure ( $\mu$ ) from the background, and determine the EXAFS fine-structure function,  $\chi(E)$ , as:

$$\chi(E) = \frac{\mu(E) - \mu_0(E)}{\Delta\mu_0(E)} \quad (2.9)$$

where  $\mu(E)$  is the measured absorption coefficient,  $\mu_0(E)$  is a smooth background that represents the absorbed isolation atom, and  $\Delta\mu_0$  is the measured absorption jump of  $\mu(E)$  at threshold energy ( $E_0$ ) (Figure 2.34) [29].

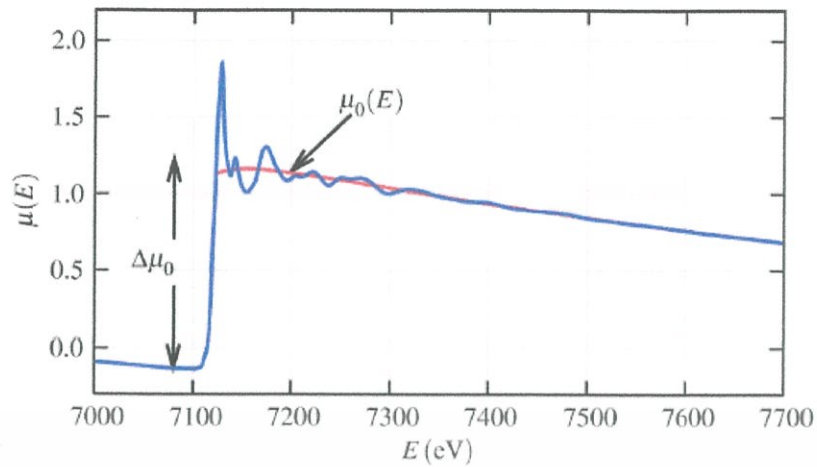


Figure 2.34 Display of  $\mu(E)$  of the  $\Delta\mu_0$  edge-step and smooth background of  $\mu_0(E)$  [29].

As visualized below, EXAFS is understood best in wave character conclusions of photoelectron creation in the absorption method. Then, it is usual to convert X-ray energy to  $k$ , the photoelectron wave number, which has a measurement of  $1/\text{distance}$ , and is identified as:

$$k = \sqrt{\frac{2m(E-E_0)}{\hbar^2}} \quad (2.10)$$

where  $m$  is the electron mass and  $E_0$  is the absorption edge. The primitive amount of EXAFS is then  $\chi(k)$ , the vibration at a different photoelectron wave number, For example, EXAFS was extracted from the Fe K-edge of FeO, as exhibited in Figure 2.35 (top). Generally, EXAFS oscillates and decays rapidly with  $k$ . To magnify the vibration,  $\chi(k)$  is normally multiplied with a power of  $k$ , such as  $k^3$  or  $k^2$ , as presented in Figure 2.35 (bottom) [29].

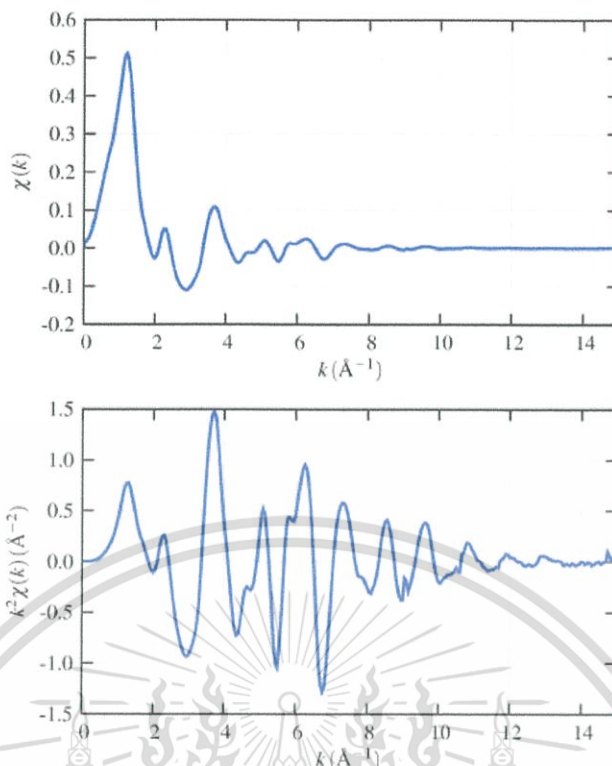


Figure 2.35 The  $\chi(k)$  EXAFS of FeO (top), and the  $k$ -weight EXAFS,  $k^2\chi(k)$  (bottom) [29].

Different frequencies are clear in the vibration of  $\chi(k)$ , according to various neighboring coordination shells, which can be explained by the model corresponding to the EXAFS equation:

$$\chi(k) = \sum_j \frac{s_0^2 N_j f_j(k) e^{-2k^2 \sigma_j^2}}{k R_j^2} \sin[2kR_j + \delta_j(k)] \quad (2.11)$$

where  $\delta(k)$  and  $f(k)$  depend on type of scattering or neighboring atoms in the  $j^{\text{th}}$  shell,  $N$  is the number of scattering atoms,  $R$  is the length to the neighboring atom, and  $\sigma^2$  is the disorder in the adjacent length. Although somewhat complicated, the EXAFS equation permits a decision on the  $R$ ,  $N$ , and  $\sigma^2$  perception of the phase-shift  $\delta(k)$  and scattering amplitude  $f(k)$ . In addition, EXAFS is sensitive also to the atomic species of the adjacent atom because these scattering factors rely on  $Z$  of the neighboring atom, [26-27].

The EXAFS signal are multiplied by  $k^n$  ( $n = 1, 2$ , or  $3$ ) and are normalized to the unit edge jump. Normalization, background subtraction of EXAFS information,  $k^n\chi(k)$  and  $k$ , such as shown in Figure 2.36, are essentially Fourier transformation

This material is reserved for educational use only, not allowed for commercial use.

Forbidden to modify the content, and cite the document when use.

without the phase shift improvement. The Fourier transforms are the important view of information analysis due to they associate the EXAFS function,  $k^n\chi(k)$ , of the photoelectron wavevector,  $k$  ( $\text{\AA}^{-1}$ ), to its complementary function,  $\Phi_n(r')$ , of distance,  $r'$  ( $\text{\AA}$ ). Therefore, the Fourier transform grant an easy physical description, pseudo-radial distribution function, of the surrounding around the X-ray absorption element. The contributions of various coordination spheres of the adjoin surrounding the absorption seem as the peaks in Fourier transform. Fourier transform peaks are often shifted from the true length,  $r$ , to the shorter ones,  $r'$ , because the influence of the phase shift that amounts to nearly 0.2-0.5  $\text{\AA}$  depend on the backscattering and the absorption atom [28].

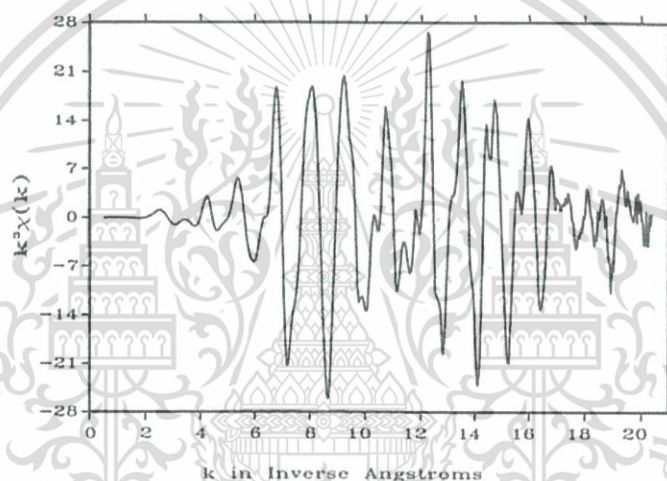


Figure 2.36 Background-subtraction, normalizing at the  $k^3$ -weight of the Mo K-edge [29].

The EXAFS Fourier transformation in Figure 2.36 is shown as a solid curve in Figure 2.37, with two high peaks at 2.38 and 2.78  $\text{\AA}$  and two small ones at 4.04 and 4.77  $\text{\AA}$ . In this sample, each peak was due to Mo-Mo scattering. Peak locations are in outstanding correspondence with crystallography that investigates radial distribution of molybdenum foil, with Mo-Mo interatomic lengths of 2.73, 3.15, 4.45, and 5.22  $\text{\AA}$ , consecutively. Fourier transformation peaks are phase shifted at about 0.39  $\text{\AA}$  from true lengths [28].

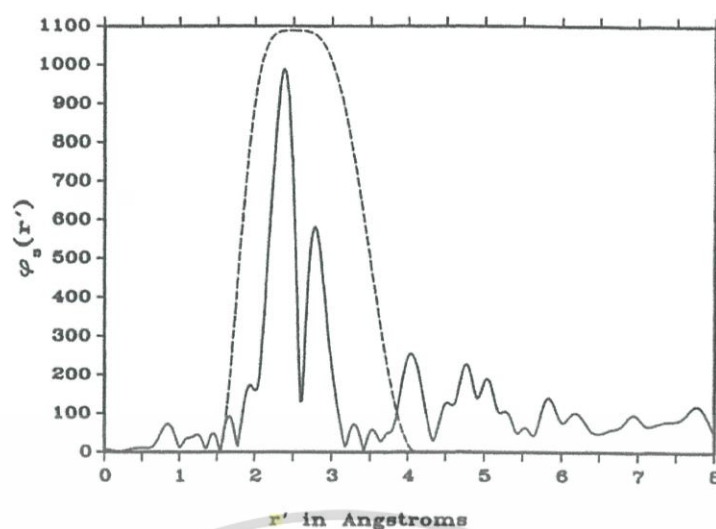


Figure 2.37 Fourier transformation (solid curve) of Mo K-edge EXAFS [29].

#### 2.4.2 XANES Interpretation

As XANES has a higher signal than EXAFS, it can be completed in smaller concentrations, and in less than perfect sample conditions. The interpretation of XANES is complex, with facts that are difficult to analyze or report physically, since the XANES region coordinates greatly with surrounding chemical information and noticeably formal valence. Figure 2.38 displays the XANES spectra of many iron compounds. Positions of the shapes and edge are clearly sensitive to the coordinated surroundings, oxidation state, and ligand type. Besides, XANES can be used as a fingerprint for phase identification [26].

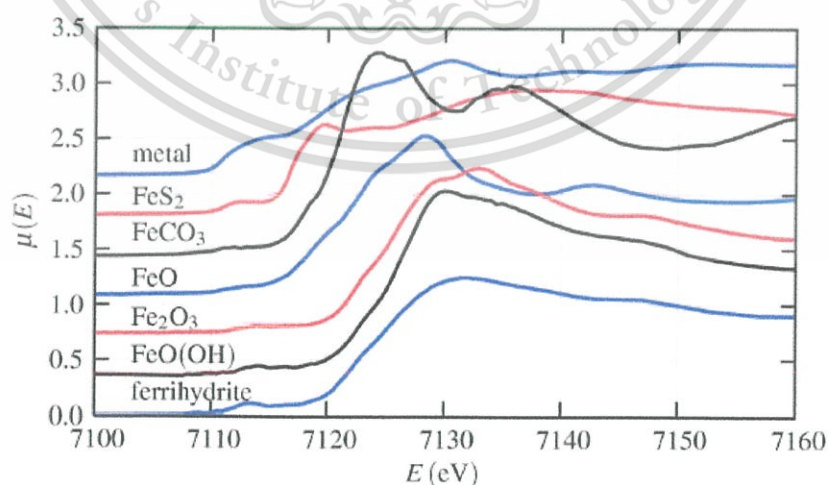


Figure 2.38 The Fe K-edge of Fe metal and some Fe compounds in XANES spectra [29].

This material is reserved for educational use only, not allowed for commercial use.

Forbidden to modify the content, and cite the document when use.

The condition of oxides can be dramatically intensive, as shown in Figure 2.39, which presents  $\text{Cr}^{6+}$  and  $\text{Cr}^{3+}$  oxides. The  $p$ - $d$  hybridization for the ions of unfilled  $d$ -electrons is adjusted dramatically in coordinated surroundings, with more powerful hybridization to tetrahedral rather than octahedral coordination. As the photoelectron makes the  $1s$  core level need  $p$ -like symmetry at the K-shell, the total overlap of orbital  $d$ -electron, near the Fermi energy level, dramatically changes the amount of accessible states to the  $p$ -electron, thus causing significant transformation in the XANES spectrum. When  $\text{Cr}^{6+}$   $p$ - $d$  hybridization appears in a largely localized molecular orbital  $d$ -electron, a well-defined peak is given under the main absorption edge, indicating transition to a boundary electronic state [26].

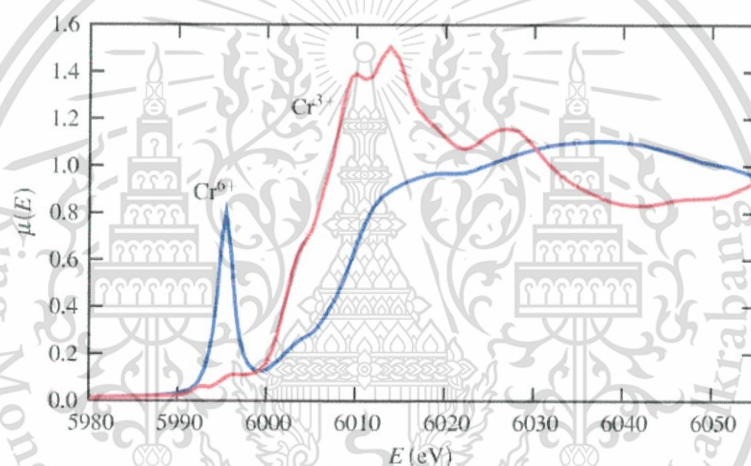


Figure 2.39 The Cr K-edge of XANES spectra in  $\text{Cr}^{6+}$  and  $\text{Cr}^{3+}$  oxides [29].

The important and typical applications of XANES use the edge location shift to examine the oxidation state. Figure 2.40 exhibits the oxidation dependence of Fe metal,  $\text{Fe}^{2+}$  oxides,  $\text{Fe}^{3+}$  oxides, and a mixture of these. In ideal spectra,  $\text{Fe}^{3+}/\text{Fe}^{2+}$  ratios can be investigated with reliability and very good accuracy. Similar proportions can be invented for other ions. The positions and altitudes of pre-edge peaks can be used reliably to decide coordination chemistry and valence states empirically. These assessments for assigning the conventional oxidation state, based on edge features and the fingerprinting method, create an easier rough understanding of XANES than they do of EXAFS, although complete physical significance of all spectral features is unavailable [26].

This material is reserved for educational use only, not allowed for commercial use.

Forbidden to modify the content, and cite the document when use.

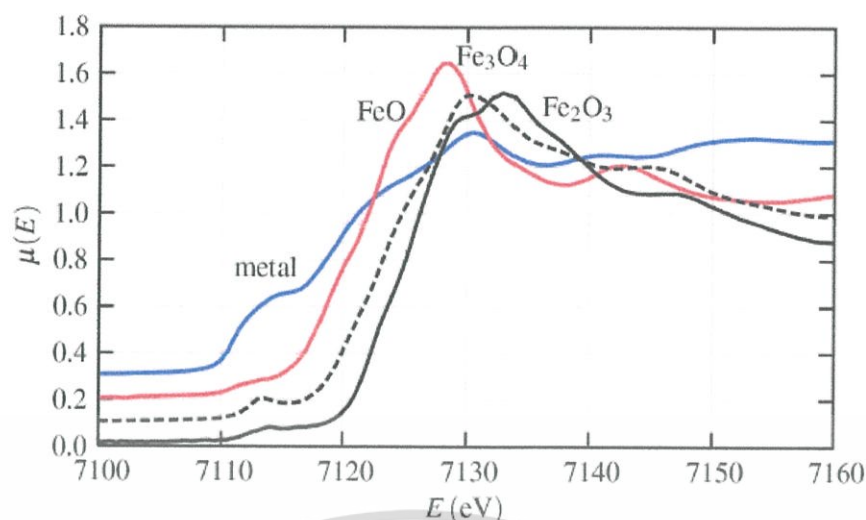
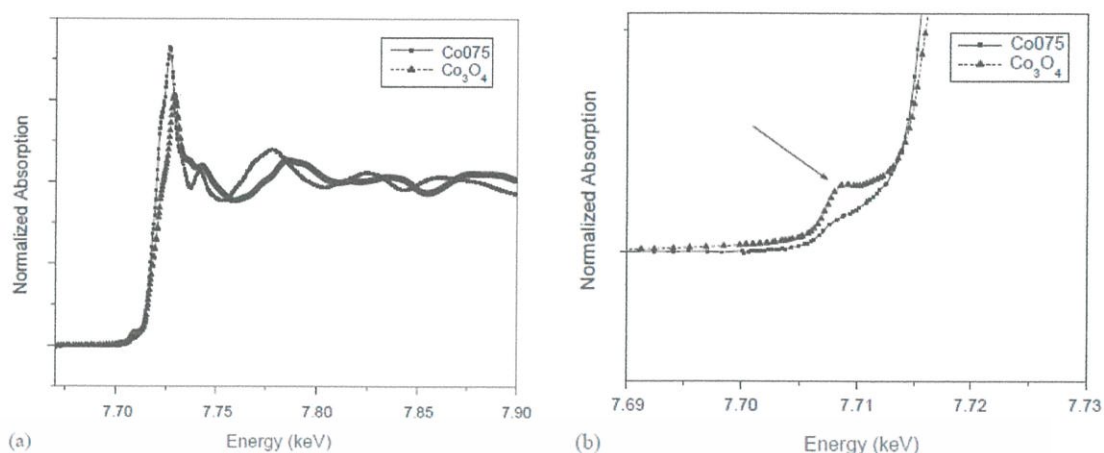


Figure 2.40 The Fe K-edge of XANES spectra in Fe metal and many Fe oxides [29].

Interpretation of XANES spectra was found in previous works. In 2004, M. F. F. Lelis *et al.* [31] prepared  $\text{Co}_x\text{Fe}_{3-x}\text{O}_4$  ( $0 \leq x \leq 0.75$ ) samples by the co-precipitation method. The XANES spectra were gained from standard compounds and samples. It can be noted accordingly that the spectra of overall samples are related to those received from the CoO standard, and  $\text{Co}^{2+}$  has a six-fold coordination with  $\text{O}^{2-}$  ions. However,  $\text{O}^{2-}$  ions clearly vary from the  $\text{Co}_3\text{O}_4$  spinel, with six- and four-fold  $\text{Co}^{3+}$  and  $\text{Co}^{2+}$  coordinating with  $\text{O}^{2-}$ , respectively. Figure 2.41a exhibits the Co075 sample spectra, as correlating with the  $\text{Co}_3\text{O}_4$  standard. The pre-edge area is enlarged in Figure 2.41b in order to allow a good view of the feature residing at 7,707 eV of the  $\text{Co}_3\text{O}_4$  spectrum, which corresponds to the  $1s$  boundary and  $3d$  orbital transition attributed to tetrahedral coordinated cations. This transition is not permitted while a reverse center exists at the metal ion, according to the matter of octahedral coordination.



**Figure 2.41** (a) XANES spectra of Co75 and  $\text{Co}_3\text{O}_4$  samples; (b) amplified picture of the Co K-edge profile in the same design as (a) [31].

The spectra received from the samples corresponded very well with the CoO standard, as shown in Figure 2.42a. Low intensity of the pre-edge peak was noticed in the samples and CoO standard, as exhibited in Figure 2.42b, and it powerfully supported the opinion that Co has octahedral coordination. Other significant features attracted from XANES analysis did not reveal a shift of K-edge to a larger energy. This suggests that the non oxidation state of  $\text{Co}^{2+}$  to  $\text{Co}^{3+}$  occurred during sample preparation.

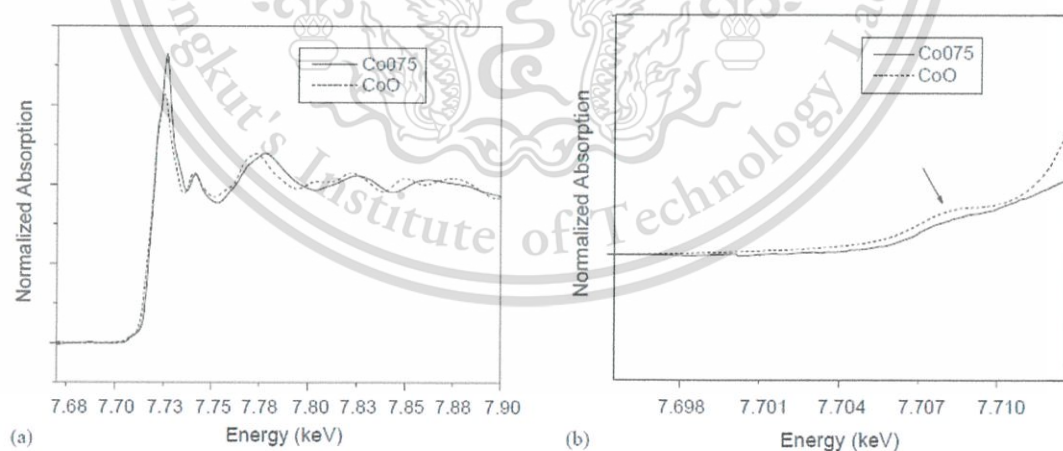


**Figure 2.42** The XANES spectrum at the Co K-edge of CoO and Co75 samples [31].

In 2008, S. Sakurai *et al.* [32] studied the oxidation state in manganese zinc using XAS. In Figure 2.43, the threshold values of Mn-Zn spinel ferrite were larger than those of FeO and iron foil, but near to  $\text{Fe}_2\text{O}_3$  energy, which induces  $\text{Fe}^{3+}$ . This material is reserved for educational use only, not allowed for commercial use.

Forbidden to modify the content, and cite the document when use.

contained in Mn-Zn ferrites. Figure 2.44 shows that the threshold peaks of the spinel ferrites are near to the ZnO standard. It is recommended that the Zn ions consist of a divalent state in octahedral coordination. The major spectra of spinel ferrites are wonderfully distinct from ZnO, and may indicate a disagreement in the atomic environment and coordination number. Figure 2.45 shows that the spectrum of manganese zinc ferrites in the threshold area are near to the MnO, and recommended as a divalent state in the octahedral site of oxygen atoms. Besides, the pre-edge curve powerfully proposes that Mn ions are in tetrahedral coordination.

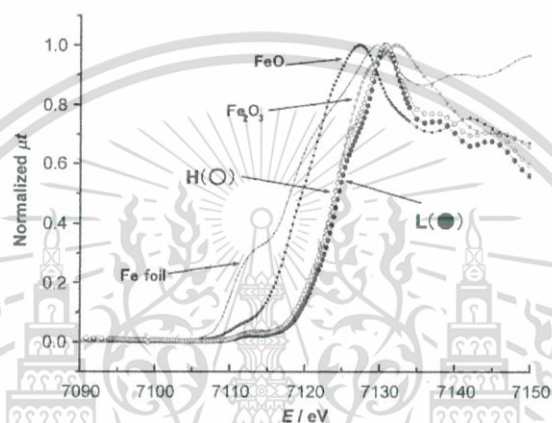


Figure 2.43 XANES curves close to the Fe K-edge of Mn-Zn samples. XANES spectra of H and L samples correlate with the iron foil, FeO and Fe<sub>2</sub>O<sub>3</sub> [32].

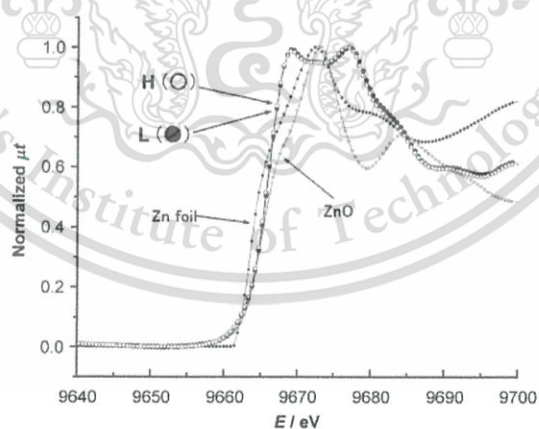


Figure 2.44 XANES curves close to the Zn K-edge of Mn-Zn samples. XANES spectra of H and L samples correlate with the zinc foil and ZnO [32].

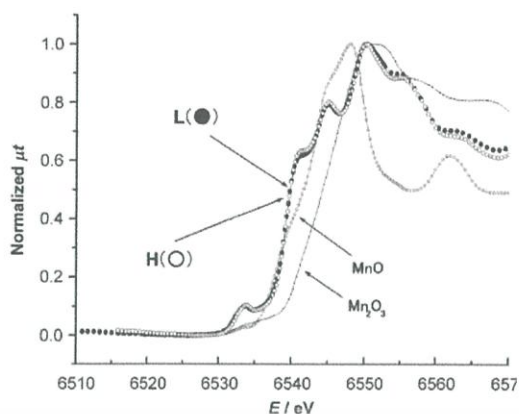


Figure 2.45 XANES curves close to the Mn K-edge of Mn–Zn ferrites. XANES spectra of H and L samples correlate with MnO and Mn<sub>2</sub>O<sub>3</sub> [32].

### 2.4.3 EXAFS Interpretation

Previous studies have researched the cation site distribution of spinel ferrites. In 1996, V. G. Harris *et al.* [23] studied the site distribution of spin sprayed Ni<sub>0.15</sub>Zn<sub>y</sub>Fe<sub>2.85-y</sub>O<sub>4</sub>, where  $y = 0.16-0.60$ , film samples. Their research of bulk powders discovered that while Zn increases in NiFe<sub>2</sub>O<sub>4</sub>, the Zn cations prefer to occupy A-sites and replace some of the Fe cations in B-sites. They presumed that as soon as Zn has increased at the cost of Fe cations, as explored in this case, a related redistribution takes place, in which Zn cations prefer to occupy A-sites and substitute the Fe cations in B-sites. It is anticipated that overall samples of Ni cations occupy B-sites. Figure 2.46 clarifies that these profiles demonstrate the characteristic of B- and A-site surroundings. It is recognized from investigations that changes are mostly Fourier transforms in the first three peaks. The large asymmetrical peak in the middle is close to 1.5 Å, in accordance with two Fe–O bond lengths and according to the Fe cations in B- and A-sites. The large divided peaks in the middle, adjacent to 2.9 Å, consist of many different atom couple associations as well as multiple scattering contributions. The low- $r$  curve contains contributions only from Fe<sub>B</sub>–M<sub>B</sub>, where M is metal cation correlations. On the other hand, the high- $r$  peak contributions consist of Fe<sub>A</sub>–M<sub>A</sub>, Fe<sub>A</sub>–O, Fe<sub>A</sub>–M<sub>B</sub>, and Fe<sub>B</sub>–O correlations. The amplitude occurs from multiple scattering contributions in approximately 12% of this peak. Figure 2.46 shows that the high- $r$  peak enlarges the amplitude by reducing Zn/Fe, when the low- $r$  peak presents the reverse trend. The middle peak close to 1.5 Å declines in amplitude with

This material is reserved for educational use only, not allowed for commercial use.

Forbidden to modify the content, and cite the document when use.

reduced Zn/Fe. These total trends can be best described as cation distribution of Fe and Zn ions by enlarging Zn/Fe. While Zn fills the sample, it prefers to reside in A-sites. This enables a larger portion of Fe cations to reside in B-sites. Trends in separate-peak features are close to 2.9 Å, and show transformation of  $Fe_B/Fe_A$  at differing Zn/Fe. The oxygen peak alters amplitude because it converts occupation by between four- and six-fold coordination at the A- and B-site, respectively.

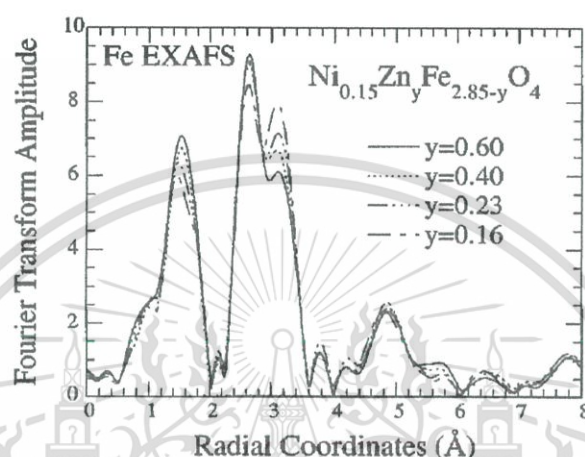


**Figure 2.46** Fourier transformed from Fe EXAFS of the  $Ni_{0.15}Zn_yFe_{2.85-y}O_4$  films. All spectra were gained by a  $k$  range of 2.5–12.4 Å<sup>-1</sup> and  $k^3$  weighting [33].

The achievements of fitting analysis are showed in Figure 2.47. Picture (a) shows Fourier transformed from Fe EXAFS information of the  $y = 0.16$  sample, and a perfect fit utilizes cooperation of B- and A-site Fourier transformed free energy force field (FEFF) data. Picture (b) shows successful fitting analysis presented in the fraction for Fe cations on the B- and A-site of all samples. The fractional B-site Fe is enhanced by Zn/Fe as the ratio on the A-site decreases. This result is in accordance with Zn preferring to reside in A-sites because a stronger portion of Fe cations is in B-sites. Picture (c) clarifies that a very good fit by unique B-site Fourier transformed FEFF does not fit information in the range of 3–3.5 Å. Nevertheless, the fit is enhanced dramatically by presenting a small part of A-site Fourier transformed FEFF. The effects of Fourier transformed EXAFS fitting are displayed in picture (d). Since Ni cations in  $NiFe_2O_4$  reside in only B-sites, it can be expected that Ni ions occupy the B-site in these samples and do not turn through Zn introduction. However, these results point to a small number of Zn ions of  $y = 0.16$ , with 13% of Ni cations

This material is reserved for educational use only, not allowed for commercial use.

Forbidden to modify the content, and cite the document when use.

occupying A-sites, and Zn/Fe enabling fractional improvement to about 25% of  $y = 0.60$ . The picture in Figure 2.47 (e) relates to the Ni ion information in picture (c), and Zn Fourier transformed EXAFS data are the best fit, with cooperation from B- and A-site Fourier transformed FEFF information. In the case of  $y = 0.16$ , 6% of B-site Fourier transformed FEFF is required to fit the information range of 2.25–2.75 Å. For other combinations, the B-site constituent of Ni ion results in picture (d). Nevertheless, the results of Ni ions were different to those of Zn ions, in that  $0.23 \leq y \leq 0.6$  was not statistically important, due to the very good fit of standard deviation that fits just as well with an absent B component. Regarding  $y = 0.16$ , 6% of Zn ions occupy B-sites.

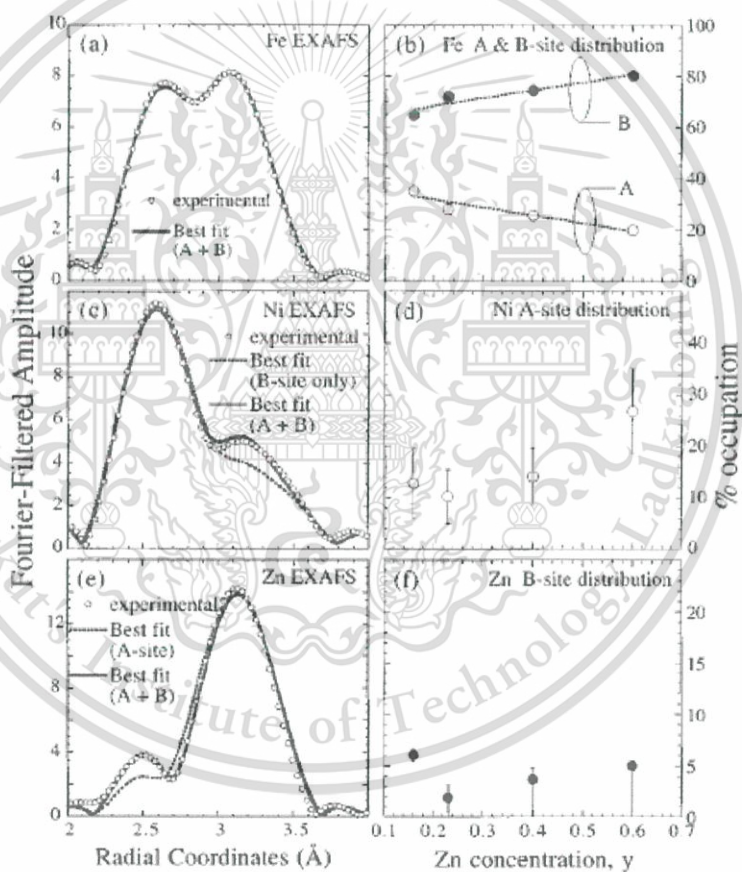


**Figure 2.47** Picture (a), (c), and (e) including EXAFS data of the  $\text{Ni}_{0.15}\text{Zn}_{0.16}\text{Fe}_{2.69}\text{O}_4$  sample. Picture (b), (d), and (f) showing trends of cation site occupancy [33].

It was referred initially that Ni ferrite has reversed cation site distribution. Therefore, its magnetization occurs only from the  $\text{Ni}^{2+}$  cations, the  $\text{Fe}^{3+}$  ions arrange antiferromagnetic and give no net magnetization. The establishment of  $\text{Zn}^{2+}$  cations

This material is reserved for educational use only, not allowed for commercial use.

that prefer the A-sites overturns the ferrite equilibrium by displacement the Fe ions from the A-sites to B-sites. The influence of a few number of Zn cation is enhancement the saturated magnetization by the imbalance Fe cation moments adding to these of Ni<sup>+2</sup> cations. In Figure 2.48, they examine the magnetization to enlarge close linearly by increasing Zn content of  $0 \leq y \sim 0.4$  and afterwards reduce of the  $y = 0.6$ . They accept that decreasing of the magnetization is because degeneration of superexchange on the B–A sites caused with lattice distortions carried by the enhancement number of Zn cations in the A-sites. They investigate as prove of this moderate 0.5% expansion for Zn<sub>A</sub>–O bond of the  $y = 0.6$  correlated by the  $0.16 \leq y \leq 0.4$  samples.

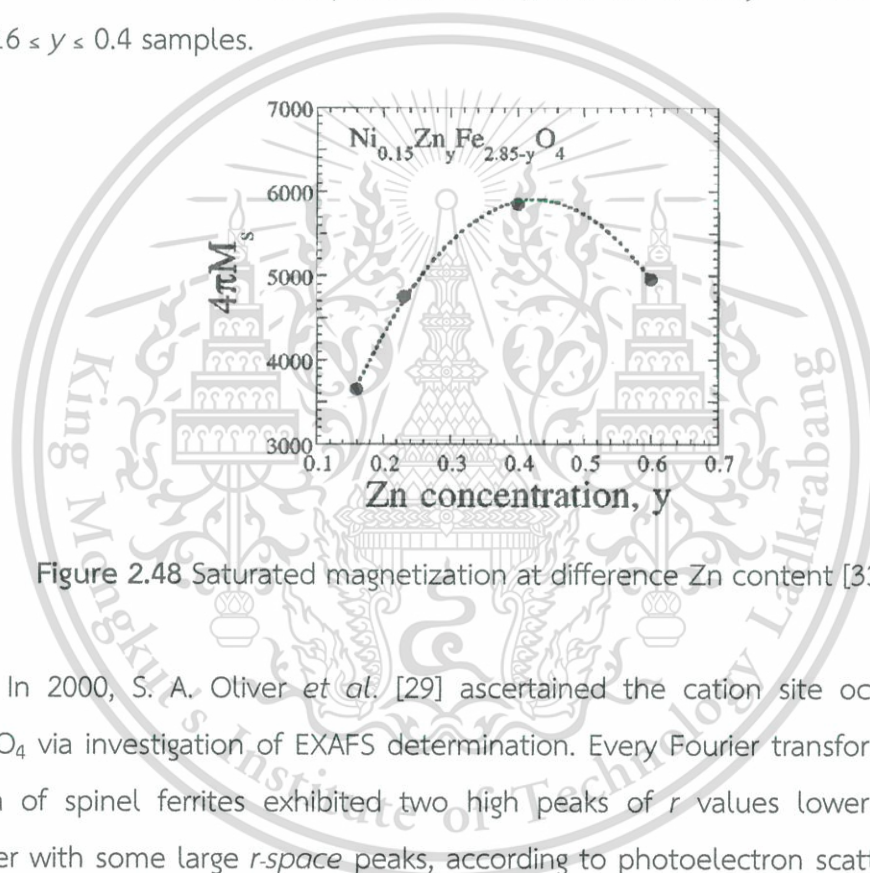


Figure 2.48 Saturated magnetization at difference Zn content [33].

In 2000, S. A. Oliver *et al.* [29] ascertained the cation site occupancy of  $(\text{tet})_{\square}(\text{oct})_{\square}\text{O}_4$  via investigation of EXAFS determination. Every Fourier transformed EXAFS spectra of spinel ferrites exhibited two high peaks of  $r$  values lower than 4 Å, together with some large  $r$ -space peaks, according to photoelectron scattering of far greater atomic shells. A high peak close to 1.5 Å occurred from scattering the closest neighboring atomic shell from oxygen ions, and also showing the ions resident at the interstitial site. The peak location in  $r$  values ranged from 2 to 4 Å, with greater significance by scattering from the second closest neighboring atomic shell. Also, the peak structure differed depending on the principle of backscattering cations residing in the octahedral or tetrahedral site. In detail, a powerful  $r$ -space peak is scaled close to 2.6 Å if the main cation inhabits the octahedral site, together with small contributions of  $r$ -space peaks in the scope of 3.0–3.3 Å. On the other hand, a

This material is reserved for educational use only, not allowed for commercial use.

powerful  $r$ -space peak is scaled close to 3.1 Å if the middle cation resides in the tetrahedral site. Therefore,  $r$ -space peak residence of the Fourier transformed adjacently to 2.6 Å matters, in that cations reside in octahedral sites, while all cations provide intensity between 3.0 and 3.3 Å. Figure 2.49 points out that EXAFS spectra of every element exhibit coupled peaks, with two large middle peaks close to 2.6 and 3.1 Å, thus presenting mechanical stimulated powder that has a significant inversion parameter.

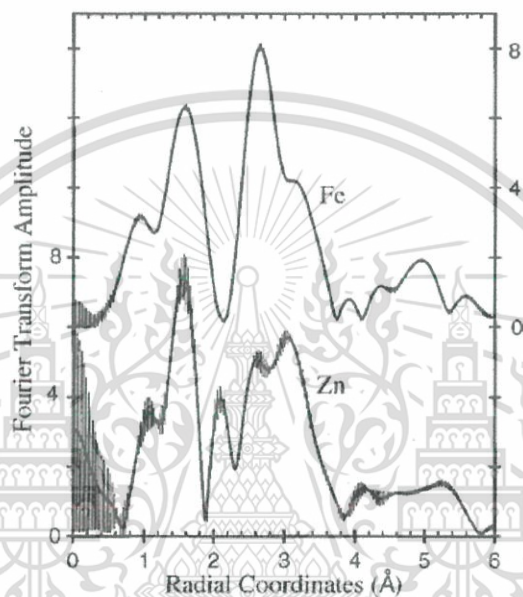
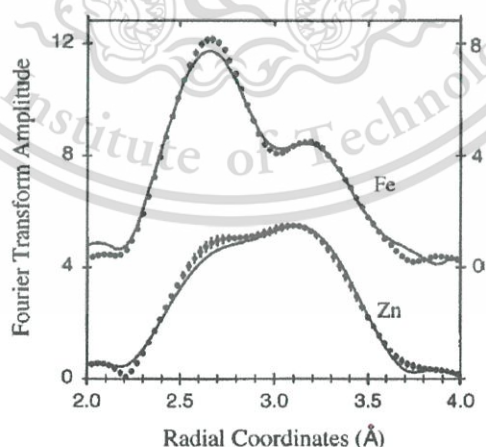


Figure 2.49 Fourier transformation of radial coordination versus Zn and Fe EXAFS data [34].

The cation distribution was quantified with the function of dividing the least-squares fittings of zinc and iron EXAFS results into backscattering imagery information sets that create the structure of spinel ferrite crystallography. Least-squares fit results of the photoelectron wave vector are displayed in Figure 2.50. Both fits of Fe almost corresponded to the information, and the least-squares fitting presented 91% of Fe ions in octahedral sites, with the surviving 9% occupying tetrahedral sites. Meanwhile, the results of zinc fitting were not as satisfactory as those gained from Fe ions. The result of fitting predicted that 55% of zinc ions fill tetrahedral sites, with 45% occupying octahedral sites. Hence, the final cation site occupation for the mechanical stimulated zinc ferrite sample is  $(\ )_{\text{tet}}\square_{\text{oct}}\text{O}_4$ , with a related error of 3%. This result exhibits great redistribution of zinc ions distinctly to the octahedral sites, This material is reserved for educational use only, not allowed for commercial use.

and also presents the non-equilibrium nature of the sample. Furthermore, the smaller than predicted redistribution of iron ions to the tetrahedral sites implies that the octahedral interstitial sites were greatly overcrowded, which correlated to stability of the samples.

The measurement of EXAFS data in total, accords well with the predicted spinel structure via the second closest neighboring atomic shell. Only significant disagreements of lower than 4 Å arise in slightly reduced Zn *r*-space peak locations in the range of 2–4 Å, which is much smaller than total Fourier transform intensities that correlate to standards results. It was first suggested that a slightly distorted spinel structure occurs near the Zn cations occupying octahedral sites, although local surroundings of iron ions do not transform. Nevertheless, the reduction of Fourier transform intensity was a predicted contributor to great structural disorder in the sample. In determining the site occupation in the structure of disordered materials, this immense redistribution of Zn ions in octahedral sites may be attributed to the ascendancy of significant bonding effects and simple geometry that are thought to be above crystal energy. The powerful relationship of zinc residing in tetrahedral sites below stable conditions was determined primarily as abnormal, due to the Zn ionic radii being higher than proportions of the tetrahedral interstitial site. Therefore, crystal energy estimations confirmed that occupation of Zn in the tetrahedral site had extreme electrostatic steadiness.



**Figure 2.50** The Fourier transformation of measurement data (dots) and the best fit (line) of Zn and Fe EXAFS results [34].

In 2006, J. A. Gomes *et al.* [32] studied the structural behavior of Cu ferrite nanoparticles. The samples were synthesized using the coprecipitation technique, which investigated both long range (XRD) and short range (EXAFS) scales. The diffraction patterns obtained were utilized for Rietveld refinement in order to define the lattice parameters present in XRD measurement at room temperature. The investigation of peak locations and related intensities of diffraction patterns proves the residence of only one phase behavior of the spinel crystallography structure. The occupation of  $\text{Fe}^{3+}$  cations at the A site is clarified as  $x = 0.80$ . The Fourier transformation is displayed by the difference of raw lengths, and not corrected by the electron phase shift, as seen in Figure 2.51 and 2.52 for Fe and Cu K-edge, respectively. A feature of Fourier transformation is behavior in the surroundings of octahedral and tetrahedral sites. In fact, it is well known that when observing two large intense peaks, the first one in the middle is close to 1.5 Å because donations of oxygen to the first shell are near Fe atoms. The second peak in the middle is close to 2.8 Å, which is in accordance with the second shell adjacent to Fe atoms. Due to the contribution of  $\text{Fe}^{3+}$  cations in both B and A interstices, these peaks are not in ideal symmetry. The illustration in Figure 2.51 shows expansion of the area between 2.2 and 3.5 Å, which exhibits separation of the second peak. As noticed here, separation of the peak occurs close to 2.6 Å (designated B) and originates from single scattering incidents of Fe cations localized at the B site. Likewise, separation of the peak close to 3 Å (indicates A-B) originates from single and multiple scattering donations of iron cations localized at B- and A-sites. Therefore, related amplitudes in the middle of these peaks indicate qualitative distribution of absorption ions at B- and A-sites. As noticed in the standard sample spectra in Figure 2.51, the proportion between amplitudes of separated peaks is approximately similar. On the other hand, in nanoparticle samples, the amplitude of separated peaks associates with only an enlarged B site contribution (close to 2.6 Å). This can be explained by the addition of  $\text{Fe}^{3+}$  cations in octahedral surroundings, thus indicating cation site distribution.

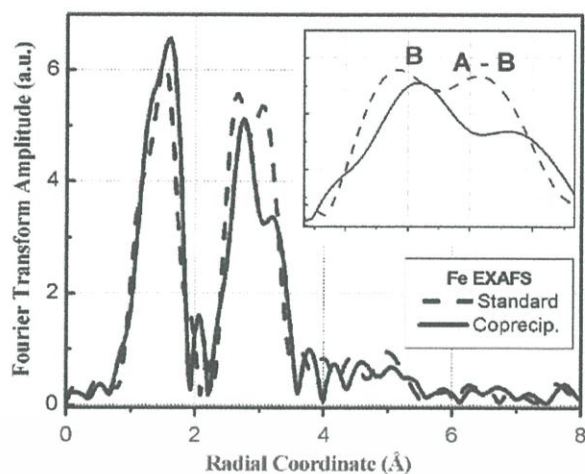


Figure 2.51 The Fourier transformation of Fe EXAFS data for copper ferrite nanoparticles and standard samples [35].

Figure 2.52 clarifies Fourier transformed spectra of the Cu K-edge, which is related to earlier analysis of the complete Fe K-edge. The amount of  $\text{Cu}^{2+}$  cations at B-sites reduces, and that of tetrahedral space subsequently enlarges, thus confirming the transformation of atoms in each site.

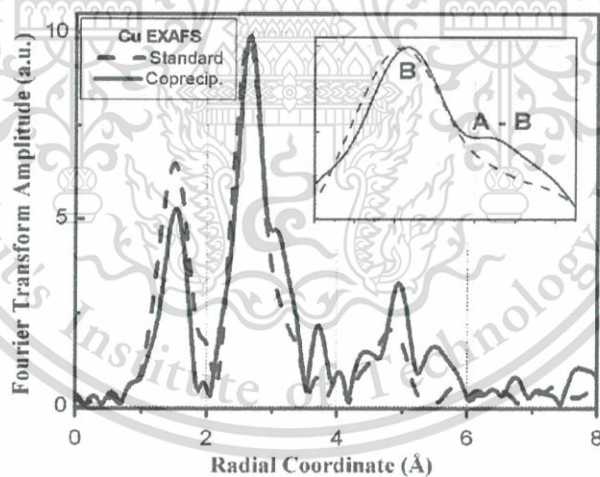


Figure 2.52 The Fourier transformation of Cu EXAFS data for copper ferrite nanoparticles and standard samples [35].

Furthermore, some researches studied the cation distribution of cobalt ferrite ( $\text{CoFe}_2\text{O}_4$ ).

In 2002, A. K. Giri *et al.* [30] prepared a cobalt ferrite nanoparticle using standard coprecipitation methods. The remanence of magnetization and coercive  
This material is reserved for educational use only, not allowed for commercial use.

Forbidden to modify the content, and cite the document when use.

field were investigated by measuring them with and without optical excitation via the optic fiber enclosed in the superconductor quantum intervention device magnetometer. The coercive field was reduced essentially to small nanoparticles, which were clarified by a white light (Figure 2.53), together with a small (about 2%) reduction of saturated magnetization. The coercive field decreased due to  $\text{Co}^{2+}$  cations being on the B-site with great single cation anisotropy, which changed to the lower anisotropy  $\text{Co}^{3+}$  cation. If the cations are on B-sites, the net moment and saturated magnetization would be the same.

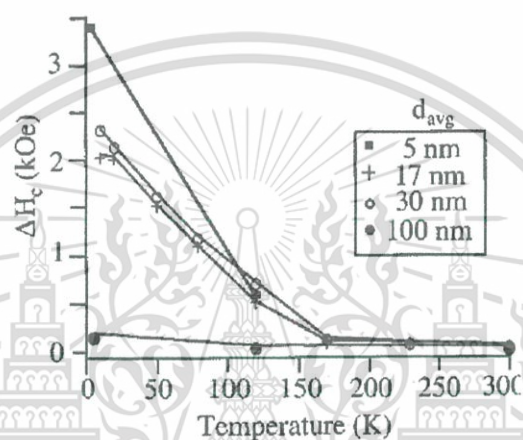
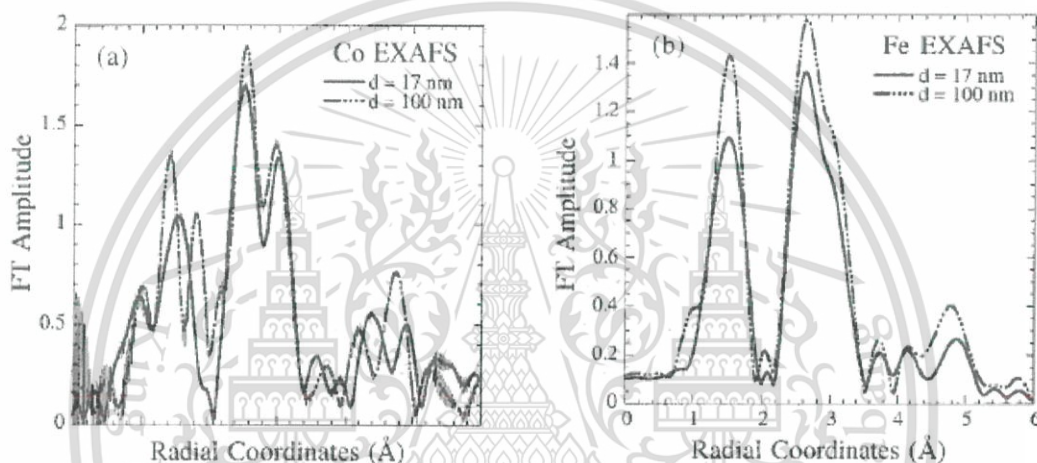


Figure 2.53 Temperature versus  $\Delta H_c$  of ferrite nanoparticles with various average sizes [36].

In order to differentiate the size-dependent features of these associations from the difference in site occupation, EXAFS estimations were used to investigate the local bonding surrounding Co and Fe ions. Figure 2.54 exhibits the Fourier transformed Co and Fe EXAFS spectra, with an uncorrected electron phase shift. The closest adjacent ion (Co, Fe)–oxygen bond occurs at  $r$  around 1.4 Å, according to the coordinated tetrahedral cation, whereas the bond of oxygen close to 1.9 Å corresponds with the coordinated octahedral absorption ion. The large middle peak is close to  $r = 2.6$  Å, according to the cation–cation length, while both the absorption cation and scattering ion occupy in the octahedral site. This unique fingerprint recognizes the absorption atom as occupying B-sites, and permits determination of octahedral site occupancy. The middle peak close to 3.1 Å appears to form an absorber in the tetrahedral site, but the recognition is not unique. To investigate cation occupancy on the B- and A-site, an  $r$ -space range of 2.0–3.5 Å was Fourier

This material is reserved for educational use only, not allowed for commercial use.

filtered to a photoelectron wave vector and fitted with FEFF codes. The Fourier transformed Fe EXAFS curve presents a total outline of amplitude expanding across the 100 nm samples related to the 17 nm samples. This can be attributed to a drop in the static disorder in bonds from 100 nm data, according to the decreased amount of vacancies in the sample. The Co EXAFS spectra that correlated to Fe information did not show a notable separation in either the close adjacent anion polyhedral or cation–cation associations. The Fe spectra also have smaller amplitudes when related to the Co spectra. Collectively, Fe surroundings are more disordered than Co surroundings.



**Figure 2.54** (a) The Fourier transformation of Co EXAFS spectra at varied radius coordination, (b) the Fourier transformation of Fe EXAFS spectra at varied radius coordination [36].

In 2007, M. H. Nilsen et al. [33] hydrothermally synthesized magnetite ( $\text{Fe}_3\text{O}_4$ ) and materials containing additional metal (cobalt) nanoparticulate ferrites. The local metal environment of the iron atoms and additional metal in the ferrites has been studied by EXAFS and XANES in order to determine the type of spinel structure. Also, XRD of the  $\text{CoFe}_2\text{O}_4$  material synthesized under hydrothermal conditions was examined. All diffraction patterns that are an indicator match with the values in the literature for this compound. The Fourier transformation and EXAFS curves of  $\text{CoFe}(16)$  and  $\text{CoFe}(39)$  cobalt ferrites are shown in Figure 2.55 and 2.56 for iron and cobalt edges, respectively. These figures clearly show that amplitudes of the higher shells are reduced considerably in the latter, when compared to the former. At

This material is reserved for educational use only, not allowed for commercial use.

Forbidden to modify the content, and cite the document when use.

around 3 Å, the peak in the Fourier transformed spectra represents the interaction between metal atoms on octahedral sites. Since both Fe<sup>3+</sup> and Co<sup>2+</sup> are coordinated octahedrally, this peak is a composite of contributions from a mixture of iron and cobalt backscatterers. It is impossible to differentiate between iron and cobalt because of their similar atomic numbers, and therefore iron backscatters were chosen for both metal shells.

Co K-edge, bulk cobalt ferrite is known to be an inverse spinel, and a multiplicity of six is expected for the Co-O bond (Table 2.8). In the case of nanophase cobalt ferrites, the extracted multiplicities are 6.2(7) and 7.2(5) for CoFe(16) and CoFe(39), respectively (Table 2.9). The significantly increased multiplicity in CoFe(39) is consistent with the above comparison between the particle sizes of the two materials, and it was suggested that the latter consists of considerably smaller particles. Accordingly, the metal-oxygen peak is a composite surface with near-surface interactions, and its amplitude reflects an attempt to fit in order to compensate for an apparently higher Debye-Waller type factor. The multiplicities extracted from Co-O, Co•••Fe, and Co•••Fe match the 6, 6, 6 of an octahedral system (inverse spinel), rather than the 4, 0, 12 of a tetrahedral system (normal spinel). This conclusion supports nonexistence of the intense pre-edge spectrum of XANES associated with the tetrahedral system. Hence, CoFe(16) is an inverse spinel.

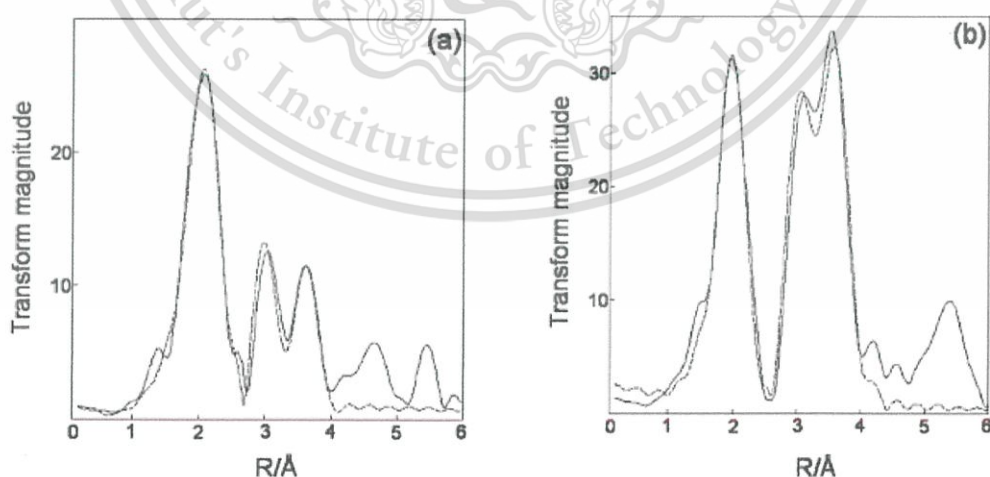


**Figure 2.55** Experimental (—) and calculated (--)  $k^3$ -weighted Fe EXAFS and its Fourier transformation for (a) CoFe(39) and (b) CoFe(16) ( $k$ -range, 2-12 Å<sup>-1</sup>) [37].

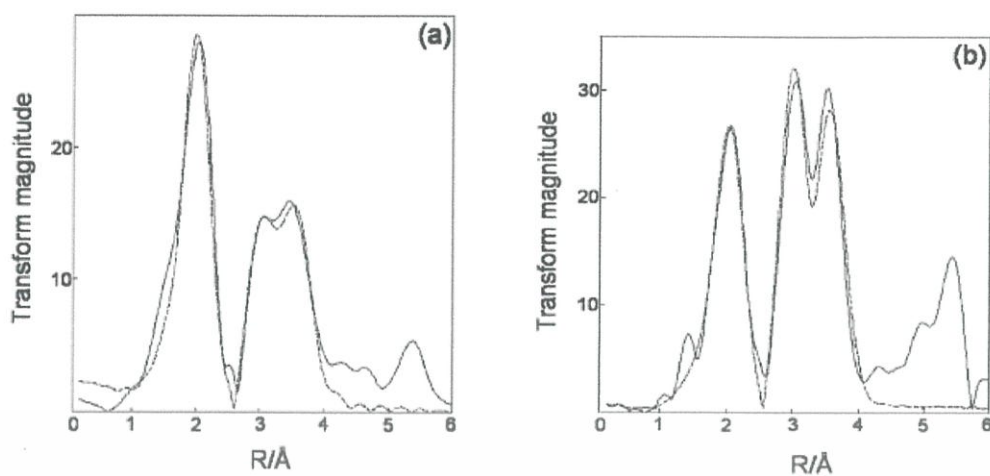


Figure 2.56 Experimental (—) and calculated (---)  $k^3$ -weighted Co EXAFS and its Fourier transformation for (a) CoFe(39) and (b) CoFe(16) ( $k$ -range, 2-13  $\text{Å}^{-1}$ ) [37].



**Table 2.8** Apparent multiplicities in EXAFS, based on the general expression;  $(A_{1-x}B_x)_{\text{tet}}(A_xB_{2-x})_{\text{oct}}O_4$ , where A is the divalent, B the trivalent cation, and x the inversion parameter [37]

spinel structure	Calculation	Apparent multiplicity in EXAFS	
		A K-edge	B K-edge
	Normal ( $x = 0$ )		
$AB_2O_4$	A-edge: A = 4 B-edge: B = 6	4	6
	Partly Inverse ( $x = 0.5$ )		
$(A_{0.5}B_{0.5})((A_{0.5}B_{1.5})O_4$	A-edge: $1/2 \times 4 = 2$ $1/2 \times 6 = 3$ B-edge: $1/4 \times 4 = 1$ $3/4 \times 6 = 4.5$	5	5.5
	Total Inverse ( $x = 1$ )		
$(B)(AB)O_4$	A-edge: A = 6 B-edge: $1/2 \times 4 = 2$ $1/2 \times 6 = 5$	6	5

**Table 2.9** Results of EXAFS Co K-edge curve-fitting [37]

Interaction	N	$r/\text{\AA}$	$2\sigma^2/\text{\AA}^2$	$E_F/\text{eV}$	R/%
Fe K-Edge					
CoFe(16)					
$\text{Fe}_{\text{tet}+\text{oct}}\text{-O}$	5.1(4)	1.953(7)	0.016(2)	0(1)	30.5
$\text{Fe}_{\text{oct}}\cdots\text{Fe}_{\text{oct}}^a$	5(1)	2.975(8)	0.016(4)		
$\text{Fe}_{\text{tet}}\cdots\text{Fe}_{\text{oct}}$	7(1)	3.477(7)	0.014(3)		
CoFe(39)					
$\text{Fe}_{\text{tet}+\text{oct}}\text{-O}$	5.5(3)	1.98(1)	0.019(2)	0.6(6)	30.6
$\text{Fe}_{\text{oct}}\cdots\text{Fe}_{\text{oct}}^a$	4(1)	2.982(1)	0.025(5)		
$\text{Fe}_{\text{tet}}\cdots\text{Fe}_{\text{oct}}$	4(1)	3.482(8)	0.018(4)		
Co K-Edge					
CoFe(16)					
$\text{Co}_{\text{oct}}\text{-O}$	6.2(7)	2.02(1)	0.022(4)	1.4(9)	39.5
$\text{Co}_{\text{oct}}\cdots\text{Fe}_{\text{oct}}^a$	6(1)	2.95(1)	0.020(4)		
$\text{Co}_{\text{oct}}\cdots\text{Fe}_{\text{tet}}$	7(2)	3.48(1)	0.019(5)		
CoFe(39)					
$\text{Co}_{\text{oct}}\text{-O}$	7.2(5)	2.05(7)	0.024(3)	1.9(6)	33.5
$\text{Co}_{\text{oct}}\cdots\text{Fe}_{\text{oct}}^a$	1.4(6)	2.97(1)	0.010(5)		
$\text{Co}_{\text{oct}}\cdots\text{Fe}_{\text{tet}}$	3(4)	3.49(2)	0.017(1)		

<sup>a</sup> The peak is a composite of both iron and the Co cation. The shell is refined as iron.

The Fe K-edge or multiplicities of the Fe-O bond are 5.1(4) [CoFe(16)] and 5.5(3) [CoFe(39)]. CoFe(16) is close to the apparent multiplicity associated with a totally inverse spinel (Table 2.8), thereby supporting the information gleaned from the cobalt edge. The iron pre-edge peak in the CoFe(39) XANES spectrum is less intense than that for CoFe(16), indicating an excess of octahedral iron. However, these results, including a multiplicity of 5.5, may not be necessarily equivalent to a partially inverse spinel, but rather a reflection of increased influence of the surface and near-surface interactions, as suggested by the authors.

Also in 2007, D. Carta *et al.* [34] used EXAFS and XANES techniques to investigate the exact inversion degree of  $\text{CoFe}_2\text{O}_4$  nanoparticles planted in the silica. This material is reserved for educational use only, not allowed for commercial use.

gel matrix prepared by sol-gel. That study quantitatively investigated the inversion degree for nanoparticles of cobalt ferrite and nanocomposite  $\text{CoFe}_2\text{O}_4\text{-SiO}_2$  gels of both the Co and Fe K-edge being discharged.

Reference compounds and fitting results for pure  $\text{CoFe}_2\text{O}_4$  of the Co and Fe K-edge are reported in Figure 2.57A and 2.57B. Good fitting results are shown in Table 2.10. Regarding the Fe K-edge, the first peak is close to 2 Å because two Fe-O bond lengths,  $\text{Fe}_B\text{-O}$  (1.98 Å) and  $\text{Fe}_A\text{-O}$  (1.84 Å), accord with octahedral and tetrahedral coordination, respectively. Double curves in the range of 2.5-4 Å overlap with the donation of  $\text{Fe}_B\text{-Fe}_B$  (2.97 Å) and a series of other donations with larger values (around 3.5 Å) of  $\text{Fe}_A\text{-Fe}_A$ ,  $\text{Fe}_A\text{-Fe}_B$ ,  $\text{Fe}_B\text{-O}$  and  $\text{Fe}_A\text{-O}$ . Related notifications can be produced at the Co K-edge. The first spectrum occurs at two distances;  $\text{Co}_B\text{-O}$  (2.06 Å) and  $\text{Co}_A\text{-O}$  (1.89 Å), due to octahedral and tetrahedral Co sites, whereas the first constituent of double peaks (2.95 Å) agrees with  $\text{Co}_B\text{-Co}_B$  lengths, and second (nearly 3.5 Å) with many contributions, such as  $\text{Co}_A\text{-Co}_A$ ,  $\text{Co}_A\text{-Co}_B$ ,  $\text{Co}_B\text{-O}$ , and  $\text{Co}_A\text{-O}$ . The fitting results of the Co and Fe K-edge imply an inversion degree of 69%. The good fits obtained for the standards confirm that the phase shift and amplitudes estimated in DL\_EXCURV can extend the sample fitting.

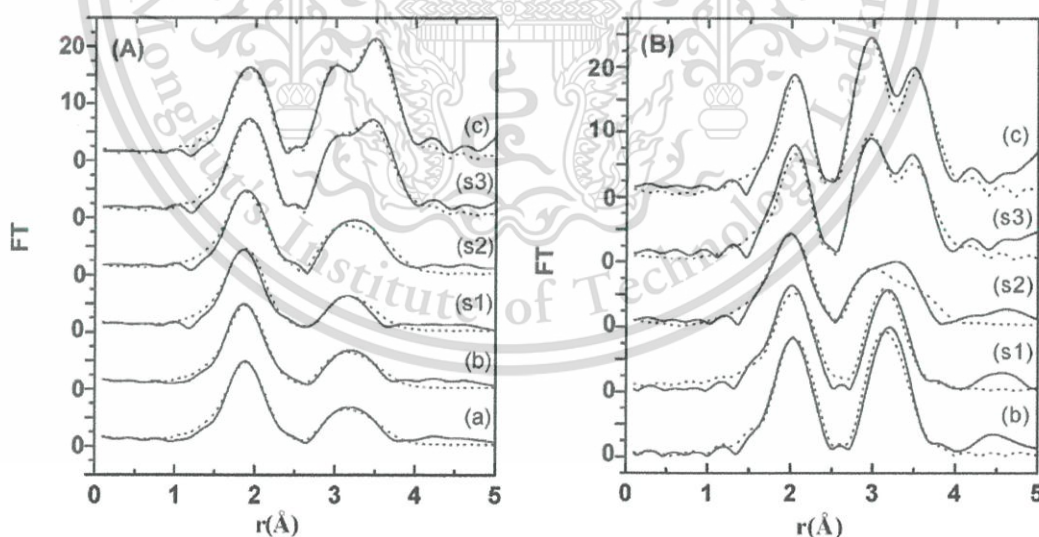


Figure 2.57 The Fourier transformation of Fe K-edge, A, and Co K-edge, B, for A10 sample fitting results (•••) and experiment (—). (A) (s3) A10\_900, (c)  $\text{CoFe}_2\text{O}_4$  and (B) (s3) A10\_900, and (c)  $\text{CoFe}_2\text{O}_4$  [38].

**Table 2.10** The interatomic lengths,  $R$ , coordination numbers,  $N$ , and Debye-Waller Factors ( $\sigma$ ) for  $\text{CoFe}_2\text{O}_4$  at the Co and Fe K-edge<sup>a</sup> [38]

Fe K-edge				Co K-edge			
CoFe <sub>2</sub> O <sub>4</sub>							
Site A	$R$ (Å)	$N$	$2\sigma^2$	Site A	$R$ (Å)	$N$	$2\sigma^2$
35%				30%			
O	1.84	4.0	0.020	O	1.89	4.0	0.023
Fe	3.48	12.0	0.014	Co	3.47	12.0	0.014
O	3.50	12.0	0.014	O	3.50	12.0	0.015
Fe	3.54	4.0	0.024	Co	3.54	4.0	0.026
Site B	$R$ (Å)	$N$	$2\sigma^2$	Site B	$R$ (Å)	$N$	$2\sigma^2$
65%				70%			
O	1.98	6.0	0.013	O	2.06	6.0	0.009
Fe	2.97	6.0	0.014	Co	2.95	6.0	0.008
Fe	3.48	6.0	0.014	Co	3.47	6.0	0.014
O	3.56	2.0	0.015	O	3.56	2.0	0.015
O	3.66	6.0	0.015	O	3.66	6.0	0.015
$R$ factor = 33%				$R$ factor = 43%			
$R^*$ factor = 15%				$R^*$ factor = 21%			

<sup>a</sup> The typical errors in  $R_i$  are about  $\pm 0.01$  Å and 10% in  $2\sigma_i^2$ , and  $N_i$

In A10 Aerogels (a nominal ratio of 10 wt %  $\text{CoFe}_2\text{O}_4/(\text{CoFe}_2\text{O}_4+\text{SiO}_2)$ ), the fitting results for A10 samples of the Co and Fe K-edge are shown in Figure 2.57A and 2.57B. Good fitting parameters are presented in Table 2.11 (A10\_900). EXAFS spectra of A10 samples relate extremely to these pure cobalt ferrite samples at 900 °C. Therefore, the same parameters are used to fit pure  $\text{CoFe}_2\text{O}_4$  as starting parameters to A10\_900 of the Co and Fe K-edge. It must be observed that Debye-Waller factors for nanocomposite gels are larger than those of  $\text{CoFe}_2\text{O}_4$ , while distances and inversion degrees are the same.

**Table 2.11** The interatomic distances,  $R$ , coordination numbers,  $N$ , and Debye-Waller Factors ( $\sigma$ ) for A10\_900 and A5\_900 at the Co and Fe K-edge<sup>a</sup> [38]

Fe K-edge							Co K-edge						
Site A	A 10_900			A 5_900			Site A	A 10_900			A 5_900		
35%	$R(\text{\AA})$	$N$	$2\sigma^2$	$R(\text{\AA})$	$N$	$2\sigma^2$	30%	$R(\text{\AA})$	$N$	$2\sigma^2$	$R(\text{\AA})$	$N$	$2\sigma^2$
O	1.84	4.0	0.017	1.84	4.0	0.023	O	1.89	4.0	0.020	1.89	4.0	0.023
Fe	3.48	12.0	0.019	3.48	12.0	0.024	Co	3.47	12.0	0.018	3.47	12.0	0.023
O	3.50	12.0	0.014	3.50	12.0	0.018	O	3.50	12.0	0.018	3.50	12.0	0.023
Fe	3.54	4.0	0.024	3.54	4.0	0.025	Co	3.54	4.0	0.026	3.54	4.0	0.026
Site B							Site B						
65%	$R(\text{\AA})$	$N$	$2\sigma^2$	$R(\text{\AA})$	$N$	$2\sigma^2$	70%	$R(\text{\AA})$	$N$	$2\sigma^2$	$R(\text{\AA})$	$N$	$2\sigma^2$
O	1.98	6.0	0.012	1.98	6.0	0.014	O	2.06	6.0	0.010	2.06	6.0	0.012
Fe	2.98	6.0	0.018	2.98	6.0	0.020	Co	2.95	6.0	0.012	2.95	6.0	0.018
Fe	3.48	6.0	0.019	3.48	6.0	0.024	Co	3.47	6.0	0.018	3.47	6.0	0.023
O	3.56	2.0	0.015	3.56	2.0	0.018	O	3.56	2.0	0.018	3.56	2.0	0.023
O	3.66	6.0	0.015	3.66	6.0	0.015	O	3.66	6.0	0.018	3.66	6.0	0.023
R factor = 27%			R factor = 24%			R factor = 37%			R factor = 33%				
R* factor = 15%			R* factor = 15%			R* factor = 22%			R* factor = 24%				

<sup>a</sup> The typical errors in  $R_i$  are about  $\pm 0.01 \text{ \AA}$  and 10% in  $2\sigma_i^2$ , and  $N_i$ .

The inversion parameter ( $i$ ) was another important parameter left free for alteration while fitting, together with the Debye-Waller factors. By fitting this parameter, correct examination of the occupation percentage for octahedral, B, sites and tetrahedral, A, sites with  $\text{Co}^{2+}$  and  $\text{Fe}^{3+}$  was accomplished. As mentioned already, cobalt ferrite has a cubic spinel structure relationship with the  $Fd\bar{3}m$  space group. The unit cell is arranged with 56 atoms, of which 32 oxygen ions are diffused in close cubic packing, and 24 cations occupy 8 of 64 tetrahedral interstitials and 16 of 32 accessible octahedral interstitials. Regarding a normal spinel, 16 trivalent cations reside in 16 octahedral sites, and 8 bivalent cations reside in 8 tetrahedral sites, while 16 trivalent ions for the inverse spinel are diffused between the octahedral and tetrahedral sites, and 8 bivalent atoms reside in 8 octahedral sites. If bivalent atoms occupy both octahedral and tetrahedral sites, the spinel would not be inverted

completely. The formula for the structure of general spinel compound ( $MN_2O_4$ ) can be noted as;



where the numbers in parenthesis illustrate the average occupation of A-sites (tetrahedral) and B-sites (octahedral). The inversion parameter ( $i$ ) implies the portion of trivalent atoms in the tetrahedral sites. The inverted spinel is  $i = 1$ , and normal spinel  $i = 0$ . The cobalt spinel ferrite is reversed partially by cobalt cations that are predominant in octahedral sites (high inversion degree). More recently, EXAFS analysis of the cobalt ferrite combined with theoretically calculated X-ray intensities gave an inversion parameter of 0.74. These results refer to bulk cobalt ferrites prepared by a standard method. Nevertheless, varied cation site distribution on octahedral and tetrahedral ferrite sites has been related to different synthetic techniques, with various individual cooling rates and annealing temperatures. Fittings of  $CoFe_2O_4$ , A10\_900, and A5\_900 (a nominal ratio of 10 and 5 wt %  $CoFe_2O_4/(CoFe_2O_4+SiO_2)$ ) were calcined at 900 °C suggest the same inversion parameter of 0.70. Therefore, according to equation 2.12, 30% and 70% of  $Co^{2+}$  reside on tetrahedral and octahedral sites, respectively, while 65% and 35% of  $Fe^{3+}$  reside on octahedral and tetrahedral sites, respectively. These results seem to indicate that cobalt spinel ferrite is synthesized by using the sol-gel method, which has a lower degree of inversion than that produced by conventional solid-state methods.

All previous work from the literature analyzed cation site distribution of many ferrite substitutions. However, the oxidation state and cation distribution of cobalt ferrite substituted by metal transition (Mn, Cu, and Zn) obtained the effect of thermal annealing, which has not been a study of interest.

## References

- [1] A. Goldman, *Modern Ferrite Technology*, USA, Pittsburgh, 2006.
- [2] Intech. (2004). **Surface Modification of Nanoparticles Used in Biomedical Applications**. Access September 20, 2015, Available from: <http://www.intechopen.com/books/modern-surface-engineering-treatments/surface-modification-of-nanoparticles-used-in-biomedical-applications>
- [3] A. J. Moulson and J. M. Herbert, *Electroceramics Materials and Application*, England, John Wiley & Sons, 2003.
- [4] R. Ramanathan. (2012). **Catalysis**. Access March 5, 2015, Available from: [http://shodhganga.inflibnet.ac.in/bitstream/10603/3687/7/07\\_chapter%201.pdf](http://shodhganga.inflibnet.ac.in/bitstream/10603/3687/7/07_chapter%201.pdf)
- [5] Y.-M. Chiang, D. P. Birnie and W. D. Kingery, *Physical Ceramic*, Canada, John Wiley & Sons, 1997.
- [6] R. C. Buchanan, *Ceramic Materials for Electronics*, USA, Marcel Dekker, 2004.
- [7] U. S. Peroxide. (2001). **Fenton's Reaction**. Access July 1, 2015, Available from: <http://www.lenntech.com/fenton-reaction.htm>
- [8] U. S. Peroxide. (2001). **Hydrogen Peroxide**. Access July 1, 2015, Available from: <http://www.lenntech.com/library/oxidation/h2o2/hydrogen-peroxide.htm>
- [9] P. Baldrian, V. Merhautova, J. Gabriel, F. Nerud, P. Stopka, M. Hruby and M. J. Benes, "Decolorization of synthetic dyes by hydrogen peroxide with heterogeneous catalysis by mixed iron oxides", *Applied Catalysis B: Environmental*, **66**, 258–264 (2006).
- [10] L. Zhao, H. Yang, X. Zhao, L. Yu, Y. Cui and S. Feng, "Magnetic properties of  $\text{CoFe}_2\text{O}_4$  ferrite doped with rare earth ion", *Mater. Lett.*, **60**, 1-6 (2006).
- [11] J. Peng, M. Hojamberdiev, Y. Xu, B. Cao, J. Wang and H. Wu, "Hydrothermal synthesis and magnetic properties of gadolinium-doped  $\text{CoFe}_2\text{O}_4$  nanoparticles", *J. Magn. Magn. Mater.*, **323**, 133-137 (2011).
- [12] E. Casbeer, V. K. Sharma and X.-Z. Li, "Synthesis and photocatalytic activity of ferrites under visible light: A review", *Sep. Purif. Technol.*, **87**, 1-14 (2012).

This material is reserved for educational use only, not allowed for commercial use.

Forbidden to modify the content, and cite the document when use.

- [13] P. C. R. Varma, R. S. Manna, D. Banerjee, M. R. Varma, K. G. Suresh and A. K. Nigam, "Magnetic properties of  $\text{CoFe}_2\text{O}_4$  synthesized by solid state, citrate precursor and polymerized complex methods: A comparative study", *J. Alloy. Compd.*, **453**, 298-303 (2008).
- [14] D. H. Kim, H. Zeng, T. C. Ng and C. S. Brazel, "T1 and T2 relaxivities of succimer-coated  $\text{MFe}_2^{3+}\text{O}_4$  ( $\text{M} = \text{Mn}^{2+}$ ,  $\text{Fe}^{2+}$  and  $\text{Co}^{2+}$ ) inverse spinel ferrites for potential use as phase-contrast agents in medical MRI", *J. Magn. Magn. Mater.*, **321** (2009).
- [15] C. S. Kim, Y. S. Yi, K.-T. Park, H. Namgung and J.-G. Lee, "Growth of ultrafine Co-Mn ferrite and magnetic properties by a sol-gel method", *J. Appl. Phys.*, **85**, 5223 (1999).
- [16] O. Caltun, G. S. N. Rao, K. H. Rao, B. Parvatheeswara Rao, I. Dumitru, C.-O. Kim and C. Kim, "The influence of Mn doping level on magnetostriction coefficient of cobalt ferrite", *J. Magn. Magn. Mater.*, **316**, e618-e620 (2007).
- [17] H. N. Choi, K. S. Baek, S. W. Hyun, I.-B. Shim and C. S. Kim, "A Study of Co Substituted Mn-Ferrite,  $\text{Mn}_{1-x}\text{Co}_x\text{Fe}_2\text{O}_4$  ( $x = 0.0, 0.5, 1.0$ )", *IEEE T. Magn.*, **45**, 6 (2009).
- [18] M. K. Shobana, S. Sankar and V. Rajendran, "Characterization of  $\text{Co}_{0.5}\text{Mn}_{0.5}\text{Fe}_2\text{O}_4$  nanoparticles", *Mater. Chem. Phys.*, **113**, 10-13 (2009).
- [19] J. Z. Msomi, H. M. I. Abdallah, T. Moyo and A. Lančok, "Structural and magnetic properties of  $\text{Mn}_x\text{Co}_{1-x}\text{Fe}_2\text{O}_4$  ferrite nanoparticles", *J. Magn. Magn. Mater.*, **323**, 471-474 (2011).
- [20] Y. Köseoğlu, F. Alan, M. Tan, R. Yilgin and M. Öztürk, "Low temperature hydrothermal synthesis and characterization of Mn doped cobalt ferrite nanoparticles", *Ceram. Int.*, **38**, 3625-3634 (2012).
- [21] Y. Köseoğlu, A. Baykal, F. Gözüak and H. Kavas, "Structural and magnetic properties of  $\text{Co}_x\text{Zn}_{1-x}\text{Fe}_2\text{O}_4$  nanocrystals synthesized by microwave method", *Polyhedron*, **28**, 2887-2892 (2009).
- [22] S. Y. An, I. S. Kim, S. H. Son, S. Y. Song, J. W. Hahn, S. W. Hyun, C. M. Kim and C. S. Kim, "Magnetic properties of  $\text{Cu}^{2+}$  substituted Co-ferrite", *Thin Solid Films*, **519**, 8296-8298 (2011).

- [23] M. Hashim, Alimuddin, S. Kumar, B. H. Koo, S. E. Shirsath, E. M. Mohammed, J. Shah, R. K. Kotnala, H. K. Choi, H. Chung and R. Kumar, "Structural, electrical and magnetic properties of Co–Cu ferrite nanoparticles", *J. Alloy. Compd.*, **518**, 11-18 (2012).
- [24] N. D. T. Education Resource Center. (2001). **Thermal Treatments**. Access July 13, 2015, Available from: <https://www.nde-ed.org/EducationResources/CommunityCollege/Materials/Structure/thermal.htm>
- [25] W. D. Callister and D. G. Rethwisch, *Materials Science and Engineering*, USA, John Wiley & Sons, 2010.
- [26] Z. J. Zhang, Z. L. Wang, B. C. Chakoumakos and J. S. Yin, "Temperature Dependence of Cation Distribution and Oxidation State in Magnetic Mn-Fe Ferrite Nanocrystals", *J. Am. Chem. Soc.*, **120**, 1800-1804 (1998).
- [27] N. Vittayakorn, G. Rujijanagul and D. P. Cann, "Investigation of the influence of the thermal treatment on the morphologies, dielectric and ferroelectric properties of PZT-based ceramics", *J. Alloy. Compd.*, **440**, 259-264 (2007).
- [28] H. M. I. Abdallah, T. Moyo and J. Z. Msomi, "The Effect of Annealing Temperature on the Magnetic Properties of  $Mn_xCo_{1-x}Fe_2O_4$  Ferrites Nanoparticles", *J. Supercond. Nov. Magn.*, **25**, 2625-2630 (2011).
- [29] M. Newville, *Fundamentals of XAFS*, USA, University of Chicago, 2004.
- [30] M. G.-Soyer, "X-ray Absorption Spectroscopy: A Tool to Study the Local Atomic and Electronic Structure of Ceramics", *Elsevier Science Limited*, **98**, 2253-2261 (1998).
- [31] M. F. F. Lelis, A. O. Porto, C. M. Gonçalves and J. D. Fabris, "Cation occupancy sites in synthetic Co-doped magnetites as determined with X-ray absorption (XAS) and Mössbauer spectroscopies", *J. Magn. Magn. Mater.*, **278**, 263-269 (2004).
- [32] S. Sakurai, S. Sasaki, M. Okube, H. Ohara and T. Toyoda, "Cation distribution and valence state in Mn–Zn ferrite examined by synchrotron X-rays", *Physica B*, **403**, 3589-3595 (2008).

- [33] V. G. Harris, N. C. Koon, C. M. Williams, Q. Zhang, M. Abe and J. P. Kirkland, "Cation distribution in NiZn-ferrite films via extended x-ray absorption fine structure", *Appl. Phys. Lett.*, **68**, 2082 (1996).
- [34] S. A. Oliver, V. G. Harris, H. H. Hamdeh and J. C. Ho, "Large zinc cation occupancy of octahedral sites in mechanically activated zinc ferrite powders", *Appl. Phys. Lett.*, **76**, 2761 (2000).
- [35] J. A. Gomes, M. H. Sousa, G. J. da Silva, F. A. Tourinho, J. Mestnik-Filho, R. Itri, G. d. M. Azevedo and J. Depeyrot, "Cation distribution in copper ferrite nanoparticles of ferrofluids: A synchrotron XRD and EXAFS investigation", *J. Magn. Magn. Mater.*, **300**, e213-e216 (2006).
- [36] A. K. Giri, E. M. Kirkpatrick, P. Moongkhamklang, S. A. Majetich and V. G. Harris, "Photomagnetism and structure in cobalt ferrite nanoparticles", *Appl. Phys. Lett.*, **80**, 2341 (2002).
- [37] M. H. Nilsen, C. Nordhei, A. L. Ramstad, D. G. Nicholson, M. Poliakoff and A. Cabañas, "XAS (XANES and EXAFS) Investigations of Nanoparticulate Ferrites Synthesized Continuously in Near Critical and Supercritical Water", *J. Phys. Chem. C.*, **111**, 6252-6262 (2007).
- [38] D. Carta, G. Mountjoy, G. Navarra, M. F. Casula, D. Loche, S. Marras and A. Corrias, "X-ray Absorption Investigation of the Formation of Cobalt Ferrite Nanoparticles in an Aerogel Silica Matrix", *J. Phys. Chem. C.*, **111**, 6308-6317 (2007).

## CHAPTER 3

### EXPERIMENTAL PROCEDURES

This chapter describes the experimental procedures employed to synthesize cobalt substituted transition metal ferrite. The effects of thermal annealing temperature, time, and atmosphere of the samples were studied. Furthermore, the characterization of phase purity, site distribution, microstructure, and magnetic and catalyst properties was investigated.

#### 3.1 Sample Preparation

Fabrications of materials, powder preparation, and ceramic fabrication were employed as follows:

##### 3.1.1 Powder Preparation

All powders in this work were prepared by a conventional solid state mixed oxide method. The starting materials used for the preparation are listed in Table 3.1, together with the suppliers, formula of weights, and percentage of purity.

Table 3.1 Specifications of the starting materials used in this study

Powder	Source	Formula of weight	Purity (%)
Fe <sub>2</sub> O <sub>3</sub>	Sigma-Aldrich	159.69	≥99.0
Co <sub>3</sub> O <sub>4</sub>	Aldrich	204.80	≥99.0
Mn <sub>2</sub> O <sub>3</sub>	Aldrich	157.87	≥99.0
CuO	Sigma-Aldrich	79.55	>99.0
ZnO	Fluka	81.38	≥99.0

The mixing process that is illustrated schematically in Figure 3.1 was employed as a routine processing procedure for all powder preparations. The relevant calculated proportions of constituents in the mixing process were weighed,

This material is reserved for educational use only, not allowed for commercial use.

Forbidden to modify the content, and cite the document when use.

suspended in ethanol and mixed in a ball-mill with alumina media for 24 h in a PVC container. The slurry was dried in a hot air oven for 24 h, and the dried powder was well ground using an agate mortar. The ground powders were calcined in a closed alumina crucible in air at 900 °C for 48 h, with a heating/cooling rate of 5 °C/min.

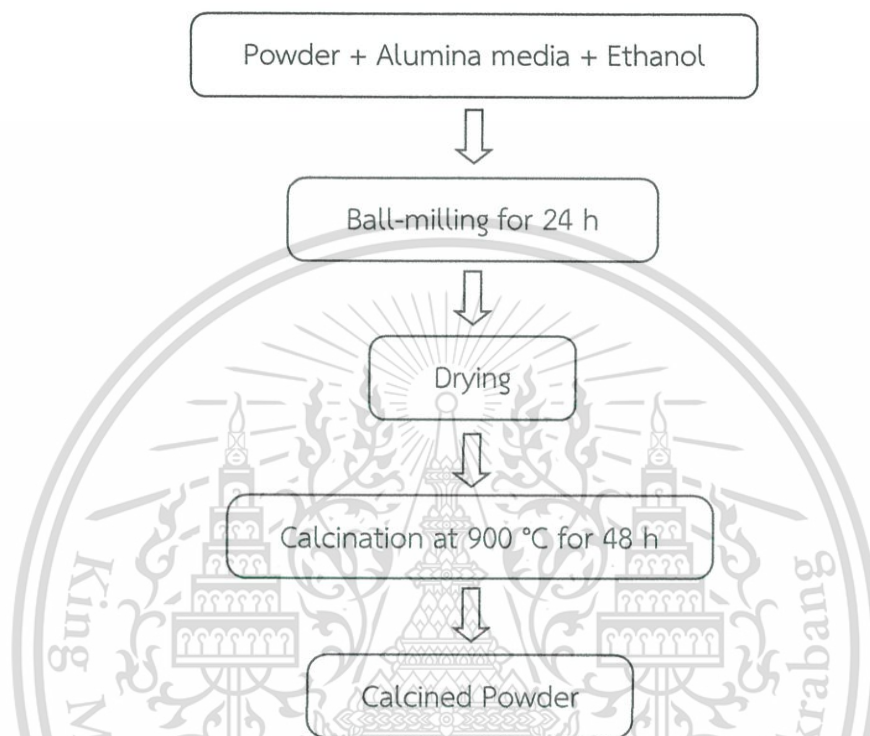


Figure 3.1 Mixing and calcination processes for powder preparation.

### 1) Preparation of $\text{CoFe}_{(2-x)}\text{Mn}_x\text{O}_4$ powders

$\text{CoFe}_{(2-x)}\text{Mn}_x\text{O}_4$  powders doped with  $x = 0.00, 0.10, 0.15, 0.20, 0.25, 1.00, 1.10,$  and  $1.15$  were prepared by using a simple synthetic mixed oxide route. The complete reactions were as follows:



This material is reserved for educational use only, not allowed for commercial use.

Forbidden to modify the content, and cite the document when use.



The starting powders of  $\text{Fe}_2\text{O}_3$ ,  $\text{Co}_3\text{O}_4$  and  $\text{Mn}_2\text{O}_3$  were used, and the mixing process, as described in 3.1.1, was followed, as shown in Figure 3.2.

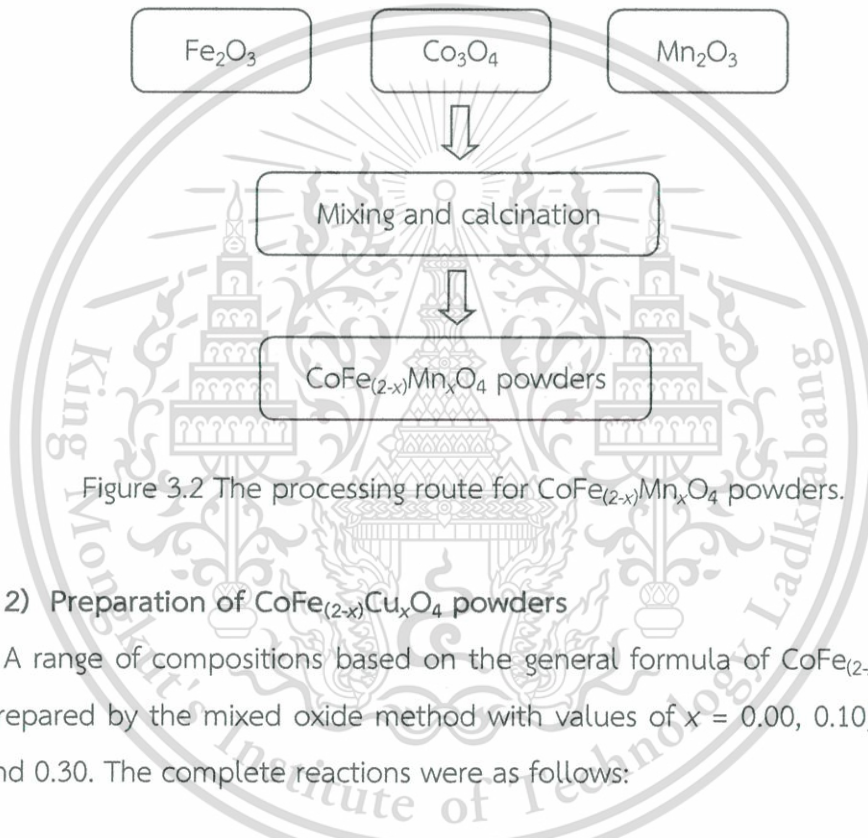


Figure 3.2 The processing route for  $\text{CoFe}_{(2-x)}\text{Mn}_x\text{O}_4$  powders.

## 2) Preparation of $\text{CoFe}_{(2-x)}\text{Cu}_x\text{O}_4$ powders

A range of compositions based on the general formula of  $\text{CoFe}_{(2-x)}\text{Cu}_x\text{O}_4$  was then prepared by the mixed oxide method with values of  $x = 0.00, 0.10, 0.15, 0.20, 0.25,$  and  $0.30$ . The complete reactions were as follows:



This material is reserved for educational use only, not allowed for commercial use.

Each composition was prepared by mixing appropriate amounts of  $\text{Fe}_2\text{O}_3$ ,  $\text{Co}_3\text{O}_4$  and  $\text{CuO}$ . This achieved  $\text{CoFe}_{(2-x)}\text{Cu}_x\text{O}_4$  powders, as shown in Figure 3.3.

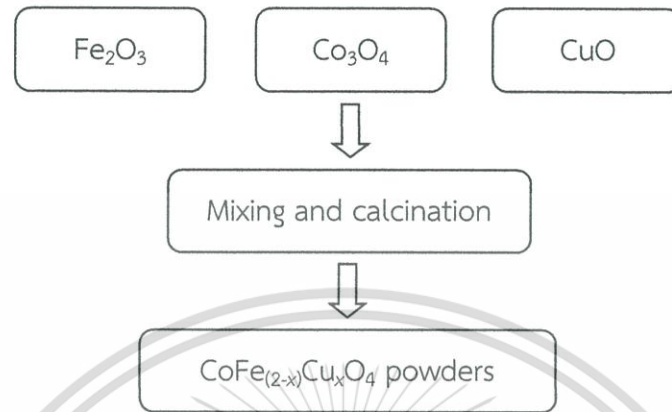


Figure 3.3 The processing route for  $\text{CoFe}_{(2-x)}\text{Cu}_x\text{O}_4$  powders.

### 3) Preparation of $\text{CoFe}_{(2-x)}\text{Zn}_x\text{O}_4$ powders

Powders of the  $\text{CoFe}_{2-x}\text{Zn}_x\text{O}_4$  system, where  $x = 0.00, 0.10, 0.15, 0.20, 0.25, 0.50, 0.55$  and  $0.60$ , were prepared by the mixed-oxide method, with mixed oxide reaction stages as follows:



The reagent grades of  $\text{Fe}_2\text{O}_3$ ,  $\text{Co}_3\text{O}_4$ , and  $\text{ZnO}$  powders were used. A schematic diagram of the preparation route for  $\text{CoFe}_{(2-x)}\text{Zn}_x\text{O}_4$  powders is illustrated in Figure 3.4.

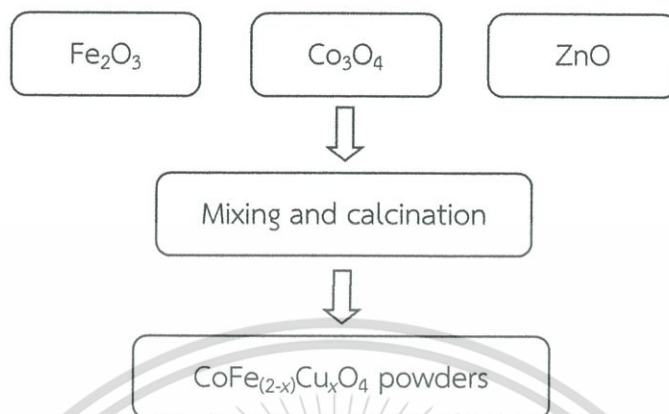


Figure 3.4 The processing route for  $\text{CoFe}_{(2-x)}\text{Zn}_x\text{O}_4$  powders.

### 3.1.2 Ceramic Fabrication

In this section, all  $\text{CoFe}_{(2-x)}\text{Mn}_x\text{O}_4$ ,  $\text{CoFe}_{(2-x)}\text{Cu}_x\text{O}_4$ , and  $\text{CoFe}_{(2-x)}\text{Zn}_x\text{O}_4$ , where  $x = 0.00, 0.10, 0.15, 0.20,$  and  $0.25$  powders, were reground by wet planetary milling for 6 h in a PVC container, using an alumina ball and ethanol as the medium. Resulting slurry was dried in a hot air oven, and the powders were well ground using an agate mortar and sieved through 325-mesh. Then, the ceramics were fabricated by pressing the powder ( $\sim 0.8$  g) of each composition uniaxially into a green pellet of 12 mm diameter and sintering at  $1,250$  °C for 4 h, with a heating/cooling rate of  $5$  °C/min in air. The samples were placed on the alumina powder-bed inside an alumina crucible. In order to reduce the loss of volatile components, the samples were surrounded by a powder atmosphere of identical chemical composition. The specimen arrangement is shown in Figure 3.5. The alumina crucible was closed with an alumina lid before being inserted into a high temperature sintering furnace (Figure 3.6).

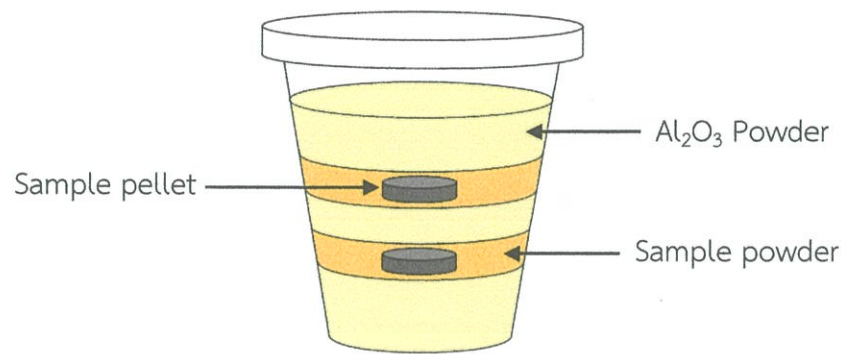


Figure 3.5 Sample arrangement of the sintering process.

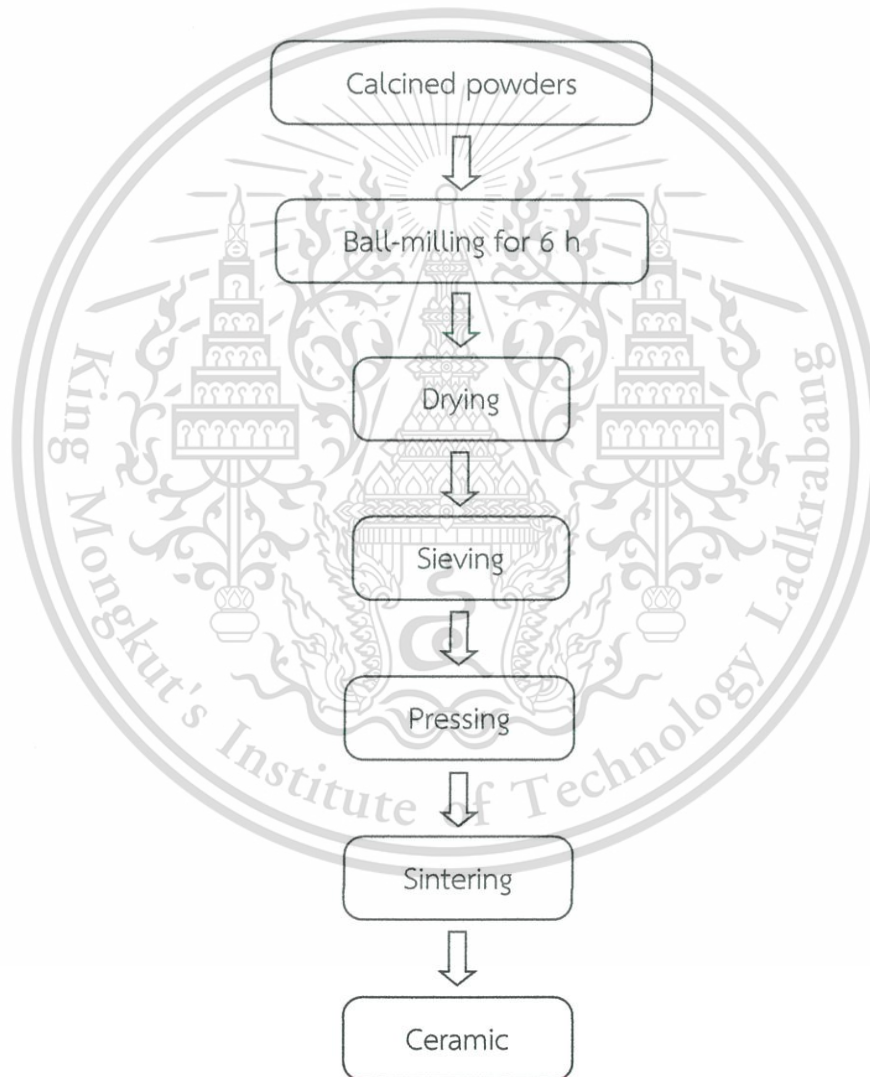


Figure 3.6 The processing route for ceramic fabrication.

### 3.2 Sample Annealing

The study of effects of the thermal annealing temperature, annealing time, and annealing atmosphere of the calcined powders was operated as follows:

#### 3.2.1 Effects of Annealing Temperature

The calcined powders of  $\text{CoFe}_{0.90}\text{Mn}_{1.10}\text{O}_4$  were annealed in a closed alumina crucible in air at different temperatures; 400, 500, 600, 700 °C for 100 h, with a heating/cooling rate of 5 °C/min.

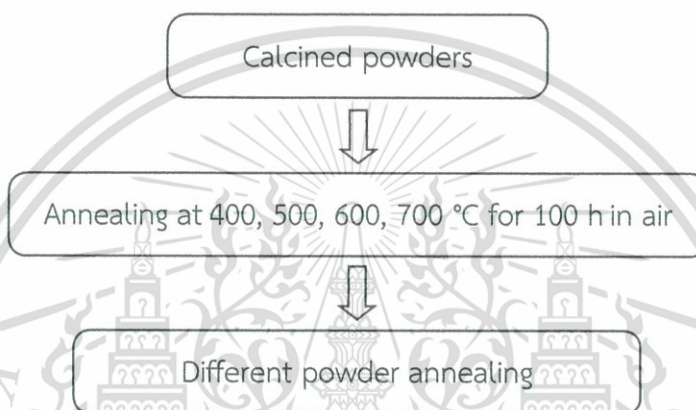


Figure 3.7 The processing route for different annealing temperatures.

#### 3.2.2 Annealing Atmosphere

The calcined powders of  $\text{CoFe}_{0.90}\text{Mn}_{1.10}\text{O}_4$  were annealed in a closed alumina crucible and different atmosphere; air,  $\text{N}_2$ ,  $\text{O}_2$ , at 500 °C for 100 h with a heating/cooling rate of 5 °C/min.

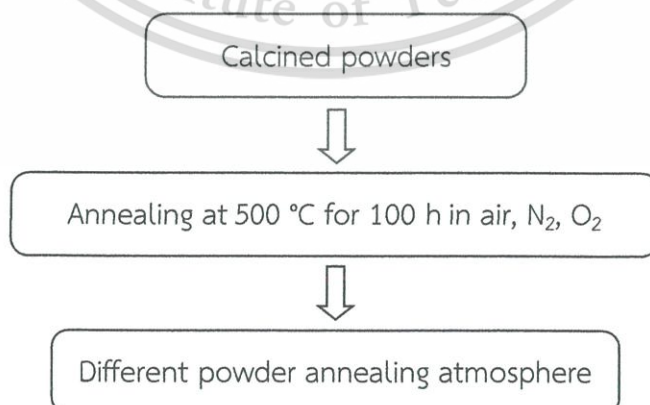


Figure 3.8 The processing route for a different annealing atmosphere.

This material is reserved for educational use only, not allowed for commercial use.

Forbidden to modify the content, and cite the document when use.

### 3.2.3 Annealing Time

The calcined powders of  $\text{CoFe}_{0.90}\text{Mn}_{1.10}\text{O}_4$ ,  $\text{CoFe}_{1.75}\text{Cu}_{0.25}\text{O}_4$ ,  $\text{CoFe}_{1.45}\text{Zn}_{0.55}\text{O}_4$  were annealed in a closed alumina crucible in air at 500 °C for different time periods of 4 h and 100 h with a heating/cooling rate of 5 °C/min.

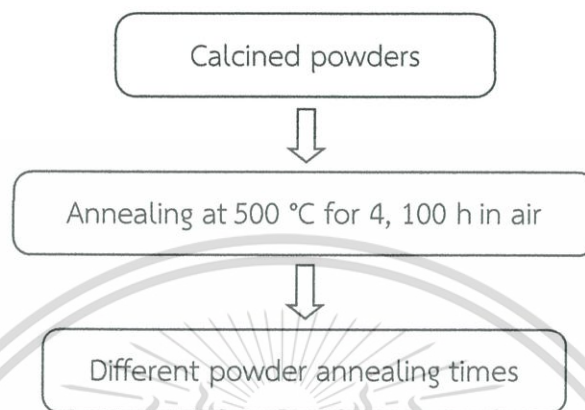


Figure 3.9 The processing route for different annealing times.

## 3.3 Sample Characterization

The following section is intended to address the main characterization techniques used to investigate the phase formation, morphology, oxidation state, cation distribution, and magnetic and catalyst properties of the materials in this study.

### 3.3.1 Phase Analysis

X-ray Diffraction (XRD) was used in this study for phase identification, and also to determine the crystal structure of materials in calcined powder at room temperature. Sample powders for XRD were prepared by grinding and packing in a sample holder. A Philips-X'Pert MPD with  $\text{CuK}\alpha$  radiation (Figure 3.10) was employed. Lattice parameters of the materials were determined from XRD patterns by the Rietveld refinement method [1].



Figure 3.10 X-ray diffractometer [2].

### 3.3.2 Densification Analysis

The densities of all the samples were determined using Archimedes' Principle [3]. The dry samples was weighed first ( $W_1$ ), then weighed again after fluid impregnation ( $W_2$ ), and finally weighed while being immersed in water ( $W_3$ ). All weights were in grams. Generally, a very thin brass wire is used to suspend the samples in the water and their weight  $W_w$  must be measured in water too. Then, the density ( $\rho$ ) can be calculated from the following equations:

$$\rho = \frac{W_1 \rho_w}{W_2 - W_3} \quad (3.26)$$

where  $\rho_w$  is the density of water (in  $\text{g/cm}^3$ ), which is slightly temperature dependent, and

$$\rho_w = 1.0017 - 0.0002315T \quad (3.27)$$

where  $T$  is the temperature of water (in degrees Celsius).

This material is reserved for educational use only, not allowed for commercial use.

Forbidden to modify the content, and cite the document when use.

### 3.3.3 Scanning Electron Microscopy (SEM)

The Hitachi S4700 (Figure 3.11) was used in this work to determine the morphology of the powder, and the as-fired surface of the ceramics. The powders were dispersed in ethanol using ultrasonic cleaner, and then coated with spluttered gold, and the as-sintered surface of the ceramics was cleaned by ultrasonic cleaner before being coated with gold. While acquiring an image, secondary electron modes were used with an accelerating voltage of 5 kV. Average grain sizes of the sintered ceramics were estimated using the linear intercept method, where random lines are drawn on a micrograph, with the number of grain boundaries intercepting these lines being counted. Grain shape of the sintered ceramics was classified by the degree concept of angularity under the ASTM designation, E112 [4].



Figure 3.11 Scanning electron microscope [5].

### 3.3.4 X-ray Absorption Spectroscopy (XAS)

The oxidation state and local structure of each element were investigated using the X-ray absorption spectroscopy (XAS) technique (Figure 3.12). The powders were ground and put in a sample holder. Both XANES and EXAFS data were collected from the Co K-edge (7709 eV) and Fe K-edge (7112 eV) in the transmission mode, and Mn K-edge (6539 eV), Cu K-edge (8979 eV), and Zn K-edge (9659 eV), in This material is reserved for educational use only, not allowed for commercial use.

Forbidden to modify the content, and cite the document when use.

the fluorescence mode at room temperature, at the XAS Facility (BL-8) of Siam Photon Laboratory, Synchrotron Light Research Institute (SLRI), Nakhon Ratchasima, Thailand.

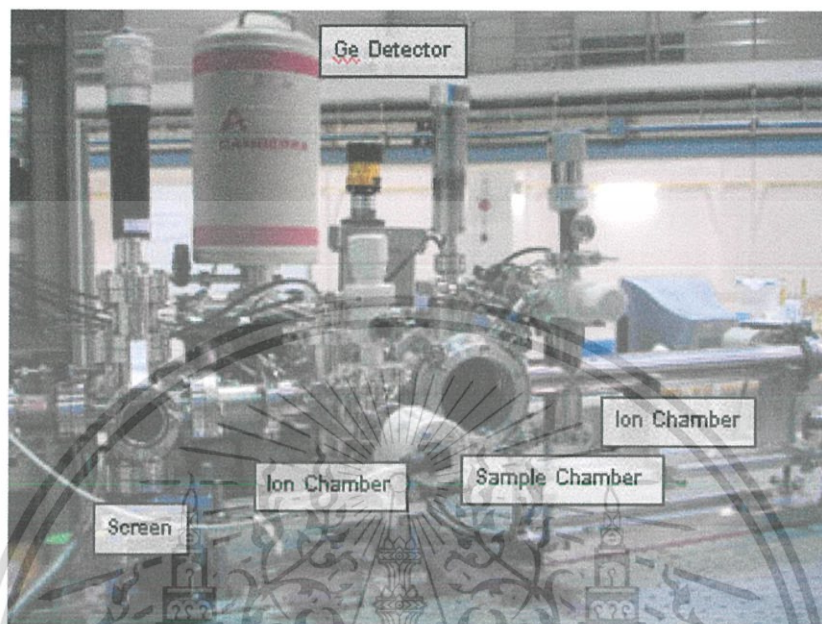


Figure 3.12 X-ray absorption spectroscopy [6].

### 3.3.5 Vibrating Sample Magnetometer (VSM)

A vibrating sample magnetometer (VSM) was employed in this study to investigate the saturated magnetization and coercivity in both powders and ceramics. The powders were prepared at a weight of about 0.01 g and packed into a holder. The ceramics were cleaned by an ultrasonic cleaner, and then mounted on the sample holder. The maximum field of 8 kOe was applied at room temperature (Figure 3.13), at the Department of Physics, Kasetsart University (KU), and a magnetization ( $M$ ) versus magnetic field strength ( $H$ ) plot was generated.

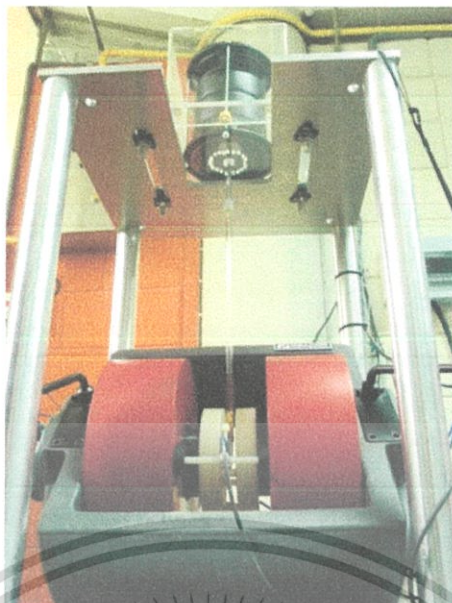


Figure 3.13 Vibrating sample magnetometer [7].

### 3.3.6 Ultraviolet–Visible Spectrophotometer (UV-Vis)

The catalyst activities of samples were examined by degradation of synthetic dyes, which comprised Naphthol Blue Black (Sigma-Aldrich, dye content 80%,  $\lambda_{\text{max}}$  618 nm), and Reactive Orange 16 (Sigma-Aldrich, dye content >70%,  $\lambda_{\text{max}}$  388 nm). Dry catalysts ( $25 \text{ mg mL}^{-1}$ ) were combined with synthetic dyes ( $50 \text{ mg L}^{-1}$ ) in water and the reaction was started by adding hydrogen peroxide ( $100 \text{ mmol L}^{-1}$ ). The reactions proceeded with slow agitation at room temperature in the dark. The catalyst was separated magnetically at each sampling time, and the supernatant was used immediately for analysis by putting it into a sample holder. The concentrations of synthetic dyes were determined using a UV–Visible Spectrophotometer (Thermo Electron Helios Gamma) in a wavelength of 400–700 nm (Figure 3.14) at the College of Nanotechnology, King Mongkut's Institute of Technology Ladkrabang (KMITL). The percentages of degradation were calculated from the decreasing maximum of the absorption peak.

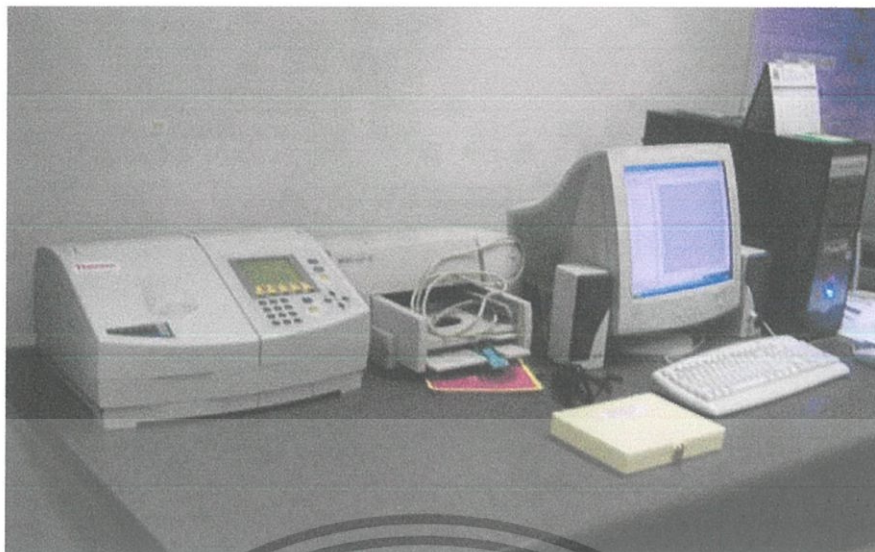


Figure 3.14 UV-Visible spectrophotometer [8].



This material is reserved for educational use only, not allowed for commercial use.

Forbidden to modify the content, and cite the document when use.

## References

- [1] H. M. Rietveld, "A profile refinement method for nuclear and magnetic structures", *J. Appl. Cryst.*, **2**, 65-71 (1969).
- [2] University of Vienna. (2014). **Research**. Access September 16, 2015, Available from: [http://www.univie.ac.at/Mineralogie/powder\\_engl\\_n.htm](http://www.univie.ac.at/Mineralogie/powder_engl_n.htm)
- [3] W. Chaisan, **Preparation and characterization of ceramic nanocomposites in the PZT-BT and TiO<sub>2</sub>-SnO<sub>2</sub> systems**, Chiang Mai, Chiang Mai University, 2006.
- [4] *Annual Book of ASTM Standards*, Philadelphia, American Society for Testing and Materials, 1970.
- [5] Michigan Technological University. (2009). **Electron Microscopy Online Training** Access September 16, 2015, Available from: [http://mcff.mtu.edu/acmal/electronmicroscopy/FE\\_Form\\_Function.htm](http://mcff.mtu.edu/acmal/electronmicroscopy/FE_Form_Function.htm)
- [6] Vcharkarn. (2013). **Synchrotron Light**. Access September 16, 2015, Available from: <http://www.vcharkarn.com/varticle/59622>
- [7] Kasetsart University. (2013). **Electricity and Magnetism Research Laboratory**. Access September 16, 2015, Available from: <http://physics.sci.ku.ac.th/?q=node/65>
- [8] College of Nanotechnology. (2011). **Equipment**. Access September 17, 2015, Available from: <http://www.nano.kmitl.ac.th/index.php/tool.html>

## CHAPTER 4

# RESULTS AND DISCUSSION

### 4.1 Effect of Transition Metal Substitution

In this chapter, the effect of transition metal substitution and thermal treatment of powder in the M doped cobalt ferrites, when M = Mn, Cu, Zn, were explored. The relationships of processing, structure, and properties were discussed in terms of phase formation, microstructure, oxidation state, cation distribution, magnetic properties, and catalyst properties. First, attention was paid to the results of characterization of the transition metal substitution of  $\text{CoFe}_{2-x}\text{Mn}_x\text{O}_4$  System (M = Mn, Cu, Zn).

#### 4.1.1 $\text{CoFe}_{2-x}\text{Mn}_x\text{O}_4$ System

##### 4.1.1.1 Phase Formation

The X-ray diffraction pattern of  $\text{CoFe}_{2-x}\text{Mn}_x\text{O}_4$  powders at various compositions and calcined at 900 °C for 48 h is displayed in Figure 4.1. The XRD patterns showed that peaks (when  $x = 0.00-1.10$ ) were of a single phase cubic structure and corresponded to JCPDS file no. 22-1086 and space group  $\text{Fd}\bar{3}\text{m}$  (no. 227) [1]. However, the XRD pattern of the  $\text{CoFe}_{0.85}\text{Mn}_{1.15}\text{O}_4$  powder detected secondary phases, which were  $\text{Fe}_3\text{O}_4$ ,  $\text{Fe}_2\text{O}_3$  and  $(\text{Co}, \text{Mn})(\text{Mn}, \text{Co})_2\text{O}_4$  which corresponded to JCPDS file no. 28-0491, 25-1402 and 18-0409, respectively. Therefore, only single phase samples were used to investigate the lattice parameters - which were analyzed from XRD data by the Rietveld refinement method using the FullProf program - and the variation of lattice constants and results of a quantitative phase analysis from the refinement with  $\text{Mn}^{2+}$  doping are presented in Figure 4.2 and Table 4.1.

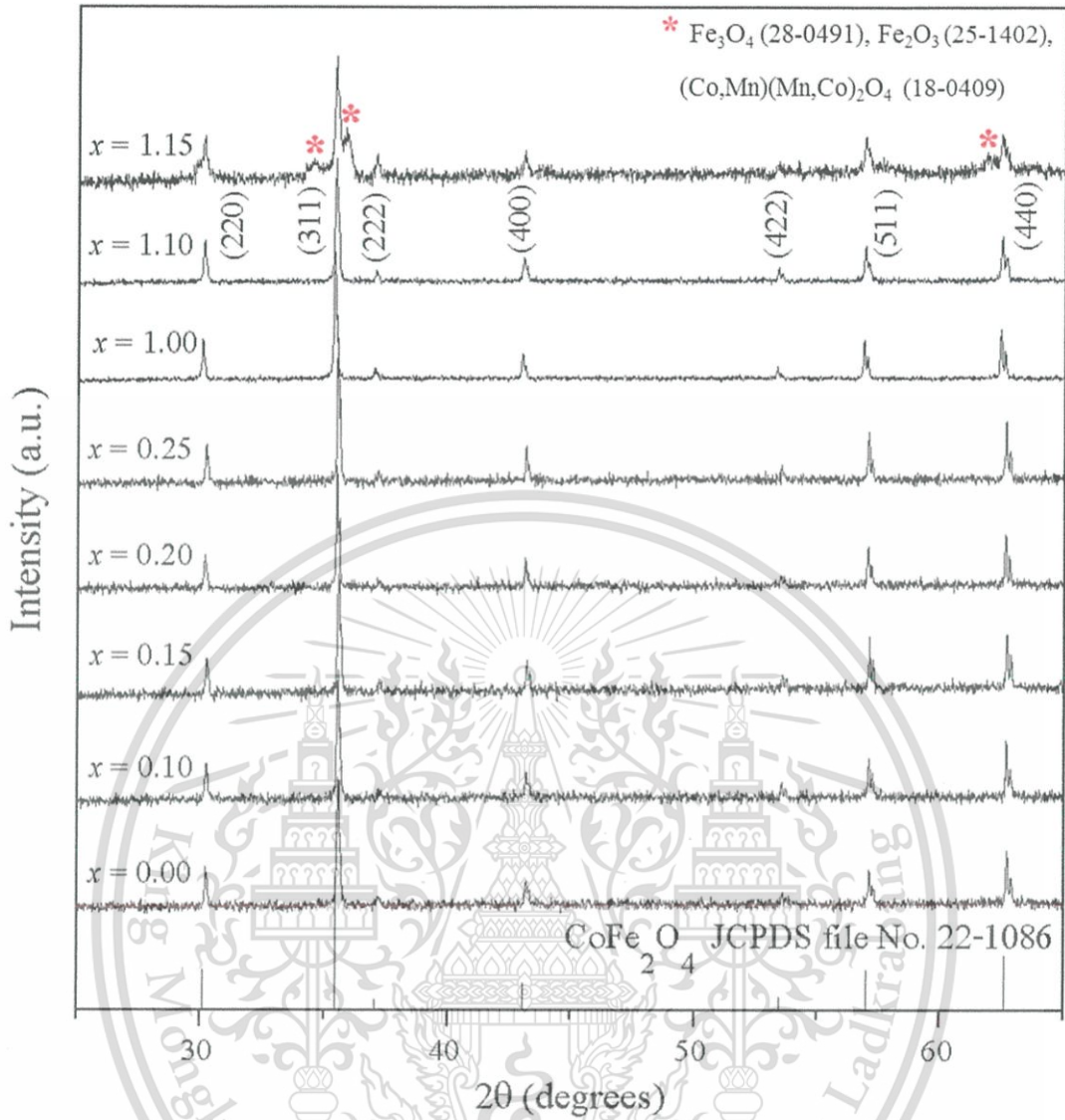


Figure 4.1 X-ray diffraction patterns of  $\text{CoFe}_{2-x}\text{Mn}_x\text{O}_4$  powders calcined at  $900\text{ }^\circ\text{C}$  for 48 h.

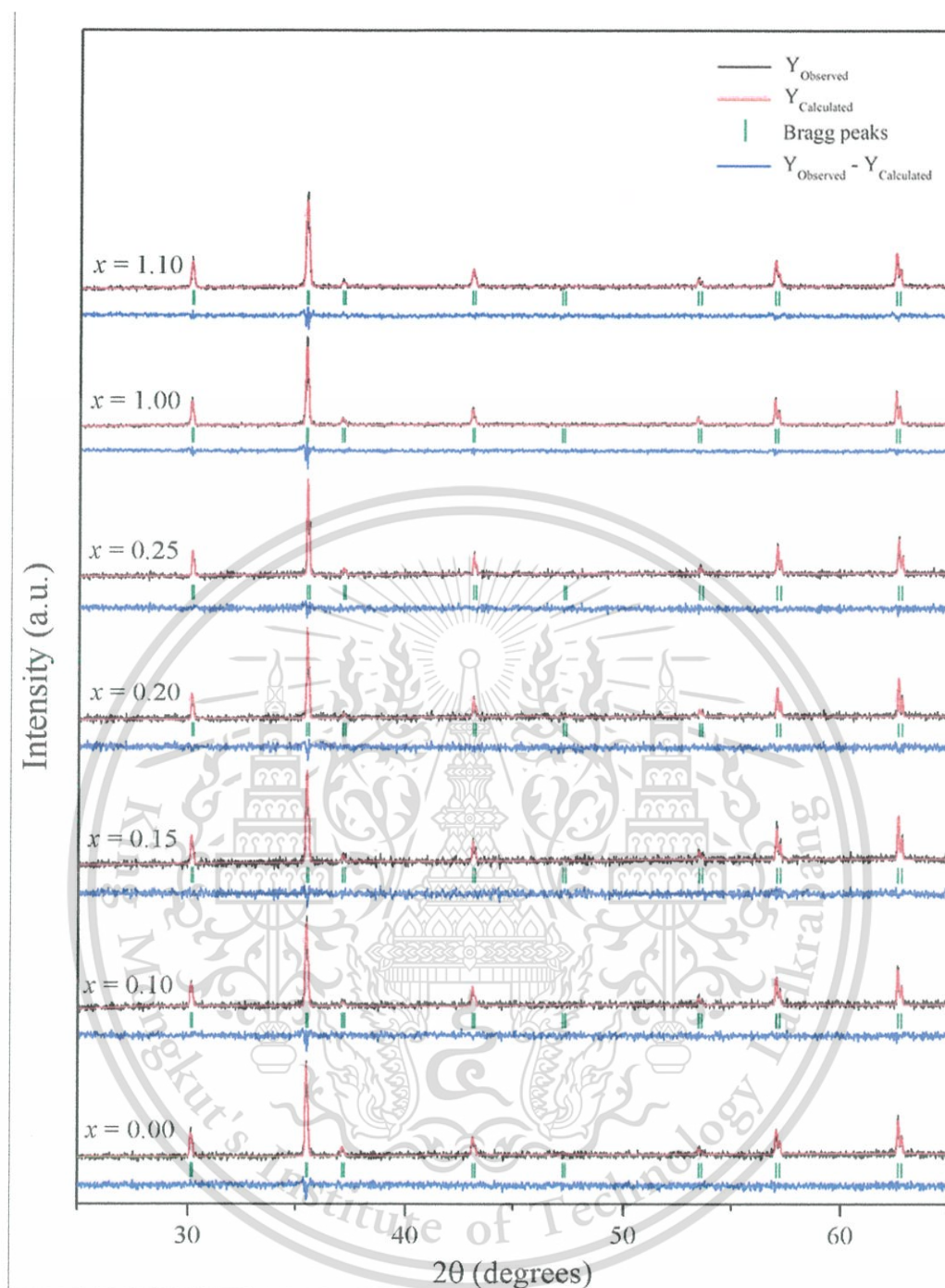


Figure 4.2 X-ray diffraction patterns and the structure refinement of  $\text{CoFe}_{2-x}\text{Mn}_x\text{O}_4$  powders calcined at 900 °C for 48 h.

The structure refinement showed the corresponding fits and confirmed that the structure was of cubic type. Data quality of structural refinement was checked basically by R-values ( $R_w$ ) and a good fit ( $\chi^2$ ). In addition, the distinction between XRD patterns, calculated data and experimental profiles displayed a small value in the intensity scale, as illustrated by the line,  $Y_{\text{Observed}} - Y_{\text{Calculated}}$  [2].

**Table 4.1** Lattice constant ( $a$ ) and Rietveld refinement result of  $\text{CoFe}_{2-x}\text{Mn}_x\text{O}_4$  powders calcined at 900 °C for 48 h.

$x$	$a$ (Å)	$V$ ( $10^6$ pm <sup>3</sup> )	$R_w$ (%)	$\chi^2$
0.00	8.3843 (6)	589.010	4.01	1.11
0.10	8.3884 (6)	589.879	4.19	1.13
0.15	8.3882 (5)	590.206	4.15	1.01
0.20	8.3904 (5)	590.401	4.45	1.19
0.25	8.3918 (4)	590.970	4.04	1.09
1.00	8.4094 (3)	594.687	2.81	1.56
1.10	8.4103 (4)	594.893	2.62	1.33

Furthermore, the results showed that the lattice constant, and unit cell volume for each composition increased with increasing Mn ions (Figure 4.3). The lattice parameter increased with doping, due to the ionic radius of  $\text{Mn}^{3+}$  cations ( $0.58 \text{ \AA}$ ) coordinating six-fold with  $\text{O}^{2-}$  ions were larger than the ionic radius of  $\text{Fe}^{3+}$  ion ( $0.55 \text{ \AA}$ ) coordinating six-fold with  $\text{O}^{2-}$  ions in the structure. This resulted in higher degrees of lattice fringe alignment [3].

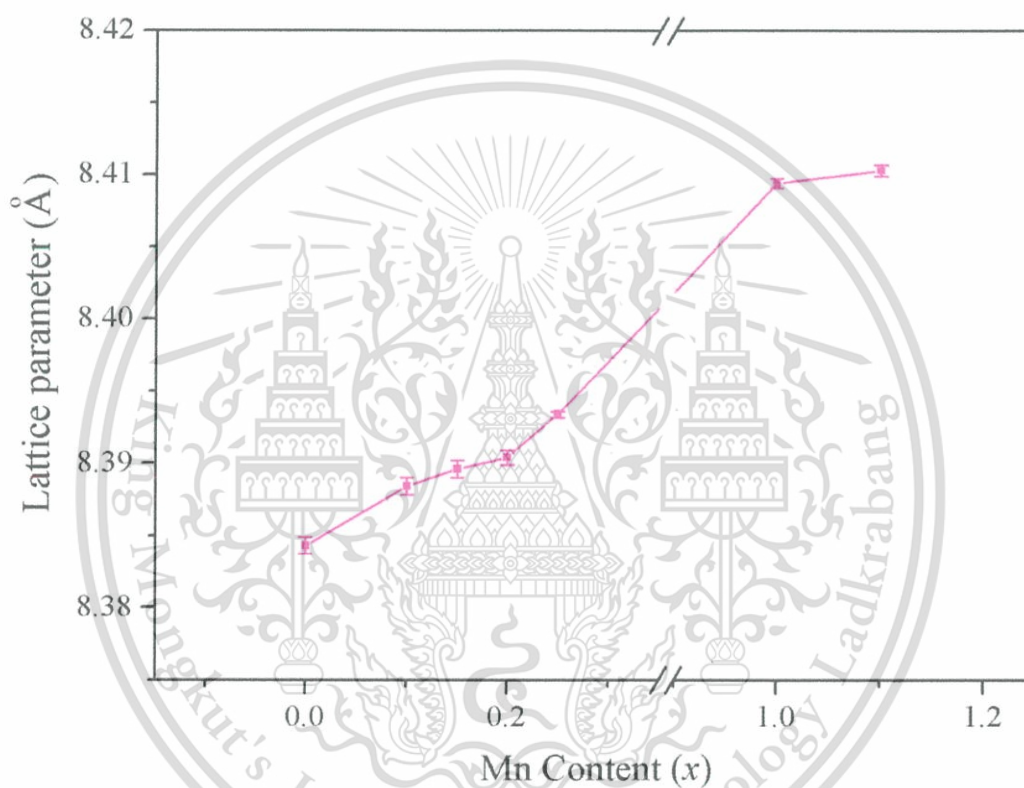


Figure 4.3 Lattice constant of  $\text{CoFe}_{2-x}\text{Mn}_x\text{O}_4$  powders calcined at  $900 \text{ }^\circ\text{C}$  for 48 h.

#### 4.1.1.2 Magnetic Properties

Figure 4.4 shows the magnetic hysteresis loop of  $\text{CoFe}_{2-x}\text{Mn}_x\text{O}_4$  powders as a function of compositions calcined at 900 °C for 48 h, and a maximum applied field of up to 8 kOe at room temperature. Generally, the magnetization curves of all samples were nonlinear which is the behavior of typical ferrimagnetic materials [4]. Figure 4.5 and Table 4.2 present the variations of saturated magnetization ( $M_s$ ) and coercivities ( $H_c$ ) for  $\text{CoFe}_{2-x}\text{Mn}_x\text{O}_4$  powders as a function of compositions calcined at 900 °C for 48 h.

Initially, the moments of magnetic constituent domains are randomly oriented; therefore there is no net magnetization. After that, the external magnetic field ( $H$ ) was applied through the samples. The domains were oriented in favorite directions to the applied field. The external applied field continuously increased the magnetic field strength. Then, saturated magnetizations were achieved when the domain rotated to the same direction with the applied field. The results showed that the saturated magnetization values for  $x = 0.10 - 0.25$  were higher than pure cobalt ferrite, because the octahedral site preference energy of  $\text{Mn}^{3+}$  ion (1.10 eV) was higher than  $\text{Co}^{2+}$  ion (0.09 eV). When the Mn cations were doped in the structure, the concentration of  $\text{Co}^{2+}$  ions in octahedral sites decreased. The net magnetization was the result of an unequal magnetic dipole moment in the tetrahedral and octahedral site. In this context,  $\text{Mn}^{3+}$  had  $4 \mu_B$  and  $\text{Co}^{2+}$   $3 \mu_B$  as its magnetic dipole moments, as when Mn content increased, saturated magnetization was also seen to increase. A further increase in doping levels;  $x = 1.00 - 1.10$ , greatly decreased saturated magnetization. This may be due to the  $\text{Mn}^{3+}$  ion in the octahedral site increasing, then the concentration of  $\text{Fe}^{3+}$  ions in this site decreased, since the octahedral site preference energy of  $\text{Mn}^{3+}$  ion (1.10 eV) was higher than  $\text{Fe}^{3+}$  ion (0.00 eV). Furthermore, the magnetic moment of  $\text{Mn}^{3+}$  cations were fixed at  $4 \mu_B$  while the magnetic dipole moments for  $\text{Fe}^{3+}$  were taken to be  $5 \mu_B$ , the  $\text{Mn}^{3+}$  ions had a smaller magnetic moment as compared to the  $\text{Fe}^{3+}$  ions. So, the saturated magnetizations were found to decrease with increasing  $\text{Mn}^{3+}$  doping. Also, the saturated magnetization values in the  $x = 1.00$  composition were greatly different from the sample of  $x = 0.25$ , therefore, the concentration of Mn doping in the structure was extremely different. The magnetization results accorded to the O. Caltun *et al.* research [5]. In the O. Caltun research, the saturated magnetization increased when  $x$

This material is reserved for educational use only, not allowed for commercial use.

= 0 - 0.4, and then decreased where  $x = 0.6$ . However, the O. Caltun research explained that the various saturated magnetization depended on the cation distribution in the spinel structure. The magnetization values of samples when  $x = 0.3$  and  $0.4$  had high values due to the small number of  $Mn^{2+}$  cations being in the middle of  $Mn^{3+}$  cations in the B site. The Bohr magneton of  $Mn^{2+}$  cations ( $5 \mu_B$ ) were higher than  $Mn^{3+}$  ions ( $4 \mu_B$ ), so the saturated magnetizations were increased. And, regarding the sample when  $x = 0.6$ , the magnetization decreased because the strength of exchange interactions decreased.

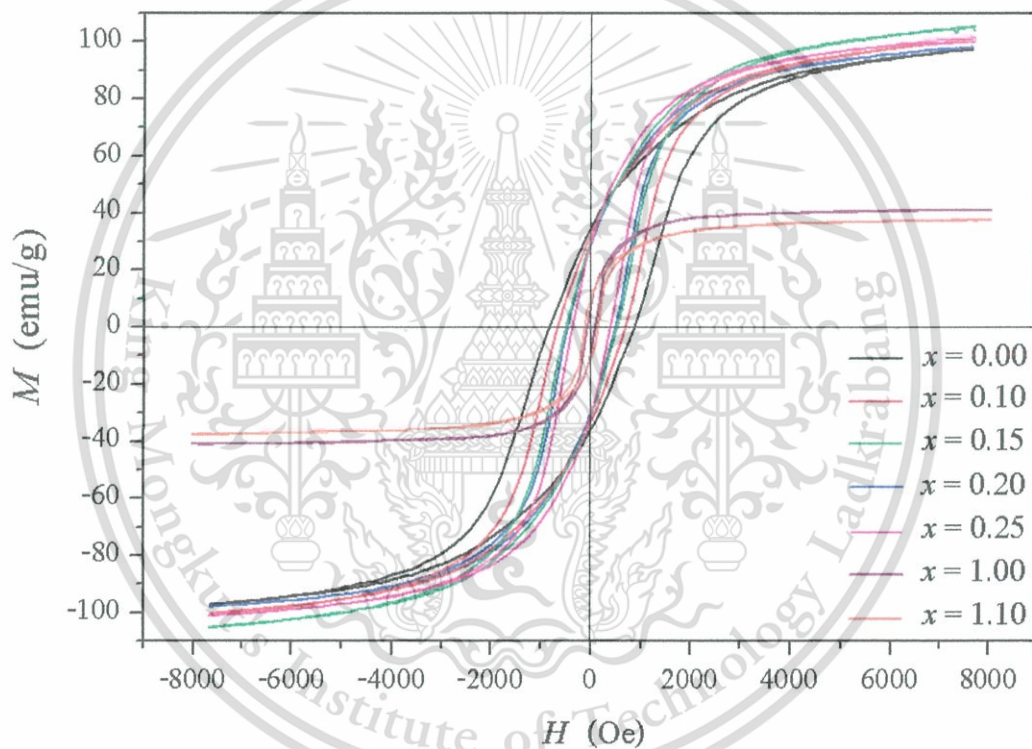
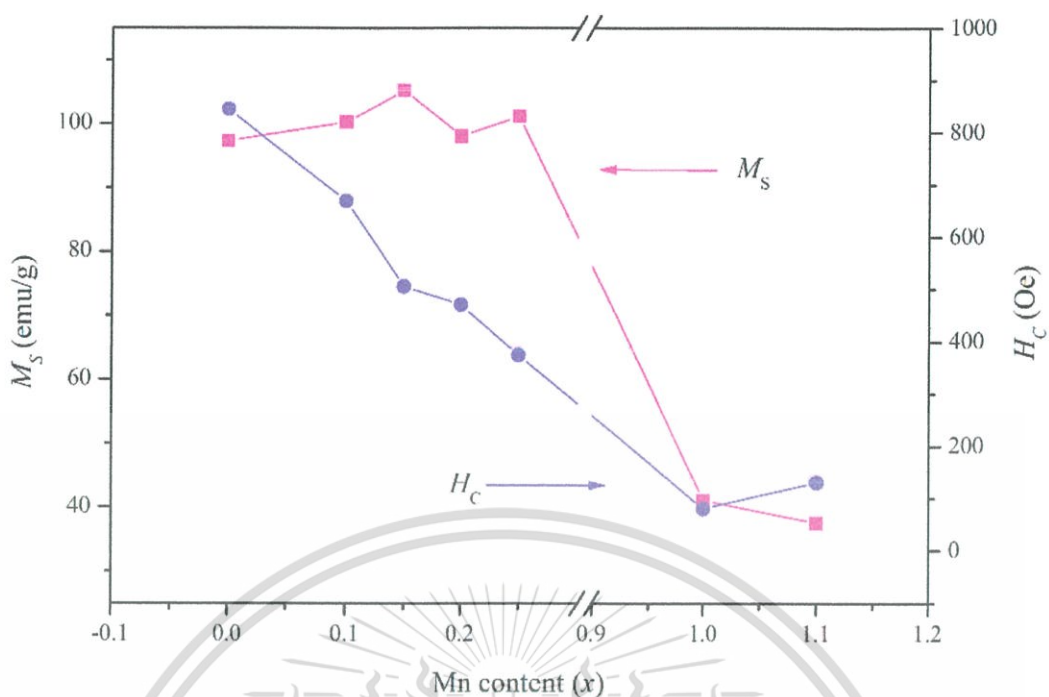


Figure 4.4 The magnetic hysteresis loop of  $CoFe_{2-x}Mn_xO_4$  powders as a function of compositions calcined at  $900\text{ }^\circ\text{C}$  for 48 h.



**Figure 4.5** Variations of saturated magnetization and coercivities for  $\text{CoFe}_{2-x}\text{Mn}_x\text{O}_4$  powders as a function of compositions calcined at  $900\text{ }^\circ\text{C}$  for 48 h.

Furthermore, the coercivity trend of the samples decreased significantly when increasing the Mn substitution because the anisotropy constant of the Co ions were higher than the Mn cations. Magnetic anisotropy strongly affected the shape of the hysteresis loops and controlled the coercivity. Presence of anisotropy led to both easy and hard directions of magnetization. In easy directions, it was easier to magnetize the material when compared to the hard directions. For each of these materials, there was one crystallographic direction in which magnetization was easiest; saturation magnetization was achieved at the lowest external applied field. This was termed as the direction of easy magnetization. The easy axis of cobalt magnetization lied in the [100] direction, and its anisotropy energy was very large compared with other ferrites, such as Mn ferrite. The easy direction of Mn ferrite lied in [111]. Conversely, a hard crystallographic direction was the direction in which saturation magnetization was the most difficult. Hard directions of Co and Mn were [111] and [100], respectively. Figure 4.6 shows the hysteresis loops of a strongly anisotropic magnet with a field applied along the easy and hard directions [6-8]. In the easy axis there was a hard magnetic

hysteresis loop, while the hard axis displayed a slim hysteresis loop. Therefore, substitution by Mn atoms with hard directions [100] and lower anisotropy induces a reduction in coercive fields. The coercive field trend corresponded to Y. Köseoğlu *et al.* research [1]. In Y. Köseoğlu research, the coercivity tended to decrease with increasing Mn content due to  $\text{MnFe}_2\text{O}_4$  being a soft ferrite which had almost no coercivity, and  $\text{CoFe}_2\text{O}_4$  - a hard ferrite - showed large coercivity.

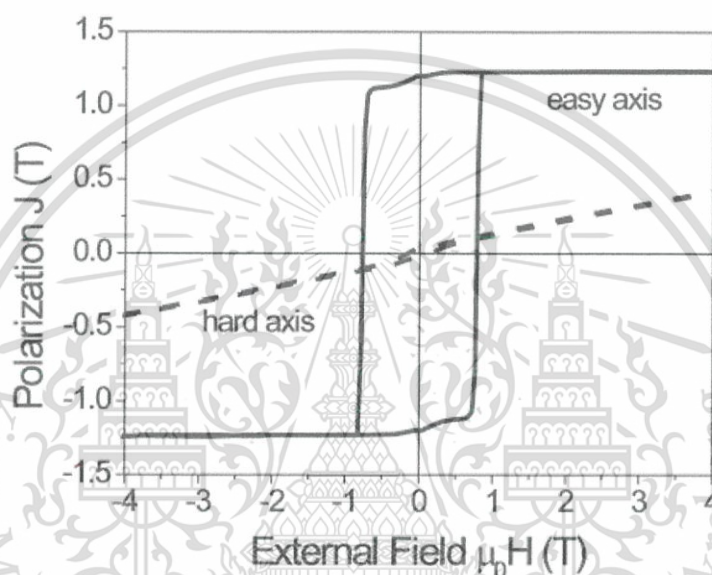


Figure 4.6 Magnetic hysteresis loop of a magnet measured with field applied along the easy and hard axis [8].

**Table 4.2** Magnetic properties and Bohr magneton of  $\text{CoFe}_{2-x}\text{Mn}_x\text{O}_4$  powders calcined at 900 °C for 48 h.

$x$	$M_s$ (emu/g)	$H_c$ (Oe)	Bohr magneton
0.00	97.3	844.1	36
0.10	100.3	668.9	47
0.15	105.2	505.3	47
0.20	98.0	470.2	46
0.25	101.2	373.9	46
1.00	41.1	79.8	28
1.10	37.5	130.4	27

Figure 4.7 shows the variations of saturated magnetization from experimental and Bohr magneton for  $\text{CoFe}_{2-x}\text{Mn}_x\text{O}_4$  powders as a function of compositions calcined at 900 °C for 48 h. And, the Bohr magneton from calculation presented in Table 4.2. The saturated magnetization results were obtained from experiments, while Bohr magneton was calculated from the model at various compositions. The results showed that the saturated magnetization slightly increased after doped Mn in the  $\text{CoFe}_2\text{O}_4$ , when  $x = 0.00-0.25$  and the maximum saturated magnetization was obtained where  $x = 0.15$ . Then, the sample when  $x = 1.00-1.10$  presented extremely decreasing values of saturated magnetization. The Bohr magneton calculation showed that the saturated magnetization increased with increasing Mn concentration, where  $x = 0.00-0.25$ , the highest saturated magnetization was shown at  $x = 0.10$ . After increasing Mn doping, when  $x = 1.00-1.10$ , the saturated magnetizations were decreased. The trend of saturated magnetization of the experiment and the calculation corresponded. After

Mn doping, where  $x = 0.00-0.25$ , the trend of saturated magnetization slightly increased and then extremely decreased when  $x = 1.00-1.10$ .

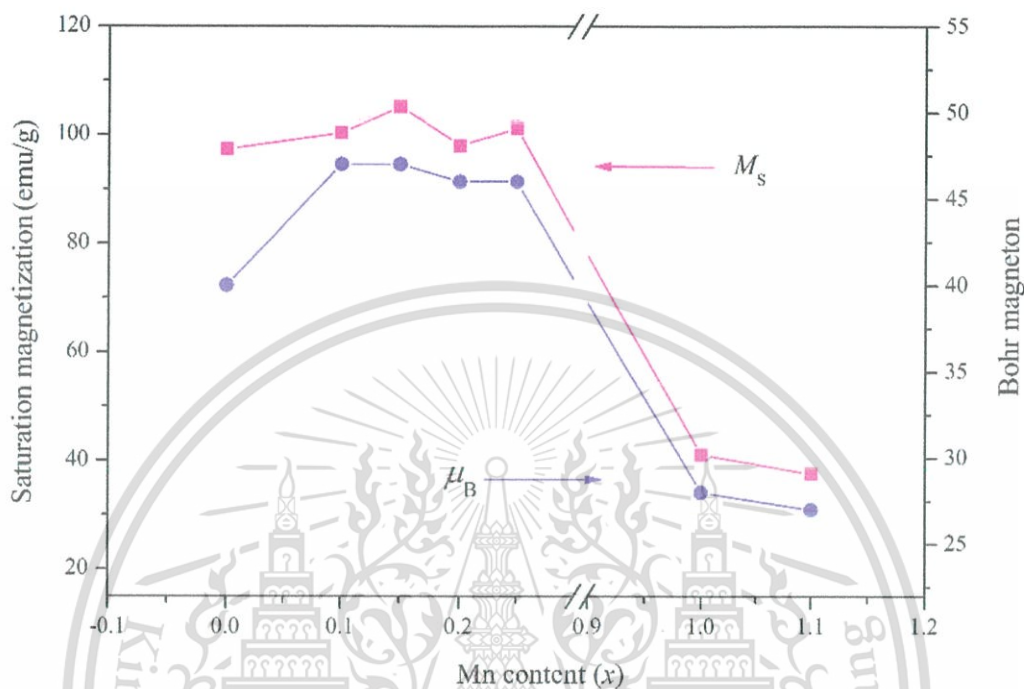


Figure 4.7 Variations of saturated magnetization and Bohr magneton for  $\text{CoFe}_{2-x}\text{Mn}_x\text{O}_4$  powders as a function of compositions calcined at  $900\text{ }^\circ\text{C}$  for 48 h.

Table 4.3 shows the variations of cation distribution in the A and B sites, and Bohr magneton calculated data for  $\text{CoFe}_{2-x}\text{Mn}_x\text{O}_4$  powders as a function of compositions calcined at  $900\text{ }^\circ\text{C}$  for 48 h. The cation distribution in A and B sites were received by modeling a method using the Vesta and Artemis program. Also, the Bohr magneton in a unit cell was calculated from cations in A and B sites and unpaired electrons of each cation. Then, the Bohr magnetons of all samples were compared with the saturated magnetization from an experiment by VSM technique.

**Table 4.3** Cation distribution and Bohr magneton result of  $\text{CoFe}_{2-x}\text{Mn}_x\text{O}_4$  powders calcined at 900 °C for 48 h.

x	Co cation		Fe cation		Mn cation		Bohr magneton
	A site	B site	A site	B site	A site	B site	
0.00	3	5	5	11	0	0	36
0.10	6	2	2	13	0	1	47
0.15	6	2	2	13	0	1	47
0.20	6	2	2	12	0	2	46
0.25	6	2	2	12	0	2	46
1.00	3	5	5	3	0	8	28
1.10	3	5	5	2	0	9	27

From the results, it can explain that when  $x = 0.00-0.25$  Mn doping on the cobalt ferrite structure, the Mn cations preferred to occupy the B site. The occupation of Co were displayed in both the A and B sites, where Co tended to occupy more on site A than site B. And, Fe cations were in both the A and B site, where Fe cations occupied on B site more than the A site. After doped Mn, when  $x = 1.00-1.10$ , Mn strongly occupied in B site due to Mn (1.10 eV) being higher than the octahedral site preference energy than Co (0.09 eV) and Fe (0.00 eV). Co and Fe cations migrated to B site and A site, respectively. This affected the saturated magnetization, increasing when slightly doped, and decreasing after extreme doping.

### 4.1.1.3 Cation Distribution

Afterwards, the calcination powders were examined by X-ray absorption spectroscopy (XAS). EXAFS investigation determined the local bonding surrounding the Co, Fe and Mn. Spectra that encompassed the Co (7709 eV), Fe (7112 eV) and Mn (6539 eV) K-edges over an energy range from 100 eV below the energy edge to 800 eV above it. The information was examined by following standard EXAFS processing, which led to the Fourier transformation (FT) of information to radial coordinates. In this form, peak amplitudes reflected the occupancy of atomic shells, and the radial coordinate of the peak reflected the distance of atom shells from the absorbed, which was not corrected for natural electron phase shift to XAS. [9]. Figure 4.6 shows the FT of Co, Fe, and Mn EXAFS data for the  $\text{CoFe}_{2-x}\text{Mn}_x\text{O}_4$  powders calcined at 900 °C for 48 h. The FT from a  $\Delta K$  range of between 2 and 10  $\text{\AA}^{-1}$ , with  $k^2$  weighting of the  $\text{CoFe}_{2-x}\text{Mn}_x\text{O}_4$  Co EXAFS spectra, is shown as a function of distance in Figure 4.6 (a). This fact could be seen better when noticing the two maximum intense peaks. The first one centered near 1.5  $\text{\AA}$  presented the first shell with oxygen around the Co atoms. The second one centered near 2.8  $\text{\AA}$ , which corresponded to the next shell neighboring the Co atoms. The second peak of the  $\text{CoFe}_{2-x}\text{Mn}_x\text{O}_4$  powders showed splitting; the peak centered near  $r$  about 2.6  $\text{\AA}$  corresponded to the Co-Co distance. This unique fingerprint identified the absorbing ion occupying the octahedral (B) sites, due to both scattering and absorbing atom occupancy on octahedral site contributions. The peak centered near 3.1  $\text{\AA}$  absorbed the tetrahedral (A) sub-lattice, including contributions from  $\text{Co}_A\text{-M}_A$ ,  $\text{Co}_A\text{-O}$ ,  $\text{Co}_A\text{-M}_B$ , and  $\text{Co}_B\text{-O}$  correlations ( $M$  is metal), but the identification was not unique. Therefore, related amplitudes of these peaks indicated qualitative distribution of the absorption cations at the B and A sites [9-11]. Before doping Mn in the cobalt ferrite [Figure 4.6 (a)], the second peak showed splitting, these peaks are not symmetrical. The amplitude of the peak at about 2.6  $\text{\AA}$  was higher than the peak amplitude at about 3.1  $\text{\AA}$ . This showed that the Co cations preferred to occupy in B site more than the A site. After doping Mn in the structure, where  $x = 0.10 - 1.10$ , the amplitude trend of the peak at about 2.6  $\text{\AA}$  decreased. And, the trend of the peak at about 3.1  $\text{\AA}$  increased, being approximately equal when  $x = 1.10$ . This can be explained; after doping Mn cations, Co ions migrated from B site to A site due to the influence of Mn doping and the excess Mn content in the structure, since Mn cations had 1.10 eV. This material is reserved for educational use only, not allowed for commercial use.

octahedral site preference energy, which was larger than Co cations (0.09 eV). When doping Mn in the cobalt ferrite, Mn ions preferred to occupy in B site, then Co cations were migrated to A site.

Figure 4.6 (b) shows the FT of Fe EXAFS data for the  $\text{CoFe}_{2-x}\text{Mn}_x\text{O}_4$  powders when  $x = 0.00 - 1.10$  calcined at 900 °C for 48 h. The Fe EXAFS spectra of the  $\text{CoFe}_2\text{O}_4$  sample showed splitting in the second peak. This peak was not perfectly symmetrical, and enlargement of the region between 2.6 Å indicated that Fe ions were localized at the B site more than the A site. The amplitude trend of Fe ion distribution after Mn doped, where  $x = 0.10 - 1.10$ , the peak at about 2.6 Å slightly decreased and the amplitude peak at about 3.1 Å increased. This can be explained as the Mn cations preferring to occupy in the B site, then Fe cations were moved to the A site. Due to the octahedral site preference, energy of Mn ions (1.10 eV) was larger than Fe cations (0.00 eV).

Also, Mn EXAFS data were shown in Figure 4.6 (c) as a function of the radial coordinate. An investigation of the  $\text{CoFe}_{2-x}\text{Mn}_x\text{O}_4$  sample where  $x = 0.00 - 1.10$  showed the enlargement of the region between 2.6 Å, a peak did not appear at around 3.1 Å, this indicated that Mn ions were occupied only at the B site. Because Mn cations were very high the octahedral site preference energy (1.10 eV). So, when doping Mn in the cobalt ferrite, Mn cations strongly preferred to occupy only in the B site. This affected Co and Fe cations migration to A site after increasing Mn concentrations. From the EXAFS results, the amplitude trend of Co, Fe, and Mn EXAFS spectra showed the occupation trend of cations in the A and B sites and accorded with the Bohr magneton results from the calculation in Table 4.3. After doping Mn in the structure, Mn cations strongly preferred to occupy in only the B site. The Bohr magneton results accorded with the saturated magnetization value from the experiment.

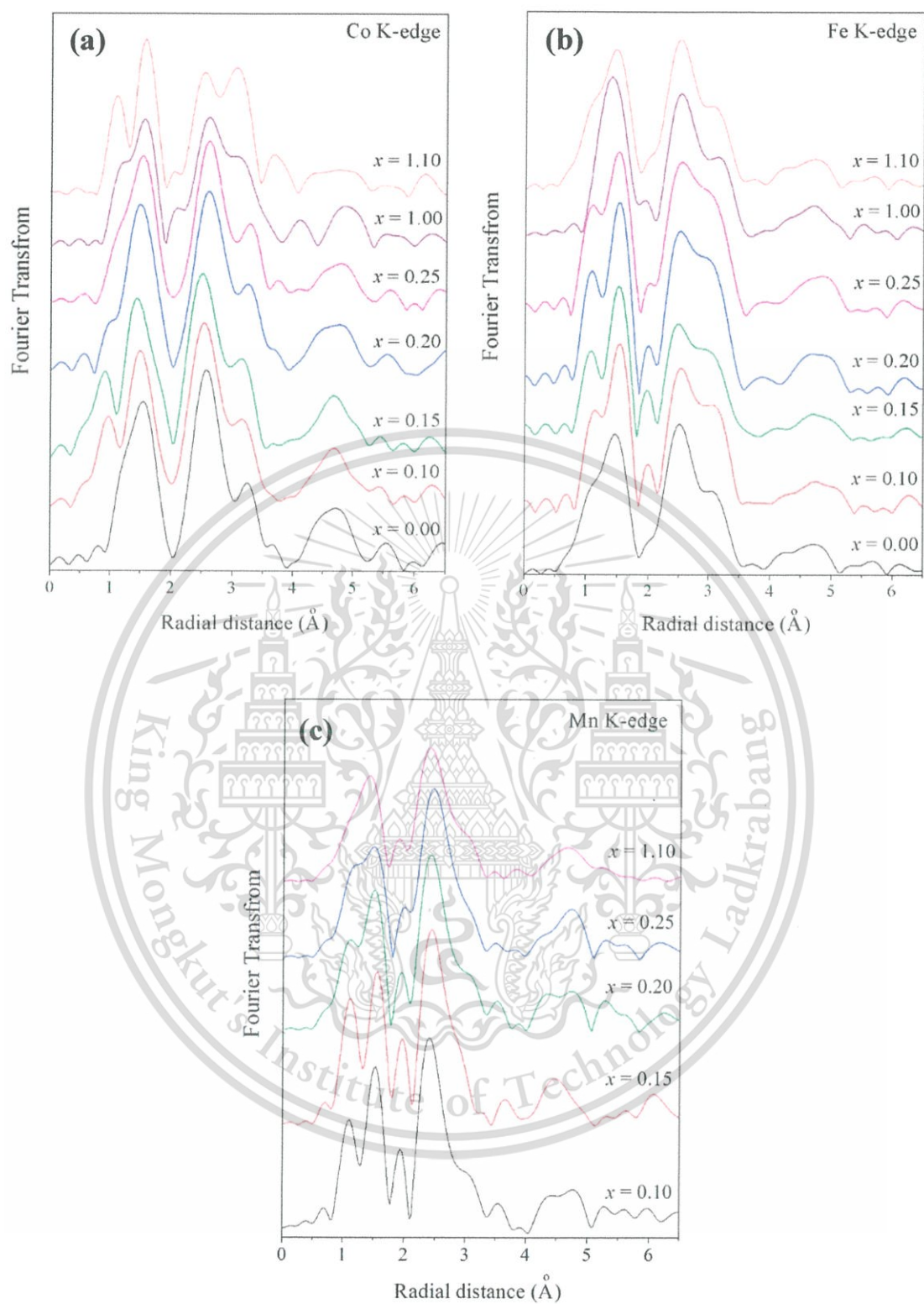
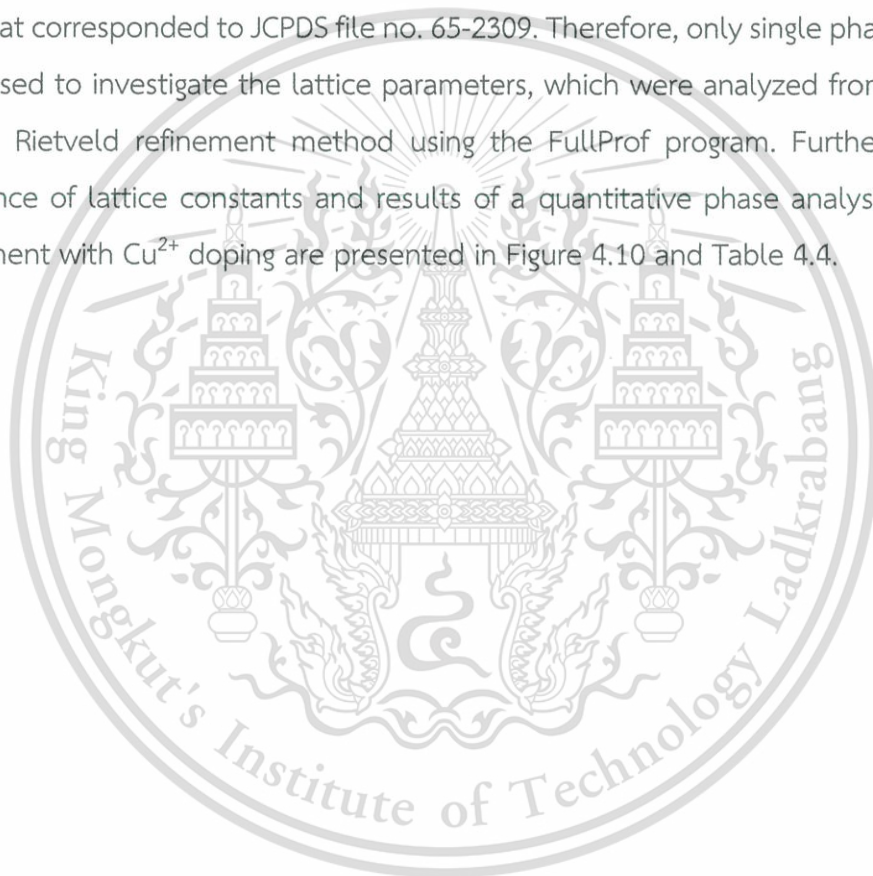


Figure 4.8 The FT of (a) Co, (b) Fe, and (c) Mn EXAFS data for the  $\text{CoFe}_{2-x}\text{Mn}_x\text{O}_4$  powders calcined at  $900\text{ }^\circ\text{C}$  for 48 h.

## 4.1.2 CoFe<sub>2-x</sub>Cu<sub>x</sub>O<sub>4</sub> System

### 4.1.2.1 Phase Formation

Figure 4.9 shows the X-ray diffraction of CoFe<sub>2-x</sub>Cu<sub>x</sub>O<sub>4</sub> powders at various compositions and calcined at 900 °C for 48 h. The XRD patterns showed that peaks (when  $x = 0.00-0.25$ ) were of a single phase cubic structure, and corresponded to JCPDS file no. 22-1086 and space group Fd3m (no. 227) [1]. However, the XRD pattern of the CoFe<sub>2-x</sub>Cu<sub>x</sub>O<sub>4</sub> powder, where  $x = 0.30$  and  $0.35$  detected secondary phases, which were CuO that corresponded to JCPDS file no. 65-2309. Therefore, only single phase samples were used to investigate the lattice parameters, which were analyzed from XRD data by the Rietveld refinement method using the FullProf program. Furthermore, the difference of lattice constants and results of a quantitative phase analysis from the refinement with Cu<sup>2+</sup> doping are presented in Figure 4.10 and Table 4.4.



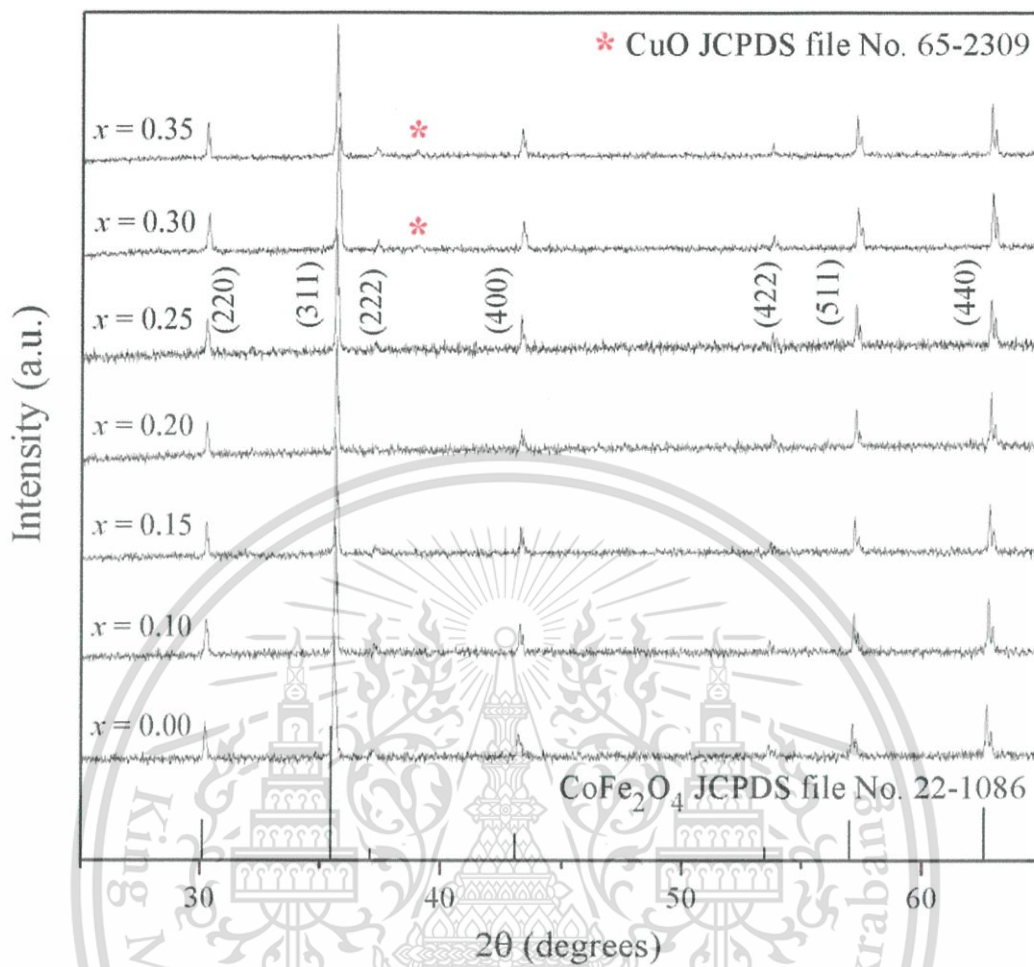


Figure 4.9 X-ray diffraction of  $\text{CoFe}_{2-x}\text{Cu}_x\text{O}_4$  powders calcined at 900 °C for 48 h.

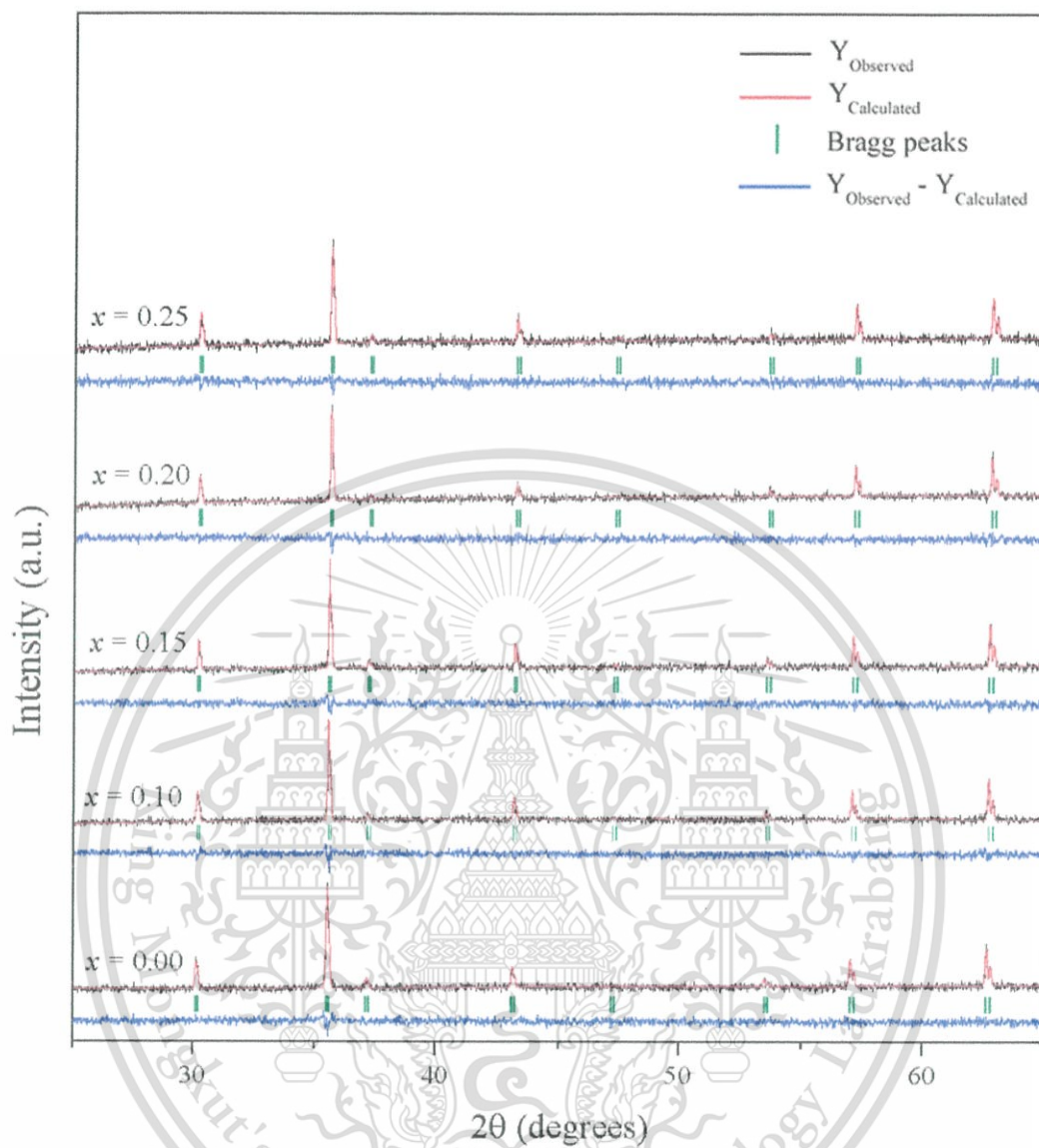


Figure 4.10 X-ray diffraction patterns and the structure refinement of  $\text{CoFe}_{2-x}\text{Cu}_x\text{O}_4$  powders calcined at 900 °C for 48 h.

The structure refinement showed the corresponding fits and confirmed that the structure was of the cubic type. Data quality of structural refinement was checked basically by R-values ( $R_w$ ) and a good fit ( $\chi^2$ ). In addition, the distinction between XRD patterns, calculated data and experimental profiles displayed a small value in the intensity scale, as illustrated by the line,  $Y_{\text{Observed}} - Y_{\text{Calculated}}$  [2]. Furthermore, the lattice constant trend of  $\text{CoFe}_{2-x}\text{Cu}_x\text{O}_4$  powders calcined at 900 °C for 48 h are shown in Figure 4.11. The results exhibited that the lattice constant for each composition decreased with increasing Cu content. The lattice parameter decreased with doping, due to the ionic radius of Cu (0.57 Å) coordinating four-fold with  $\text{O}^{2-}$  ions, which were smaller than the ionic radius of Fe (0.645 Å) coordinating six-fold with  $\text{O}^{2-}$  ions in the structure [3].

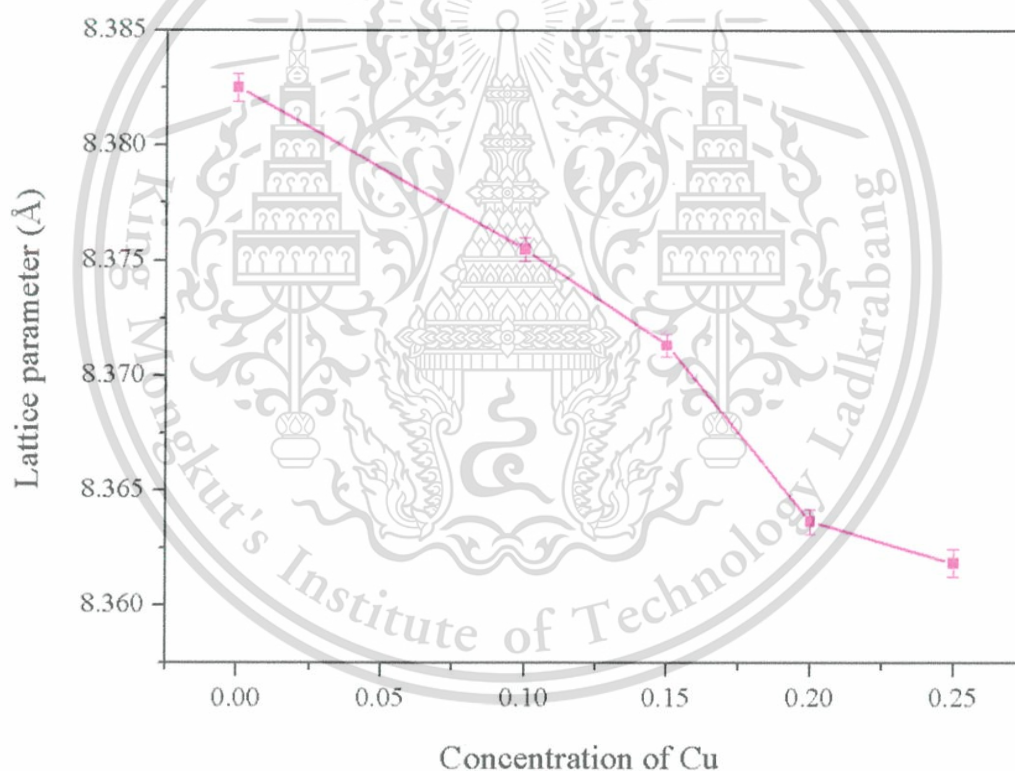


Figure 4.11 Lattice constant of  $\text{CoFe}_{2-x}\text{Cu}_x\text{O}_4$  powders calcined at 900 °C for 48 h.

**Table 4.4** Lattice constant ( $a$ ) and Rietveld refinement result of  $\text{CoFe}_{2-x}\text{Cu}_x\text{O}_4$  powders calcined at 900 °C for 48 h.

$x$	$a$ (Å)	$V$ ( $10^6 \text{ pm}^3$ )	$R_w$ (%)	$\chi^2$
0.00	8.3825 (6)	589.010	4.01	1.11
0.10	8.3755 (5)	590.261	4.07	1.10
0.15	8.3713 (5)	590.508	4.20	1.08
0.20	8.3637 (5)	590.674	4.57	1.11
0.25	8.3619 (6)	591.317	4.45	1.08

#### 4.1.2.2 Magnetic Properties

Figure 4.12 shows the magnetic hysteresis loop of  $\text{CoFe}_{2-x}\text{Cu}_x\text{O}_4$  powders as a function of compositions calcined at 900 °C for 48 h, and a maximum applied field of up to 8 kOe at room temperature. Basically, the magnetization curves of all samples were nonlinear and typically ferrimagnetic materials [4]. Figure 4.13 and Table 4.5 present the variations of saturated magnetization ( $M_s$ ) and coercivities ( $H_c$ ) for  $\text{CoFe}_{2-x}\text{Cu}_x\text{O}_4$  powders as a function of compositions calcined at 900 °C for 48 h. The results showed that the saturated magnetization greatly decreased with Cu content, since the Cu ions have  $1 \mu_B$ , which is less than  $5 \mu_B$  of Fe ions. Therefore, when doping Cu in cobalt ferrite, it affected the saturated magnetization. The results accorded to M. Hashim *et al.* [12] research. In M. Hashim's research, it was observed that the saturated magnetization decreased with increasing the Cu cations concentration. This behavior can be explained as the net magnetic moment of  $\text{Cu}^{2+}$  ions being  $1 \mu_B$ , the magnetic moment of  $\text{Cu}^{2+}$  cations were less than  $\text{Fe}^{3+}$  and  $\text{Co}^{2+}$  cations, so the saturated magnetization was found to decrease with  $\text{Cu}^{2+}$  doping. Furthermore, the coercivity trend of the samples decreased significantly when increasing the Cu substitution, This material is reserved for educational use only, not allowed for commercial use.

because the anisotropy constant of the Co ion were higher than the Cu cations. Due to the easy axis of cobalt magnetization lying in the [100] direction, and its anisotropy energy being very large compared with other ferrites, the easy direction of Cu ferrite lied in [111]. Conversely, hard directions of Co and Cu were [111] and [100], respectively [6-8]. Therefore, substitution by hard direction cation in the structure with a lower anisotropy constant induced a decrease in coercive fields according to S. Y. An *et al.* [13]. The result showed that the decreasing of the saturated magnetization and coercivity were the effect of doping Cu cations and different compositions on magnetic properties.

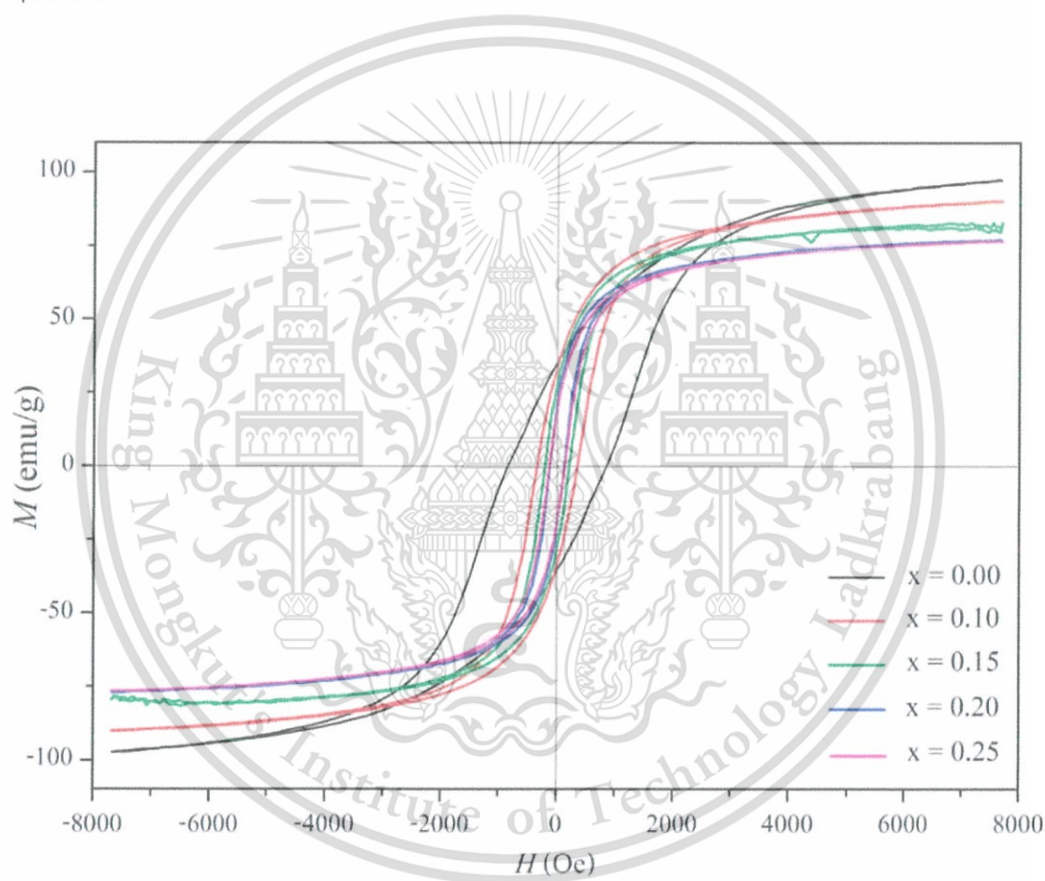


**Figure 4.12** The magnetic hysteresis loop of  $\text{CoFe}_{2-x}\text{Cu}_x\text{O}_4$  powders as a function of compositions calcined at 900 °C for 48 h.

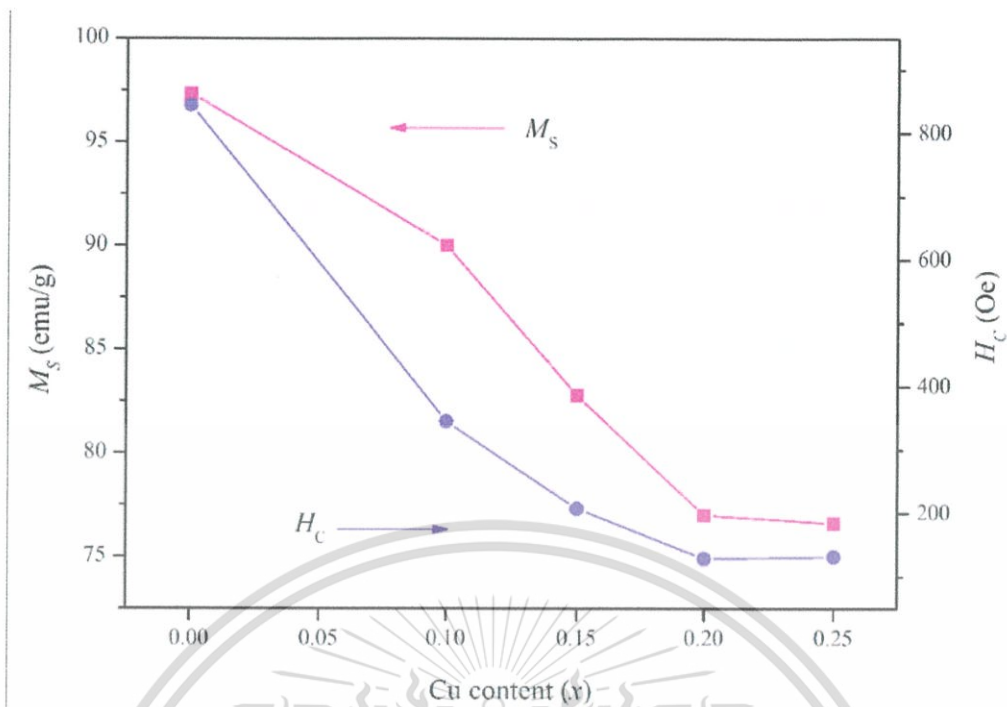


Figure 4.13 Variations of saturated magnetization and coercivities for  $\text{CoFe}_{2-x}\text{Cu}_x\text{O}_4$  powders as a function of compositions calcined at  $900\text{ }^\circ\text{C}$  for 48 h.

Table 4.5 Magnetic properties and Bohr magneton of  $\text{CoFe}_{2-x}\text{Cu}_x\text{O}_4$  powders calcined at  $900\text{ }^\circ\text{C}$  for 48 h.

$X$	$M_s$ (emu/g)	$H_c$ (Oe)	Bohr magneton
0.00	97.3	844.1	36
0.10	90.0	344.7	28
0.15	82.8	207.3	28
0.20	77.0	128.5	24
0.25	76.6	131.4	24

The Bohr magneton calculated data and cation distribution on the A and B sites of  $\text{CoFe}_{2-x}\text{Cu}_x\text{O}_4$  powders are present in Table 4.6. In addition, Figure 4.14 displays variations of saturated magnetization and Bohr magneton for  $\text{CoFe}_{2-x}\text{Cu}_x\text{O}_4$  powders as a function of compositions calcined at 900 °C for 48 h. From the results, after Cu doped  $\text{CoFe}_2\text{O}_4$ , the saturated magnetization decreased, corresponding with the Bohr magneton data due to unpaired electrons of Cu cations ( $1 \mu_B$ ) being smaller than Co ( $3 \mu_B$ ) and Fe ions ( $5 \mu_B$ ). Furthermore, the Cu cations preferred to occupy only the B site after doping Cu in cobalt ferrite of all compositions according with the octahedral site preference energy (OSPE). Meanwhile, Co and Fe cations occupied both the A and B sites due to there were smaller the octahedral site preference energy than Cu ions. The octahedral site preference energy of Cu cations were 0.68 eV and Co and Fe cations were 0.09 and 0.00 eV, respectively.

**Table 4.6** Cation distribution and Bohr magneton result of  $\text{CoFe}_{2-x}\text{Cu}_x\text{O}_4$  powders calcined at 900 °C for 48 h.

x	Co cation		Fe cation		Cu cation		Bohr magneton
	A site	B site	A site	B site	A site	B site	
0.00	3	5	5	11	0	0	36
0.10	2	6	6	9	0	1	28
0.15	2	6	6	9	0	1	28
0.20	2	6	6	8	0	2	24
0.25	2	6	6	8	0	2	24

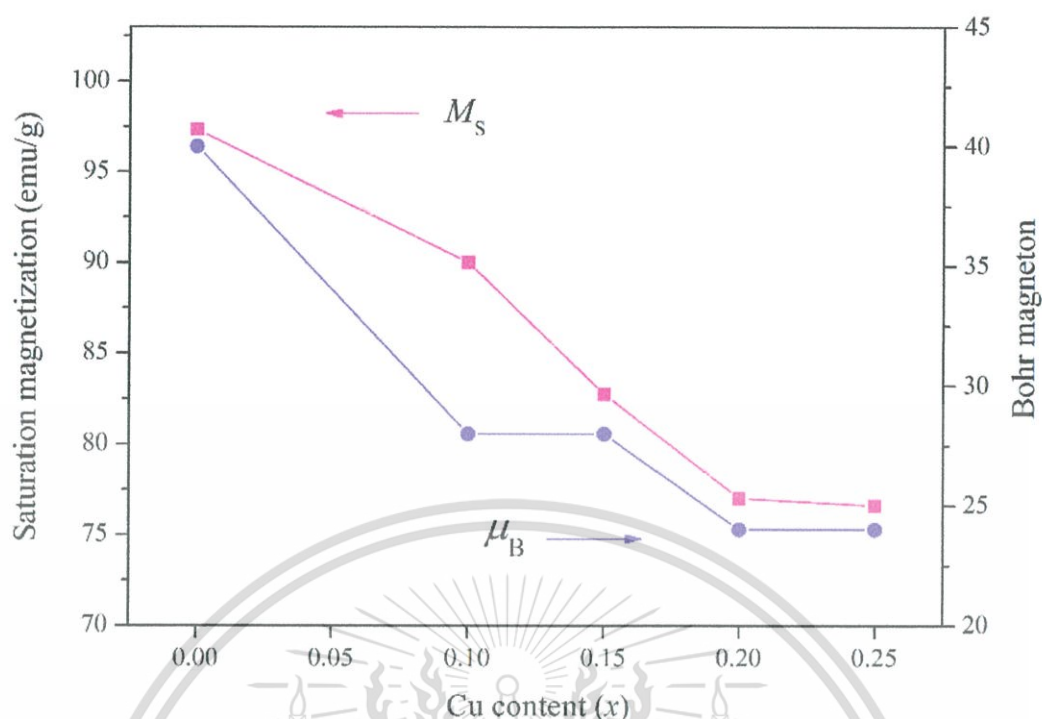


Figure 4.14 Trend of saturated magnetization and Bohr magneton for  $\text{CoFe}_{2-x}\text{Cu}_x\text{O}_4$  powders calcined at  $900\text{ }^\circ\text{C}$  for 48 h.

#### 4.1.2.3 Cation Distribution

Afterwards, the calcination powders were examined by X-ray absorption spectroscopy (XAS). EXAFS investigation determined the local bonding environment of the Cu, Co and Fe. Spectra that encompassed the Co (7709 eV), Fe (7112 eV) and Cu (8979 eV) K-edges. Figure 4.15 shows the FT of Cu, Co, and Fe EXAFS data for the  $\text{CoFe}_{2-x}\text{Cu}_x\text{O}_4$  powders calcined at  $900\text{ }^\circ\text{C}$  for 48 h. The FT from a  $\Delta K$  range of between  $2$  and  $10\text{ \AA}^{-1}$ , with  $k^2$  weighing of the  $\text{CoFe}_{2-x}\text{Cu}_x\text{O}_4$  Co EXAFS spectra, this is shown as a function of distance in Figure 4.15 (a). Investigation of the  $\text{CoFe}_{2-x}\text{Cu}_x\text{O}_4$  sample, where  $x = 0.00 - 0.25$ , shows splitting in the second peak, these peaks are not symmetrical. The peaks at about  $2.6\text{ \AA}$  were higher than the peaks at around  $3.1\text{ \AA}$ . This can be described as the Co ions occupying at the B site more than the A site.

Also, Fe EXAFS data are shown in Figure 4.15 (b) as a function of the radial coordinate. The Fe EXAFS spectra of the  $\text{CoFe}_2\text{O}_4$  sample showed splitting in the second peak. This peak was not perfectly symmetrical, and enlargement of the region. This material is reserved for educational use only, not allowed for commercial use.

at about 2.6 Å indicated that Fe ions were localized at the B site more than the A site. The amplitude trend of peak at about 2.6 Å slightly decreased after doping the Cu content. This can be explained as that after the doping Cu cations, the Fe cations migrated to the A site due to Cu cations preferring to occupy in the B site since, Cu cations (0.68 eV) were larger the octahedral site preference energy than Fe cations (0.00 eV).

Figure 4.15 (c) shows the FT of Fe EXAFS data for the  $\text{CoFe}_{2-x}\text{Cu}_x\text{O}_4$  powders, where  $x = 0.10 - 0.25$ , calcined at 900 °C for 48 h. The results showed the large peaks at about 2.6 Å and very small peaks at about 3.1 Å. This can be indicated that Cu ions occupied only at the B site of all compositions. Because of the octahedral site preference energy of Cu cations being higher than Co (0.09 eV) and Fe cations (0.00 eV). Therefore, when doping Cu cations in the structure, Cu cations strongly preferred to occupy in site B only, then Fe cations were migrated from the B site to the A site. Meanwhile, Co cation occupied both B and A sites. These EXAFS results corresponded with the cation distribution in A and B sites from calculation data (Table 4.6). Furthermore, the Bohr magneton of calculation data related to the magnetic properties of the samples.

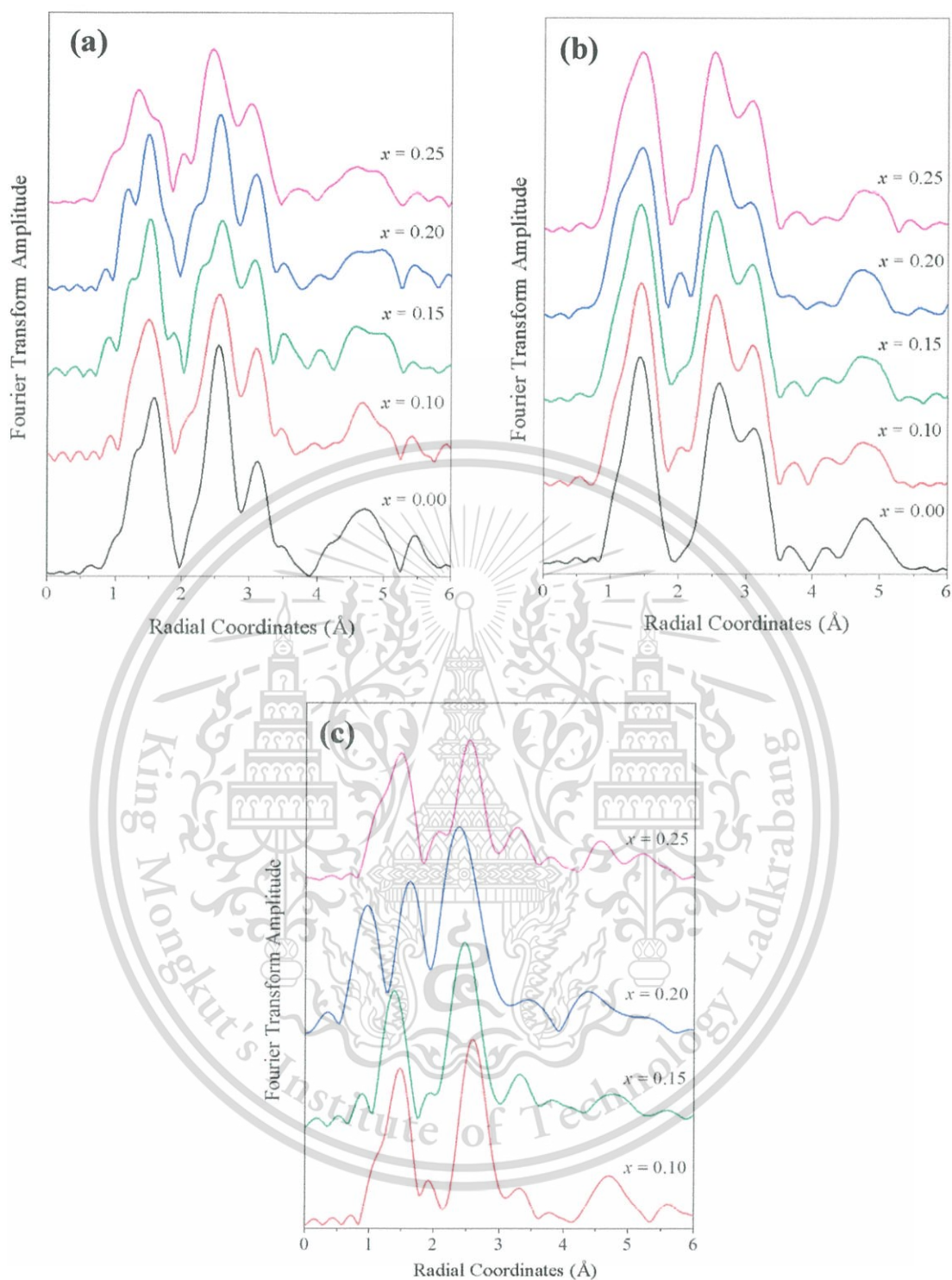


**Figure 4.15** The FT of (a) Co, (b) Fe, and (c) Cu EXAFS data for the  $\text{CoFe}_{2-x}\text{Cu}_x\text{O}_4$  powders calcined at 900 °C for 48 h.

#### 4.1.2.4 Oxidation State

After that, the oxidation state of each metal in the structure were confirmed due to the different oxidation states of each cation presenting the number of unpaired electrons, and it affected the saturated magnetization of the materials. Therefore, the oxidation state should be investigated to explain the magnetic properties. The sample and the standard were examined the valence state by XANES spectra using the X-ray absorption spectroscopy (XAS) technique. The XANES spectra for the samples were measured at the Fe K-, Co K- and Cu K-edges at room temperature. As observed, the spectra for all samples were similar at each edge and their shift was not seen. Figure 4.16 (a) shows XANES spectra of  $\text{CoFe}_{1.75}\text{Cu}_{0.25}\text{O}_4$  sample calcination at 900 °C for 48 h in air, Co foil, CoO and  $\text{Co}_3\text{O}_4$  in the vicinity of the Co K-edge. The valence state of Co in the samples was determined from the energy of the main maximal in the spectra ( $E_0$ ) [14]. The value of all samples and the standard are presented in Table 4.7. As observed, the spectra for the samples are similar to those obtained for the CoO standard, in which  $\text{Co}^{2+}$  is coordinated six-fold by  $\text{O}^{2-}$  ions, which suggests that Co ions exist in a divalent state in six coordinated oxygen atoms [15]. The oxidation state results confirmed that the  $\text{Co}^{2+}$  cations had 3  $\mu_B$ , which can explain the magnetic properties. XANES spectra at the Fe K-edge of the sample and standard compounds are show in Figure 4.16 (b) and the  $E_0$  values are exhibited in Table 4.7. The results showed that the threshold energy of  $\text{CoFe}_{1.75}\text{Cu}_{0.25}\text{O}_4$  samples is higher than that of Fe foil, FeO and  $\text{Fe}_3\text{O}_4$ , but close to the energy of  $\text{Fe}_2\text{O}_3$ . They lead to  $\text{Fe}^{3+}$  existing in the samples, where the  $\text{Fe}^{3+}$  cations were 5  $\mu_B$ . Besides, XANES spectra at the Cu K-edge are shown in Figure 4.16 (c). The  $E_0$  of  $\text{CoFe}_{1.75}\text{Cu}_{0.25}\text{O}_4$ , Cu foil,  $\text{Cu}_2\text{O}$  and CuO are shown in Table 4.7. From the threshold region, the curves of samples were close to that of CuO, suggesting existence of the divalent state in octahedral coordination for oxygen atoms [14]. This confirmed that copper in the structure was  $\text{Cu}^{2+}$  cation where it had 2  $\mu_B$ . The oxidation state from the XANES spectra of each cation revealed the number of Bohr magneton, which can explain and correspond with the saturated magnetization.

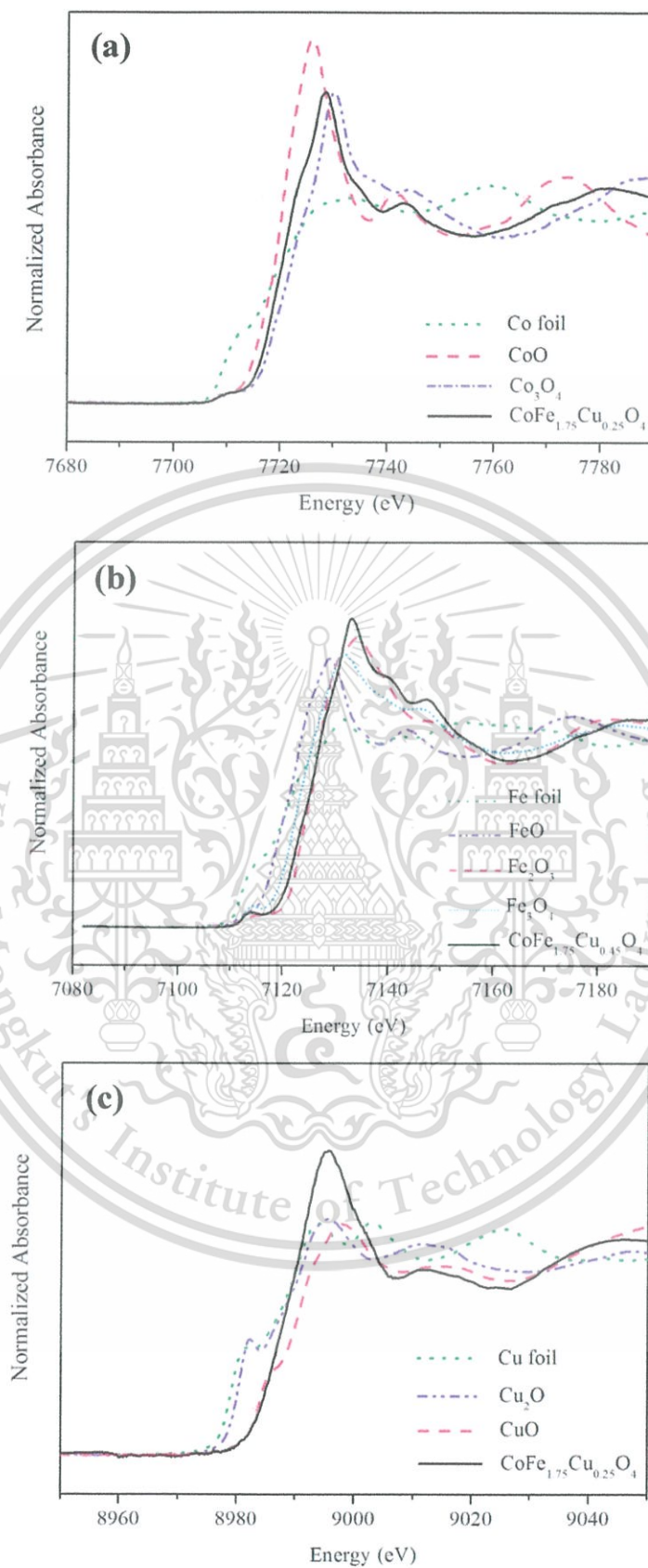


Figure 4.16 XANES spectra of  $\text{CoFe}_{1.75}\text{Cu}_{0.25}\text{O}_4$  samples and the standards obtained at (a) Co K-edge, (b) Fe K-edge and (c) Cu K-edge.

This material is reserved for educational use only, not allowed for commercial use.

Forbidden to modify the content, and cite the document when use.

**Table 4.7** The  $E_0$  value of  $\text{CoFe}_{1.75}\text{Cu}_{0.25}\text{O}_4$  sample calcined at 900 °C for 48 h in air and the various standard.

Sample	$E_0$ (eV)	Sample	$E_0$ (eV)	Sample	$E_0$ (eV)
Co foil	7709.05	Fe foil	7112.01	Cu foil	8979.01
$\text{Co}_3\text{O}_4$	7723.04	FeO	7123.00	$\text{Cu}_2\text{O}$	8980.61
CoO	7720.19	$\text{Fe}_3\text{O}_4$	7125.53	CuO	8983.84
$\text{CoFe}_{1.75}\text{Cu}_{0.25}\text{O}_4$	7720.20	$\text{Fe}_2\text{O}_3$	7127.48	$\text{CoFe}_{1.75}\text{Cu}_{0.25}\text{O}_4$	8983.80
		$\text{CoFe}_{1.75}\text{Cu}_{0.25}\text{O}_4$	7127.45		

#### 4.1.2.5 Catalyst Properties

The  $\text{CoFe}_{2-x}\text{Cu}_x\text{O}_4$  system were not outstanding in magnetic properties, however, the material in this system showed excellent catalyst properties [16]. Therefore, the catalyst properties of this system were characterized. The concentrations of synthetic dyes ( $C/C_0$ ) were detected and determined after the proceeding reactions for 0.5, 1, 2, 4, 6, and 24 h. The degradation percentages were calculated from the decreasing maximum of absorption peak. Figure 4.17 shows the de-colorization of reactive orange 16 ( $50 \text{ mg L}^{-1}$ ) in the  $25 \text{ mg mL}^{-1}$  of  $\text{CoFe}_{2-x}\text{Cu}_x\text{O}_4$  catalysts and  $100 \text{ mM H}_2\text{O}_2$ . The  $C/C_0$  percentages and degradation are displayed in Table 4.8. The results showed that the de-colorization after 24 h of incubation highly decreased the absorption peak and the trend of degradation increased with increasing Cu content, since the  $\text{CuFe}_2\text{O}_4$  were the better efficient catalysts with reactive orange 16 than  $\text{CoFe}_2\text{O}_4$  [16]. Because by the degradation process, the cations in the structure produce hydroxyl radicals  $\cdot\text{OH}$  which is the primary oxidant in the oxidation of organic compounds [17]. The redox potential of Cu (1.90) ions is higher than the redox potential of Co (1.88) cations and Fe (1.83) [18]. Therefore, when Cu was doped in the  $\text{CoFe}_2\text{O}_4$ , the degradation percentages were found to increase with Cu concentration. This material is reserved for educational use only, not allowed for commercial use.

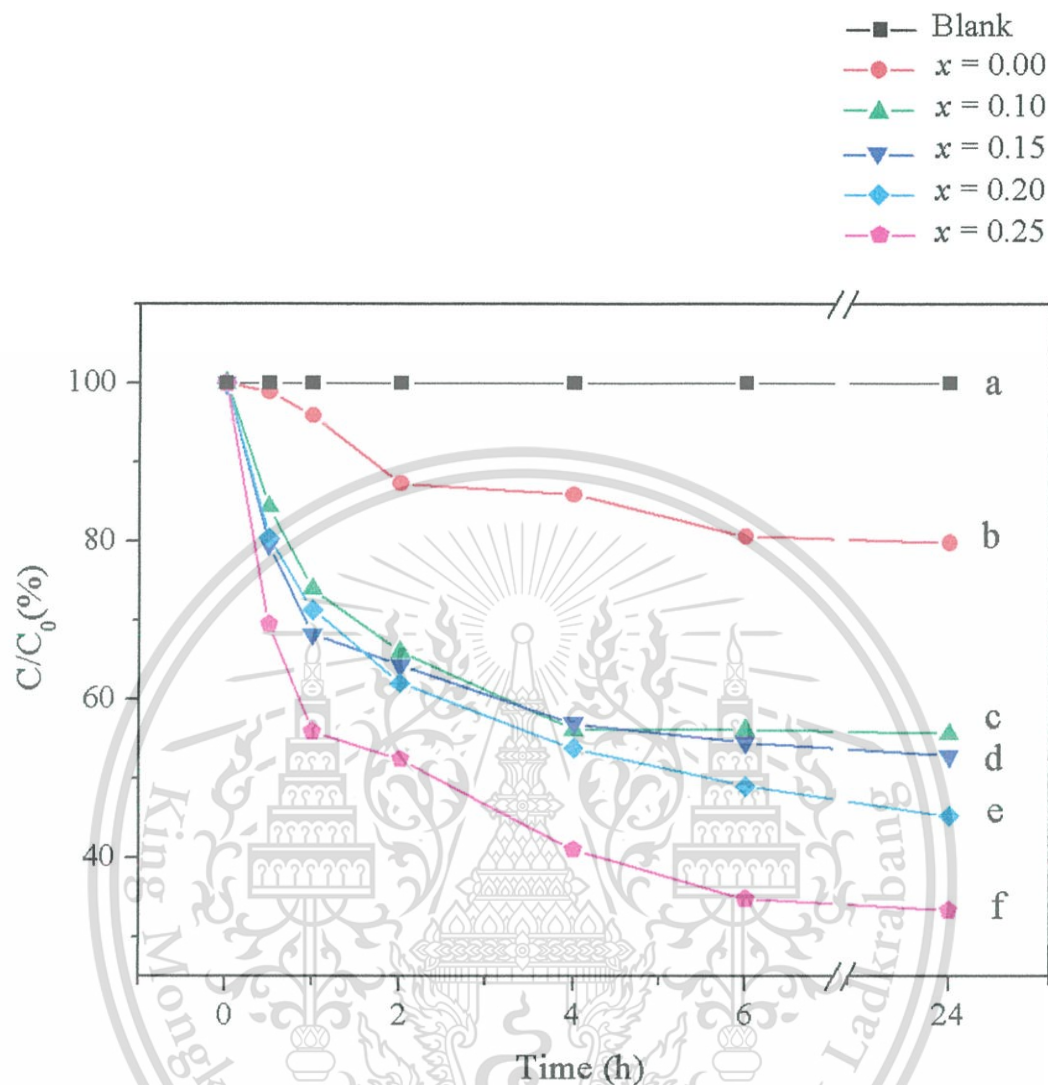
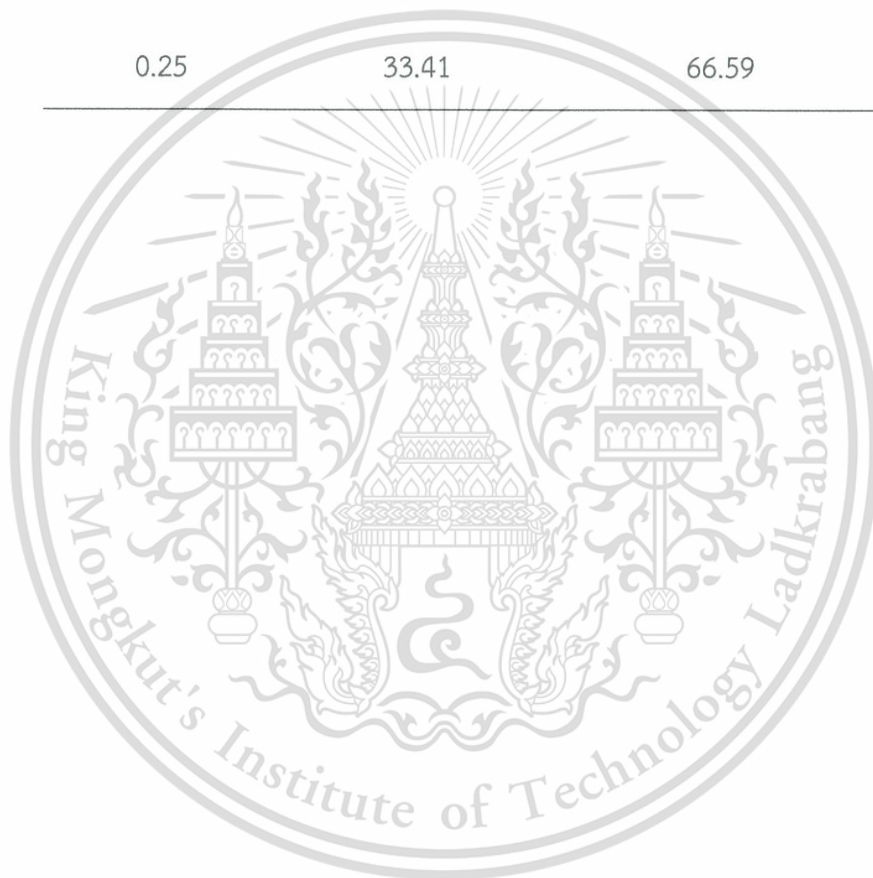


Figure 4.17 Decrease of color after 24 h treatment of reactive orange 16 with  $\text{CoFe}_{2-x}\text{Cu}_x\text{O}_4$  catalysts.

**Table 4.8** Degradation result of  $\text{CoFe}_{2-x}\text{Cu}_x\text{O}_4$  powders calcined at 900 °C for 48 h.

$X$	$C/C_0$ (%)	Degradation (%)
0.00	79.83	20.17
0.10	55.71	44.29
0.15	52.89	47.11
0.20	45.28	54.72
0.25	33.41	66.59



### 4.1.3 $\text{CoFe}_{2-x}\text{Zn}_x\text{O}_4$ System

#### 4.1.3.1 Phase Formation

Figure 4.18 shows the X-ray diffraction of  $\text{CoFe}_{2-x}\text{Zn}_x\text{O}_4$  powders at various compositions and calcined at 900 °C for 48 h. The XRD patterns showed that peaks (when  $x = 0.00-0.55$ ) were of a single phase cubic structure and corresponded to JCPDS file no. 22-1086 and space group  $\text{Fd}\bar{3}\text{m}$  (no. 227) [1]. However, the XRD pattern of the  $\text{CoFe}_{2-x}\text{Zn}_x\text{O}_4$  powder, where  $x = 0.60$  detected secondary phases, which were ZnO this corresponded with JCPDS file no. 89-1397. Therefore, only single phase samples were used to investigate the lattice parameters, which were analyzed from XRD data by the Rietveld refinement method using the FullProf program. Furthermore, the difference of lattice constants and results of a quantitative phase analysis from the refinement with  $\text{Zn}^{2+}$  doping are presented in Figure 4.19 and Table 4.9.



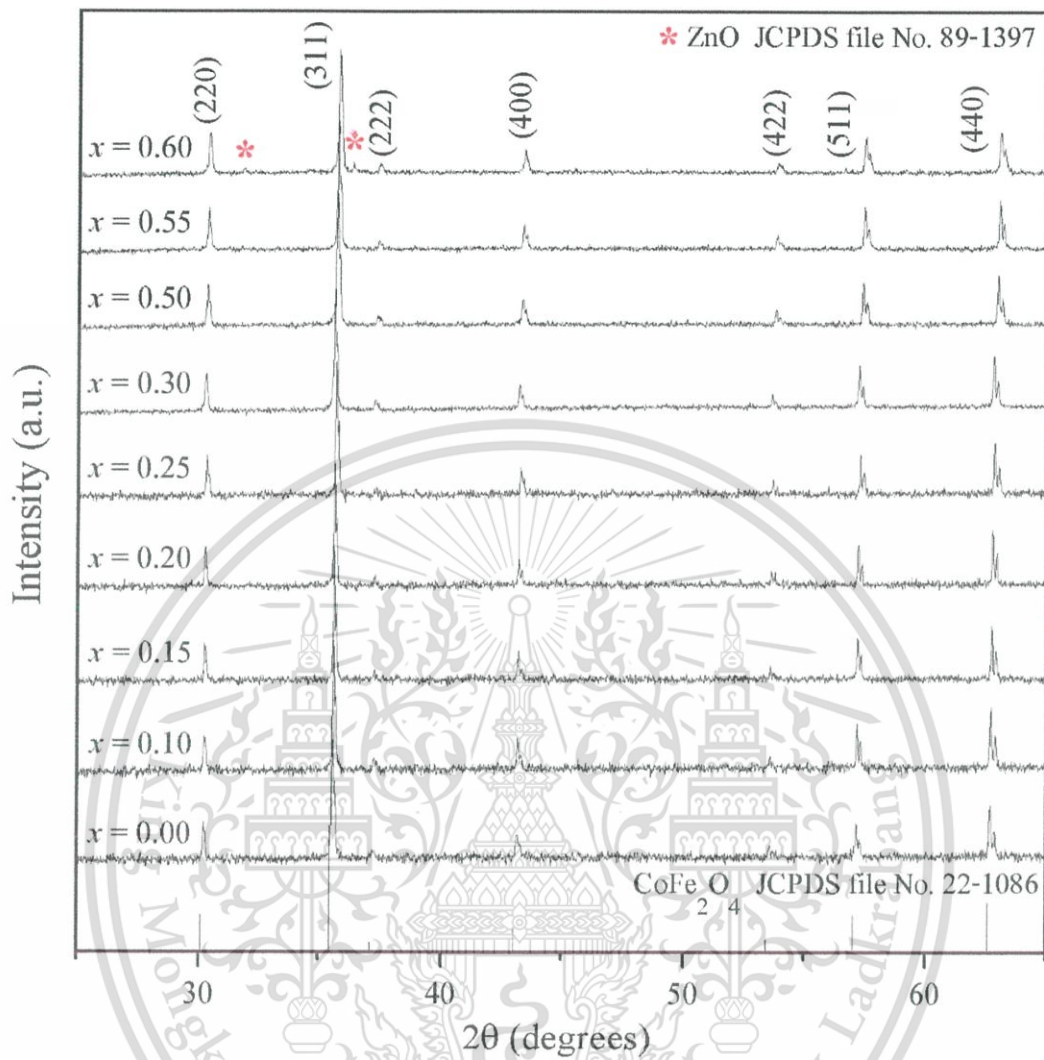


Figure 4.18 X-ray diffraction patterns of  $\text{CoFe}_{2-x}\text{Zn}_x\text{O}_4$  powders calcined at 900 °C for 48 h.

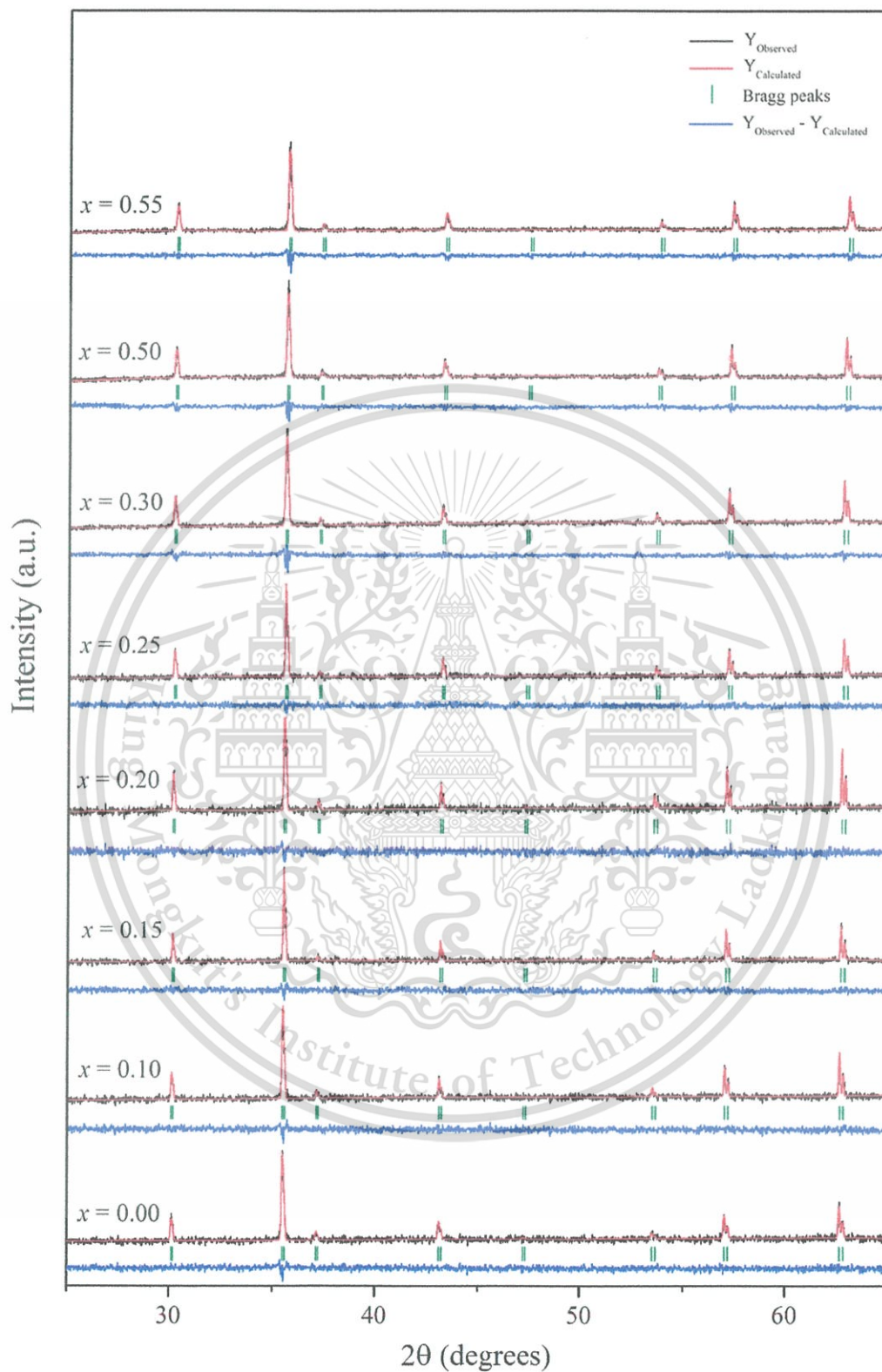


Figure 4.19 X-ray diffraction patterns and the structure refinement of  $\text{CoFe}_{2-x}\text{Zn}_x\text{O}_4$  powders calcined at 900 °C for 48 h.

This material is reserved for educational use only, not allowed for commercial use.

Forbidden to modify the content, and cite the document when use.

The structure refinement showed the corresponding fits and confirmed that the structure was of cubic type. Data quality of structural refinement was checked basically by R-values ( $R_w$ ) and a good fit ( $\chi^2$ ). In addition, the distinction between XRD patterns, calculated data and experimental profiles displayed small values in the intensity scale, as illustrated by the line,  $Y_{\text{Observed}} - Y_{\text{Calculated}}$  [2]. Furthermore, the trend of the lattice constant of  $\text{CoFe}_{2-x}\text{Zn}_x\text{O}_4$  powders calcined at 900 °C for 48 h is shown in Figure 4.20. The results showed that the lattice constant for each composition decreased with decreasing Zn ion. The lattice parameter decreased with doping, due to the ionic radius of Zn (0.6 Å) coordinating four-fold with  $\text{O}^{2-}$  ions, which were smaller than the ionic radius of Fe (0.645 Å) coordinating six-fold with  $\text{O}^{2-}$  ions in the structure [3]. Therefore, after doping, Zn in the structure affected the decreasing of the lattice parameter.

**Table 4.9** Lattice constant ( $a$ ) and Rietveld refinement result of  $\text{CoFe}_{2-x}\text{Zn}_x\text{O}_4$  powders calcined at 900 °C for 48 h.

$x$	$a$ (Å)	$V$ ( $10^6 \text{ pm}^3$ )	$R_w$ (%)	$\chi^2$
0.00	8.3825 (6)	589.010	4.01	1.11
0.10	8.3828 (4)	589.066	4.13	1.11
0.15	8.3795 (4)	588.409	4.17	1.14
0.20	8.3757 (4)	590.508	4.15	1.11
0.25	8.3696 (4)	586.290	4.12	1.10
0.30	8.3676 (3)	585.867	2.48	1.53
0.50	8.3450 (3)	581.140	2.62	1.53
0.55	8.3396 (3)	579.999	2.53	1.57

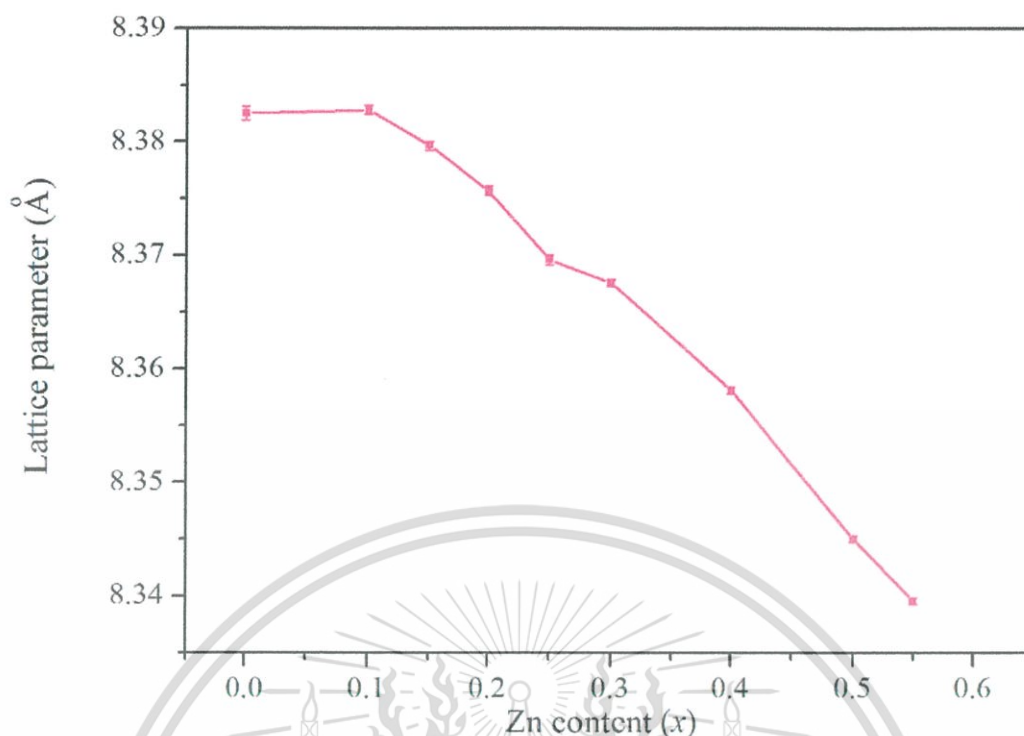


Figure 4.20 Lattice constant of  $\text{CoFe}_{2-x}\text{Zn}_x\text{O}_4$  powders calcined at  $900\text{ }^\circ\text{C}$  for 48 h.

#### 4.1.3.2 Magnetic Properties

Figure 4.21 shows the magnetic hysteresis loop of  $\text{CoFe}_{2-x}\text{Zn}_x\text{O}_4$  powders at room temperature, with a maximum applied field of up to 8 kOe. The saturated magnetization, remanence and coercivity are summarized in Table 4.10. Also, Figure 4.22 presents variations of saturated magnetization and coercivities for  $\text{CoFe}_{2-x}\text{Zn}_x\text{O}_4$  powders as a function of compositions calcined at  $900\text{ }^\circ\text{C}$  for 48 h. The magnetization value of doped samples increased sharply with the external magnetic field strength at the low field region. The highest saturated magnetization can be obtained in  $x = 0.1$  Zn doped cobalt ferrites. Increases in saturated magnetization can be attributed to the influence of the cationic stoichiometry and its occupancy in specific sites. The magnetic order in the cubic system of ferromagnetic spinels was due to the occurrence of the super-exchange interaction mechanism between metal ions in the tetrahedral A-site and octahedral B-site [19]. When the nonmagnetic zinc ion was substituted by the cobalt ferrite lattice, due to the zinc ferrite being a normal spinel, it had a stronger

preference for the tetrahedral site and thus reduced the amount of  $\text{Fe}^{3+}$  in the A site. The net result, due to antiferromagnetic coupling, was an increase in magnetic moments on the B lattice and an increase in saturated magnetization. However, at high levels of zinc substitution in  $x > 0.1$ , the A-site magnetic ion became so diluted that coupling between the two lattices was lost, and the saturated magnetization dropped [20]. Furthermore, the changes in coercivity of the samples by increasing the Zn content can be attributed to the magnetic character and anisotropic nature of cobalt. Magnetic anisotropy strongly affected the shape of the hysteresis loops and controls the coercivity. The anisotropy constant of the Co ion was larger than the Zn cations, then the cobalt ferrite was the hard magnetic shape of the hysteresis loop, which had high coercivity ( $\sim 800$  Oe). Meanwhile, Zn ion was smaller the anisotropy constant than Co cations, which it was soft magnetic shape of hysteresis loop. As more Zn ions replaced the cobalt ferrite by increasing the “x”, the coercivity decreases [4].

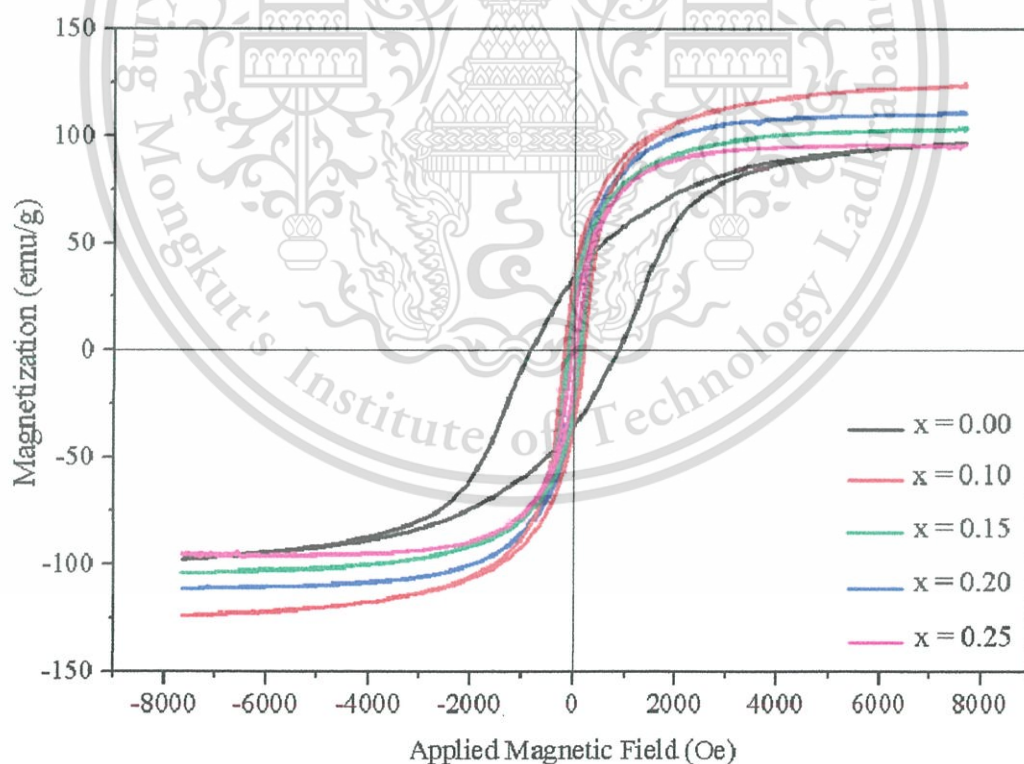


Figure 4.21 Magnetic hysteresis loops of  $\text{CoFe}_{2-x}\text{Zn}_x\text{O}_4$  powders at room temperature.

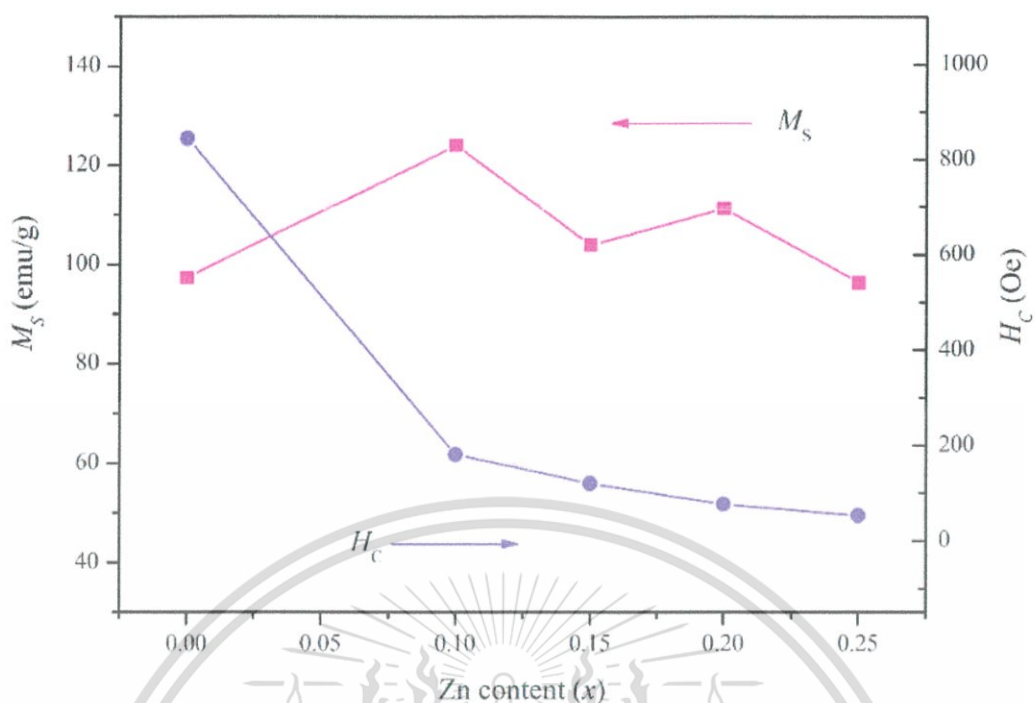


Figure 4.22 Variations of saturated magnetization and coercivities for  $\text{CoFe}_{2-x}\text{Zn}_x\text{O}_4$  powders as a function of compositions calcined at  $900^\circ\text{C}$  for 48 h.

Table 4.10 Magnetic properties and Bohr magneton of  $\text{CoFe}_{2-x}\text{Zn}_x\text{O}_4$  calcined at  $900^\circ\text{C}$  for 48 h.

$x$	$M_s$ (emu/g)	$H_c$ (Oe)	Bohr magneton
0.00	97.3	844.1	36
0.10	124.0	181.1	53
0.15	103.9	119.8	53
0.20	111.3	75.9	54
0.25	96.3	52.6	50

In addition, cation distribution and Bohr magneton result of  $\text{CoFe}_{2-x}\text{Zn}_x\text{O}_4$  powders calcined at 900 °C for 48 h were present in Table 4.11. And, Figure 4.23 shows saturated magnetization and Bohr magneton of  $\text{CoFe}_{2-x}\text{Zn}_x\text{O}_4$  powders as a function of compositions. From the experiment, results exposed that after Zn doped  $\text{CoFe}_2\text{O}_4$ , the saturated magnetization increased and the maximum saturated magnetization was composition  $x = 0.10$  due to Zn cations having no unpaired electrons. The amount of Fe cations in the A site were reduced, thus magnetic moments on the B site increased, and then increased the saturated magnetization. From the Bohr magneton data, the saturated magnetization increased after doping Zn in the structure, and the highest saturated magnetization was obtained at composition  $x = 0.20$ . However, the trend of saturated magnetization from the experiment and calculation corresponded by increasing after doping Zn cations. Furthermore, after doping Zn in cobalt ferrite, Zn cations strongly preferred the A site due to a very small the octahedral site preference energy (0.00 eV). Meanwhile, Co and Fe cations occupied both B and A sites. It can explain that doping Zn ion at different compositions affects the cation distribution in this system.

**Table 4.11** Cation distribution and Bohr magneton result of  $\text{CoFe}_{2-x}\text{Zn}_x\text{O}_4$  powders calcined at 900 °C for 48 h.

X	Co cation		Fe cation		Zn cation		Bohr magneton
	A site	B site	A site	B site	A site	B site	
0.00	3	5	5	11	0	0	36
0.10	6	2	1	14	1	0	53
0.15	6	2	1	14	1	0	53
0.20	5	3	1	13	2	0	54
0.25	4	4	2	12	2	0	50

This material is reserved for educational use only, not allowed for commercial use.

Forbidden to modify the content, and cite the document when use.

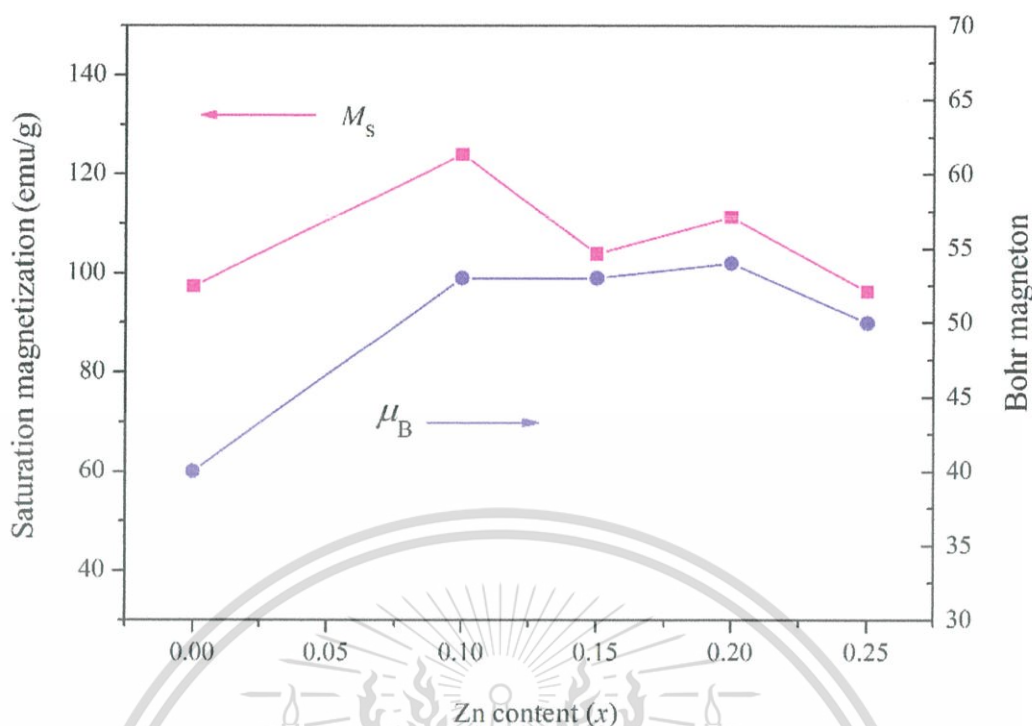


Figure 4.23 Trend of saturated magnetization and Bohr magneton for  $\text{CoFe}_{2-x}\text{Zn}_x\text{O}_4$  powders calcined at 900 °C for 48 h.

#### 4.1.3.3 Cation Distribution

Afterwards, the calcination powders were examined by X-ray absorption spectroscopy (XAS). EXAFS investigation determined the local bonding surrounding the Co, Fe and Zn. Spectra that encompassed the Co (7709 eV), Fe (7112 eV) and Zn (9659 eV) K-edges. Figure 4.24 shows the FT of Zn, Fe, and Co EXAFS data for the  $\text{CoFe}_{2-x}\text{Zn}_x\text{O}_4$  powders calcined at 900 °C for 48 h. The FT from a  $\Delta K$  range of between 2 and  $10 \text{ \AA}^{-1}$ , with  $k^2$  weighting of the  $\text{CoFe}_{2-x}\text{Zn}_x\text{O}_4$  Co EXAFS spectra, is shown as a function of distance in Figure 4.24 (a). Investigation of the  $\text{CoFe}_{2-x}\text{Zn}_x\text{O}_4$  powders where  $x = 0.00 - 0.55$  showed that the peak of the region between  $2.6 \text{ \AA}$  was larger than the peak centered near  $3.1 \text{ \AA}$ . This indicated that Co ions were localized at the A and B sites.

Figure 4.24 (b) shows the FT of Fe EXAFS data for the  $\text{CoFe}_{2-x}\text{Zn}_x\text{O}_4$  powders where  $x = 0.00 - 0.55$  calcined at 900 °C for 48 h. The Fe EXAFS spectra of the sample showed splitting in the second peak. This peak was not perfectly symmetrical, and

enlargement of the region between 2.6 Å more than the peak near 3.1 Å indicated that Fe ions were occupied in both B and A sites.

Furthermore, Zn EXAFS data are shown in Figure 4.24 (c) as a function of the radial coordinate. The second peak of the  $\text{CoFe}_{2-x}\text{Zn}_x\text{O}_4$  powders where  $x = 0.10-0.55$  did not split. The peaks were near 3.1 Å, this can be described as the Zn ions occupying only at the A site. After doping and excess Zn cations in the structure, the Zn cations did not occupy in the B site since, the lowest of estimated octahedral site preference energies of Zn cations (0.00 eV) then the Zn cations strongly preferred to occupy in the A site. The EXAFS results accorded with the cation distribution from calculation data (Table 4.11).



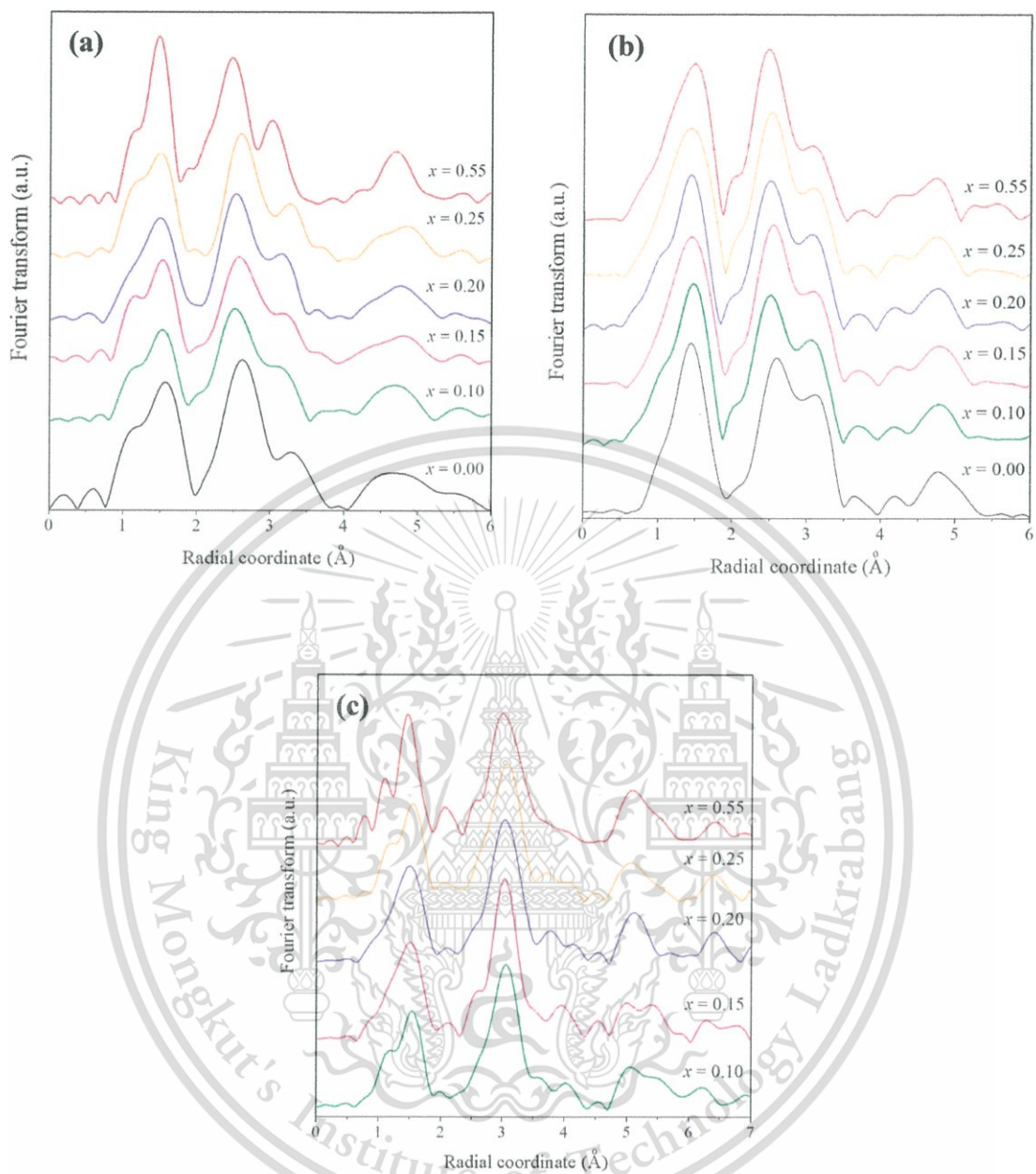


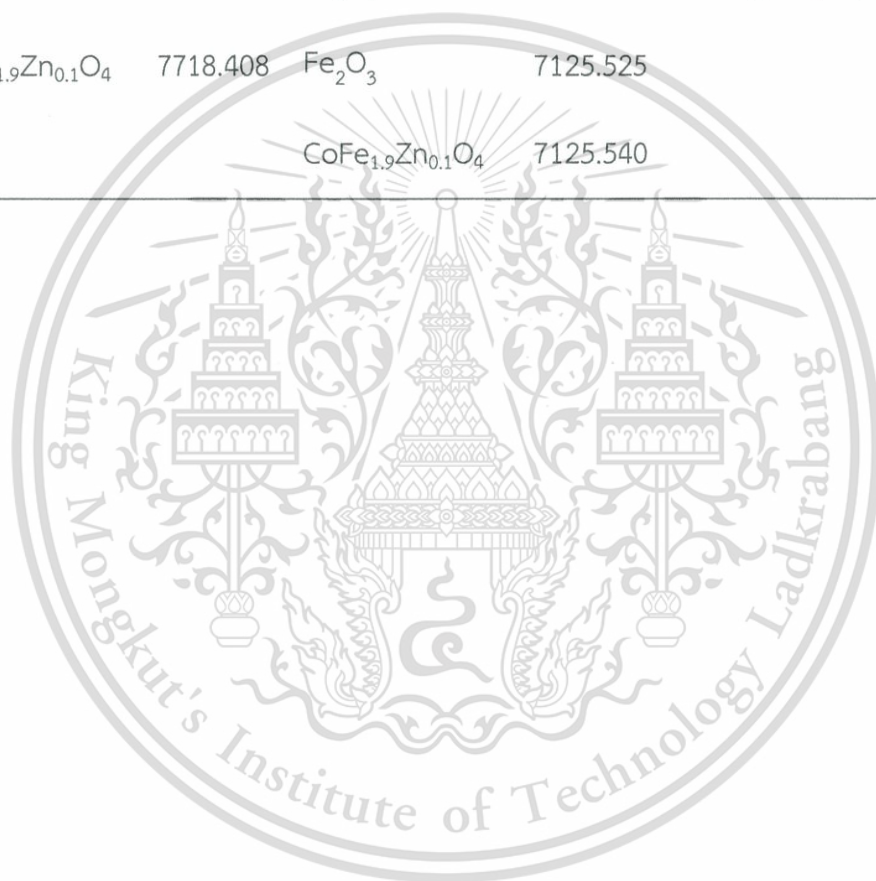
Figure 4.24 The FT of (a) Co, (b) Fe, and (c) Zn EXAFS data for the  $\text{CoFe}_{2-x}\text{Zn}_x\text{O}_4$  powders calcined at 900 °C for 48 h.

#### 4.1.3.4 Oxidation State

The XANES regions of the absorption spectrum are important because they contain electronic information on the immediate environment of the absorbing atom, which in principle can be translated into spatial, geometrical information. The first derivative of the XANES spectra is useful because it highlights the features around the absorption edge and facilitates determination of the oxidative state [15, 21]. Oxidation states were confirmed after preparation of the samples for indication of the Bohr magneton of each cation in the structure. Figure 4.25 (a) shows the XANES spectra of  $\text{CoFe}_{1.9}\text{Zn}_{0.1}\text{O}_4$  samples and varied cobalt standards obtained at the Co K-edge. The valence state of Co in the ferrite samples was determined from energy of the main maxima in the spectra [14]. The curves of samples in the threshold region are close to that of CoO, suggesting the existence of a divalent state.  $E_0$  of  $\text{CoFe}_{1.9}\text{Zn}_{0.1}\text{O}_4$  samples, Co foil, CoO and  $\text{Co}_3\text{O}_4$  is 7718.408, 7708.960, 7718.750 and 7721.194, respectively. As observed, the spectra for the samples were similar to those obtained for the CoO standard, in which  $\text{Co}^{2+}$  is coordinated six-fold with  $\text{O}^{2-}$  ions, suggesting that Co ions exist in a divalent state in six coordinated oxygen atoms [15], where the  $\text{Co}^{2+}$  was 3  $\mu_B$ . Figure 4.25 (b) shows XANES spectra of  $\text{CoFe}_{1.9}\text{Zn}_{0.1}\text{O}_4$ , Fe foil, FeO,  $\text{Fe}_3\text{O}_4$  and  $\text{Fe}_2\text{O}_3$  in the vicinity of the Fe K-edge, with their  $E_0$  being 7125.540, 7112.061, 7121.192, 7124.186 and 7125.525, respectively, which leads to the existence of  $\text{Fe}^{3+}$  in the samples with 5  $\mu_B$ . Figure 4.25 (c) shows that the threshold energy of  $\text{CoFe}_{1.9}\text{Zn}_{0.1}\text{O}_4$  samples is higher than that of Zn foil, but close to the energy of ZnO. The  $E_0$  of  $\text{CoFe}_{1.9}\text{Zn}_{0.1}\text{O}_4$ , Zn foil and ZnO is 9661.148, 9658.964 and 9661.104, respectively, suggesting an existence of a divalent state of Zn in the samples. The  $\text{Zn}^{2+}$  had no unpaired electrons. The threshold value of  $\text{CoFe}_{1.9}\text{Zn}_{0.1}\text{O}_4$  sample calcined at 900 °C for 48 h in air and the various standard are shown in Table 4.12.

**Table 4.12** The  $E_0$  value of  $\text{CoFe}_{1.9}\text{Zn}_{0.1}\text{O}_4$  sample calcined at 900 °C for 48 h in air and the various standard.

Sample	$E_0$ (eV)	Sample	$E_0$ (eV)	Sample	$E_0$ (eV)
Co foil	7708.960	Fe foil	7112.061	Zn foil	9658.964
$\text{Co}_3\text{O}_4$	7721.194	FeO	7121.192	ZnO	9661.104
CoO	7718.750	$\text{Fe}_3\text{O}_4$	7124.186	$\text{CoFe}_{1.9}\text{Zn}_{0.1}\text{O}_4$	9661.148
$\text{CoFe}_{1.9}\text{Zn}_{0.1}\text{O}_4$	7718.408	$\text{Fe}_2\text{O}_3$	7125.525		
		$\text{CoFe}_{1.9}\text{Zn}_{0.1}\text{O}_4$	7125.540		



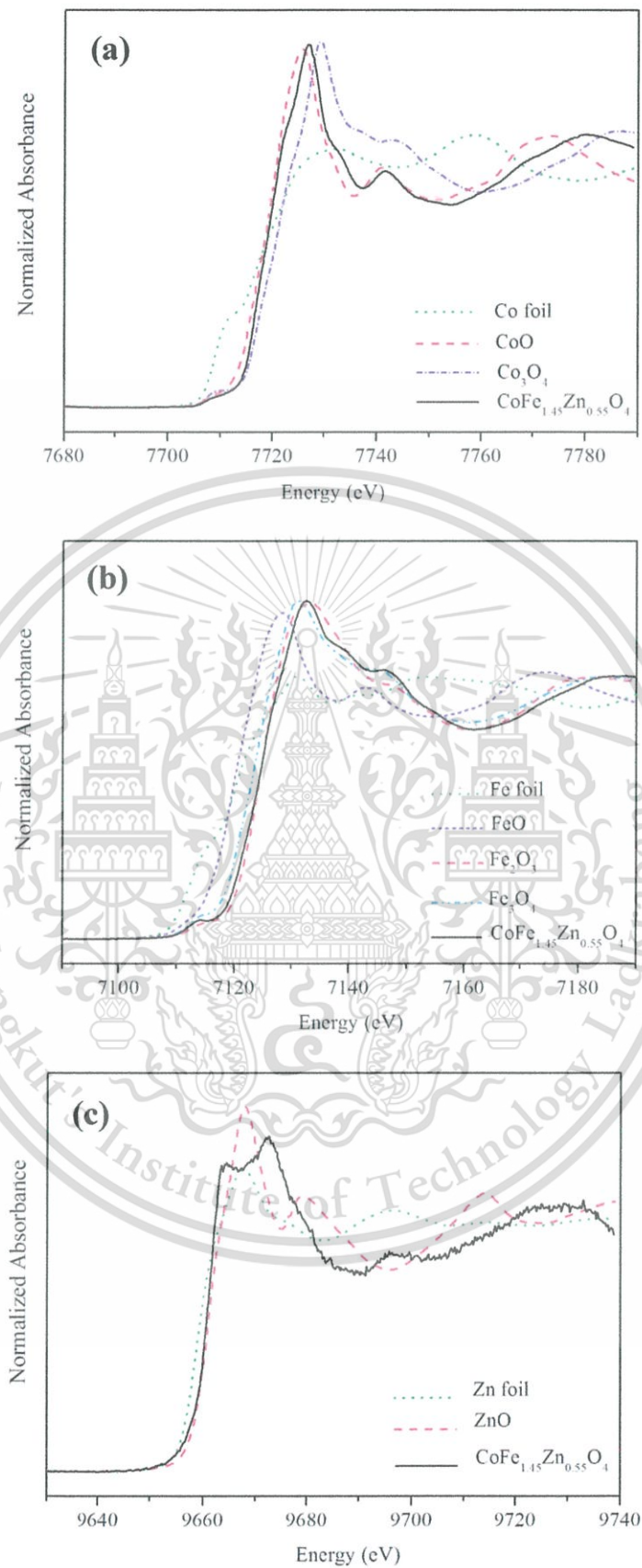


Figure 4.25 XANES spectra of CoFe<sub>1.9</sub>Mn<sub>0.1</sub>O<sub>4</sub> samples and the standards obtained at (a) Co K-edge, (b) Fe K-edge and (c) Zn K-edge.

This material is reserved for educational use only, not allowed for commercial use.

Forbidden to modify the content, and cite the document when use.

## 4.2 Effect of Thermal Treatment

Then, the investigation moved on to the effect of thermal treatment on the microstructure, cation distribution, and properties of  $\text{CoFe}_{2-x}\text{Mn}_x\text{O}_4$  system ( $M = \text{Mn}, \text{Cu}, \text{Zn}$ ).

### 4.2.1 $\text{CoFe}_{2-x}\text{Mn}_x\text{O}_4$ System

From the X-ray diffraction pattern results of the samples in the  $\text{CoFe}_{2-x}\text{Mn}_x\text{O}_4$  system, where  $x = 0.00-1.15$ , it was indicated that the  $\text{CoFe}_{0.90}\text{Mn}_{1.10}\text{O}_4$  powders would be studied, with regards to the effect of thermal annealing. Due to this composition, with excessive doping of the Mn cations in the structure, the single phase of spinel structure was still detected. In this composition, the cations were forced to be in the structure. As expected, after thermal treatment for a long time, the cations in this composition easily migrated to their preference site. Therefore, the  $\text{CoFe}_{0.90}\text{Mn}_{1.10}\text{O}_4$  powders were annealed at various temperatures for 100 h to find the suitable temperature for annealing. The suitable temperature was the temperature in which the average particle sizes did not change after annealing. The average particle sizes were confirmed using a scanning electron microscope (SEM) technique.

#### 4.2.1.1 Microstructure

##### 1) $\text{CoFe}_{0.9}\text{Mn}_{1.1}\text{O}_4$ powders as a function of annealing temperatures

The  $\text{CoFe}_{0.90}\text{Mn}_{1.10}\text{O}_4$  sample was annealed at 400-700 °C for 100 h in air. The sample was investigated regarding average particle sizes by SEM. Figure 4.26 displays the SEM micrographs of  $\text{CoFe}_{0.90}\text{Mn}_{1.10}\text{O}_4$  powders as a function of annealing temperatures for 100 h in air. Generally, the particles were agglomerated and irregular in shape. Table 4.13 presents the average particle sizes of the powders that were estimated from SEM micrographs. The results showed that the average particle sizes did not change with annealing temperatures. It ranged from  $0.66 \pm 0.20 \mu\text{m}$  to  $0.80 \pm 0.24 \mu\text{m}$ . These observations showed that annealing temperatures had no effect on

This material is reserved for educational use only, not allowed for commercial use.

Forbidden to modify the content, and cite the document when use.

the average particle sizes. The results indicated that annealing temperatures can be used at around 400-700 °C due to these temperatures not affecting the average particle sizes. However, the best annealing temperature was chosen. Then, the annealing samples were characterized by their magnetic properties (Section 4.2.1.2). The results showed that an annealing temperature of 500 °C created the highest saturated magnetization. Therefore, thermal treatment at 500 °C was chosen, this temperature accorded to H.M.I. Abdallah *et al.* [22] and Z. J. Zhang *et al.* [23].



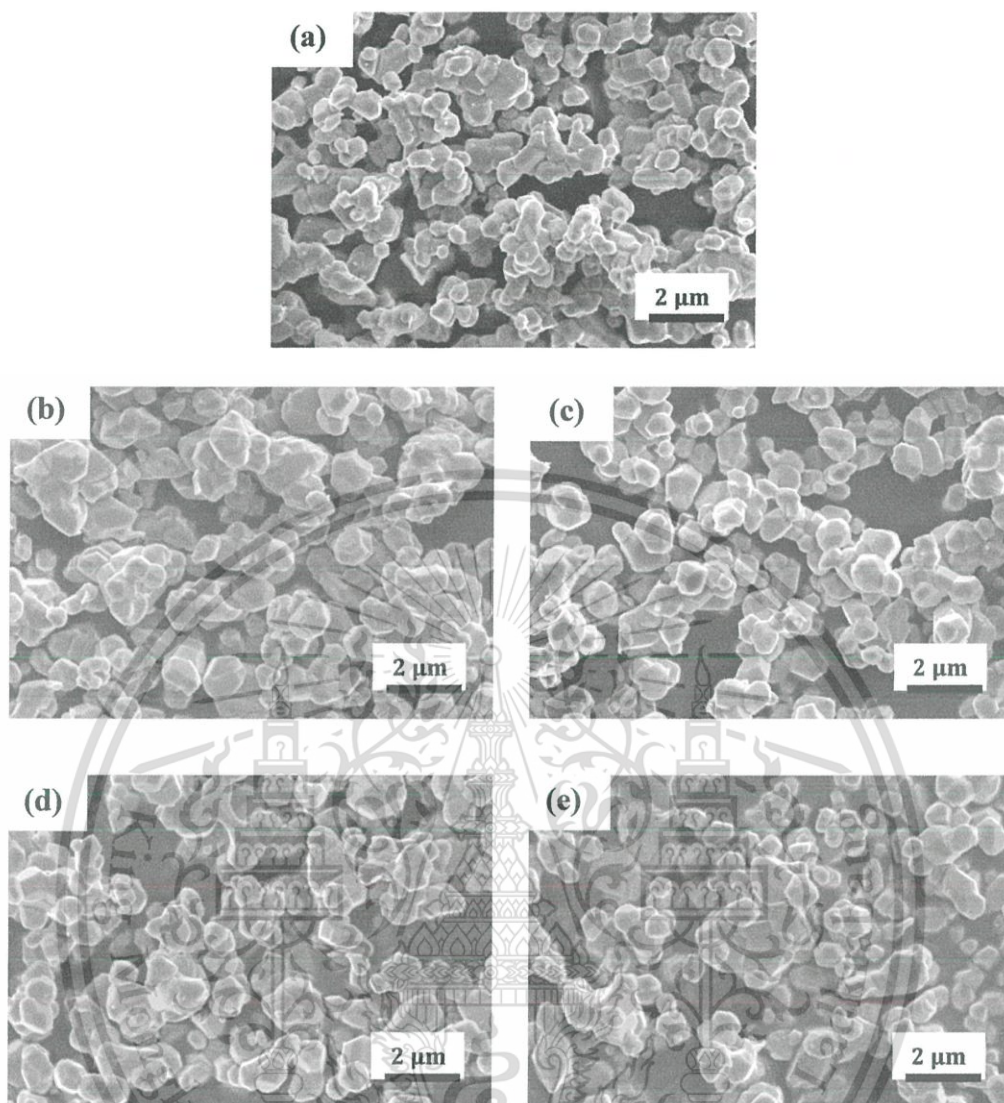


Figure 4.26 The SEM micrographs of  $\text{CoFe}_{0.90}\text{Mn}_{1.10}\text{O}_4$  powders annealed at (a) non annealing (b) 400 , (c) 500, (d) 600, and (e) 700 °C for 100 h in air.

**Table 4.13** Average particle size of  $\text{CoFe}_{0.9}\text{Mn}_{1.1}\text{O}_4$  powders as a function of annealing temperatures for 100 h in air.

Temperature (°C)	Average particle size ( $\mu\text{m}$ )
No annealing	$0.66 \pm 0.20$
400	$0.80 \pm 0.24$
500	$0.78 \pm 0.23$
600	$0.79 \pm 0.24$
700	$0.79 \pm 0.26$

## 2) $\text{CoFe}_{0.9}\text{Mn}_{1.1}\text{O}_4$ powders as a function of annealing time

After obtaining the annealing temperature, the influence of the annealing time was then studied. The  $\text{CoFe}_{0.90}\text{Mn}_{1.10}\text{O}_4$  sample was annealed at 500 °C for 4 and 100 h in air. After that, the average particle sizes of the annealing samples were confirmed using scanning electron microscopy (SEM) technique.

Figures 4.27 (a)–(c) shows the morphology and particle size distribution of  $\text{CoFe}_{0.90}\text{Mn}_{1.10}\text{O}_4$  powders as a function without annealing, and with annealing at 500 °C for 4 and 100 h. Basically, the particles were of irregular shape and generally agglomerate. The average particle sizes of the powder were estimated from SEM micrographs and are presented in Table 4.14. The results showed that the average particle sizes did not change with annealing time, and they ranged from  $0.66 \pm 0.20 \mu\text{m}$  to  $0.79 \pm 0.23 \mu\text{m}$ . Furthermore, all samples showed a small particle size distribution, as observed in the figures. The size distribution of powders without annealing mainly ranged from 0.57 to  $0.83 \mu\text{m}$ , and slightly increased with annealing time. However, general size distribution still ranged from 0.57 to  $0.83 \mu\text{m}$ . This minor increasing of size distribution certainly would not have a significant effect on cation

distribution. These observations revealed that annealing time had no effect on average particle sizes, however, it affected cation distribution and the magnetic properties.



This material is reserved for educational use only, not allowed for commercial use.

Forbidden to modify the content, and cite the document when use.

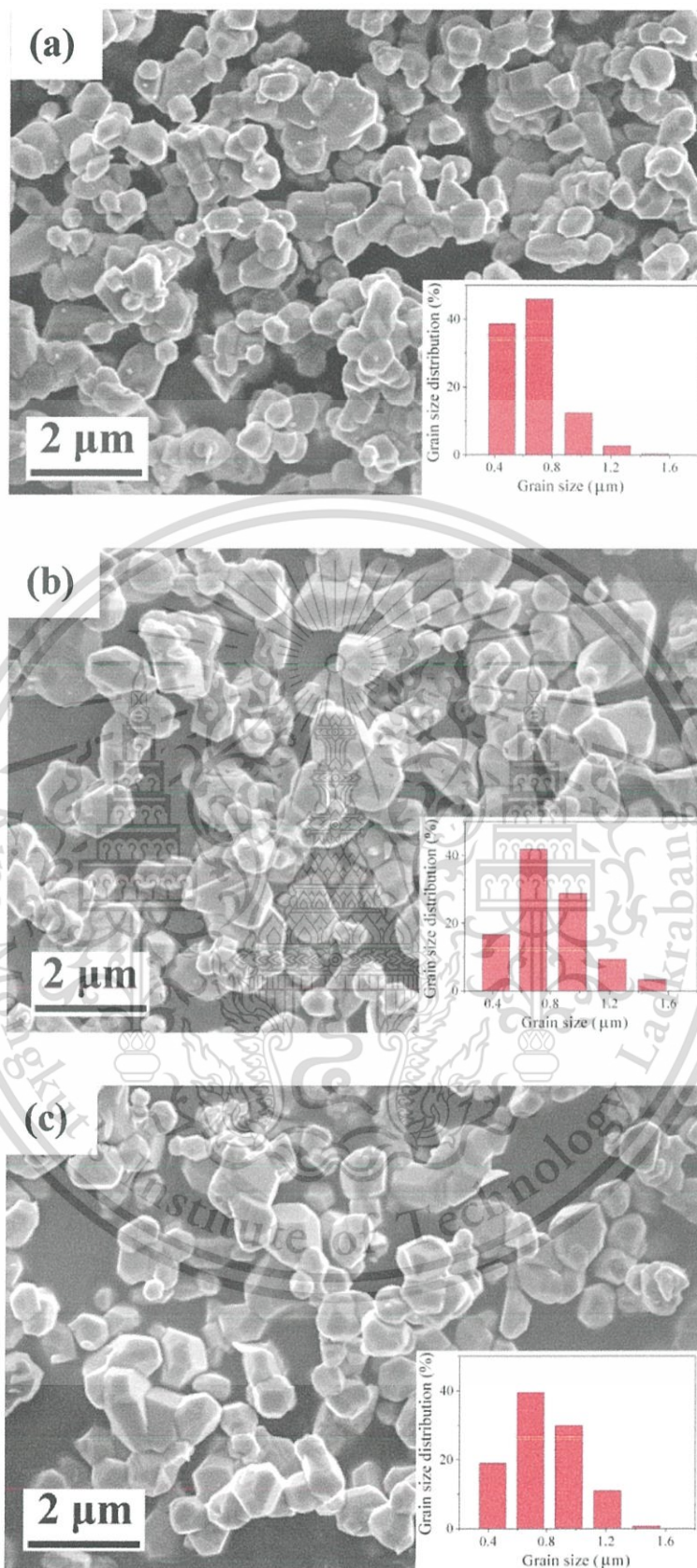


Figure 4.27 SEM micrographs of  $\text{CoFe}_{0.90}\text{Mn}_{1.10}\text{O}_4$  powders with (a) no annealing, (b) annealing at 500 °C for 4 h and (c) annealing at 500 °C for 100 h.

This material is reserved for educational use only, not allowed for commercial use.

Forbidden to modify the content, and cite the document when use.

**Table 4.14** Average particle size of  $\text{CoFe}_{0.9}\text{Mn}_{1.1}\text{O}_4$  as a function of annealing time.

Annealing time (h)	Average particle size ( $\mu\text{m}$ )
no annealing	$0.66 \pm 0.20$
4	$0.79 \pm 0.25$
100	$0.79 \pm 0.23$

#### 4.2.1.2 Magnetic Properties

##### 1) $\text{CoFe}_{0.9}\text{Mn}_{1.1}\text{O}_4$ powders as a function of annealing temperatures

After annealing the  $\text{CoFe}_{0.9}\text{Mn}_{1.1}\text{O}_4$  sample at 400-700 °C for 100 h in air and confirming the average particle sizes, the annealing samples were then investigated with regards to their magnetic properties, using the vibrating sample magnetometer (VSM) to find the best annealing temperature.

The magnetic properties of the annealing sample at different temperatures for 100 h in air were characterized at room temperature with a maximum applied field of up to 8 kOe, as shown in Figure 4.28 and Table 4.15. The saturated magnetization and coercive field trends are summarized in Figure 4.29. Results showed the various saturated magnetizations after annealing at different annealing temperatures. The highest saturated magnetization was obtained in the sample annealed at 500 °C for 100 h. Therefore, 500 °C temperature was chosen for annealing in this system, due to this temperature being able to change the cations in the structure and improve their magnetic properties. This temperature was suitable for annealing according to H. M. I. Abdallah *et al.* [22] and Z. J. Zhang *et al.* [23]. However, after annealing, the coercivity did not change due to the average particle sizes after annealing at different temperatures having no change.

**Table 4.15** Magnetic properties and Bohr magneton of  $\text{CoFe}_{0.9}\text{Mn}_{1.1}\text{O}_4$  powders as a function of annealing temperatures for 100 h in air.

Temperature ( $^{\circ}\text{C}$ )	$M_s$ (emu/g)	$H_c$ (Oe)	Bohr Magnetron
No annealing	37.5	128.9	31
400	37.7	189.1	31
500	42.2	167.6	31
600	33.4	167.6	31
700	38.6	167.6	31

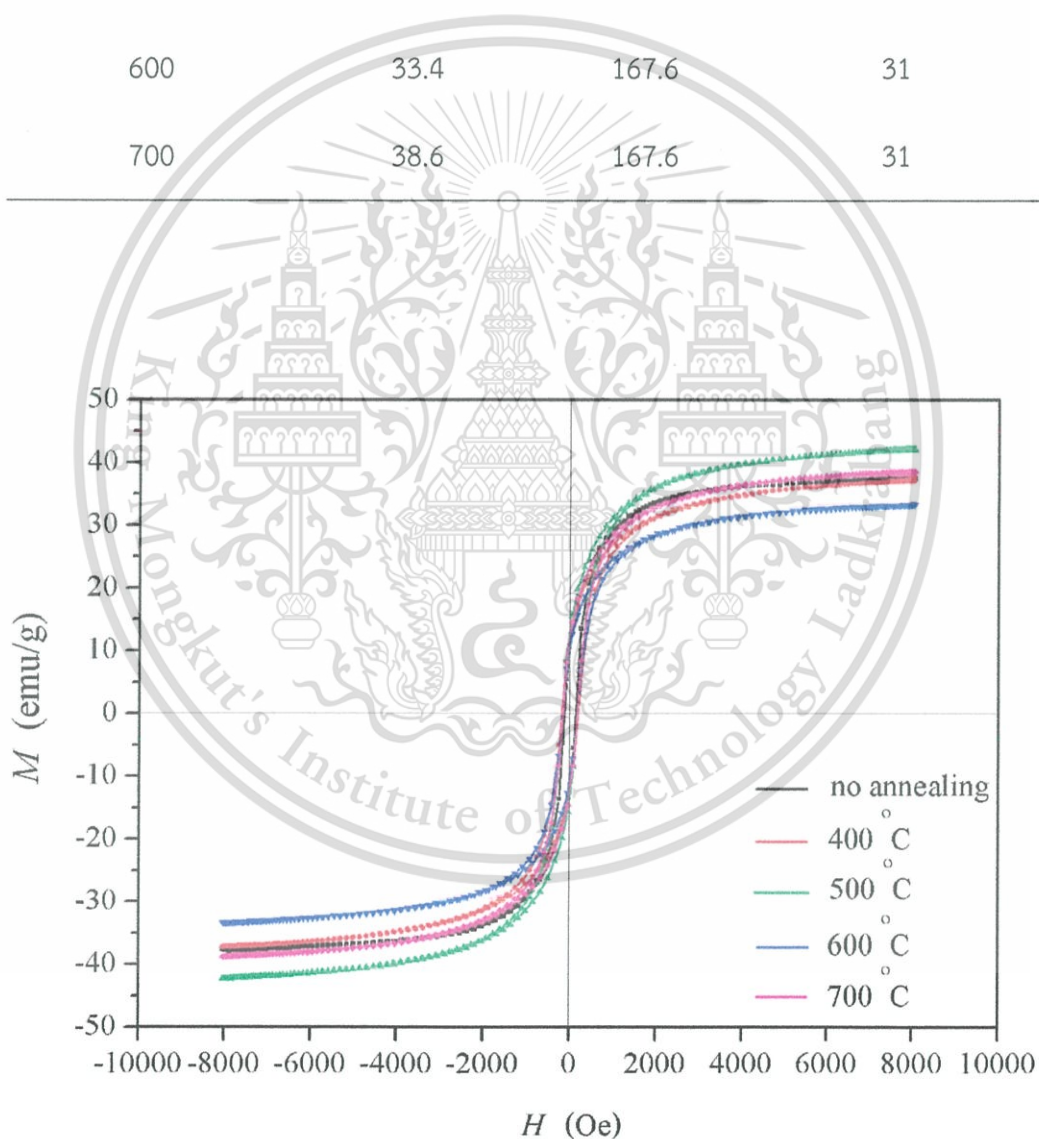


**Figure 4.28** The magnetic hysteresis loop of  $\text{CoFe}_{0.90}\text{Mn}_{1.10}\text{O}_4$  powders as a function of annealing temperature for 100 h in air.

This material is reserved for educational use only, not allowed for commercial use.

Forbidden to modify the content, and cite the document when use.

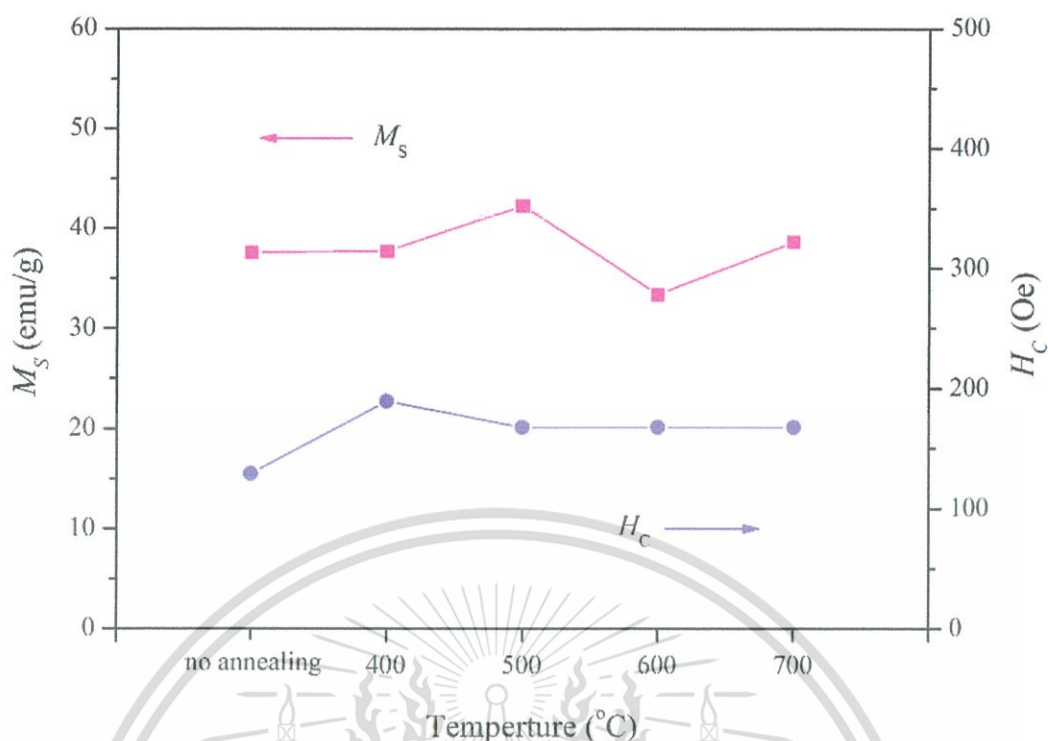


Figure 4.29 Variations of saturated magnetization and coercivity of  $\text{CoFe}_{0.90}\text{Mn}_{1.10}\text{O}_4$  powders as a function of annealing temperature for 100 h in air.

The Bohr magneton of  $\text{CoFe}_{0.90}\text{Mn}_{1.10}\text{O}_4$  powders as a function of annealing temperature were calculated and are shown in Table 4.15. The variations of saturated magnetization and Bohr magneton of  $\text{CoFe}_{0.90}\text{Mn}_{1.10}\text{O}_4$  powders as a function of annealing temperature for 100 h in air are presented in Figure 4.30. The results from the experiment showed the same trend of saturated magnetization, which accorded with the Bohr magneton from the calculation.

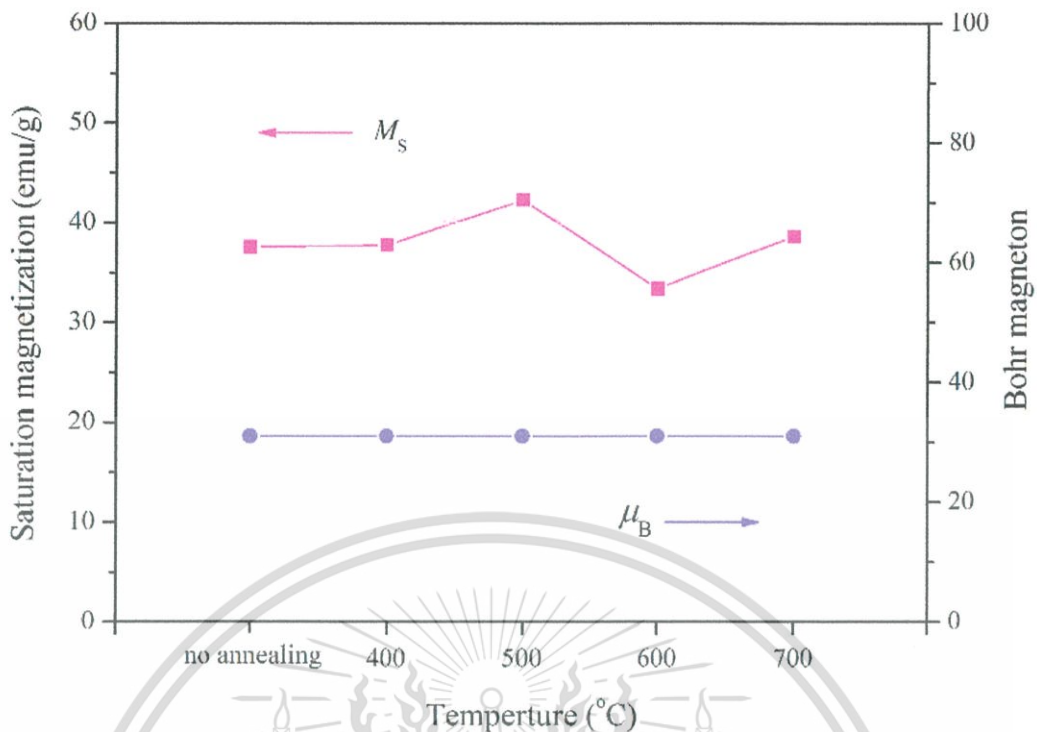


Figure 4.30 Saturated magnetization and Bohr magneton of  $\text{CoFe}_{0.90}\text{Mn}_{1.10}\text{O}_4$  powders as a function of annealing temperature for 100 h in air.

## 2) $\text{CoFe}_{0.9}\text{Mn}_{1.1}\text{O}_4$ powders as a function of annealing time

The  $\text{CoFe}_{0.9}\text{Mn}_{1.1}\text{O}_4$  powders annealing at different temperature showed that the suitable temperature was 500 °C. Afterwards, the influence of the annealing time was studied through annealing the  $\text{CoFe}_{0.90}\text{Mn}_{1.10}\text{O}_4$  samples at 500 °C for 4 and 100 h in air. Since annealing time had an effect on the cation distribution and the magnetic properties of materials. The cation distribution and magnetic properties were characterized by the X-ray absorption spectroscopy (XAS) and vibrating sample magnetometer (VSM), respectively.

Figure 4.31 shows the magnetic hysteresis loop of  $\text{CoFe}_{0.90}\text{Mn}_{1.10}\text{O}_4$  powders as a function without annealing, and with annealing at 500 °C for 4 h and 100 h at room temperature. Basically, the magnetization curves of all samples were nonlinear and typically ferrimagnetic materials [4]. The variations of saturated magnetization ( $M_s$ ) and coercivities ( $H_c$ ) for  $\text{CoFe}_{0.90}\text{Mn}_{1.10}\text{O}_4$  powder as a function of annealing time are exhibited in Figure 4.32 and Table 4.16. The results displayed that saturated

This material is reserved for educational use only, not allowed for commercial use.

magnetization before annealing was 37.67 emu/g. After increasing the annealing time to 100 h, the trend of saturated magnetization increased with 42.24 emu/g. The increasing result of saturated magnetization confirmed that the annealing time affected cations to migrate to their preference site. Since, the net magnetic moment was the result of a super-exchange interaction of metal ions in the A and B sites [19]. After annealing the sample at 500 °C for 100 h, the Co cations in octahedral site decreased, and the Fe ions in the same site increased. Since the Bohr magneton of Co cations were  $3 \mu_B$ , while Fe cations were  $5 \mu_B$ . Hence, the net magnetic moment uncompensated and then increased the saturated magnetization. Furthermore, the coercivity of the samples was slightly changed with increasing of the annealing time. This can be attributed to the annealing time having an effect on structural distortion. Its influence was to increase the anisotropy of the Co cations and increase the coercivity in annealed samples [9].

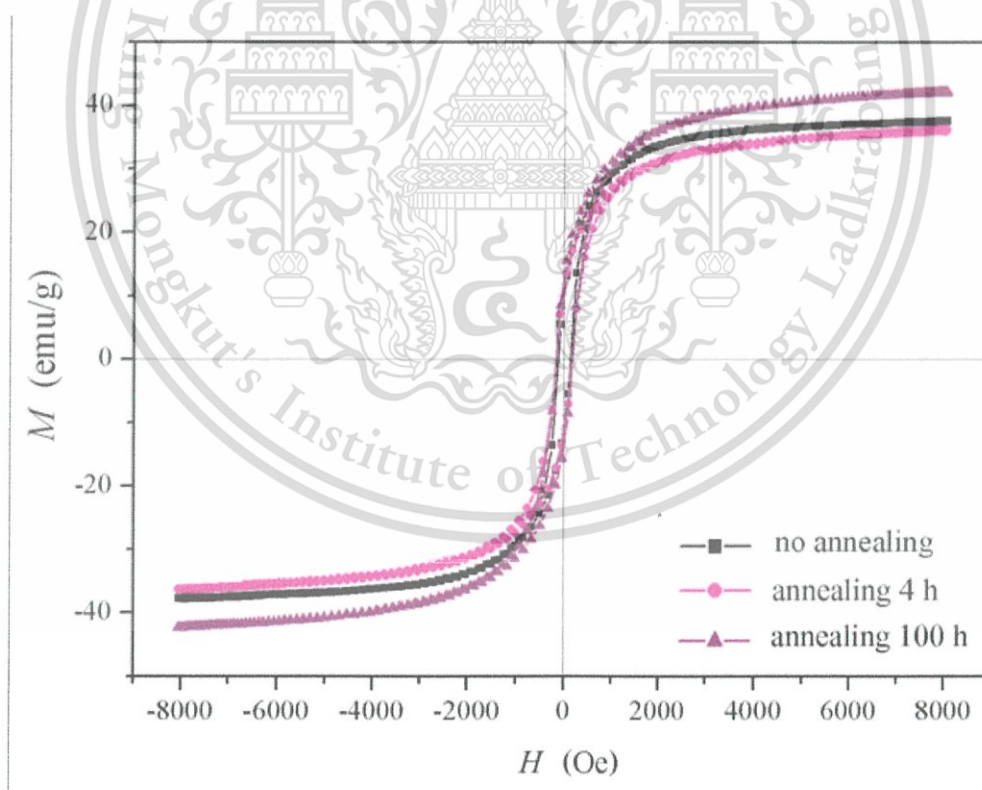


**Figure 4.31** Magnetic hysteresis loops of  $\text{CoFe}_{0.90}\text{Mn}_{1.10}\text{O}_4$  powders without annealing, and with annealing at 500 °C for 4 and 100 h.

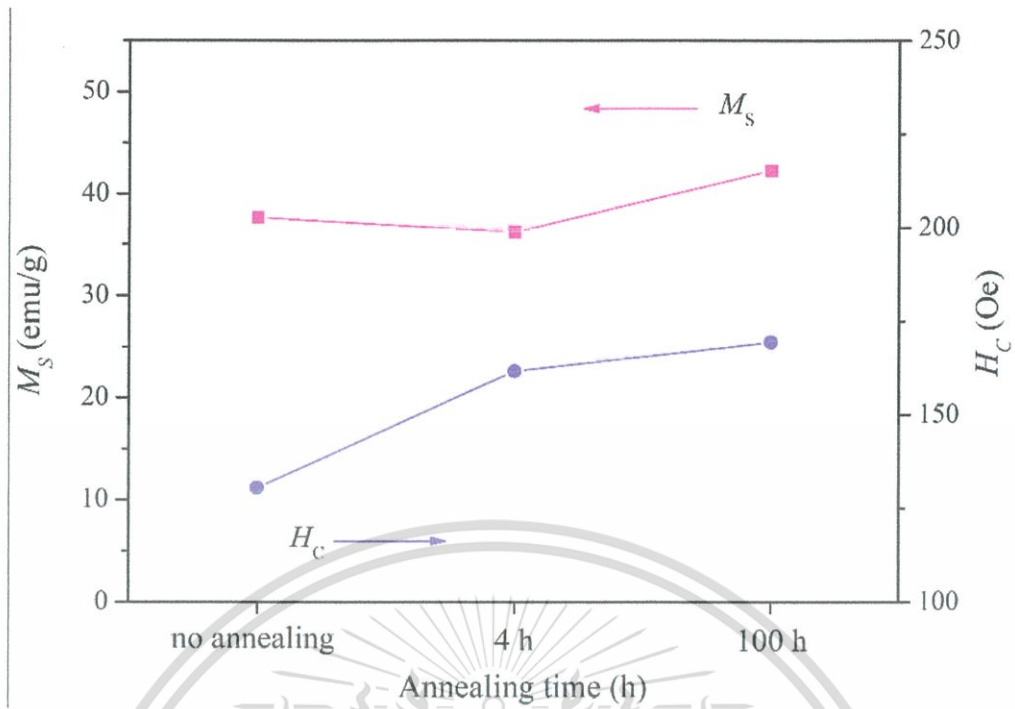


Figure 4.32 Variations of saturated magnetization and coercivities for  $\text{CoFe}_{0.90}\text{Mn}_{1.10}\text{O}_4$  powders as a function of annealing time.

Table 4.16 Magnetic properties and Bohr magneton of  $\text{CoFe}_{0.9}\text{Mn}_{1.1}\text{O}_4$  powders as a function of annealing time.

Annealing time (h)	$M_s$ (emu/g)	$H_c$ (Oe)	Bohr Magneton
no annealing	37.7	130.4	27
4	36.2	161.6	27
100	42.2	169.4	31

Figure 4.33 presents the trend of saturated magnetization and Bohr magneton of  $\text{CoFe}_{0.90}\text{Mn}_{1.10}\text{O}_4$  powders as a function of annealing time. The Bohr magneton before and after annealing of  $\text{CoFe}_{0.90}\text{Mn}_{1.10}\text{O}_4$  powders are shown in Table 4.16. From the experiment results, the saturated magnetization increased after annealing at 500

This material is reserved for educational use only, not allowed for commercial use.

Forbidden to modify the content, and cite the document when use.

°C for 100 h in air, experiment results also corresponded to the Bohr magneton from calculated results. It suggests that the annealing time for 100 h affected the cation distribution of  $\text{CoFe}_{0.90}\text{Mn}_{1.10}\text{O}_4$  sample.

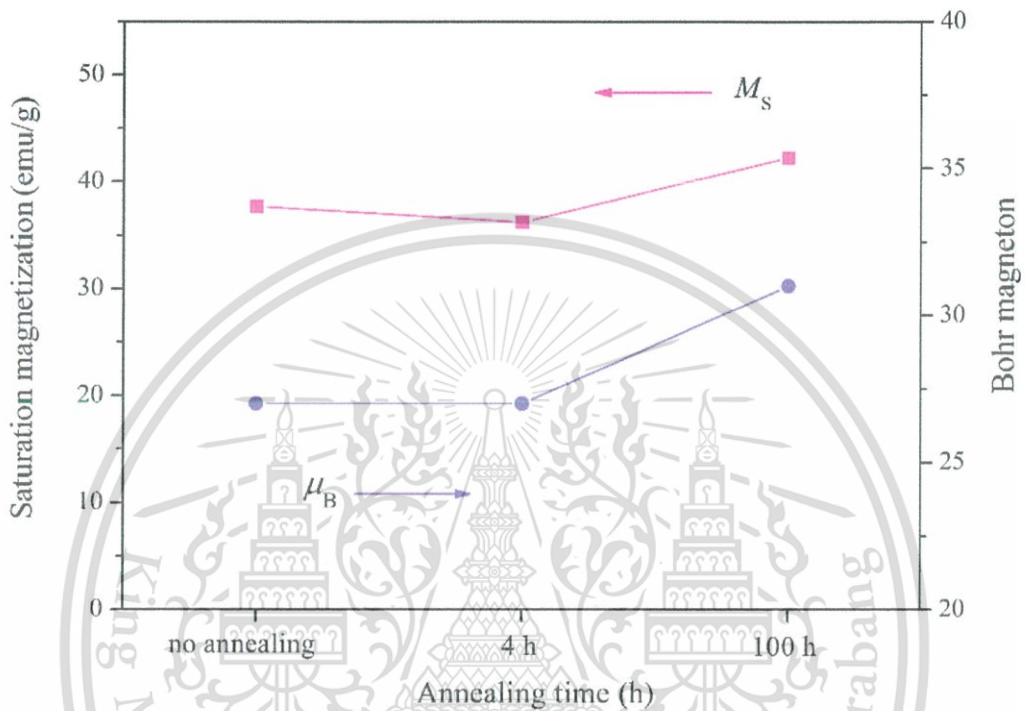


Figure 4.33 Variations of saturated magnetization and Bohr magneton for  $\text{CoFe}_{0.90}\text{Mn}_{1.10}\text{O}_4$  powders as a function of annealing time.

### 4.2.1.3 Cation Distribution

Then, the annealed and non-annealed samples were examined by X-ray absorption spectroscopy (XAS). Figure 4.34 shows the FT of Co, Fe, and Mn EXAFS data for the  $\text{CoFe}_{0.90}\text{Mn}_{1.10}\text{O}_4$  powders without annealing and with annealing at 500 °C for 4 and 100 h. The FT of the non-annealed Co EXAFS spectra is shown as a function of distance in Figure 4.34 (a). The non-annealed sample showed splitting in the first and second peak, with the ratio between the second peak being approximately equal. This showed that the Co cations occupied in A and B sites. Then, after annealing at 500 °C for 4 and 100 h, the amplitude trend of the peak at about 2.6 Å increased. This can be explained as the Co cations having migrated, thus the annealing time effected Co cation distribution.

Then, Fe EXAFS data as a function of the radial coordinate are shown in Figure 4.34 (b). The Fe EXAFS spectra of the sample showed splitting in the second peak before annealing. This peak was not perfectly symmetrical, and enlargement of the region between 2.6 Å indicated that Fe ions were occupied in the A and B sites. The amplitude peak of Fe ion at about 2.6 Å slightly changed after annealing at 500 °C for 4 and 100 h. This indicated that annealing times influenced Fe cation distribution.

Also, the examination of Figure 4.34 (c) indicated that the Mn EXAFS spectra without annealing sample showed the amplitude of a large peak centered near 2.6 Å, and this peak was not splitting. After annealing at 500 °C for 4 and 100 h, the peaks were not splitting. This exhibited that Mn cations did not migrate, it can be explained as the annealing time having had no effect on Mn cation distribution in the structure because the octahedral site preference energy of Mn cations (1.10 eV) strongly preferred the B site, although the very long annealing time did not change the cation distribution of Mn cations.

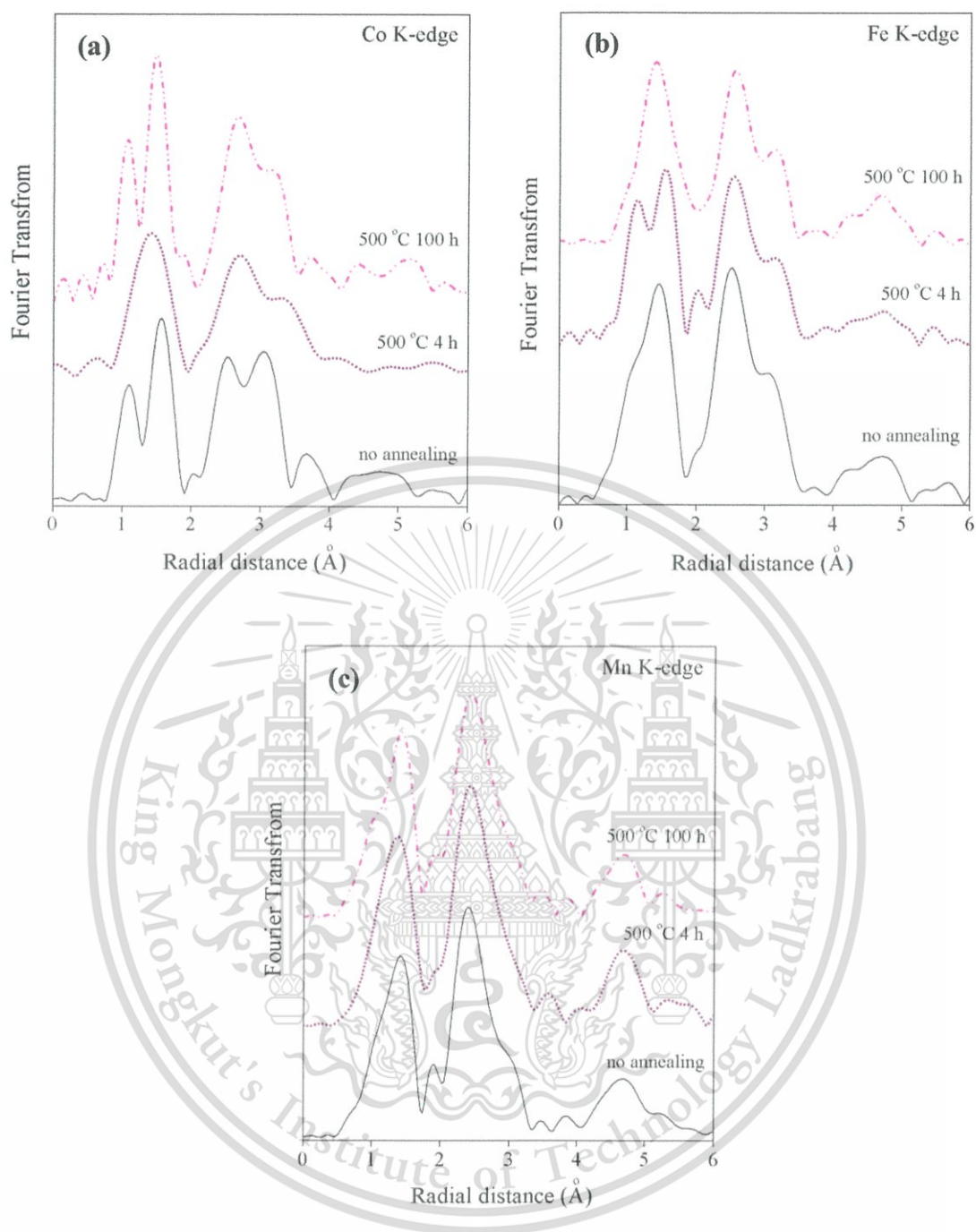


Figure 4.34 Fourier transformation of (a) Co, (b) Fe and (c) Mn EXAFS data for  $\text{CoFe}_{0.90}\text{Mn}_{1.10}\text{O}_4$  powders.

#### 4.2.1.4 Oxidation State

After the suitable annealing temperature was found, then the effect of atmosphere on the oxidation state was studied. Because the atmosphere differed during annealing, this had an influence on the oxidation state of Mn ions, which affects the magnetic properties as in the  $\text{MnFe}_2\text{O}_4$  research [23]. Therefore, the  $\text{CoFe}_{0.90}\text{Mn}_{1.10}\text{O}_4$  sample was annealed at 500 °C for 100 h in air,  $\text{N}_2$ , and  $\text{O}_2$ . After that, the annealing sample and the standard were examined in the valence state by XANES spectra using the X-ray absorption spectroscopy (XAS) technique.

The XANES spectra for the samples were measured at the Fe K-, Co K- and Mn K-edges at room temperature. As observed, the spectra for all samples were similar at each edge and their shift was not seen. Figure 4.35 (a) shows XANES spectra of  $\text{CoFe}_{0.90}\text{Mn}_{1.10}\text{O}_4$  sample annealing at 500 °C for 4 h in air, Co foil, CoO and  $\text{Co}_3\text{O}_4$  in the vicinity of the Co K-edge. The valence state of Co in the samples was determined from energy of the main maximal in the spectra ( $E_0$ ) [14]. The value of all samples and the standard are presented in Table 4.17. As observed, the spectra for the samples were similar to those obtained for the CoO standard, in which  $\text{Co}^{2+}$  was coordinated six-fold by  $\text{O}^{2-}$  ions, which suggested that Co ions existed in a divalent state in six coordinated oxygen atoms [15] and the  $\text{Co}^{2+}$  cations had  $3 \mu_B$ . XANES spectra at the Fe K-edge of the sample and standard compounds, this is shown in Figure 4.35 (b) and the  $E_0$  values are exhibited in Table 4.17. The results showed that the threshold energy of  $\text{CoFe}_{0.90}\text{Mn}_{1.10}\text{O}_4$  samples was higher than that of Fe foil, FeO and  $\text{Fe}_3\text{O}_4$ , but close to the energy of  $\text{Fe}_2\text{O}_3$ . They led to  $\text{Fe}^{3+}$  existing in the samples with  $5 \mu_B$ . Besides, XANES spectra at the Mn K-edge are shown in Figure 4.35 (c). The  $E_0$  of  $\text{CoFe}_{0.90}\text{Mn}_{1.10}\text{O}_4$ , Mn foil, MnO and  $\text{Mn}_2\text{O}_3$  is shown in Table 4.17. From the threshold region, the curves of the samples were close to that of  $\text{Mn}_2\text{O}_3$ , suggesting an existence of the trivalent state in octahedral coordination for oxygen atoms [14]. Besides, the  $4 \mu_B$  was found in the  $\text{Mn}^{3+}$  cations. The results showed that the annealing at differing atmospheres in this system did not change the oxidation state, which can be explained as the annealing having had no effect on the oxidation state. Although, in the Z. J. Zhang *et al.* [23] research, the authors reported that after annealing the  $\text{MnFe}_2\text{O}_4$  sample at 500 °C, the oxidation state of Mn cations were changed. However, sample preparation in Z. J. Zhang research was different from this research. Z. J. Zhang prepared their sample

This material is reserved for educational use only, not allowed for commercial use.

by the sol-gel method using a temperature of 200 °C in the preparation process. Then, after annealing at 500 °C, the oxidation states of Mn cations were changed. However, in this research, the high temperature (900 °C) was used in the sample preparation by solid state reaction method, so the oxidation states were not changed after annealing at 500 °C for 100 h.

**Table 4.17** The  $E_0$  value of  $\text{CoFe}_{0.90}\text{Mn}_{1.10}\text{O}_4$  sample annealed at 500 °C for 100 h in difference atmosphere and the various standard.

Sample	$E_0$ (eV)	Sample	$E_0$ (eV)	Sample	$E_0$ (eV)
Co foil	7709.06	Fe foil	7112.1	Mn foil	6539.02
$\text{Co}_3\text{O}_4$	7723.09	FeO	7123.23	MnO	6548.25
CoO	7720.23	$\text{Fe}_3\text{O}_4$	7125.89	$\text{Mn}_2\text{O}_3$	6553.40
$\text{CoFe}_{0.9}\text{Mn}_{1.1}\text{O}_4$ (Air)	7720.29	$\text{Fe}_2\text{O}_3$	7127.71	$\text{CoFe}_{0.9}\text{Mn}_{1.1}\text{O}_4$ (Air)	6553.29
$\text{CoFe}_{0.9}\text{Mn}_{1.1}\text{O}_4$ ( $\text{N}_2$ )	7720.09	$\text{CoFe}_{0.9}\text{Mn}_{1.1}\text{O}_4$ (Air)	7127.72	$\text{CoFe}_{0.9}\text{Mn}_{1.1}\text{O}_4$ ( $\text{N}_2$ )	6553.37
$\text{CoFe}_{0.9}\text{Mn}_{1.1}\text{O}_4$ ( $\text{O}_2$ )	7720.07	$\text{CoFe}_{0.9}\text{Mn}_{1.1}\text{O}_4$ ( $\text{N}_2$ )	7127.61	$\text{CoFe}_{0.9}\text{Mn}_{1.1}\text{O}_4$ ( $\text{O}_2$ )	6553.36
		$\text{CoFe}_{0.9}\text{Mn}_{1.1}\text{O}_4$ ( $\text{O}_2$ )	7127.52		

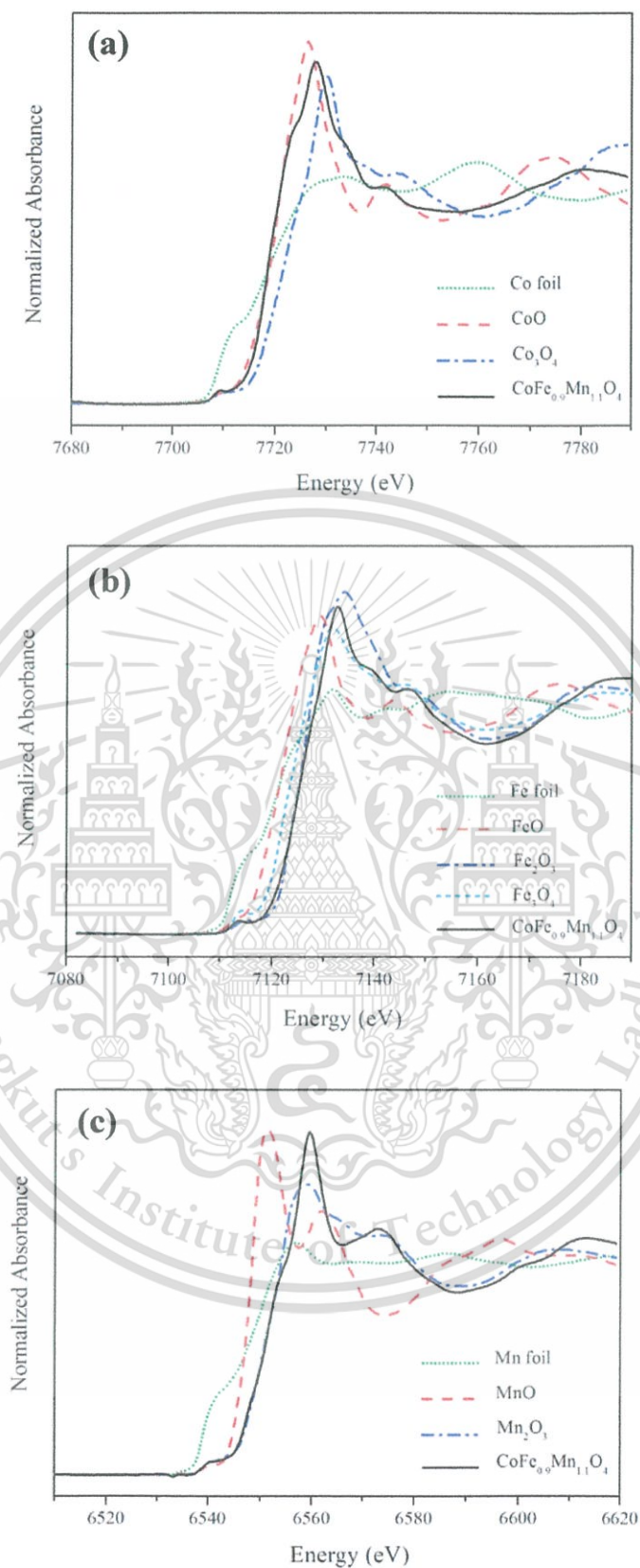


Figure 4.35 XANES spectra of CoFe<sub>0.90</sub>Mn<sub>1.10</sub>O<sub>4</sub> samples and the standards obtained at (a) Co K-edge, (b) Fe K-edge and (c) Mn K-edge.

This material is reserved for educational use only, not allowed for commercial use.

Forbidden to modify the content, and cite the document when use.

## 4.2.2 CoFe<sub>2-x</sub>Cu<sub>x</sub>O<sub>4</sub> System

The XRD results of CoFe<sub>2-x</sub>Cu<sub>x</sub>O<sub>4</sub> system showed the single phase of spinel, where  $x = 0.00-0.25$ . From the XRD results, the CoFe<sub>1.75</sub>Cu<sub>0.25</sub>O<sub>4</sub> sample would be annealed due to this composition being almost at the saturation point with excess Cu cations in the structure. As expected, cations in this sample will easily migrate to their preference site after thermal treatment for a long time. The CoFe<sub>1.75</sub>Cu<sub>0.25</sub>O<sub>4</sub> powders were annealed at 500 °C for 4, 100 h in air. And then the annealing samples were confirmed concerning their average particle sizes using a scanning electron microscopy (SEM) technique. Afterwards, the cation distribution and catalyst properties were investigated using the X-ray absorption spectroscopy (XAS) and ultraviolet-visible spectrophotometer (UV-Vis) technique, respectively.

### 4.2.2.1 Microstructure

The CoFe<sub>1.75</sub>Cu<sub>0.25</sub>O<sub>4</sub> sample was annealed and the microstructure was examined. Figures 4.36 (a)–(c) shows the morphology of CoFe<sub>1.75</sub>Cu<sub>0.25</sub>O<sub>4</sub> powders as a function without annealing, and with annealing at 500 °C for 4 and 100 h. Generally, the particles were irregular in shape and agglomerated. The average particle sizes of the powder were estimated from SEM micrographs and are presented in Table 4.18. The results showed that the average particle sizes of powders without annealing was  $0.81 \pm 0.59 \mu\text{m}$ , and sizes slightly decreased with annealing time. However, general average particle sizes still ranged from  $0.81 \pm 0.59$  to  $0.67 \pm 0.24 \mu\text{m}$ . This minor decreasing of average particle sizes certainly would not have a significant effect on cation distribution. These observations revealed that annealing time had no effect on average particle sizes. It can be explained, as the average particle sizes were controlled, and had no effect on magnetic and catalysts properties.

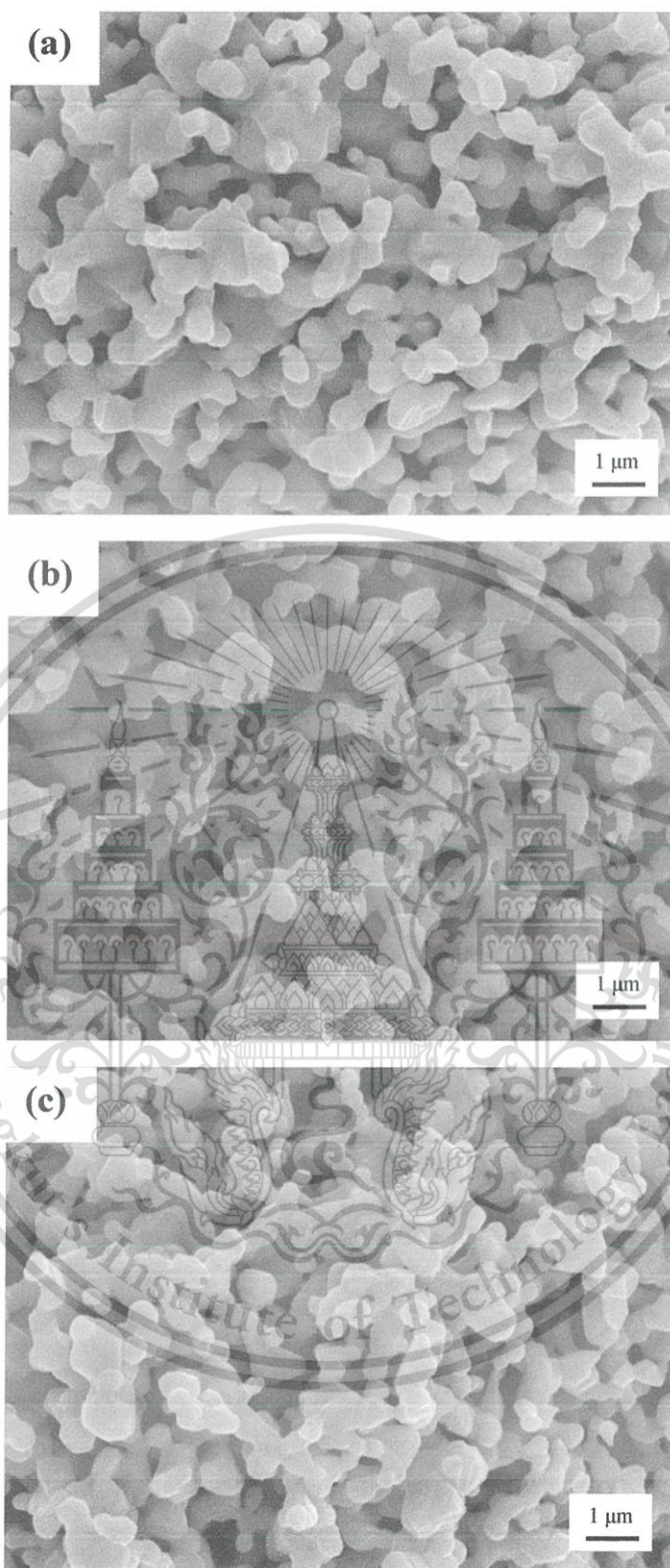


**Figure 4.36** SEM micrographs of  $\text{CoFe}_{1.75}\text{Cu}_{0.25}\text{O}_4$  powders with (a) no annealing, (b) annealing at 500 °C for 4 h and (c) annealing at 500 °C for 100 h.

**Table 4.18** Average particle size of  $\text{CoFe}_{1.75}\text{Cu}_{0.25}\text{O}_4$  as a function of annealing time.

Annealing time (h)	Average particle size ( $\mu\text{m}$ )
no annealing	$0.81 \pm 0.59$
4	$0.73 \pm 0.26$
100	$0.67 \pm 0.24$

#### 4.2.2.2 Cation Distribution

Then, the annealed and non-annealed samples were examined by X-ray absorption spectroscopy (XAS). Figure 4.37 shows the FT of Cu, Co, and Fe EXAFS data for the  $\text{CoFe}_{1.75}\text{Cu}_{0.25}\text{O}_4$  powders without annealing and with annealing at 500 °C for 100 h. The FT of the non-annealed Co EXAFS spectra is shown as a function of distance in Figure 4.37 (a). The Co EXAFS spectra without an annealed sample showed the amplitude of a large peak centered near 2.6 Å, this mean that Co cations occupied in B and A sites. After annealing at 500 °C for 100 h, the cation distribution trend of Co cations did not change. It showed that the Co cations were not migrating.

Then, Fe EXAFS data are shown in Figure 4.37 (b) as a function of the radial coordinate. The Fe EXAFS spectra of the sample showed splitting in the second peak before annealing. This peak was not perfectly symmetrical, and enlargement of the region between 2.6 Å indicated that Fe ions were localized at the B and A sites. The amplitude trend of the peak at about 2.6 Å slightly decreased after annealing at 500 °C for 100 h. This indicated that annealing times influenced the Fe ion distribution. The Fe cations migrated to A site after annealing, due to their low octahedral site preference energies (0.00 eV).

Also, interpretation of the Cu EXAFS spectra is shown in Figure 4.37 (c). The non-annealed sample showed splitting in the second peak. Then, after annealing at 500 °C for 100 h, the amplitude trend of the peak at about 2.6 Å increased. This can be explained as the Cu ions in the octahedral site increasing, which affected the

This material is reserved for educational use only, not allowed for commercial use.

annealing time on Cu cation distribution. After annealing, the migration of Cu cations on B site were clearly observed in the EXAFS spectra. Since, the octahedral site preference energies of Cu cations (0.68 eV) were higher than Co (0.09 eV) and Fe cations (0.00 eV) then Cu cations strongly preferred to occupy in the B site [24].



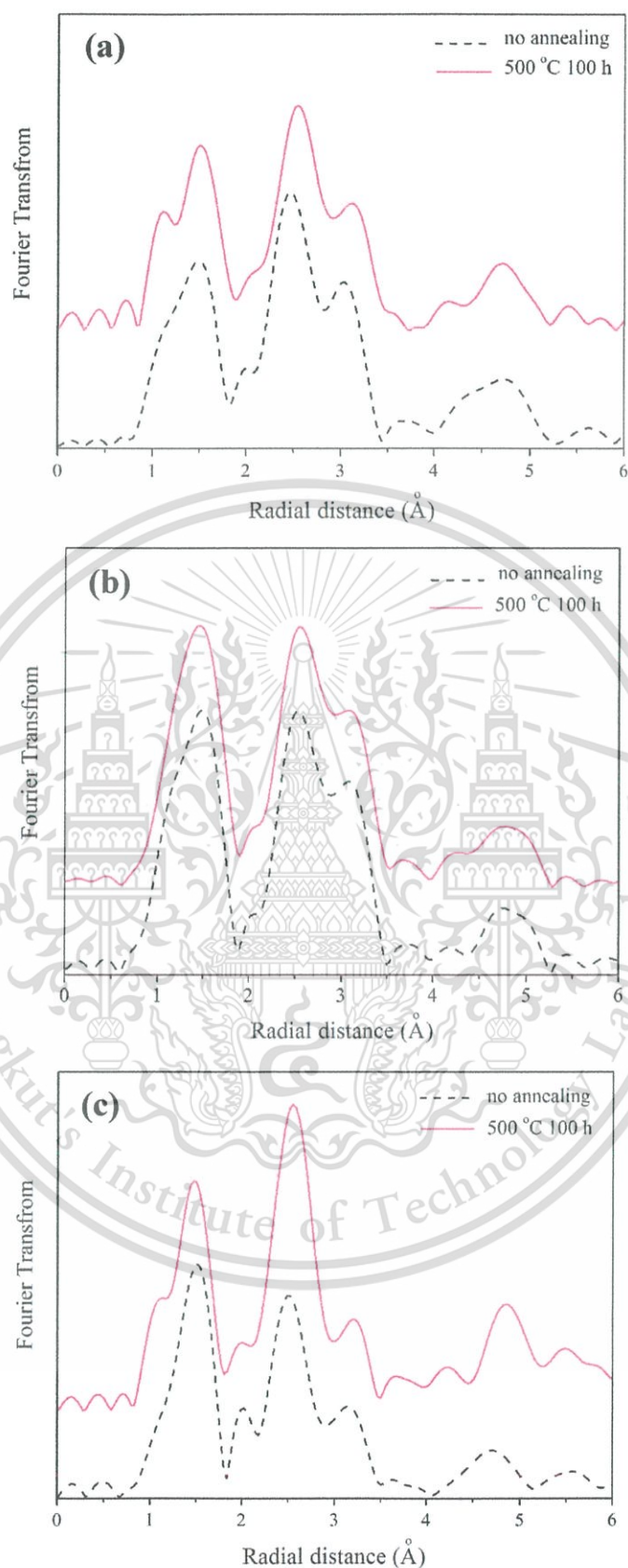


Figure 4.37 Fourier transformation of (a) Co, (b) Fe and (c) Cu EXAFS data for

$\text{CoFe}_{1.75}\text{Cu}_{0.25}\text{O}_4$  powders.

This material is reserved for educational use only, not allowed for commercial use.

Forbidden to modify the content, and cite the document when use.

### 4.2.2.3 Catalyst Properties

After annealing the  $\text{CoFe}_{1.75}\text{Cu}_{0.25}\text{O}_4$  sample at 500 °C for 4 and 100 h, the annealing samples were characterized by their catalyst properties. Figure 4.38 and Table 4.19 present the concentration and degradation percentage of reactive orange 16 in the  $\text{CoFe}_{1.75}\text{Cu}_{0.25}\text{O}_4$  catalysts without annealing and with annealing sample at 500 °C for 4 and 100 h. The results exhibited that the de-colorization of all samples after 1 h of incubation increased with increasing time. And then, the results pointed out that degradation after 24 h of the without annealing sample was 62.81 %. Also, in the sample with annealing for 4 h, the degradation percentage after 24 h did not change; this might not be enough time for the changing of cation distribution. However, after increasing the annealing time for 100 h, the de-colorization trend increased, the degradation percentage after 24 h was 72.09 %. This confirmed that annealing for a long time increased the degradation percentage. Since, in the de-colorization process, only cations in the octahedral site reacted to a catalyst in the solution. Due to low index planes in B (111) and D (110) (Figure 4.39) were on the surface in the spinel structure. From these planes, only cations in the octahedral site were on the surface and reacted with the synthesis dye [24]. The de-colorization results showed the increasing of degradation percentage in the annealing sample for 100 h. This can be explained; after annealing, Cu cations migrated to octahedral site. This result corresponded to the cation distribution results. Also, Cu ion (1.90) had a higher the redox potential than Co (1.88) and Fe cations (1.83), thus the degradation percentage was increased.

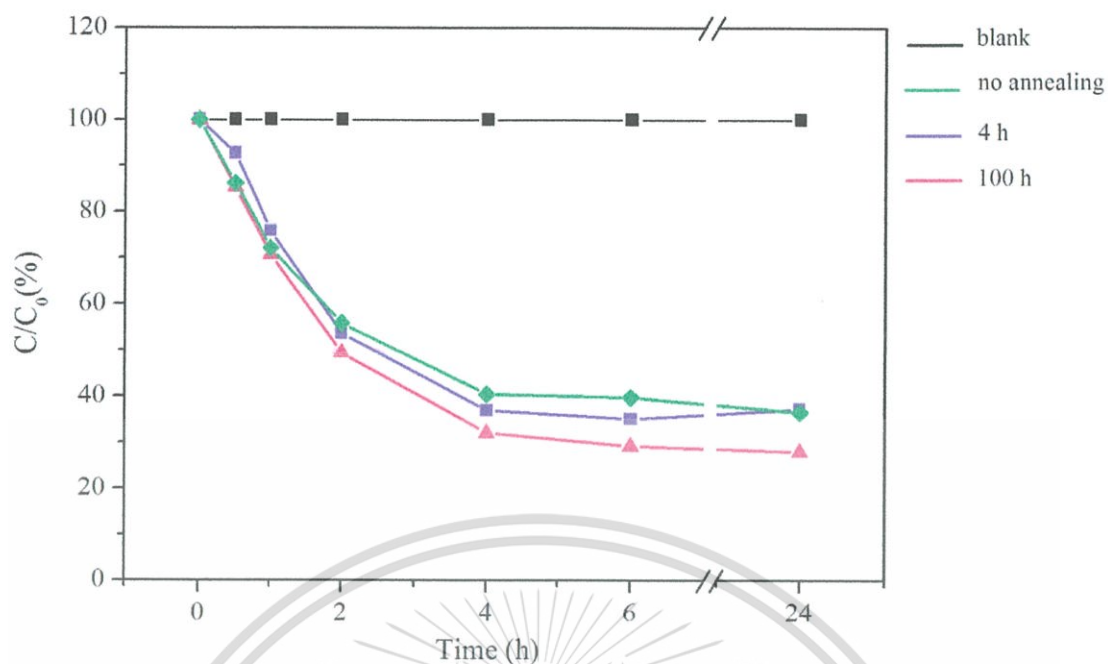
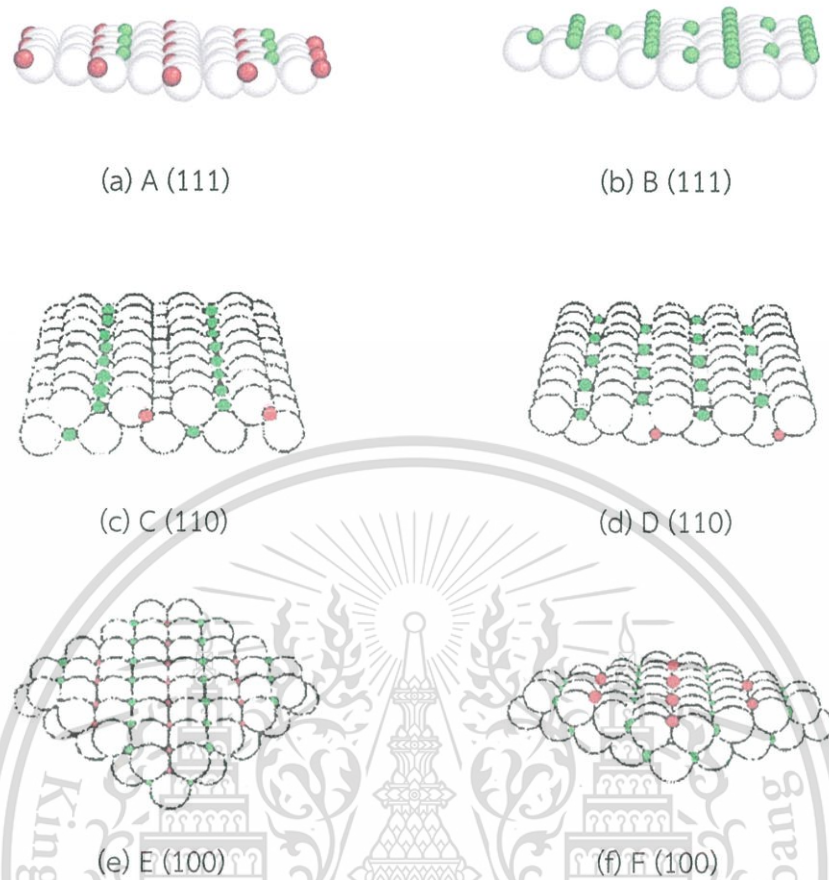


Figure 4.38 The degradation of reactive orange 16 in the  $\text{CoFe}_{1.75}\text{Cu}_{0.25}\text{O}_4$  catalysts without annealing and with annealing powder at  $500^\circ\text{C}$  for 4 and 100 h.

Table 4.19 Degradation of  $\text{CoFe}_{1.75}\text{Cu}_{0.25}\text{O}_4$  powders as a function of annealing time.

Annealing time (h)	$C/C_0$ (%)	Degradation (%)
no annealing	37.19	62.81
4	36.45	63.55
100	27.91	72.09



**Figure 4.39** The low index planes of spinel structure of (a) A (111), (b) B (111), (c) C (110), (d) D (110), (e) E (100), and (f) F (100). The white spheres represent the oxygen anions, the green spheres the octahedral cations and red spheres the tetrahedral cations [24].

### 4.2.3 CoFe<sub>2-x</sub>Zn<sub>x</sub>O<sub>4</sub> System

The XRD results of CoFe<sub>2-x</sub>Zn<sub>x</sub>O<sub>4</sub> system showed the single phase of spinel, where  $x = 0.00-0.55$ . From the XRD results, the CoFe<sub>1.45</sub>Zn<sub>0.55</sub>O<sub>4</sub> sample would be annealed due to this composition being almost at the saturation point with excess Zn cations in the structure. As expected, cations in this sample will easily migrate to their preference site after thermal treatment for a long time. The CoFe<sub>1.45</sub>Zn<sub>0.55</sub>O<sub>4</sub> powders were annealed at 500 °C for 4, 100 h in air. And then the annealing samples were confirmed, regarding their average particle sizes using scanning electron microscopy (SEM) technique. Afterwards, cation distribution was investigated using the X-ray absorption spectroscopy (XAS).

#### 4.2.3.1 Microstructure

The CoFe<sub>2-x</sub>Zn<sub>x</sub>O<sub>4</sub> sample was annealed and the microstructure was examined. Figures 4.40 (a)–(c) show the morphology of CoFe<sub>1.45</sub>Zn<sub>0.55</sub>O<sub>4</sub> powders as a function without annealing, and with annealing at 500 °C for 4 and 100 h. Generally, the particles were irregular in shape and generally agglomerated. The average particle sizes of the powder were estimated from SEM micrographs and are presented in Table 4.20. The results showed that the average particle sizes of powders without annealing was  $0.48 \pm 0.15 \mu\text{m}$ , and sizes slightly increased with annealing time. However, general average particle sizes still ranged from  $0.48 \pm 0.15$  to  $0.55 \pm 0.19 \mu\text{m}$ . This minor increasing in average particle size certainly would not have a significant effect on cation distribution. These observations revealed that annealing time had no effect on average particle sizes.

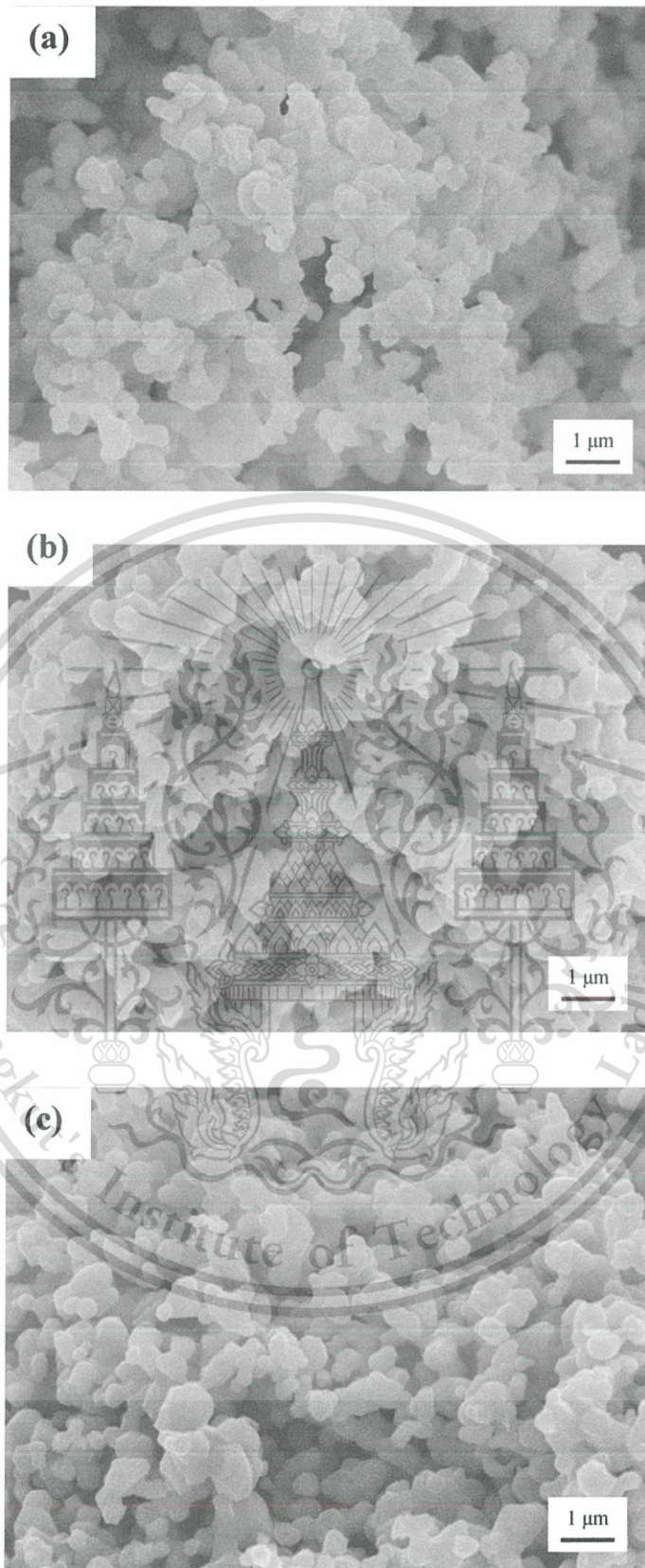


**Figure 4.40** SEM micrographs of  $\text{CoFe}_{1.45}\text{Zn}_{0.55}\text{O}_4$  powders with (a) no annealing, (b) annealing at  $500\ ^\circ\text{C}$  for 4 h and (c) annealing at  $500\ ^\circ\text{C}$  for 100 h.

This material is reserved for educational use only, not allowed for commercial use.

Forbidden to modify the content, and cite the document when use.

**Table 4.20** Average particle size of  $\text{CoFe}_{1.45}\text{Zn}_{0.55}\text{O}_4$  as a function of annealing time.

Annealing time (h)	Average particle size ( $\mu\text{m}$ )
no annealing	$0.48 \pm 0.15$
4	$0.54 \pm 0.20$
100	$0.55 \pm 0.19$

#### 4.2.3.2 Cation Distribution

Then, the annealed and non-annealed samples were examined by X-ray absorption spectroscopy (XAS). Figure 4.41 shows the FT of Zn, Fe, and Co EXAFS data for the  $\text{CoFe}_{1.45}\text{Zn}_{0.55}\text{O}_4$  powders without annealing and with annealing at 500 °C for 100 h. The FT of the non-annealed Co EXAFS spectra is shown as a function of distance in Figure 4.41 (a). The Co EXAFS spectra of the sample showed splitting in the second peak before annealing. This peak was not perfectly symmetrical, and enlargement of the region between 2.6 Å indicated that Co ions were localized at the B and A sites. The amplitude trend of Co ion distribution did not change after annealing at 500 °C for 100 h. It showed that the Co cations did not migrate.

Also, interpretation of the Fe EXAFS spectra is shown in Figure 4.41 (b) this indicated that the Fe EXAFS spectra without annealing sample showed a large peak at the center near 2.6 Å. This indicated that Fe cations were localized at the B and A sites. After annealing at 500 °C for 100 h, the cation distribution trend of Fe cations did not change. It means that the Fe cations did not migrate after annealing.

Zn EXAFS data are shown in Figure 4.41 (c) as a function of the radial coordinate. Before annealing, the second peak was at about 3.1 Å, and this peak did not split. This can be explained as the Zn cations occupying only in the A site. After annealing at 500 °C for 100 h, the amplitude trend of peak did not change. It presented that after annealing, Zn cations did not migrate due to the low octahedral site preference energies (0.00 eV). Therefore, after annealing the Zn ion still strongly preferred to occupy in the A site.

This material is reserved for educational use only, not allowed for commercial use.

Forbidden to modify the content, and cite the document when use.

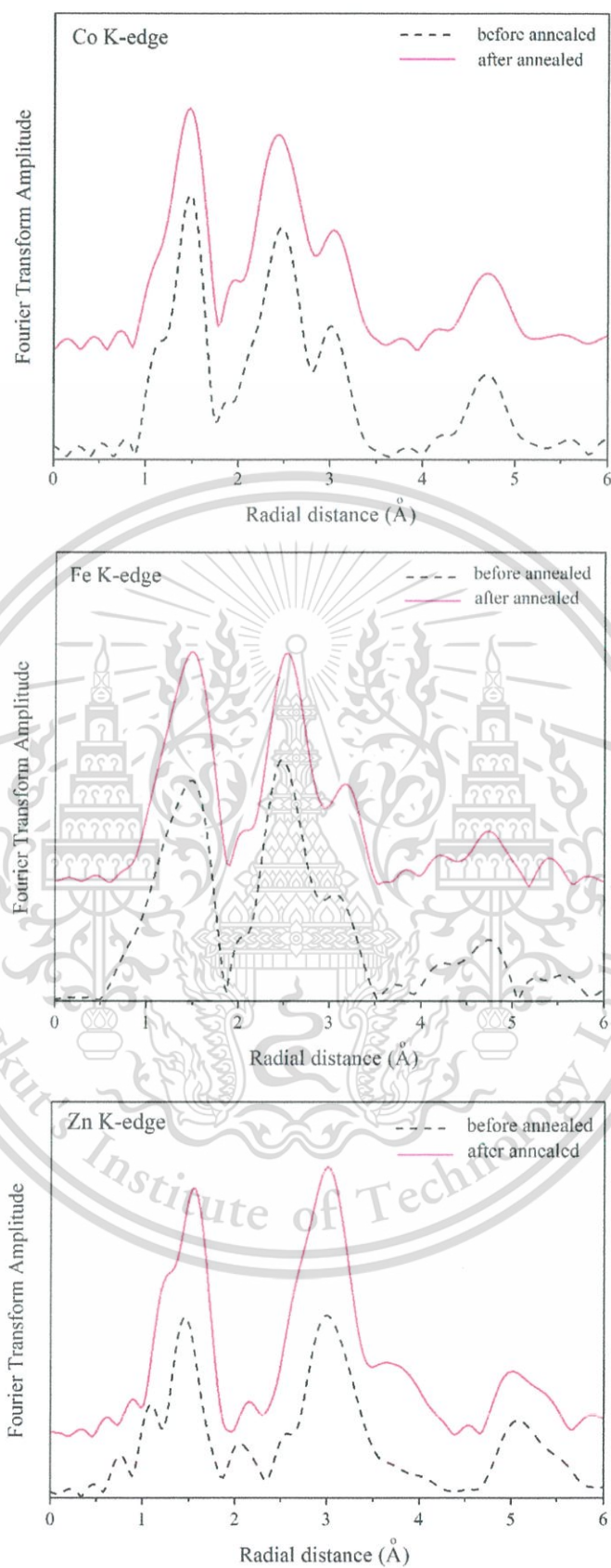


**Figure 4.41** Fourier transformation of Co, Fe and Zn EXAFS data for  $\text{CoFe}_{1.45}\text{Zn}_{0.55}\text{O}_4$  powders.

This material is reserved for educational use only, not allowed for commercial use.

Forbidden to modify the content, and cite the document when use.

### 4.3 References

- [1] Y. Köseoğlu, F. Alan, M. Tan, R. Yilgin and M. Öztürk, "Low temperature hydrothermal synthesis and characterization of Mn doped cobalt ferrite nanoparticles", *Ceram. Int.*, **38**, 3625-3634 (2012).
- [2] S. Parida, S. K. Rout, L. S. Cavalcante, E. Sinha, M. S. Li, V. Subramanian, N. Gupta, V. R. Gupta, J. A. Varela and E. Longo, "Structural refinement, optical and microwave dielectric properties of BaZrO<sub>3</sub>", *Ceram. Int.*, **38**, 2129-2138 (2012).
- [3] R. D. Shannon, "Revised Effective Ionic Radii and Systematic Studies of Interatomic Distances in Halides and Chalcogenides", *Acta Crystallogr.*, **A32**, 751-767 (1976).
- [4] A. J. Moulson and J. M. Herbert, *Electroceramics Materials and Application*, England, John Wiley & Sons, 2003.
- [5] O. Caltun, G. S. N. Rao, K. H. Rao, B. Parvatheeswara Rao, I. Dumitru, C.-O. Kim and C. Kim, "The influence of Mn doping level on magnetostriction coefficient of cobalt ferrite", *J. Magn. Magn. Mater.*, **316**, e618-e620 (2007).
- [6] W. D. Callister and D. G. Rethwisch, *Materials Science and Engineering*, USA, John Wiley & Sons, 2010.
- [7] M. Tachiki, "Origin of the Magnetic Anisotropy Energy of Cobalt Ferrite", *Prog. Theor. Phys.*, **23**, 1055-1072 (1960).
- [8] A. K. Patra, *Crystal structure, anisotropy and spin reorientation transition of highly coercive, epitaxial Pr-Co films*, Germany, Cuvillier Verlag.
- [9] A. K. Giri, E. M. Kirkpatrick, P. Moongkhamklang, S. A. Majetich and V. G. Harris, "Photomagnetism and structure in cobalt ferrite nanoparticles", *Appl. Phys. Lett.*, **80**, 2341 (2002).
- [10] V. G. Harris, N. C. Koon, C. M. Williams, Q. Zhang, M. Abe and J. P. Kirkland, "Cation distribution in NiZn-ferrite films via extended x-ray absorption fine structure", *Appl. Phys. Lett.*, **68**, 2082 (1996).
- [11] A. Goldman, *Modern Ferrite Technology*, USA, Pittsburgh, 2006.
- [12] M. Hashim, Alimuddin, S. Kumar, B. H. Koo, S. E. Shirsath, E. M. Mohammed, J. Shah, R. K. Kotnala, H. K. Choi, H. Chung and R. Kumar, "Structural, electrical and magnetic properties of Co–Cu ferrite nanoparticles", *J. Alloy. Compd.*, **518**, 11-18 (2012).

- [13] S. Y. An, I. S. Kim, S. H. Son, S. Y. Song, J. W. Hahn, S. W. Hyun, C. M. Kim and C. S. Kim, "Magnetic properties of  $\text{Cu}^{2+}$  substituted Co-ferrite", *Thin Solid Films*, **519**, 8296-8298 (2011).
- [14] G. Bonsel, M. A. Denecke, K. Schäfer, S. Christen, H. Langbein and W. Gunßer, "X-ray absorption spectroscopic and Mössbauer studies of redox and cation-ordering processes in manganese ferrite", *Solid State Ionics*, **101-103**, 351-357 (1997).
- [15] M. F. F. Lelis, A. O. Porto, C. M. Gonçalves and J. D. Fabris, "Cation occupancy sites in synthetic Co-doped magnetites as determined with X-ray absorption (XAS) and Mössbauer spectroscopies", *J. Magn. Mater.*, **278**, 263-269 (2004).
- [16] P. Baldrian, V. Merhautová, J. Gabriel, F. Nerud, P. Stopka, M. Hrubý and M. J. Benes, "Decolorization of synthetic dyes by hydrogen peroxide with heterogeneous catalysis by mixed iron oxides", *Applied Catalysis B: Environmental*, **66**, 258-264 (2006).
- [17] E. Casbeer, V. K. Sharma and X.-Z. Li, "Synthesis and photocatalytic activity of ferrites under visible light: A review", *Sep. Purif. Technol.*, **87**, 1-14 (2012).
- [18] Wikipedia. (2015). **Electronegativity**. Access April 3, 2015, Available from: <https://en.wikipedia.org/wiki/Electronegativity>
- [19] Y. Köseoğlu, A. Baykal, F. Gözüak and H. Kavas, "Structural and magnetic properties of  $\text{Co}_x\text{Zn}_{1-x}\text{Fe}_2\text{O}_4$  nanocrystals synthesized by microwave method", *Polyhedron*, **28**, 2887-2892 (2009).
- [20] R. C. Buchanan, *Ceramic Materials for Electronics*, USA, Marcel Dekker, 2004.
- [21] M. H. Nilsen, C. Nordhei, A. L. Ramstad, D. G. Nicholson, M. Poliakoff and A. Cabañas, "XAS (XANES and EXAFS) Investigations of Nanoparticulate Ferrites Synthesized Continuously in Near Critical and Supercritical Water", *J. Phys. Chem. C.*, **111**, 6252-6262 (2007).
- [22] H. M. I. Abdallah, T. Moyo and J. Z. Msomi, "The Effect of Annealing Temperature on the Magnetic Properties of  $\text{Mn}_x\text{Co}_{1-x}\text{Fe}_2\text{O}_4$  Ferrites Nanoparticles", *J. Supercond. Nov. Magn.*, **25**, 2625-2630 (2011).
- [23] Z. J. Zhang, Z. L. Wang, B. C. Chakoumakos and J. S. Yin, "Temperature Dependence of Cation Distribution and Oxidation State in Magnetic Mn-Fe Ferrite Nanocrystals", *J. Am. Chem. Soc.*, **120**, 1800-1804 (1998).

[24] R. Ramanathan. (2012). **Catalysis**. Access March 5, 2015, Available from: [http://shodhganga.inflibnet.ac.in/bitstream/10603/36877/07\\_chapter%201.pdf](http://shodhganga.inflibnet.ac.in/bitstream/10603/36877/07_chapter%201.pdf)



This material is reserved for educational use only, not allowed for commercial use.

Forbidden to modify the content, and cite the document when use.

## CHAPTER 5

# CONCLUSIONS

The series of  $\text{CoFe}_{2-x}\text{M}_x\text{O}_4$  ferrite, where  $\text{M} = \text{Mn, Cu, Zn}$ , at difference concentration were successfully synthesized by the solid state reaction method. The effect of the type of transition metal substitution, composition, and thermal annealing were studied. It has been demonstrated that these effect plays an important role in phase formation, morphology, and cation distribution including the magnetic and catalyst properties of these systems.

In the Mn doped cobalt ferrite, the phase development showed a single phase cubic spinel structure when  $x = 0.00-1.10$ . The Rietveld refinement confirmed lattice parameters that increased with doping Mn cation. The magnetic properties result revealed that the  $\text{CoFe}_{1.85}\text{Mn}_{0.15}\text{O}_4$  powders was the highest saturated magnetization and then decreased with increasing Mn concentration. Coercivity tend showed decreasing with Mn content. Furthermore, EXAFS spectra suggested that Mn cation preferred to occupy on B site and Co and Fe cation occupied both A and B site which it accorded to the octahedral site preference energy. Afterwards, the  $\text{CoFe}_{0.90}\text{Mn}_{1.10}\text{O}_4$  sample were studied the effect of thermal treatment. The microstructure showed that the average particle sizes did not change with annealing time and temperature. In addition, the difference atmosphere of annealing were no influence on the oxidation state of each cation. XANES spectra confirm that the structure contained  $\text{Co}^{2+}$ ,  $\text{Fe}^{3+}$  and  $\text{Mn}^{3+}$  ions. However, the saturated magnetization increased after annealing at  $500\text{ }^\circ\text{C}$  for 100 h in air. The EXAFS spectra revealed that Mn distribution after annealing still preference occupied in B site, while amplitude of Co EXAFS spectra increased the B site. This confirmed that, as a result of increased saturated magnetization, the suitable condition of thermal annealing affected on cation migration to the site preference.

In Cu doped  $\text{CoFe}_2\text{O}_4$  powders, the structural characteristics revealed that samples had a single phase spinel structure where  $x = 0.00-0.25$  while, Rietveld refinement data show decreasing lattice parameters with Cu cation concentration. The Cu doped cobalt ferrites showed lower saturated magnetization and lower

This material is reserved for educational use only, not allowed for commercial use.

Forbidden to modify the content, and cite the document when use.

coercivity than pure cobalt ferrite due to Bohr magneton of Cu cations were lower than Co and Fe ions. Nevertheless, trend of degradation percentages increased with increasing Cu content because the redox potential of Cu cations is higher than of Co and Fe ion. And, XANES spectra suggested that  $\text{Co}^{2+}$ ,  $\text{Fe}^{3+}$  and  $\text{Cu}^{2+}$  ions were the valence states of element in the structure. The cation distribution results showed that Co and Fe cation occupied both A and B site, but the Cu cation almost occupied in the B site due to the octahedral site preference energy of Cu was larger than Co and Fe cation. Then, the  $\text{CoFe}_{1.75}\text{Cu}_{0.25}\text{O}_4$  sample was annealed. The unchanged average particle sizes of non-annealed and annealed samples were confirmed. Furthermore, the degradation result increased after annealing at 500 °C for 100 h. The EXAFS spectra exhibited increasing of Cu cation in B site which it influenced from thermal treatment.

Finally, zinc doped  $\text{CoFe}_2\text{O}_4$  powders were synthesized successfully by the mixed-oxide method. The structural characteristics revealed that samples where  $x = 0.00-0.55$  have a single spinel structure. And, Rietveld refinement showed that the lattice parameters were decreased by Zn content, whereas the average particles size increased. VSM measurements showed that saturated magnetization of the samples increased when  $x = 0.10-0.20$  and then decreased, it is contained at maximum in  $\text{CoFe}_{1.9}\text{Zn}_{0.1}\text{O}_4$  powders. The value of coercivity decreased with zinc doped concentration. Additionally, the  $\text{Co}^{2+}$ ,  $\text{Fe}^{3+}$ , and  $\text{Zn}^{2+}$  ions are the valence states of element in the structure. Then, the EXAFS results presented that Zn cation preferred to occupy in the A site, while Co and Fe ion occupied both A and B site with according to the octahedral site preference energy. The  $\text{CoFe}_{1.45}\text{Zn}_{0.55}\text{O}_4$  sample were annealed and investigated, it can be confirmed from the morphology that the average particle size before and after annealing remained unchanged. Furthermore, the distribution of Zn, Co, and Fe cations were slightly differenced after annealing at 500 °C for 100 h in air.



This material is reserved for educational use only, not allowed for commercial use.

Forbidden to modify the content, and cite the document when use.

## Effect of Annealing Time on the Cation Distribution in Mn Doped $\text{CoFe}_2\text{O}_4$

RACHANUSORN ROONGTAO,<sup>1,2</sup> NARATIP VITAYAKORN,<sup>1,3</sup>  
WANTANA KLYSUBUN,<sup>2</sup> AND WANWILAI C. VITAYAKORN<sup>1</sup>

<sup>1</sup>Electroceramic Research Laboratory, College of Nanotechnology, King Mongkut's Institute of Technology Ladkrabang, Bangkok 10520, Thailand

<sup>2</sup>National Synchrotron Research Center, 111 University Avenue, Muang District, Nakhon Ratchasima 30000, Thailand

<sup>3</sup>Advanced Materials Science Research Unit, Department of Chemistry, Faculty of Science, King Mongkut's Institute of Technology Ladkrabang, Bangkok 10520, Thailand

*In this work, the series of  $\text{CoFe}_{2-x}\text{Mn}_x\text{O}_4$  powders were synthesized using the solid state method. The structure and lattice parameter of the samples were determined by the X-ray diffraction (XRD) and Rietveld refinement method. The morphology was confirmed without annealing and with annealing at 500°C for 4 and 100 h, with the samples examined by scanning electron microscopy (SEM). Then, the distribution of migrating cations was analyzed using X-ray absorption spectroscopy (XAS). Also, magnetic properties were examined by a vibrating sample magnetometer (VSM). It can be confirmed from the morphology that the average particle size before and after annealing remained unchanged, and ranged from  $0.66 \pm 0.20 \mu\text{m}$  to  $0.79 \pm 0.26 \mu\text{m}$ . Furthermore, the distribution of cations was no different after annealing Mn ions at 500°C for 100 h. However, the distribution of cations migrated to their site of preference after annealing Co and Fe ions in the structure. The result of migrations induced a saturated magnetization increase to 42.24 emu/g.*

**Keywords** Cation distribution; X-ray absorption; EXAFS; cobalt ferrite; annealing

### 1. Introduction

Cobalt ferrite is an inverse spinel and important technological material, which exhibits moderate saturated magnetization (about 80 emu/g) and high coercivity (5400 Oe) as well as high resistance to wear and significant mechanical hardness [1–2]. In addition, the partial substitutions of Mn were found to be appropriate for magnetomechanical, embedded high magnetostriction applications and stress-sensing [3–4], since magnetic, electronic, and catalytic physical and chemical properties depend on cation distribution among the octahedral (B) and tetrahedral (A) sites. Thus, deciding on cation distribution between octahedral and tetrahedral sites in spinel ferrites plays an important role in determining the use of these materials, and has been the subject of many studies [5–7]. It is

Received October 26, 2014; in final form February 15, 2015.

Corresponding author: E-mail: wvittayakorn@yahoo.com

Color versions of one or more figures in this article can be found online at [www.tandfonline.com/gfer](http://www.tandfonline.com/gfer).

acknowledged that causes of cation distribution over the spinel structure are composed of [8] particle size [9–10], synthetic methods [11], annealing temperature [12], octahedral site preference energy [13], size of interstices and ionic radii of ions, and annealing time [14].

V. G. Harris *et al.* [8] studied cation distribution in NiZn ferrite films, where Zinc concentration varied. The results showed that the Zinc cations occupied the A site only. The Fe cations were found to occupy both the B and A site, as did Nickel ions, but with a preference for the B site. Harris *et al.* believed that a large portion of the A site Nickel ions was natural to the thin film structure. Then, J. A. Gomes *et al.* [11] investigated cation distribution on the A and B site of copper ferrite nanoparticles that were prepared by coprecipitation and compared with copper ferrite by using the standard method. As a result, the nanoparticle sample presented dissimilar cation redistribution from the theory of copper ferrite, as it performed different cation distribution over A and B sites in ferrite, which was related to the different particle sizes obtained with various synthetic routes. Also, Z. J. Zhang *et al.* [12] determined the cation distribution in Mn ferrite spinel nanoparticles, using neutron diffraction at various temperatures. The Rietveld method was used for fitting in order to obtain the cation distribution. The results of refinement suggest portions of Mn and Fe are on both the B and A site. Furthermore, the cation distribution can be modified by heat treatment in a vacuum. The literature reviews did not contain information about the effect of annealing time on the cation distribution of spinel ferrites. Thermal annealing was efficient noticeably on dielectric properties, ferroelectric properties, and crystal structure similar to PZT–PZN ceramic. A research by N. Vittayakorn *et al.* [15] prepared PZT–10PZN powders using the columbite precursor method. Thermal annealing was efficient noticeably when improving piezoelectric responses and dielectric PZT based ferroelectric ceramics. It also proved that annealing time has an influence on the electrical properties in 0.9PZT–0.1PZN ceramics.

Therefore, this work aimed to study the influence of annealing time on cation distribution in cobalt ferrite synthesized by a conventional mixed-oxide method. The samples were prepared by excess Mn doped cobalt ferrite, and the single phase ferrite composition was used to investigate the cation distribution in the structure. This composition made the cation sites apparent when the structure was restricted. Furthermore, transference of the cation to the preferred site was expected when the samples were annealed for a very long time. Also, control of the same average particle size of the samples was desirable for eliminating other effects of cation distribution. Thus, the samples were annealed at 500°C, due to the annealing temperature being controlled at their same average particle size, even if the annealing time took a long time. In addition, the annealing time was used for up to 100 h, due to expectation that a long annealing time would be suitable for cations changing between A and B sites.

A variety of probes can be considered for information on cation distribution; for instance, X-ray diffraction, Mössbauer spectroscopy and neutron diffraction. However, the neutron diffraction and X-ray diffraction used were limited by the low percentage of composition in the samples. Mössbauer spectroscopy was effective in deciding the surroundings of Fe ions, but did not provide information on the Mn cations and Co cation because the main purpose of this research was to emphasize cation site distribution for the structural study of spinel ferrite. Hence, extended X-Ray absorption fine structure (EXAFS) spectroscopy was chosen to detail information on the effect of annealing temperatures on manganese-doped cobalt ferrite, since EXAFS is seen as a powerful technique for presenting element specificity, chemical sensitivity and local structure. In

addition, EXAFS has been found recently as a useful method for investigating the cation distribution in spinel ferrites [7–8].

Consequently, this research focused on studying the effect of annealing time on cation distribution in Mn doped cobalt ferrite by using the X-ray absorption spectroscopy (XAS) technique. The crystal structures of  $\text{CoFe}_{2-x}\text{Mn}_x\text{O}_4$  powders and confirmation of average particle size by scanning electron microscope (SEM) were reported. Furthermore, the magnetic properties between before and after annealing were discussed.

## 2. Experimental Procedure

Samples of the  $\text{CoFe}_{2-x}\text{Mn}_x\text{O}_4$  system, where  $x = 0.00, 0.10, 0.20, 1.00, 1.10,$  and  $1.15$ , were prepared by a mixed-oxide method. The reagent grades of  $\text{Fe}_2\text{O}_3$  (Sigma-Aldrich,  $\geq 99.0\%$  purity),  $\text{Co}_3\text{O}_4$  and  $\text{Mn}_2\text{O}_3$  (Aldrich,  $\geq 99.0\%$  purity) were used as starting materials. The raw materials were weighed and mixed by the ball milling technique for 24 h in a PVC container using an alumina ball and ethanol as the medium. The mixed powders were dried in a hot oven and calcined at  $900^\circ\text{C}$  for 48 h with a heating/cooling rate of  $5^\circ\text{C}/\text{min}$  in an alumina crucible in air. The calcined powders were well ground using an agate mortar, and an X-ray diffractometer (XRD), Philips-XPert MPD, was employed at room temperature to identify the phase formation for all samples.  $\text{Cu K}\alpha$  radiation was applied with a step size of  $0.02^\circ$  and a scan rate of 3 s per step. Lattice parameters of the materials were determined from XRD patterns by the Rietveld refinement method using the FullProf program. The influence of thermal annealing was identified by the  $\text{CoFe}_{0.90}\text{Mn}_{1.10}\text{O}_4$  powders being annealed at  $500^\circ\text{C}$  for 4 and 100 h with a heating/cooling rate of  $5^\circ\text{C}/\text{min}$ . The unchanging average particle sizes were confirmed by scanning electron microscopy (SEM), Hitachi S4700, with an accelerating voltage of 5 kV. The cation distribution without annealing and with annealing at  $500^\circ\text{C}$  for 4 and 100 h was characterized using EXAFS data from the Co K-edge (7709 eV), Fe K-edge (7112 eV), and Mn K-edge (6539 eV) in the transmission mode at room temperature, in the Siam Photon Laboratory at the XAS facility (BL-8), Synchrotron Light Research Institute. Also, magnetization measurements before and after annealing the samples were measured by a vibrating sample magnetometer (VSM) under a maximum applied magnetic field of 8 kOe at room temperature.

## 3. Results and Discussion

Figure 1 displays the X-ray diffraction of  $\text{CoFe}_{2-x}\text{Mn}_x\text{O}_4$  powders at various compositions and calcined at  $900^\circ\text{C}$  for 48 h. The XRD patterns showed that peaks (when  $x = 0.00$ – $1.10$ ) were of a single phase cubic structure and corresponded to JCPDS file no. 22–1086 and space group  $\text{Fd}3\text{m}$  (no. 227) [16]. However, the XRD pattern of the  $\text{CoFe}_{0.85}\text{Mn}_{1.15}\text{O}_4$  powder detected secondary phases, which were  $\text{Fe}_3\text{O}_4$ ,  $\text{Fe}_2\text{O}_3$  and  $(\text{Co}, \text{Mn})(\text{Mn}, \text{Co})_2\text{O}_4$  that corresponded to JCPDS file no. 28–0491, 25–1402 and 18–0409, respectively. Therefore, only single phase samples were used to investigate the lattice parameters, which were analyzed from XRD data by the Rietveld refinement method using the FullProf program, and the variation of lattice constants and results of a quantitative phase analysis from the refinement with  $\text{Mn}^{2+}$  doping are presented in Table 1. The structure refinement showed the corresponding fits and confirmed that the structure was cubic type. Data quality of structural refinement was checked basically by R-values ( $R_w$ ) and a good fit ( $\chi^2$ ). In addition, the distinction between XRD patterns, calculated data and experimental profiles displayed small value in the intensity scale, as

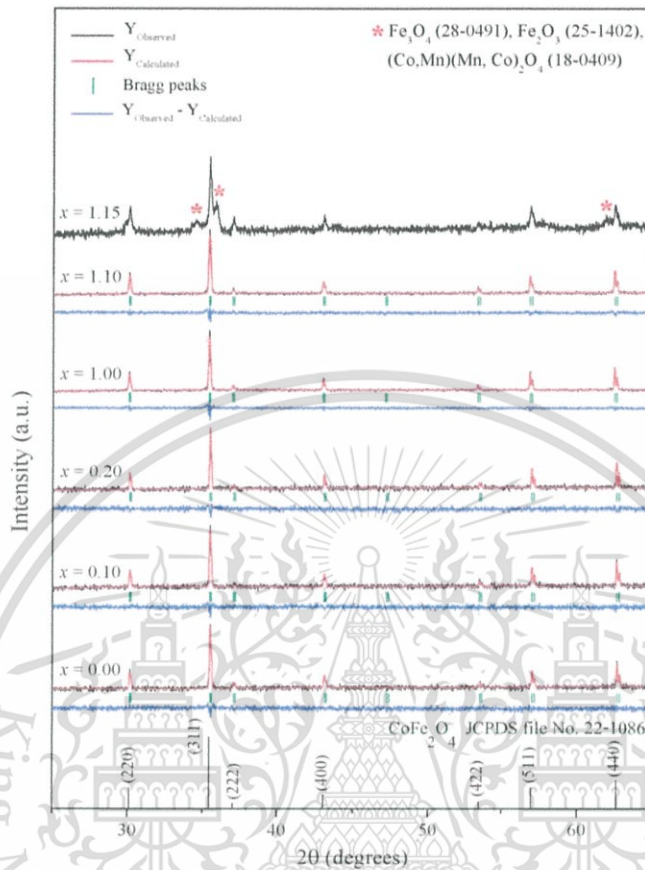


Figure 1. X-ray diffraction patterns of  $\text{CoFe}_{2-x}\text{Mn}_x\text{O}_4$  powders calcined at  $900^\circ\text{C}$  for 48 h.

illustrated by the line,  $Y_{\text{Observed}} - Y_{\text{Calculated}}$  [17]. Furthermore, the results showed that the lattice constant and unit cell volume for each composition increased with increasing Mn ion, and gradually exhibited an almost linear dependence and linear regression with  $R^2 = 0.9940$ , which is in accordance with Vegard's law [16]. This showed that powders in the system are completed for continuous substitution, where atoms or ions existed [16]. The lattice parameter increased with doping, due to the ionic

Table 1

Lattice constant ( $a$ ) and Rietveld refinement result of  $\text{CoFe}_{2-x}\text{Mn}_x\text{O}_4$  powders calcined at  $900^\circ\text{C}$  for 48 h

$X$	$a$ (Å)	$V$ ( $10^6 \text{ pm}^3$ )	$R_w$ (%)	$\chi^2$
0.00	8.3843 (6)	589.010	4.01	1.11
0.10	8.3884 (6)	589.879	4.19	1.13
0.20	8.3904 (5)	590.401	4.45	1.19
1.00	8.4094 (3)	594.687	2.81	1.56
1.10	8.4103 (4)	594.893	2.62	1.33

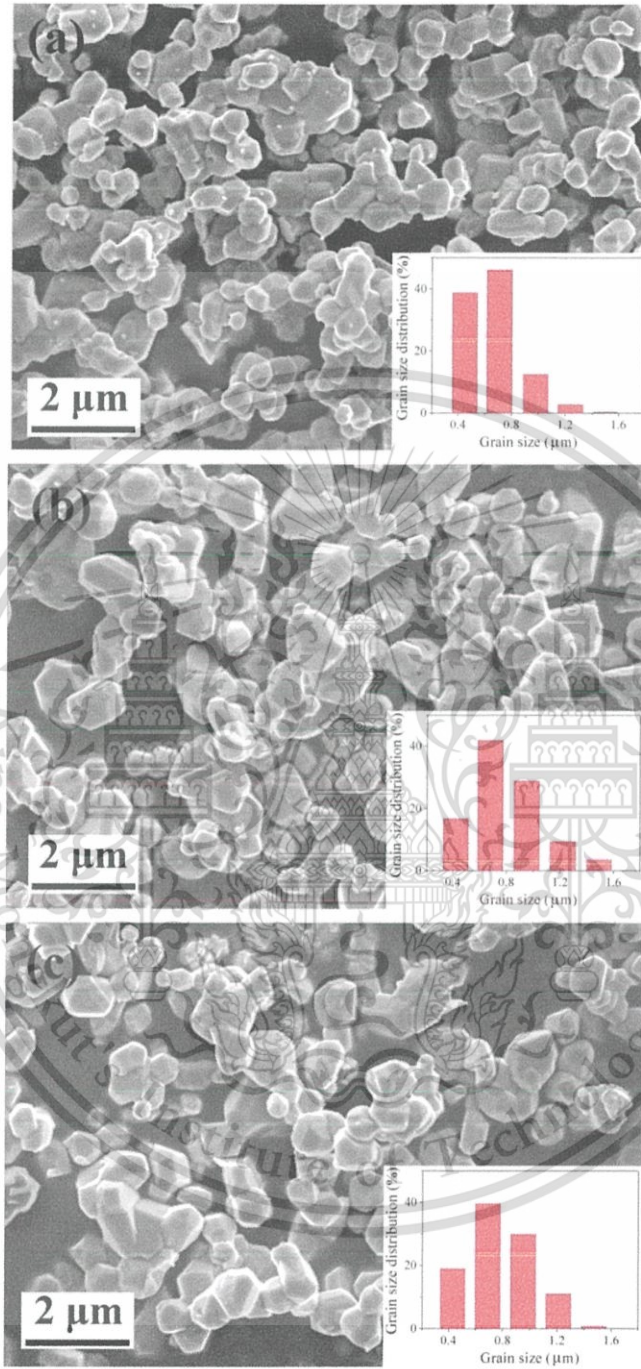


**Figure 2.** SEM micrographs of  $\text{CoFe}_{0.90}\text{Mn}_{1.10}\text{O}_4$  powders with (a) no annealing, (b) annealing at 500°C for 4 h and (c) annealing at 500°C for 100 h.

**Table 2**  
Average particle size, saturated magnetization, and coercivity of  $\text{CoFe}_{0.9}\text{Mn}_{1.1}\text{O}_4$  powders as a function of annealing time.

Annealing time (h)	Average particle size ( $\mu\text{m}$ )	$M_s$ (emu/g)	$H_c$ (Oe)
no annealing	$0.66 \pm 0.20$	37.67	130.43
4	$0.79 \pm 0.25$	36.21	161.58
100	$0.79 \pm 0.23$	42.24	169.37



**Figure 3.** Fourier transformation of (a) Co, (b) Mn and (c) Fe EXAFS data for  $\text{CoFe}_{0.9}\text{Mn}_{1.1}\text{O}_4$  powders.

radius of Mn coordinating six-fold with  $\text{O}^{2-}$  ions, which were larger than the ionic radius of Fe coordinating six-fold with  $\text{O}^{2-}$  ions in the structure [18].

The XRD results indicated that the  $\text{CoFe}_{0.90}\text{Mn}_{1.10}\text{O}_4$  powders would be annealed, due to their composition having excess Mn dope in the structure. As expected, the cations in this composition were migrated easily to a preferred cation site when taking enough annealing time. Then, the  $\text{CoFe}_{0.90}\text{Mn}_{1.10}\text{O}_4$  powders were annealed at  $500^\circ\text{C}$  for 4 and 100 h, with the average particle sizes confirmed by scanning electron microscope (SEM).

Figures 2 (a)–(c) show the morphology and particle size distribution of  $\text{CoFe}_{0.90}\text{Mn}_{1.10}\text{O}_4$  powders as a function without annealing, and with annealing at  $500^\circ\text{C}$  for 4 and 100 h. Basically, the particles were of irregular shape and generally agglomerated. The average particle sizes of the powder were estimated from SEM micrographs and are presented in Table 2. The results showed that the average particle sizes did not change with annealing time, and they ranged from  $0.66 \pm 0.20 \mu\text{m}$  to  $0.79 \pm 0.23 \mu\text{m}$ . Furthermore, all samples showed small particle size distribution, as observed in the figures. The size distribution of powders without annealing mainly ranged from 0.57 to  $0.83 \mu\text{m}$ , and slightly increased with annealing time. However, general size distribution still ranged from 0.57 to  $0.83 \mu\text{m}$ . This minor increase in size distribution certainly would not have significant effect on cation distribution. These observations revealed that annealing time has no effect on average particle sizes, which affect cation distribution.

Then, the annealed and non-annealed samples were examined by X-ray absorption spectroscopy (XAS). EXAFS investigation determined the local bonding surrounding the Co, Fe and Mn. Spectra that encompassed the Co (7709 eV), Fe (7112 eV) and Mn (6539 eV) K-edges over an energy range from 100 eV below the energy edge to 800 eV above it. The information was examined by following standard EXAFS processing, which led to the Fourier transformation (FT) of information to radial coordinates. In this form, peak amplitudes reflected the occupancy of atomic shells, and the radial coordinate of the peak reflected the distance of atom shells from the absorber, which was not corrected for natural electron phase shift to XAS. [9]. Figure 3 shows the FT of Co, Fe, and Mn EXAFS data for the  $\text{CoFe}_{0.90}\text{Mn}_{1.10}\text{O}_4$  powders without annealing and with annealing at  $500^\circ\text{C}$  for 4 and 100 h. The FT from a  $\Delta k$  range of between 2 and  $10 \text{ \AA}^{-1}$ , with  $k^2$  weighting of the non-annealed Co EXAFS spectra, is shown as a function of distance in Figure 3 (a). This fact could be seen better when noticing the two maximum intense peaks. The first one centered near  $1.5 \text{ \AA}$  presented the first shell with oxygen around the Co atoms. The second one centered near  $2.8 \text{ \AA}$ , which corresponded to the next shell neighboring the Co atoms. The first peak showed splitting; the nearest metal Co-O bond neighbor appeared at  $r$  about  $1.4 \text{ \AA}$ , according to the tetrahedral coordinating cation, whereas the oxygen bond near  $1.9 \text{ \AA}$  corresponded to the octahedral coordinating cation. The second peak also showed splitting; the peak centered near  $r$  about  $2.6 \text{ \AA}$  corresponded to the Co-Co distance. This unique fingerprint identified the absorbing ion occupying the octahedral (B) sites, due to both scattering and absorbing atom occupancy on octahedral site contributions. The peak centered near  $3.1 \text{ \AA}$  absorbed the tetrahedral (A) sublattice, including contributions from  $\text{Co}_A\text{-}M_A$ ,  $\text{Co}_A\text{-O}$ ,  $\text{Co}_A\text{-}M_B$ , and  $\text{Co}_B\text{-O}$  correlations ( $M$  is metal), but the identification was not unique. Therefore, related amplitudes of these peaks indicate qualitative distribution of the absorption cation at the B and A site [8–9, 14]. The non-annealed sample [Figure 3 (a)] shows splitting in the first and second peak, with the ratio between the second peak being approximately equal. Then, after annealing at  $500^\circ\text{C}$  for 4 and 100 h [Figure 3 (a)], the trend of amplitude in the second peak split associated only with the increased B site contribution at about  $2.6 \text{ \AA}$  [Figure 4 (a)]. This can be explained by the increment of Co ions surrounding the octahedral site

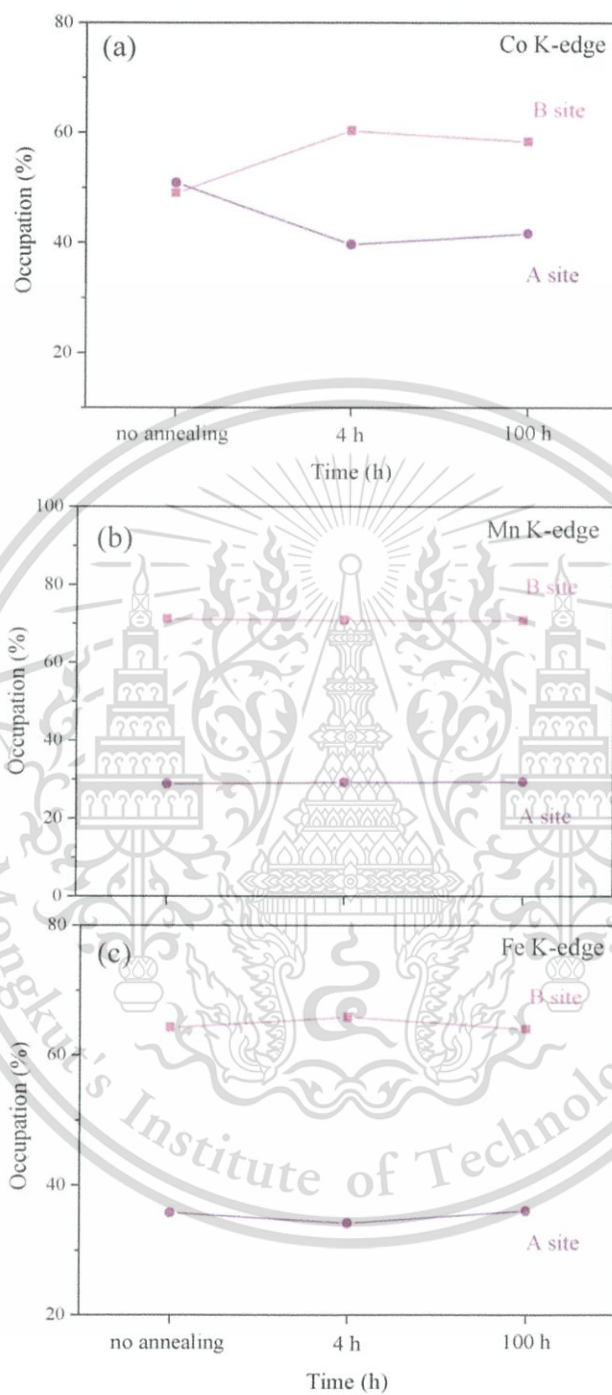


**Figure 4.** Trends in site occupation determined from amplitude as a function of annealing time for (a) Co, (b) Mn and (c) Fe K-edge.

that affects the annealing time for cation distribution. After annealing, the migration of Co ions to the B site was observed clearly in the EXAFS spectra because the cation distribution was determined by the preferred cation site, which related to the octahedral site preference energy (OSPE). The OSPE was estimated from a variety of thermodynamic data, in which the OSPE of Co ions exhibited a preference for B sites [11].

Also, interpretation of the Mn EXAFS spectra was related to the previous investigation carried out on the Co EXAFS. Examination of Figure 3 (b) and 4 (b) indicated that the Mn EXAFS spectra without an annealed sample showed the amplitude of a large peak centered near 2.6 Å of non-annealed powders that were relative to the B site contribution only. After annealing at 500°C for 4 and 100 h, the migration of Mn cations did not change, which can be explained by the annealing time having no effect on Mn ion distribution in the structure. Due to OSPE, Mn ions preferred the A or B site when taking a long annealing time, and the cation distribution trend did not change.

Then, Fe EXAFS data were shown in Figure 3 (c) and 4 (c) as a function of the radial coordinate. The Fe EXAFS spectra of the sample showed splitting in the second peak before annealing. This peak was not perfectly symmetric, and enlargement of the region between 2.6 Å indicated that Fe ions were localized at the B site. The amplitude trend of Fe ion distribution, which was relative to the B-site contribution only, decreased slightly after annealing at 500°C for 4 and 100 h. This indicated that annealing times influenced Fe ion distribution, and Fe ion OSPE was shown to prefer the A or B site [11]. Furthermore, the state of oxidation caused Fe ion migration. Basically, the chemical formula in spinel ferrite Fe ion was trivalent ions, which are generally smaller than divalent ones because the larger charge produces greater electrostatic attraction and therefore pulls the outer orbits inward [13, 19]. Also, the ionic radius of Fe ions was smaller than that of Mn ones [18]. Therefore, Fe ions were transferred to the tetrahedral (A) site more easily than Mn ions.

Figure 5 shows the magnetic hysteresis loop of  $\text{CoFe}_{0.90}\text{Mn}_{1.10}\text{O}_4$  powders as a function without annealing, and with annealing at 500°C for 4 h and 100 h, and a maximum applied field of up to 8 kOe at room temperature. Basically, the magnetization curves of all samples were normal S-shaped and typically ferrimagnetic materials [19]. The variations of saturated magnetization ( $M_s$ ) and coercivities ( $H_c$ ) for  $\text{CoFe}_{0.90}\text{Mn}_{1.10}\text{O}_4$  powder

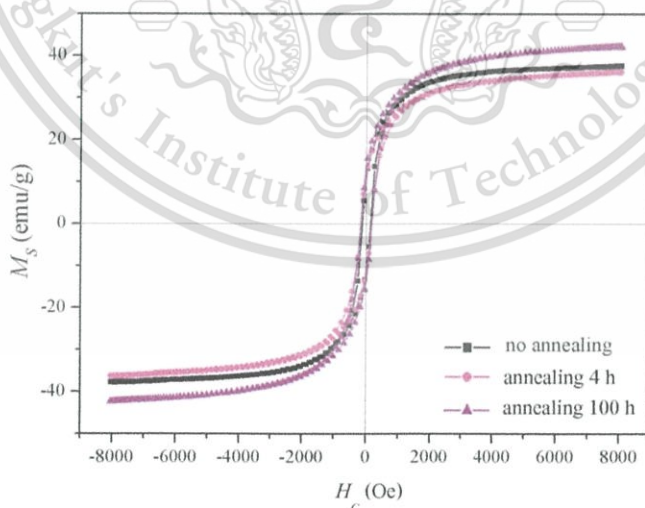


**Figure 5.** Magnetic hysteresis loops of  $\text{CoFe}_{0.90}\text{Mn}_{1.10}\text{O}_4$  powders without annealing, and with annealing at 500°C for 4 and 100 h.

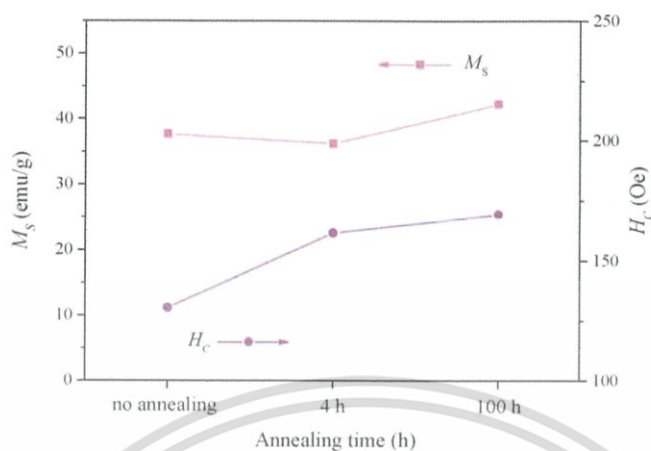


**Figure 6.** Variations of saturated magnetization and coercivities for  $\text{CoFe}_{0.90}\text{Mn}_{1.10}\text{O}_4$  powders as a function of annealing time.

as a function of annealing time are exhibited in Figure 6 and Table 2. The results pointed out that saturated magnetization before annealing was 37.67 emu/g, but when the trend increased with increasing annealing time to 100 h, saturated magnetization read 42.24 emu/g. This confirmed that, as a result of increased saturated magnetization, the annealing time affected cation migration to the preferred site. The cation distribution results can explain the magnetic properties that determine the increase of saturated magnetization in  $\text{CoFe}_{0.90}\text{Mn}_{1.10}\text{O}_4$  powders after annealing Co and Fe ions. Since net magnetic properties resulted from super exchange interaction of metal ions in the A and B site [6], increasing Co ions in the octahedral site with  $3 \mu_B$ , and decreasing Fe ions very slightly in the octahedral site with  $5 \mu_B$ , resulted in a net uncompensated moment of magnetization, and increasing saturated magnetization. Furthermore, the changing coercivity of the samples, when increasing the annealing time, can be attributed to annealing time having impact on structural distortion. Changing coercivity also increased the anisotropy of the Co ion, which was in accordance with large coercivities that were noticeable in the annealed samples [9].

#### 4. Conclusion

In summary, Mn doped  $\text{CoFe}_2\text{O}_4$  powders were synthesized successfully by the conventional mixed-oxide method. The structural characteristics revealed that samples had a single phase spinel structure. The unchanged average particle sizes of non-annealed and annealed samples were confirmed. Furthermore, annealing of  $\text{CoFe}_{0.90}\text{Mn}_{1.10}\text{O}_4$  powders at  $500^\circ\text{C}$  for 100 h influenced cation distribution and increased magnetic properties to 42.24 emu/g.

#### Acknowledgment

The authors would like to thank the Department of Physics, Kasetsart University (KU) for its VSM measurement.

#### Funding

This research was supported by the KMITL Research Fund, and partly supported by grants from the National Research Council of Thailand (NRCT), National Nanotechnology

Center (NANOTEC) NSTDA, through its Center of Excellence Network, and the Thailand Research Fund (Grant No. BRG5680006). R. Roongtao would like to acknowledge the Ph.D. scholarship provided by Synchrotron Light Research Institute (Public Organization).

## References

1. C. S. Kim, Y. S. Yi, K. T. Park, H. Namgung, J. G. Lee, Growth of ultrafine Co–Mn ferrite and magnetic properties by a sol–gel Method. *J Appl Phys.* **85**, 5223 (1999).
2. P. C. R. Varma, R. S. Manna, D. Banerjee, M. R. Varma, K. G. Suresh, A. K. Nigamc, Magnetic properties of  $\text{CoFe}_2\text{O}_4$  synthesized by solid state, citrate precursor and polymerized complex methods: A comparative study. *J Alloy Compd.* **453**, 298–303 (2008).
3. H. M. I. Abdallah, T. Moyo, J. Z. Maomi, J. Supercond, The effect of annealing temperature on the magnetic properties of  $\text{Mn}_x\text{Co}_{1-x}\text{Fe}_2\text{O}_4$  Ferrites Nanoparticles. *Nov Magn.* 2011; doi:10.1007/s10948-011-1231-4.
4. R. Roongtao, R. Baitahe, N. Vittayakorn, P. Seecharaj, W. C. Vittayakorn, Influence of Mn Doping on the Magnetic Properties of  $\text{CoFe}_2\text{O}_4$ . *Ferroelectrics.* **459**, 119–127 (2014).
5. S. S. More, R. H. Kadam, A. B. Kadam, A. R. Shite, D. R. Mane, K. M. Jadhav, Cation distribution in nanocrystalline  $\text{Al}^{3+}$  and  $\text{Cr}^{3+}$  co-substituted  $\text{CoFe}_2\text{O}_4$ . *J Alloy Compd.* **502**, 477–479 (2010).
6. Y. Köseoğlu, A. Baykal, F. Gözüak, H. Kavas, Structural and magnetic properties of  $\text{Co}_x\text{Zn}_{1-x}\text{Fe}_2\text{O}_4$  nanocrystals synthesized by microwave method. *Polyhedron.* **28**, 2887–2892 (2009).
7. D. Carta, G. Mounjoy, G. Navarra, et al. “X-ray Absorption Investigation of the Formation of Cobalt Ferrite Nanoparticles in an Aerogel Silica Matrix.” *J Phys Chem C.* **111**, 6308–6317 (2007).
8. V. G. Harris, N. C. Koon, C. M. Williams, Q. Zhang, M. Abe, J. P. Kirkland, Cation distribution in NiZn-ferrite films via extended X-ray absorption fine structure. *Appl Phys Lett.* **68**, 15 (1996).
9. A. K. Giri, E. M. Kirkpatrick, P. Moongkhamklang, S. A. Majetich. “Photomagnetism and structure in cobalt ferrite nanoparticles. *Appl Phys Lett.* **80**, 13 (2002).
10. M. H. Nilsen, C. Nordhei, A. L. Ramstad, D. G. Nicholson, M. Poliakoff, A. Cabanas, XAS (XANES and EXAFS) Investigations of Nanoparticulate Ferrites Synthesized Continuously in Near Critical and Supercritical Water. *J Phys Chem C.* **111**, 6252–6262 (2007).
11. J. A. Gomes, M. H. Sousa, G. J. Silva, et al. “Cation distribution in copper ferrite nanoparticles of ferrofluids: A synchrotron XRD and EXAFS investigation. *J Magn Magn Mater.* **300**, e213–e216 (2006).
12. Z. J. Zhang, Z. L. Wang, B. C. Chakoumakos, J. S. Yin, Temperature Dependence of Cation Distribution and Oxidation State in Magnetic Mn-Fe Ferrite Nanocrystals. *J Am Chem Soc.* **120**, 1800–1804 (1998).
13. R. C. Buchanan. *Ceramic Materials for Electronics*, USA, Marcel Dekker, 2004.
14. A. Goldman. *Modern Ferrite Technology*. USA: Pittsburgh; 2006.
15. N. Vittayakorn, G. Rujijanagul, D. P. Cann, Investigation of the influence of thermal treatment on the morphologies, dielectric and ferroelectric properties of PZT-based ceramics. *J Alloy Compd.* **440**, 259–264 (2007).
16. Y. Köseoğlu, F. Alan, M. Tan, R. Yilgin, M. Öztürk, Low temperature hydrothermal synthesis and characterization of Mn doped cobalt ferrite nanoparticles. *Ceram Int.* 2012; in press.
17. S. Parida, S. K. Rout, L. S. Cavalcante, et al. Structural refinement, optical and microwave dielectric properties of  $\text{BaZrO}_3$ . *Ceram Int.* 2012; **38**, 2129–2138.
18. R. D. Shannon, Revised Effective Ionic Radii and Systematic Studies of Interatomic Distances in Halides and Chalcogenides. *Acta Crystallogr.* **A32**, 751–767 (1976).
19. A. J. Moulson, J. M. Herbert. *Electroceramics*. England: John Wiley & Sons; 2003.

## Influence of Mn Doping on the Magnetic Properties of $\text{CoFe}_2\text{O}_4$

RACHANUSORN ROONGTAO,<sup>1,2</sup> RATTANAI BAITAHE,<sup>1</sup>  
NARATIP VITTAYAKORN,<sup>1,3</sup> PANPAILIN SEEHARAJ,<sup>4</sup>  
AND WANWILAI C. VITTAYAKORN<sup>1,\*</sup>

<sup>1</sup>College of Nanotechnology, King Mongkut's Institute of Technology  
Ladkrabang, Bangkok 10520, Thailand

<sup>2</sup>National Synchrotron Research Center, 111 University Avenue, Muang District,  
Nakhon Ratchasima 30000, Thailand

<sup>3</sup>Advanced Materials Science Research Unit, Department of Chemistry, Faculty  
of Science, King Mongkut's Institute of Technology Ladkrabang, Bangkok  
10520, Thailand

<sup>4</sup>Department of Chemistry, Faculty of Science, King Mongkut's Institute of  
Technology Ladkrabang, Bangkok 10520, Thailand

*A series of  $\text{CoFe}_{2-x}\text{Mn}_x\text{O}_4$  ceramics were synthesized successfully by conventional solid state reaction. The X-ray diffraction analysis proved that all samples were found to have a cubic spinel structure. Diffractograms were used for Rietveld refinement to determine lattice parameters, of which lattice parameter increased with increasing Mn concentration. The microstructure of the samples was studied using scanning electron microscopy. The vibrating sample magnetometer measurements showed that the highest saturated magnetization of 118.11 emu/g and coercivity of 46.89 Oe were observed in  $\text{CoFe}_{1.85}\text{Mn}_{0.15}\text{O}_4$  ceramic. Furthermore, X-ray absorption spectra of the samples were recorded to determine the Co, Fe and Mn valence states and their preferentially sites of the spinel structure.*

**Keywords** Cobalt ferrite; manganese doping; magnetic properties; XANES spectra

### Introduction

Cubic spinel ferrites are a subject of great interest and have been investigated extensively over the last few decades, due to their potential and importance in many technological applications such as magnetic recording, electronic communication devices and sensors [1]. They are represented by the chemical formula,  $\text{MOFe}_2\text{O}_3$ , where  $\text{Fe}_2\text{O}_3$  is iron oxide and MO refers to a combination of two or more divalent metal oxides. Additionally, the physical magnetic and electrical properties of this spinel structure are determined by the composition and cation distribution among the tetrahedral (A) and octahedral (B) site [2]. The cobalt ferrite ( $\text{CoFe}_2\text{O}_4$ ) is a hard magnetic material that has interesting magnetic properties such as very high cubic magnetocrystalline anisotropy and moderately saturated magnetization

---

Received December 11, 2012; in final form March 15, 2013.

\*Corresponding author. E-mail: w.vittayakorn@yahoo.com

[1531]/119

as well as remarkable chemical stability and mechanical hardness [3]. Also, the partial substitution of transition metal in the  $\text{CoFe}_2\text{O}_4$  offers an excellent opportunity to engineer specific magnetic interactions in the crystal lattice. Manganese is the transition metal series that has five unpaired electrons in  $3d$  orbital, in which the moment of magnetization is a result of the numbers of unpaired electrons [4]. Furthermore, O. Caltun *et al.* [1] prepared the  $\text{CoMn}_x\text{Fe}_{2-x}\text{O}_4$  system by using the standard powder ceramic technique. Their results reported that a significant increase in saturated magnetization could be achieved by doping Mn ion in  $\text{CoFe}_2\text{O}_4$  at a weight percentage of smaller than 0.4. This could be understood because of the small number of  $\text{Mn}^{2+}$  ion contributions in the midst of  $\text{Mn}^{3+}$  ions in the B sites. H.M.I. Abdallah *et al.* [5] discovered that Mn doped with  $x = 0.5$  exhibited the highest saturated magnetization, which prepared the  $\text{Mn}_x\text{Co}_{1-x}\text{Fe}_2\text{O}_4$  ferrite via a glycol-thermal method using a stirred pressure reactor. They reported that the oxidation states of Fe ions are in trivalent state in the A- and B-sites of the spinel structure, and Co and Mn are expected to be the divalent state distributed amongst those sites. Furthermore, Y. Köseoğlu *et al.* [6] prepared the  $\text{Mn}_x\text{Co}_{1-x}\text{Fe}_2\text{O}_4$  nanoparticles by low temperature hydrothermal synthesis. From the result, highly saturated magnetization can be obtained in  $x = 0.8$  Mn doped cobalt ferrites. Also, their research expected that  $\text{Fe}^{3+}$ ,  $\text{Co}^{2+}$  and  $\text{Mn}^{2+}$  exist among the A- and B-sites. However, their research did not seriously study the cation valence states of the Mn doped cobalt ferrite system. Therefore, this work aimed to study the synthesis of manganese substituted cobalt ferrites by a conventional mixed-oxide method. The oxidation states of an absorber atom and local information on the symmetry of the coordination site in the ferrite samples are determine in particular by XANES [7]. Furthermore, the crystallographic structures of the samples employed Rietveld structure refinement of X-ray powder diffraction. The microstructure and magnetic properties were characterized using scanning electron microscopy (SEM) and a vibrating sample magnetometer (VSM), respectively.

### Experimental Procedure

The sample of the  $\text{CoFe}_{2-x}\text{Mn}_x\text{O}_4$  system, where  $x = 0.00, 0.10, 0.15, 0.20$  and  $0.25$  was prepared by a mixed-oxide method. The reagent grades of  $\text{Fe}_2\text{O}_3$  (Sigma-Aldrich,  $\geq 99.0\%$  purity),  $\text{Co}_3\text{O}_4$  and  $\text{Mn}_2\text{O}_3$  (Aldrich,  $\geq 99.0\%$  purity) were used as starting materials in this system. The raw materials were weighed and mixed by the ball milling technique for 24 h in a PVC container using an alumina ball and ethanol as the medium. Resulting slurry was dried in a hot air oven and the powder was well ground using an agate mortar. The ground powder was calcined at  $900^\circ\text{C}$  for 48 h with a heating/cooling rate of  $5^\circ\text{C}/\text{min}$  in air. Then, the calcined powders were reground by wet planetary milling for 6 h. After milling, the slurry was dried in a hot air oven and ground with an agate mortar. The ground powders were sieved through 325-mesh and uniaxially pressed into pellets with a diameter and thickness of 12 mm and 1.5 mm, respectively. The green bodies were placed in an alumina crucible and sintered at  $1,250^\circ\text{C}$  for 4 h with a heating/cooling rate of  $5^\circ\text{C}/\text{min}$  in air. Densities of sintered ceramics were measured by Archimedes' method, and an X-ray diffractometer was employed at room temperature to identify the phases formed for all samples. The grain morphology was imaged directly using scanning electron microscopy. The magnetization measurements of the samples were carried out using a vibrating sample magnetometer at room temperature under a maximum applied magnetic field of 8 kOe. XAS data were collected from the Co K-edge (7709 eV), Fe K-edge (7112 eV) and Mn K-edge (6539 eV) at room temperature in the transmission mode at the XAS facility (BL-8) of the Siam Photon Laboratory, Synchrotron Light Research Institute, Nakhon Ratchasima.

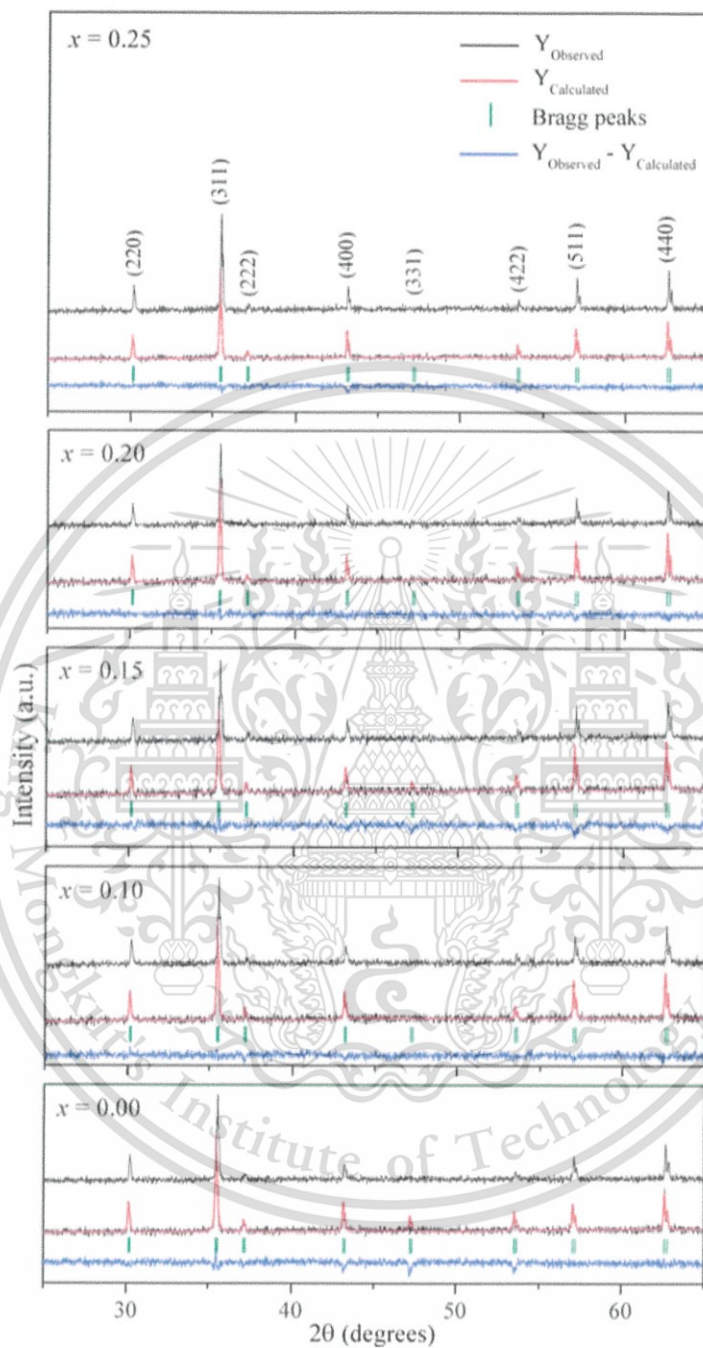


**Figure 1.** XRD patterns and Rietveld refinement plots of  $\text{CoFe}_{2-x}\text{Mn}_x\text{O}_4$  powder calcined at  $900^\circ\text{C}$  for 48 h.

## Results and Discussion

The XRD patterns and Rietveld refinement of  $\text{CoFe}_{2-x}\text{Mn}_x\text{O}_4$  powder, calcined at  $900^\circ\text{C}$  for 48 h as a function of dopant amount  $x$ , are shown in Fig. 1. The XRD pattern indicated that the major reflection peaks corresponded to the cubic spinel structure. All peaks of the XRD pattern were indexed by JCPDS file no. 22–1086, with the lattice parameters,  $a = 8.3910 \text{ \AA}$ , and space group  $\text{Fd}3\text{m}$  (no. 227) [6]. Furthermore, no secondary phases were detected in X-ray diffraction patterns with increased  $\text{Mn}^{3+}$  contents. Increasing the doping content gradually leads to a higher lattice volume, as indicated by lower angles of the XRD peak shifts (or higher  $d$  values). Structure refinement by the Rietveld method was performed to confirm that the structure is truly cubic. The lattice parameters, unit cell volume,  $R_w$  and  $\chi^2$  are presented in Table 1. From results of the Rietveld refinement method, good agreement between XRD patterns were observed experimentally and calculated theoretically. Quality of data from structural refinement is checked generally by  $R$ -values ( $R_w$ ) and a good fit ( $\chi^2$ ). Also, the difference between XRD patterns, experimental profiles and calculated data displays small differences in the scale of intensity, as illustrated by the line,  $Y_{\text{Observed}} - Y_{\text{Calculated}}$  [8]. Furthermore, the lattice constant was affected by cationic stoichiometry. The lattice parameter,  $a$ , and unit cell volume increased with increasing amount of dopant because  $\text{Mn}^{3+}$  ion ( $0.58 \text{ \AA}$ ) had a larger ionic radius compared to that of  $\text{Fe}^{3+}$  ion ( $0.55 \text{ \AA}$ ) [9], in which  $\text{Mn}^{3+}$  and  $\text{Fe}^{3+}$  were coordinated six-fold by  $\text{O}^{2-}$  ion into the spinel network that leads to lattice distortion. This resulted in higher degrees of lattice fringe alignment. The parameters that were increased gradually exhibited an almost linear dependence, which satisfied Vegard's law [6]. Therefore, the ceramics in this system were confirmed as developing completely for continuous substitution in which atoms or ions existed.

The microstructure and grain size distribution of the ferrite sample currently investigated was analyzed by using SEM microphotographs as show in Fig. 2 (a)–(e). It was observed that pure cobalt ferrite samples had irregular shape and some degree of porosity on the surface. It was revealed that samples of the composition,  $0.10 \leq x \leq 0.25$ , had irregular shape without pores on the surface to grain boundaries. The figure shows the network of channels on the surface. This process enlarged the grains, including the smaller ones, by controlling the diffusion at the inter-granular limit. A gradient of defect concentration led to displacement of the inter-granular limits by ion diffusion [10]. Furthermore, SEM micrographs exhibited good densification, and the theoretical densities of ceramics in this range enhanced densification in the sintering process. Calculated values from the figure showed

**Table 1**  
Rietveld refinement result, relative density, average grain size, and magnetic properties at room temperature of  $\text{CoFe}_{2-x}\text{Mn}_x\text{O}_4$

$x$	$a$ ( $\text{\AA}$ )	$V$ ( $10^6 \text{ pm}^3$ )	$R_w$ (%)	$\chi^2$	Relative density (%)	Average grain size ( $\mu\text{m}$ )	$M_s$ (emu/g)	$H_c$ (Oe)
0.00	8.3843 (6)	589.385	4.823	1.408	$94.43 \pm 0.03$	$5.42 \pm 2.20$	115.33	78.86
0.10	8.3884 (6)	590.261	5.058	1.397	$94.99 \pm 0.04$	$5.49 \pm 2.07$	116.82	40.89
0.15	8.3896 (6)	590.508	5.222	1.378	$95.31 \pm 0.05$	$5.87 \pm 2.51$	118.11	46.89
0.20	8.3904 (5)	590.674	5.144	1.305	$95.50 \pm 0.03$	$6.44 \pm 2.56$	113.97	40.89
0.25	8.3934 (2)	591.317	2.795	0.411	$96.39 \pm 0.05$	$6.86 \pm 3.00$	112.81	37.97

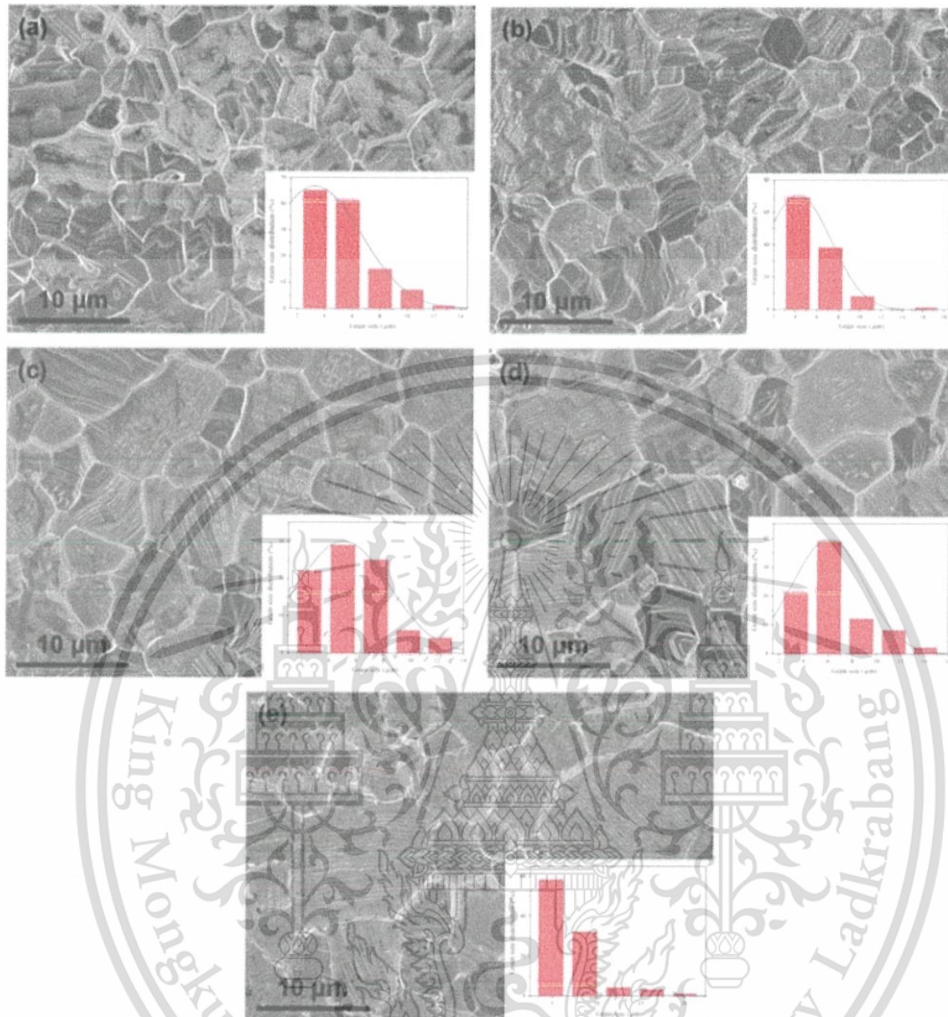


**Figure 2.** Microstructure and grain size distribution of the  $\text{CoFe}_2-x\text{Mn}_x\text{O}_4$  ceramics for (a)  $x = 0.00$ , (b)  $x = 0.10$ , (c)  $x = 0.15$ , (d)  $x = 0.20$  and (e)  $x = 0.25$ . (Color figure available online.)

that average grain sizes increased with increasing doping ion concentration. The reason for the variation of grain size in these composition ranges was due to Mn ions promoting grain growth, while increasing the doping levels [1]. The relative density and average grain size are shown in Table 1.

The magnetic properties of Mn substituted cobalt ferrite were performed at room temperature with a maximum applied field of up to 8 kOe, as shown in Fig. 3. The saturated magnetization and coercive field are summarized in Table 1. Variations of the saturated magnetization depend on the cation distribution in a spinel lattice. It has been observed from these loops that the saturated magnetization values for  $x = 0.10$  and  $x = 0.15$  are higher than those for pure cobalt ferrite. This is understandable because the preferential occupancy of  $\text{Mn}^{3+}$  ion to the octahedral site in the ferrite spinel structure results in decreasing concentration of  $\text{Co}^{2+}$  ions in these sites. The magnetization is related

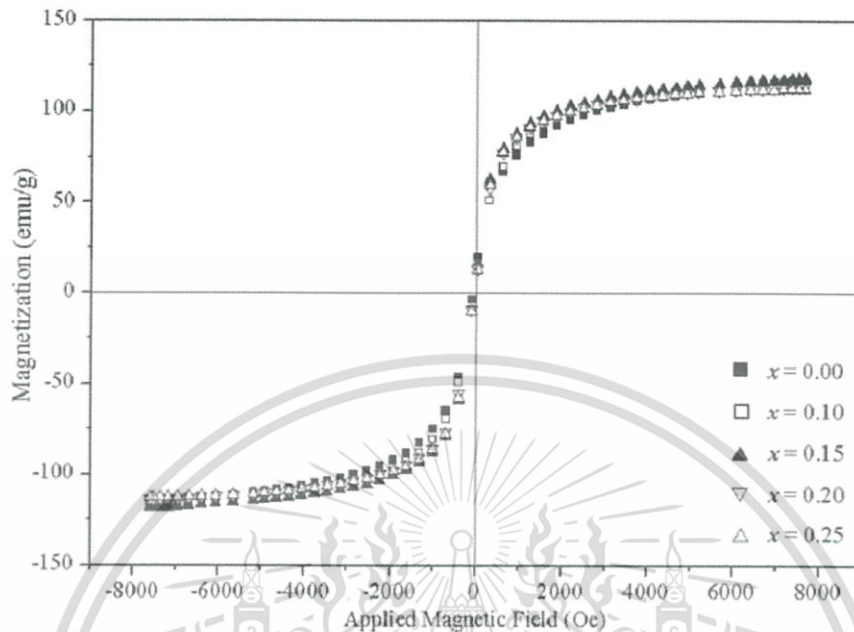
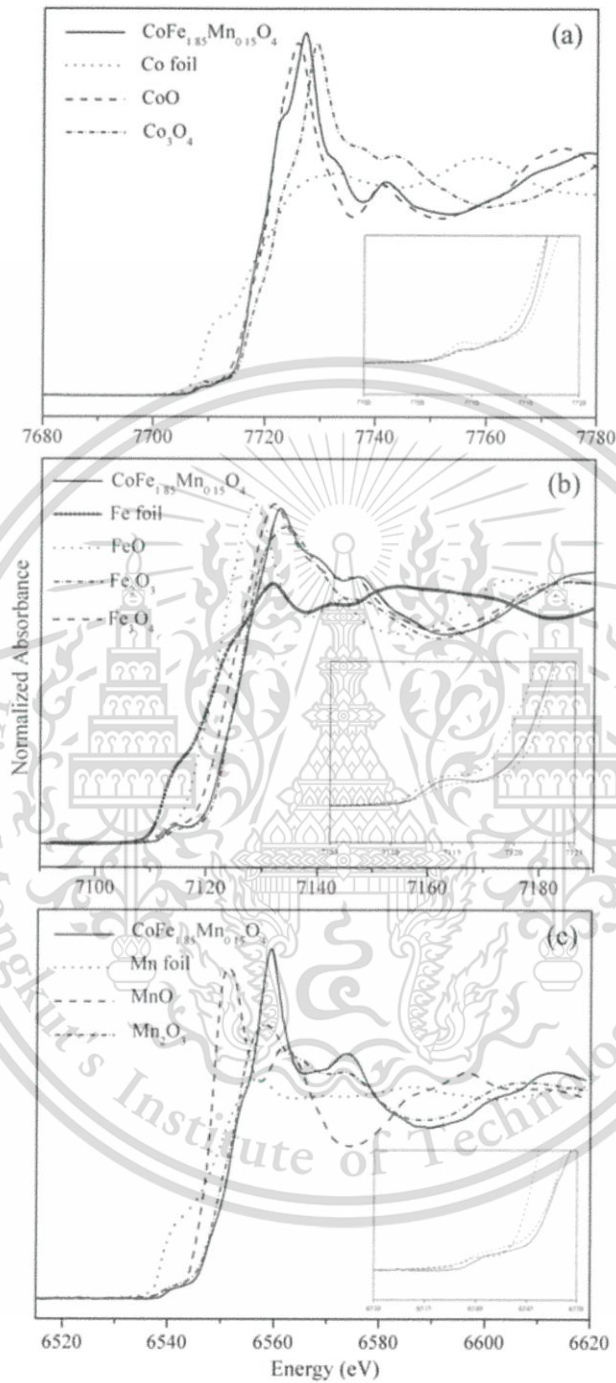


Figure 3. Magnetic hysteresis loops of  $\text{CoFe}_{2-x}\text{Mn}_x\text{O}_4$  ceramics at room temperature.

to the magnitude of electron magnetic dipole moment. In this context,  $\text{Mn}^{3+}$  has  $4 \mu_B$  and  $\text{Co}^{2+}$   $3 \mu_B$  as its magnetic dipole moments, as when Mn content increased, saturated magnetization also was seen to increase. A further increase in doping levels that decreased saturated magnetization may be due to the  $\text{Mn}^{3+}$  ion in the octahedral site decreasing the concentration of  $\text{Fe}^{3+}$  ions, of which the magnetic moment of  $\text{Fe}^{3+}$  cations was fixed at  $5 \mu_B$ . When the net magnetic moment for  $\text{Mn}^{3+}$  was taken to be  $4 \mu_B$ , the  $\text{Mn}^{3+}$  ions had a smaller magnetic moment as compared to the  $\text{Fe}^{3+}$  ions, and therefore, the saturated magnetization was found to decrease with  $\text{Mn}^{3+}$  doping. Additionally, the coercive fields were reduced significantly by Mn substitution. This was probably due to  $\text{CoFe}_2\text{O}_4$  being known to have high coercivity, due to strong anisotropy associated with Co atom. Hence, substitution by Mn atoms with lower anisotropy leads to a reduction in coercive fields according to O. Caltun *et al.* [1], H. M. I. Abdallah *et al.* [5] and Y. Köseoğlu *et al.* [6].

The XANES spectra for the samples were measured at the Fe K-, Co K- and Mn K-edges at room temperature. As observed, the spectra for all samples are similar at each edge and their shift was not seen. Fig. 4(a) shows XANES spectra of  $\text{CoFe}_{1.85}\text{Mn}_{0.15}\text{O}_4$  sample, Co foil, CoO and  $\text{Co}_3\text{O}_4$  in the vicinity of the Co K-edge, with their  $E_0$  being 7716.69, 7708.94, 7716.89 and 7717.52, respectively. The valence state of Co in the samples was determined from energy of the main maxima in the spectra ( $E_0$ ) [24]. As observed, the spectra for the samples are similar to those obtained for the CoO standard, in which  $\text{Co}^{2+}$  is coordinated six-fold by  $\text{O}^{2-}$  ions, which suggests that Co ions exist in a divalent state in six coordinated oxygen atoms [7]. In addition, to determine the mean oxidation states, the spectra contain information about the Co cation distribution between tetrahedral and octahedral sites in the spinels. As shown in the magnified picture in Fig. 4(a), the K-edge spectra of the transition elements exhibit a small pre-edge peak on the low energy side. This peak results from normally forbidden dipole transitions from 1s to 3d levels. Previous



**Figure 4.** XANES spectra of  $\text{CoFe}_{1.85}\text{Mn}_{0.15}\text{O}_4$  samples and the standards obtained at (a) Co K-edge, (b) Fe K-edge and (c) Mn K-edge.

X-ray absorption studies of transition metal compounds have shown an enhancement of the pre-edge peak with an increase in the amount of tetrahedrally coordinated cations [11–12]. The low intensity pre-edge feature observed in the samples match very well with the one of the CoO standard, which strongly supports the idea that Co is octahedrally coordinated [7]. XANES spectra at the Fe K-edge of the sample and standard compounds are shown in Fig. 4 (b). The threshold energy of  $\text{CoFe}_{1.85}\text{Mn}_{0.15}\text{O}_4$  samples is higher than that of Fe foil, FeO and  $\text{Fe}_3\text{O}_4$ , but close to the energy of  $\text{Fe}_2\text{O}_3$ . The  $E_0$  of  $\text{CoFe}_{1.85}\text{Mn}_{0.15}\text{O}_4$ , Fe foil, FeO,  $\text{Fe}_3\text{O}_4$  and  $\text{Fe}_2\text{O}_3$  is 7122.85, 7112.01, 7718.63, 7122.20 and 7122.79, respectively, which leads to  $\text{Fe}^{3+}$  existing in the samples. As shown in the magnified picture in Fig. 4(b), the spectra obtained from the samples match very well with the one of the  $\text{Fe}_3\text{O}_4$  standard, which shows that the sample contains metal atoms in both tetrahedral and octahedral sites within the oxide sublattices [11]. XANES spectra at the Mn K-edge are shown in Fig. 4(c). In the threshold region, the curves of samples are close to that of  $\text{Mn}_2\text{O}_3$ , suggesting existence of the trivalent state. The  $E_0$  of  $\text{CoFe}_{1.85}\text{Mn}_{0.15}\text{O}_4$ , Mn foil, MnO and  $\text{Mn}_2\text{O}_3$  is 6551.53, 6538.80, 6548.25 and 6551.128, respectively. As shown in the magnified picture in Fig. 4(c), the curves of the sample are close to that of  $\text{Mn}_2\text{O}_3$ , suggesting existence of the trivalent state in octahedral coordination for oxygen atoms [12].

## Conclusion

A series of  $\text{CoFe}_{2-x}\text{Mn}_x\text{O}_4$  ferrite samples were prepared successfully by the solid state reaction method. The phase development showed a single phase cubic spinel structure in all samples, and Rietveld refinement confirmed lattice parameters that increased with doping  $\text{Mn}^{3+}$  ion. Furthermore, the average grain sizes increased by increasing the doping. The results revealed that the Mn doped cobalt ferrites showed higher saturated magnetization and lower coercivity than pure cobalt ferrite, and XANES spectra suggested a valence state with preferential sites of all samples.

## Acknowledgments

The author would like to gratefully acknowledge the support from KMITL Research Fund (KMITL Fund), National Research Council of Thailand (NRCT) and National Nanotechnology Center (NANOTEC) through its program of Center of Excellence Network for fund. R. Roongtao acknowledges Synchrotron Light Research Institute (Public Organization) (SLRI) for financial support and beam time.

## References

1. O. Caltun, G. S. N. Rao, K. H. Rao, B. P. Rao, I. Dumitru, C.-O. Kim, and C. G. Kim, The influence of Mn doping level on magnetostriction coefficient of cobalt ferrite. *J Magn Magn Mater.* **316**, e618–e620 (2007).
2. L. Zhao, H. Yang, X. Zhao, L. Yu, Y. Cui, and S. Feng, Magnetic properties of  $\text{CoFe}_2\text{O}_4$  ferrite doped with rare earth ion. *Materials Letter.* **60**, 1–6 (2006).
3. S. Y. An, I. S. Kim, S. H. Son, S. Y. Song, J. W. Hahn, S. W. Hyun, C. M. Kim, and C. S. Kim, Magnetic properties of  $\text{Cu}^{2+}$  substituted co-ferrite. *Thin Solid Films.* **519**, 8296–8298 (2011).
4. A. Goldman, *Modern Ferrite Technology. USA: Pittsburgh* (2006).
5. H. M. I. Abdallah, T. Moyo, J. Z. Maomi, and J. Supercond, The effect of annealing temperature on the magnetic properties of  $\text{Mn}_x\text{Co}_{1-x}\text{Fe}_2\text{O}_4$  ferrites nanoparticles. *Nov Magn.* doi:10.1007/s10948-011-1231-4 (2011).

6. Y. Köseoğlu, F. Alan, M. Tan, R. Yilgin, and M. Öztürk, Low temperature hydrothermal synthesis and characterization of Mn doped cobalt ferrite nanoparticles. *Ceram Int.* in press (2012).
7. M. F. F. Lelis, A. O. Porto, C. M. Gonçalves, and J. D. Fabris, Cation occupancy sites in synthetic co-doped magnetites as determined with X-ray absorption (XAS) and Mössbauer Spectroscopies. *J Magn Magn Mater.* **278**, 263–269 (2004).
8. S. Parida, S. K. Rout, L. S. Cavalcante, E. Sinha, M. S. Li, V. Subramanian, N. Gupta, V. R. Gupta, J. A. Varela, and E. Longo: Structural refinement, optical and microwave dielectric properties of  $\text{BaZrO}_3$ . *Ceram Int.* in press (2011).
9. R. D. Shannon, Revised effective ionic radii and systematic studies of interatomic distances in halides and chalcogenides. *Acta Crystallogr.* **A32**, 751–767 (1976).
10. V. Musat, O. Potecasu, R. Belea, and P. Alexandru, Magnetic materials from co-precipitated ferrite nanoparticles. *Mat Sci Eng B.* **167**, 85–90 (2010).
11. M. H. Nilsen, C. Nordhei, A. L. Ramstad, D. G. Nicholson, M. Poliakoff, A. Cabañas, XAS (XANES and EXAFS) Investigations of nanoparticulate ferrites synthesized continuously in near critical and supercritical water. *J Phys Chem C.* **111**, 6252–6262 (2007).
12. G. Bonsdorf, M. A. Denecke, K. Schäfer, S. Christen, H. Langbein, and W. Gunßer, X-ray absorption spectroscopic and Mössbauer studies of redox and cation-ordering processes in manganese ferrite. *Solid State Ionics.* 101–103, 351–357 (1997).



## Structural and Magnetic Properties of Zn Doped $\text{CoFe}_2\text{O}_4$

RACHANUSORN ROONGTAO,<sup>1,2</sup> RATTANAI BAITAHE,<sup>1</sup>  
NARATIP VITTAYAKORN,<sup>1,3</sup> WANTANA KLYSUBUN,<sup>2</sup>  
AND WANWILAI C. VITTAYAKORN<sup>1,\*</sup>

<sup>1</sup>College of Nanotechnology, King Mongkut's Institute of Technology  
Ladkrabang, Bangkok 10520, Thailand

<sup>2</sup>National Synchrotron Research Center, 111 University Avenue, Muang District,  
Nakhon Ratchasima 30000, Thailand

<sup>3</sup>Advanced Materials Science Research Unit, Department of Chemistry, Faculty  
of Science, King Mongkut's Institute of Technology Ladkrabang, Bangkok  
10520, Thailand

<sup>4</sup>Department of Chemistry, Faculty of Science, King Mongkut's Institute of  
Technology Ladkrabang, Bangkok 10520, Thailand

*Zinc doped cobalt ferrite powders were prepared by the solid state reaction method. The effect of zinc substitution on structure, morphology and magnetic properties was investigated. The X-ray analysis confirmed existence of the single phase cubic spinel structure, while Rietveld refinement data showed increasing of lattice parameters with zinc content. In addition, saturated magnetization increased with increasing zinc concentration and it was contained at maximum in  $\text{CoFe}_{1.9}\text{Zn}_{0.1}\text{O}_4$  powders. However, the value of coercivity was decreased with zinc doped content. Furthermore, the oxidative states were characterized by X-ray absorption spectroscopy. The results confirm that the structure contained  $\text{Co}^{2+}$ ,  $\text{Fe}^{3+}$  and  $\text{Zn}^{2+}$  ions.*

**Keywords** Cobalt ferrite; zinc doping; magnetic properties; XANES spectra

### Introduction

Cobalt ferrite is a ferromagnetic cubic spinel and important in many technological applications such as magnetic recording media, magnetic refrigerators, microwave devices and other high frequency appliances [1]. It is a well-known hard ferrite material that has been studied in detail, due to its very high cubic magnetocrystalline anisotropy, reasonably saturated magnetization, high wear resistance and good electrical insulation [2]. It shows various magnetic properties depending on the thermal history, composition and site preference of the cations among the tetrahedral (A) and octahedral (B) sites [1–3]. The partial substitution of transition metal in the  $\text{CoFe}_2\text{O}_4$  offers an excellent opportunity for engineering specific magnetic interactions in the crystal lattice [4]. The addition of nonmagnetic zinc in cobalt ferrite raises saturated magnetization, due to zinc being the transition metal with strong

---

Received December 9, 2012; in final form August 25, 2013.

\*Corresponding author. E-mail: w.vittayakorn@yahoo.com

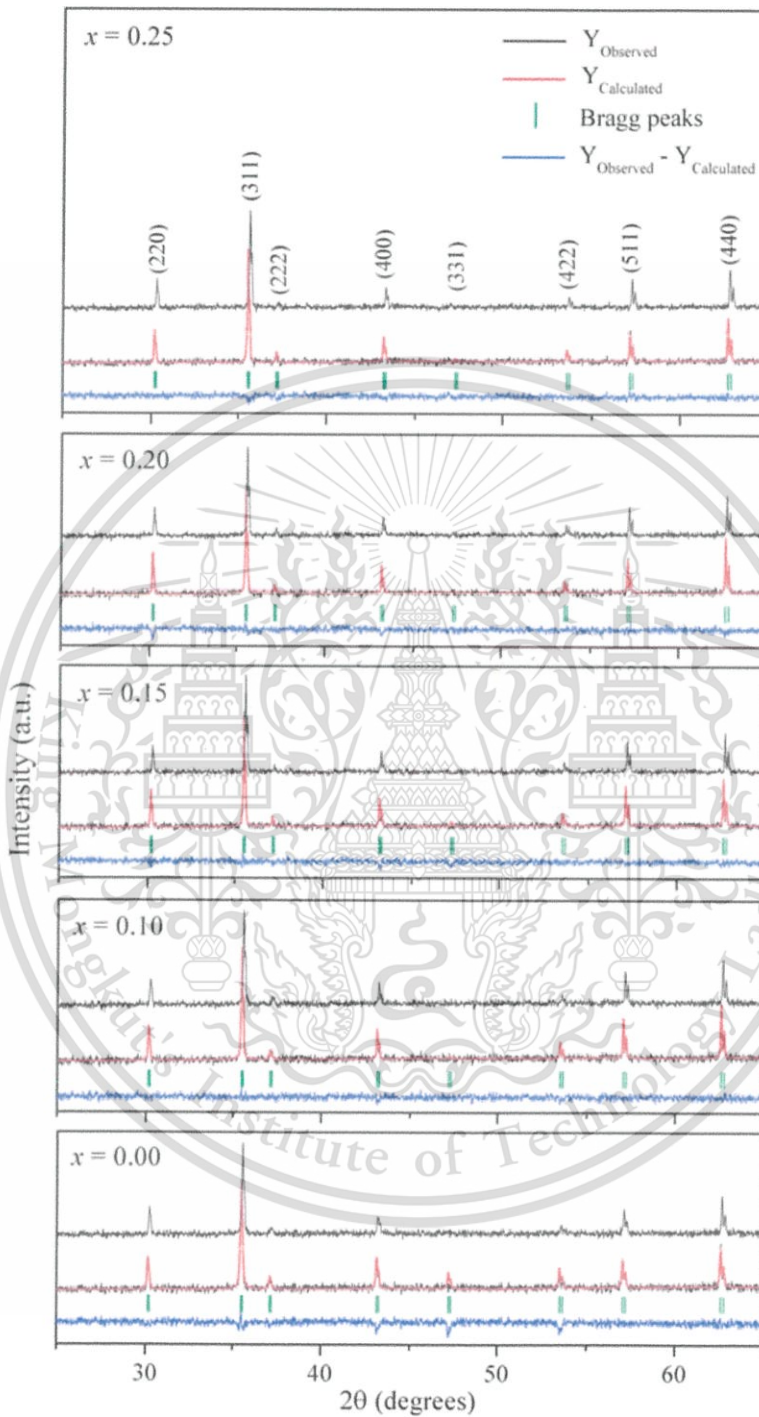


**Figure 1.** XRD patterns and Rietveld refinement plots of  $\text{CoFe}_{2-x}\text{Zn}_x\text{O}_4$  powder calcined for 48 h at  $900^\circ\text{C}$ . (Color figure available online.)

A-site preference [3]. Thus, Y. Köseoğlu *et al.* [2] prepared a cobalt zinc ferrite nanoparticle by using the microwave method. It was reported from the magnetic properties studied that the composition,  $\text{Co}_{0.8}\text{Zn}_{0.2}\text{Fe}_2\text{O}_4$ , has the highest value of saturated magnetization. However, the oxidative state of each element in the samples has yet to be investigated in any great extent. Therefore, this work aimed to study the valence state of structural elements by synthesizing  $\text{CoFe}_{2-x}\text{Zn}_x\text{O}_4$  powders using solid state reaction, which is a very simple and the most economical method [5]. The samples were characterized by various techniques and then studied for their structure, magnetic behavior and oxidative state of each structural element.

### Experimental Procedure

A series of  $\text{CoFe}_{2-x}\text{Zn}_x\text{O}_4$  ferrites (where  $x = 0.00, 0.10, 0.15, 0.20, 0.25$ ) were prepared by conventional ceramic processing. Raw material of  $\text{Fe}_2\text{O}_3$  (Sigma-Aldrich,  $\geq 99.0\%$  purity),  $\text{Co}_3\text{O}_4$  (Aldrich,  $\geq 99.0\%$  purity) and  $\text{ZnO}$  (Fluka,  $\geq 99.0\%$  purity) powders were weighed and mixed by the ball milling technique for 24 h in a PVC container, using an alumina ball and ethanol as the medium. The mixed powders were dried in a hot air oven and calcined at  $900^\circ\text{C}$  for 48 h with a heating/cooling rate of  $5^\circ\text{C}/\text{min}$  in air. The calcined powders were well ground using an agate mortar, and a single phase of spinel ferrite was confirmed at room temperature by X-ray diffractometer (XRD). The morphologic characterizations of the samples were performed by scanning electron microscopy (SEM). The saturated magnetization and coercivity of the powder were measured with a vibrating sample magnetometer (VSM) at a maximum applied field of 8 kOe at room temperature. The oxidative states of the element in the samples were measured using X-ray absorption spectroscopy (XAS). XANES data were collected from the Co K-edge (7709 eV) and Fe K-edge (7112 eV) in the transmission mode, and Zn K-edge (9659 eV) at room temperature in the fluorescence mode, at the XAS facility (BL-8) of the Siam Photon Laboratory, Synchrotron Light Research Institute, Nakhon Ratchasima.

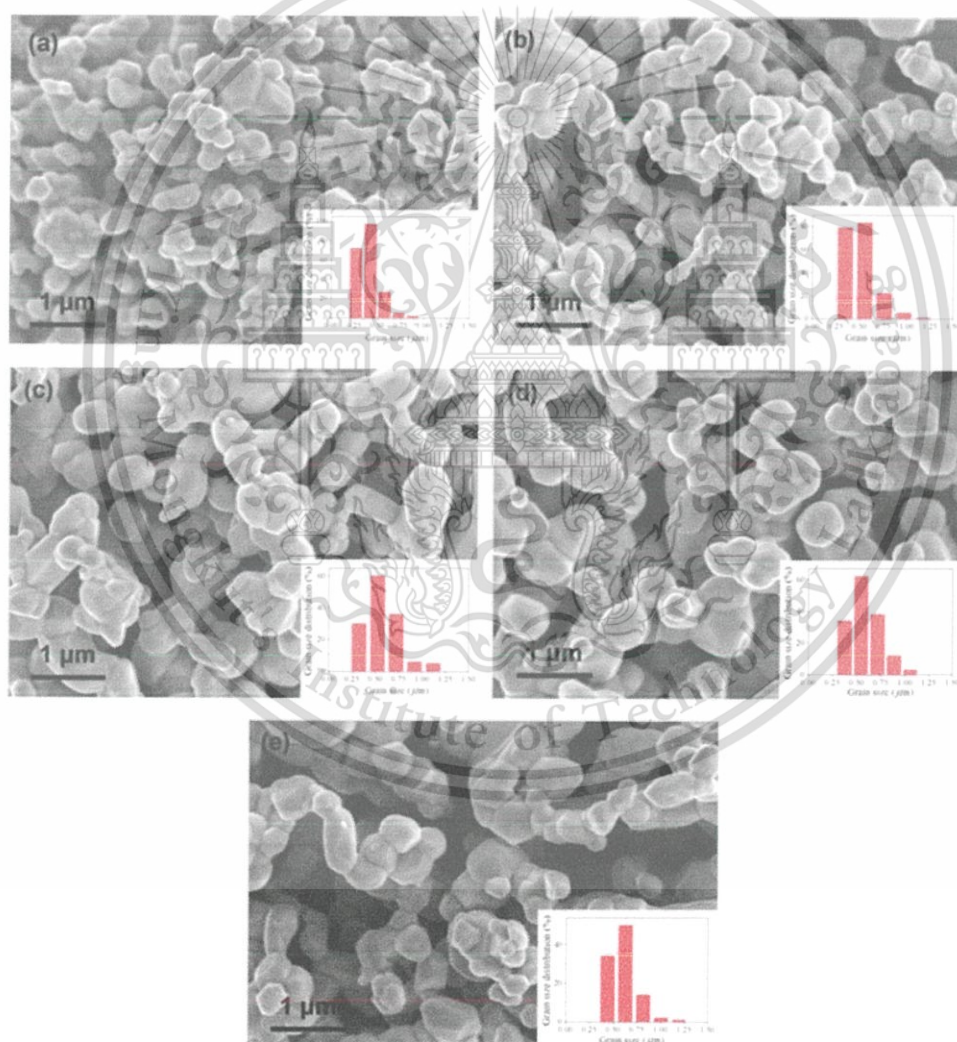
### Results and Discussion

Figure 1 shows the X-ray diffraction pattern and Rietveld refinement of  $\text{CoFe}_{2-x}\text{Mn}_x\text{O}_4$  ( $0.00 \leq x \leq 0.25$ ) powder, calcined at  $900^\circ\text{C}$  for 48 h. All peaks in the pattern correspond

**Table 1**  
Rietveld refinement result, average particle size, and magnetic properties of  $\text{CoFe}_{2-x}\text{Zn}_x\text{O}_4$  at room temperature

x	a (Å)	V ( $10^6\text{pm}^3$ )	$R_w$ (%)	$\chi^2$	Average particle size ( $\mu\text{m}$ )	$M_s$ (emu/g)	$M_r$ (emu/g)	$H_c$ (Oe)
0.00	8.3843 (6)	589.385	4.823	1.408	$0.40 \pm 0.12$	97.32	34.55	844.10
0.10	8.3851 (5)	589.554	5.304	1.525	$0.52 \pm 0.21$	124.02	33.53	181.09
0.15	8.3820 (4)	588.897	5.124	1.470	$0.57 \pm 0.19$	103.91	22.86	119.75
0.20	8.3776 (4)	587.982	5.228	1.432	$0.59 \pm 0.16$	111.25	17.22	75.94
0.25	8.3720 (5)	586.799	5.028	1.418	$0.60 \pm 0.14$	96.30	9.21	52.57

to the cubic  $\text{CoFe}_2\text{O}_4$  phase, according to the standard JCPDS file no. 22-1086, with the lattice parameters,  $a = 8.3910 \text{ \AA}$ , and space group, Fd3m (no. 227) [6]. No other impurity phases with increased zinc contents were observed. This confirms the formation of a single spinel phase, and the lattice parameters were performed by the Rietveld refinement method. The lattice parameters and results of a quantitative phase analysis from the refinement are given in Table 1. The structure refinement shows the corresponding fits and confirms that the structure is a truly cubic type. Furthermore, the lattice constant and unit cell volume for each composition were seen to decrease with increasing Zn substitution. This was probably due to the ionic radius of  $0.65 \text{ \AA}$  for low spin and  $0.745 \text{ \AA}$  for high spin of  $\text{Co}^{2+}$  ions.  $\text{Co}^{2+}$  ions coordinated six-fold with  $\text{O}^{2-}$  ions was larger than the  $0.6 \text{ \AA}$  for  $\text{Zn}^{2+}$  ions, which were coordinated four-fold with  $\text{O}^{2-}$  ions in the spinel structure [7]. Also, the unit cell

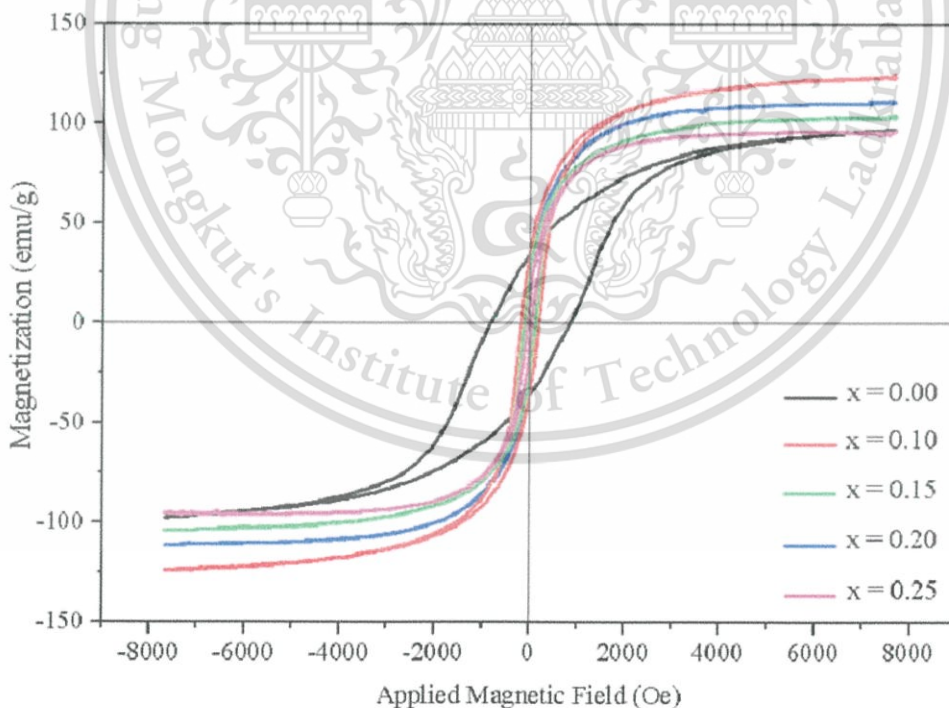


**Figure 2.** Morphology and particle size distribution of the  $\text{CoFe}_{2-x}\text{Zn}_x\text{O}_4$  powders for (a)  $x = 0.00$ , (b)  $x = 0.10$ , (c)  $x = 0.15$ , (d)  $x = 0.20$  and (e)  $x = 0.25$ . (Color figure available online.)

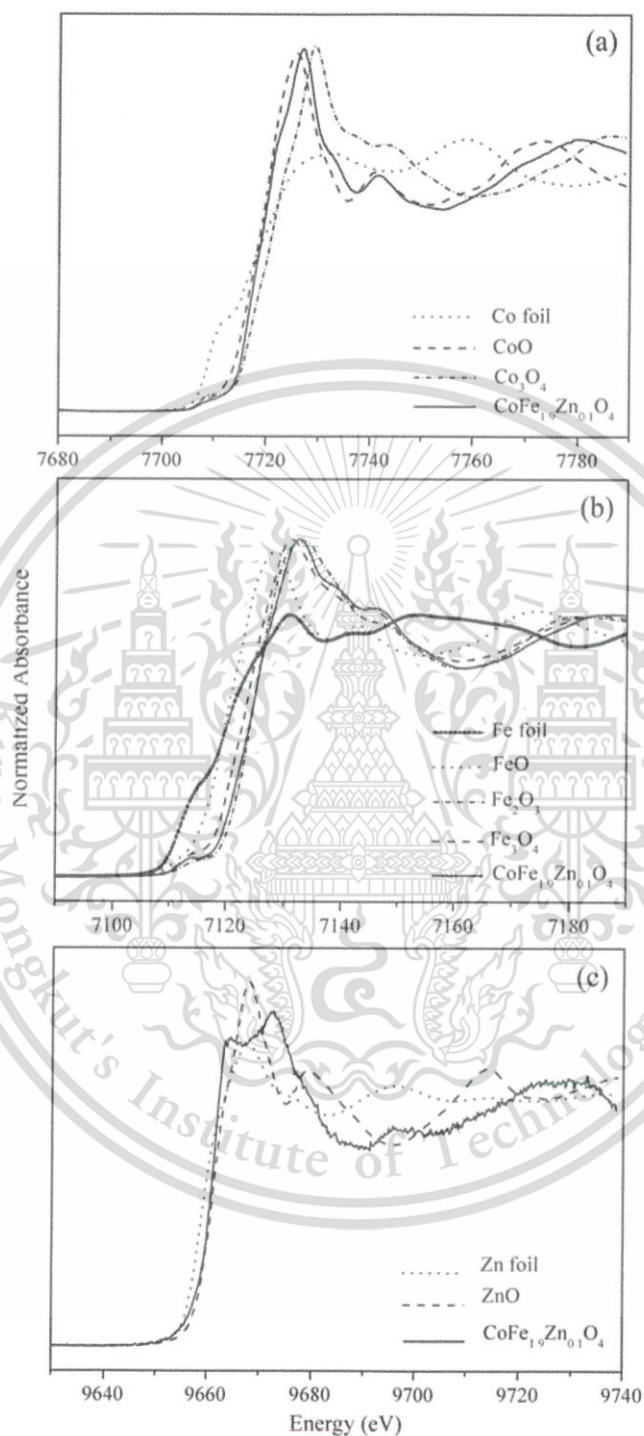
parameters varied linearly with the composition for continuous substitution, in which ions that substitute each other are distributed randomly according to Vegard's law [6].

Figure 2(a)–(e) shows SEM micrographs and particle size distribution measurement of the  $\text{CoFe}_{2-x}\text{Zn}_x\text{O}_4$  powders, with different Zn doped content, calcined at  $900^\circ\text{C}$  for 48 h. From the morphology, all powders are agglomerated and basically irregular in shape, with a substantial variation in particle sizes. Heating resulted in calcinations for the well-faceted particle to form solid bodies [2]. Results of the average particle sizes are shown in Table 1, in which they increase with increasing amount of dopant, due to any Zn content having corresponding effect on the resulting particle size. In addition, the particle size distribution observed from the SEM image had narrow range distribution and increased with increasing Zn doping.

Figure 3 shows the magnetic hysteresis loop of  $\text{CoFe}_{2-x}\text{Zn}_x\text{O}_4$  powders at room temperature, with a maximum applied field of up to 8 kOe. The saturated magnetization, remanence and coercivity are summarized in Table 1. The magnetization value of doped samples increases sharply with the external magnetic field strength at the low field region. The highest saturated magnetization can be obtained in  $x = 0.1$  of Zn doped cobalt ferrites. Increases in saturated magnetization can be attributed to influence of the cationic stoichiometry and its occupancy in specific sites. The magnetic order in the cubic system of ferromagnetic spinels is due to occurrence of the super-exchange interaction mechanism between metal ions in the tetrahedral A-site and octahedral B-site [2]. When the nonmagnetic zinc ion is substituted by the cobalt ferrite lattice, due to the zinc ferrite being a normal spinel, it has a stronger preference for the tetrahedral site and thus reduces the amount of



**Figure 3.** Magnetic hysteresis loops of  $\text{CoFe}_{2-x}\text{Zn}_x\text{O}_4$  powders at room temperature. (Color figure available online.)



**Figure 4.** XANES spectra of  $\text{CoFe}_{1.9}\text{Mn}_{0.1}\text{O}_4$  samples and the standards obtained at (a) Co K-edge, (b) Fe K-edge and (c) Zn K-edge.

$\text{Fe}^{3+}$  in the A site. The net result, due to antiferromagnetic coupling, is an increase in magnetic moment on the B lattice and an increase in saturated magnetization. However, at high levels of zinc substitution in  $x > 0.1$ , the A-site magnetic ion becomes so diluted that coupling between the two lattices is lost, and the saturated magnetization drops [3]. Furthermore, the changes in remanence and coercivity of the samples by increasing the Zn content can be attributed to the magnetic character and anisotropic nature of cobalt. As more Zn ions are replaced with Co ions by increasing the “ $x$ ”, the remanence and coercivity decreases [8].

The XANES regions of the absorption spectrum are important because they contain electronic information on the immediate environment of the absorbing atom, which in principle can be translated into spatial, geometrical information. The first derivative of the XANES spectra is useful because it highlights the features around the absorption edge and facilitates determination of the oxidative state [9–10]. Figure 4(a) shows the XANES spectra of  $\text{CoFe}_{1.9}\text{Zn}_{0.1}\text{O}_4$  samples and varied cobalt standards obtained at the Co K-edge. The valence state of Co in the ferrite samples was determined from energy of the main maxima in the spectra [11]. The curves of samples in the threshold region are close to that of CoO, suggesting existence of a divalent state. The  $E_0$  values of  $\text{CoFe}_{1.9}\text{Zn}_{0.1}\text{O}_4$  samples, Co foil, CoO and  $\text{Co}_3\text{O}_4$  are 7718.408, 7708.960, 7718.750 and 7721.194, respectively. As observed, the spectra for the samples are similar to those obtained for the CoO standard, in which  $\text{Co}^{2+}$  is coordinated six-fold with  $\text{O}^{2-}$  ions, suggesting that Co ions exist in a divalent state in six coordinated oxygen atoms [12]. Figure 4 (b) shows XANES spectra of  $\text{CoFe}_{1.9}\text{Zn}_{0.1}\text{O}_4$ , Fe foil, FeO,  $\text{Fe}_3\text{O}_4$  and  $\text{Fe}_2\text{O}_3$  in the vicinity of the Fe K-edge, with their  $E_0$  of 7125.540, 7112.061, 7121.192, 7124.186 and 7125.525, respectively, which leads to existence of  $\text{Fe}^{3+}$  in the samples. Fig. 4 (c) shows that the threshold energy of  $\text{CoFe}_{1.9}\text{Zn}_{0.1}\text{O}_4$  samples is higher than that of Zn foil, but close to the energy of ZnO. The  $E_0$  values of  $\text{CoFe}_{1.9}\text{Zn}_{0.1}\text{O}_4$ , Zn foil and ZnO are 9661.148, 9658.964 and 9661.104, respectively, suggesting existence of a divalent state of Zn in the samples.

## Conclusion

In summary, zinc doped  $\text{CoFe}_2\text{O}_4$  powders were synthesized successfully by the mixed-oxide method. The structural characteristics revealed that all samples have a single spinel structure, and Rietveld refinement showed that the lattice parameters were decreased by Zn content, whereas the size of particles increased. VSM measurements showed that saturated magnetization of the samples increased with increasing Zn content. The coercivity and remnant magnetization of the samples decreased with increasing Zn content, which attributed to the anisotropic nature of Co ions. Furthermore,  $\text{Co}^{2+}$ ,  $\text{Fe}^{3+}$  and  $\text{Zn}^{2+}$  ions are the valence states of element in the structure.

## Acknowledgments

This work has been fully supported by research fund from KMITL research Fund. This research is also partly supported by grants from the National Research Council of Thailand (NRCT), National Nanotechnology Center (NANOTEC) NSTDA, through its Center of Excellence Network, and the Thailand Research Fund (Grant No. BRG5680006). R. Roongtao would like to acknowledge the Ph.D. scholarship provided by Synchrotron Light Research Institute (Public Organization). The authors would like to thank Department of Physics, Kasetsart University (KU) for VSM measurement.

## References

1. L. Zhao, H. Yang, X. Zhao, L. Yu, Y. Cui, and S. Feng, Magnetic properties of  $\text{CoFe}_2\text{O}_4$  ferrite doped with rare earth ion. *Materials Letter*. **60**, 1–6 (2006).
2. Y. Köseoğlu, A. Baykal, F. Gözüak, and H. Kavas, Structural and magnetic properties of  $\text{Co}_x\text{Zn}_{1-x}\text{Fe}_2\text{O}_4$  nanocrystals synthesized by microwave method. *Polyhedron*. **28**, 2887–2892 (2009).
3. R. C. Buchanan, *Ceramic Materials for Electronics*. USA: Marcel Dekker, 2004.
4. A. Goldman, *Modern Ferrite Technology*. USA: Pittsburgh, 2006.
5. G. H. Haertling, Ferroelectric ceramics: history and technology. *J Am Ceram Soc*. **82**, 797–818 (1999).
6. Y. Köseoğlu, F. Alan, M. Tan, R. Yilgin, and M. Öztürk, *Low temperature hydrothermal synthesis and characterization of Mn doped cobalt ferrite nanoparticles*. *Ceram Int*. 2012 (in press).
7. R. D. Shannon, Revised Effective Ionic Radii and Systematic Studies of Interatomic Distances in Halides and Chalcogenides. *Acta Crystallogr*. **A32**, 751–767 (1976).
8. A. J. Moulson and J. M. Herbert, *Electroceramics*. England: John Wiley & Sons, 2003.
9. M. H. Nilsen, C. Nordhei, A. L. Ramstad, D. G. Nicholson, M. Poliakoff, and A. Cabañas, XAS (XANES and EXAFS) Investigations of nanoparticulate ferrites synthesized continuously in near critical and supercritical water. *J Phys Chem C*. **111**, 6252–6262 (2007).
10. M. F. F. Lelis, A. O. Portob, C. M. Gonçalvesb, and J. D. Fabris, Cation occupancy sites in synthetic Co-doped magnetites as determined with X-ray absorption (XAS) and Mössbauer Spectroscopies. *J Magn Magn Mater*. **278**, 263–269 (2004).
11. G. Bonsdorf, M. A. Denecke, K. Schäfer, S. Christen, H. Langbein, and W. Gunßer, X-ray absorption spectroscopic and Mössbauer studies of redox and cation-ordering processes in manganese ferrite. *Solid State Ionics*. **101–103**, 351–357 (1997).
12. M. F. F. Lelis, A. O. Portob, C. M. Gonçalvesb, and J. D. Fabris, Cation occupancy sites in synthetic Co-doped magnetites as determined with X-ray absorption (XAS) and Mössbauer Spectroscopies. *J Magn Magn Mater*. **278**, 263–269 (2004).



## BIOGRAPHY

Name - Surname : Rachanusorn Roongtao

Date of Birth : 1 July 1983

Province : Nakhon Ratchasima

Education : B. Sc. (Gemological Technology), Burapha University,  
Chon Buri (2005)  
M. S. (Materials Science), Chiang Mai University,  
Chiang Mai (2010)

Scholarship : Ph. D. scholarship from Synchrotron Light Research  
Institute (Public Organization)

### Publication:

1. Rachanusorn Roongtao, Rattana Baitahe, Naratip Vittayakorn, Wantana Klysubun and Wanwilai C. Vittayakorn, "Structural and Magnetic Properties of Zn Doped  $\text{CoFe}_2\text{O}_4$ ", *Integrated Ferroelectrics*, **148**, 145–152 (2013).
2. Rachanusorn Roongtao, Rattana Baitahe, Naratip Vittayakorn, Panpailin Seeharaj and Wanwilai C. Vittayakorn, "Influence of Mn Doping on the Magnetic Properties of  $\text{CoFe}_2\text{O}_4$ ", *Ferroelectrics*, **459**, 119–127 (2014).
3. Rachanusorn Roongtao, Naratip Vittayakorn, Wantana Klysubun, Wanwilai C. Vittayakorn, "Effect of Annealing Time on the Cation Distribution in Mn Doped  $\text{CoFe}_2\text{O}_4$  via Extended X-Ray Absorption Fine Structure", *Ferroelectrics*, **492**, 43–53 (2016).

### International Conferences:

1. Rachanusorn Roongtao, Naratip Vittayakorn, Wanwilai Vittayakorn "Doping effects on the phase formation, microstructural and magnetic properties of manganese doped cobalt ferrites" *The 38<sup>th</sup> Congress on Science and Technology of Thailand (STT 38)*, 17-19 October 2012, Chiang Mai, Thailand (Oral presentation).

This material is reserved for educational use only, not allowed for commercial use.

Forbidden to modify the content, and cite the document when use.

2. **Rachanusorn Roongtao**, Rattanai Baitahe, Naratip Vittayakorn, Panpailin Seeharaj and Wanwilai C. Vittayakorn, "Influence of Mn Doping on the Magnetic Properties of  $\text{CoFe}_2\text{O}_4$ " *The 8<sup>th</sup> Asian Meeting on Ferroelectrics (AMF-8)*, December 11-14, 2012, Amari Orchid Hotel, Pattaya, Thailand (Oral presentation).

3. **Rachanusorn Roongtao**, Rattanai Baitahe, Naratip Vittayakorn, Panpailin Seeharaj and Wanwilai C. Vittayakorn, "Structural and Magnetic Properties of Zn Doped  $\text{CoFe}_2\text{O}_4$ " *Special International Workshop and Symposium on Emerging Frontiers in Multiferroics and Electronic Metamaterials (INAMM)*, December 9-10, 2012, Amari Orchid Hotel, Pattaya, Thailand (Poster presentation).

4. **Rachanusorn Roongtao**, Naratip Vittayakorn, Wantana Klysubun, Wanwilai C. Vittayakorn, "Effect of Annealing Time on the Cation Distribution in Mn Doped  $\text{CoFe}_2\text{O}_4$  via Extended X-Ray Absorption Fine Structure" *The Joint Conference of 9<sup>th</sup> Asian Meeting on Ferroelectrics & 9<sup>th</sup> Asian Meeting on Electroceramics (AMF-AMEC-9)*, October 25-31, 2014, International Convention Center Shanghai, Shanghai, China (Oral presentation).

#### National Conferences:

1. **Rachanusorn Roongtao**, Naratip Vittayakorn and Wanwilai Vittayakorn "Magnetic Properties of Manganese-Doped Cobalt Ferrite by Solid State Method" *The 7<sup>th</sup> Annual Conference of the Thai Physics Society (SPC2012)*, 9-12 May 2012, The Krungsri River, Phranakhon Si Ayutthaya, Thailand (Poster presentation).